eurad

European Joint Programme on Radioactive Waste Management

Deliverable 15.6: Novel materials and processes for the optimisation of long-term container performance

Work Package 15 ConCorD

Document information

Project Acronym	**EURAD**
Project Title	**European Joint Programme on Radioactive Waste Management**
Project Type	**European Joint Programme (EJP)**
EC grant agreement No.	**847593**
Project starting / end date	**1st June 2019 – 30 May 2024**
Work Package No.	**15**
Work Package Title	**Container Corrosion under Disposal conditions**
Work Package Acronym	**ConCorD**
Deliverable No.	**15.6**
Deliverable Title	**Novel materials and processes for the optimisation of long-term container performance**
Lead Beneficiary	**VTT Technical Research Centre of Finland**
Contractual Delivery Date	**30/04/2024**
Actual Delivery Date	**06/05/2024**
Type	**Report**
Dissemination level	**Public**
Authors	**Roberto Gaggiano (ONDRAF/NIRAS), Aurélien Debelle (ANDRA), Fabrice Rossignol (Unilim), Inaki Cornu (Unilim), Cedric Bosch (EMSE), Patrick Ganster (EMSE), Rita De Cassia Costa Dias (EMSE), Sergey Sayenko (KIPT), Alex Kuprin (KIPT), Andressa Trentin (VTT), Jukka Vaari (VTT), Janne Pakarinen (VTT)**

To be cited as:

Gaggiano, R., Debelle, A., Rossignol F., Cornu, I., Bosch, C., Ganster, P., Dias, R. De C. C. D., Sayenko, S., Kuprin, A., Trentin, A., Vaari J., Pakarinen, J. (2024): Deliverable 15.6: Novel materials and processes for the optimisation of long-term container performance. Final version as of 06.05.2024 of deliverable D15.6 of the HORIZON 2020 project EURAD. EC Grant agreement no: 847593.

Disclaimer

All information in this document is provided "as is" and no guarantee or warranty is given that the information is fit for any particular purpose. The user, therefore, uses the information at its sole risk and liability. For the avoidance of all doubts, the European Commission or the individual Colleges of EURAD (and their participating members) has no liability in respect of this document, which is merely representing the authors' view.

EURAD (Deliverable n° 15.6) - Novel materials and processes for the optimisation of long-term container performance
Dissemination level: Public
Date of issue of this report: **06/05/2024**

Page

Acknowledgement

This document is a deliverable of the European Joint Programme on Radioactive Waste Management (EURAD). EURAD has received funding from the European Union's Horizon 2020 research and innovation programme under grant agreement No 847593.

Status of deliverable		
	By	*Date*
Delivered (Lead Beneficiary)	Janne Pakarinen	03.05.2024
Verified (WP Leader)	Nikitas Diomidis	06.05.2024
Reviewed (Reviewers)	Fraser King, Bharti Reddy, Guido Bracke, Satoru Suzuki, Chrstina Lilja	21.04.2024
Approved (PMO)		
Submitted to EC (Coordinator)	Andra (Coordinator)	06.05.2024

EURAD (Deliverable n° 15.6) - Novel materials and processes for the optimisation of long-term container performance
Dissemination level: Public
Date of issue of this report: **06/05/2024**

Page

Executive Summary

Task 2 of the Container Corrosion under Disposal conditions (ConCorD) work package aimed to explore the potential of novel materials and processes for the optimization of long-term container performance for high-level waste disposal. The task focused on the experimental work on ceramic and metallic materials for bulk containers and coatings. The main achievements of the task include the development of new alumina-based materials for sealing bulk ceramic containers by microwave heating, the determination of the optimal parameters for sintering high-density silicon carbide, the comparison of the performance of different copper grades in simulated groundwater, and the production and testing of various ceramic and metallic coatings by cathodic arc evaporation and cold spray processes.

The task also outlines the future research directions for the development of novel materials for containers. Ceramic materials have high corrosion resistance and low gas formation, but their mechanical strength and sealing processes need to be improved. Metallic materials can offer corrosion resistance depending on the alloy composition and the coating technology, but the overall understanding of their degradation mechanisms under repository conditions requires further work. Alumina-based ceramics can be sealed by microwave heating with specially designed sealing materials, and hetero-aggregation can be used to improve the microwave coupling of the sealing material via a nano-structuration process. SiC-based ceramics can be doped with Cr to increase their fracture toughness and corrosion resistance and can be joined by laser or glass-ceramic methods. CrN-based and TiO_2-based coatings, whose properties can be tailored by varying the deposition parameters, can provide high corrosion protection for steel substrates.

EURAD (Deliverable n° 15.6) - Novel materials and processes for the optimisation of long-term container performance
Dissemination level: Public
Date of issue of this report: 06/05/2024

Page

1. Table of Contents

EURAD (Deliverable n° 15.6) - Novel materials and processes for the optimisation of long-term container performance
Dissemination level: Public
Date of issue of this report: 06/05/2024

Page

List of Figures

EURAD (Deliverable n° 15.6) - Novel materials and processes for the optimisation of long-term container performance
Dissemination level: Public
Date of issue of this report: 06/05/2024

Page

eurad
European Joint Programme
on Radioactive Waste Management

EURAD (Deliverable n° 15.6) - Novel materials and processes for the optimisation of long-term container performance
Dissemination level: Public
Date of issue of this report: 06/05/2024

Page

EURAD (Deliverable n° 15.6) - Novel materials and processes for the optimisation of long-term container performance
Dissemination level: Public
Date of issue of this report: 06/05/2024

Page

EURAD (Deliverable n° 15.6) - Novel materials and processes for the optimisation of long-term container performance
Dissemination level: Public
Date of issue of this report: 06/05/2024

Page

EURAD (Deliverable n° 15.6) - Novel materials and processes for the optimisation of long-term container performance
Dissemination level: Public
Date of issue of this report: 06/05/2024

Page

European Joint Programme on Radioactive Waste Management

List of Tables

EURAD (Deliverable n° 15.6) - Novel materials and processes for the optimisation of long-term container performance
Dissemination level: Public
Date of issue of this report: 06/05/2024

Page

EURAD (Deliverable n° 15.6) - Novel materials and processes for the optimisation of long-term container performance
Dissemination level: Public
Date of issue of this report: 06/05/2024

Page

List of Abbreviations

BWR	Boiling Water Reactor
CAE	Cathodic Arc Evaporation
CE	Counter Electrode
CNA	Common Neighbor analysis
CR	Corrosion Rate
CS	Cold Spray
EEC	Electrical Equivalent Circuit
EIS	Electrochemical Impedance Spectroscopy
FCC	Face-Centered-Cubic
FESEM	Field Emission Scanning Electron Microscope
FIB	Focused Ion Beam
HCP-Cu	High Conductivity Phosphorous copper
HLW	High Level Waste
HMMS	Hot Melt Mass Spectroscopy
IPD	Integrated Passive Device
IR	Infrared
LWR	Light Water Reactors
MIC	Microbially Induced Corrosion
MMC	Metal-Matrix Composite
MS	Magnetron Sputtering
MSD	Mean Square Displacement
NWMO	Canadian Nuclear Waste Management Organization
OCP	Open Circuit Potential
OFP-Cu	Oxygen-Free Phosphorus-doped copper
PVD	Physical Vapor Deposition
RF	Radiofrequency
SCC	Stress Corrosion Cracking
SCE	Saturated Calomel Electrode
SNF	Spent Nuclear Fuel
VNA	Vector Network Analyzer

EURAD (Deliverable n° 15.6) - Novel materials and processes for the optimisation of long-term container performance
Dissemination level: Public
Date of issue of this report: 06/05/2024

Page

2. Introduction

Consideration of candidate material solutions for the containment and storage of nuclear waste has been the topic of research during the past 40-50 years. The options range from carbon steel with an adequate corrosion allowance, or outer corrosion resistant barrier, to passive metals and ultimately to ceramics. A wide range of alloys have been considered as candidate container materials for the disposal of nuclear waste (Holdsworth 2013, Holdsworth 2014, Holdsworth 2018). The waste container is the main barrier in the overall waste-disposal system and is therefore an essential part of the multibarrier systems designed for deep geological disposal. For the disposal of Spent Nuclear Fuel (SNF) or vitrified High Level Waste (HLW), the container is required to provide absolute containment for a given period (e.g. during a period of significant heat emission, typically several thousand years). In the currently researched disposal concepts, the canister must enclose the spent fuel and prevent dispersion of radioactivity to the surroundings, be watertight, withstand corrosion processes, and withstand mechanical stresses (Nuclear Energy Agency 2003).

To select a material and associated design for HLW/SF containers, different factors that influence their durability over the whole life cycle, from manufacture to eventual failure at long times post closure need to be understood. A wide range of container materials and designs are currently being considered and developed in different national programs (Table 1). The choice of container material and design is always site and disposal concept-specific, but it is also important to consider the expected durability of a variety of designs in a range of plausible geochemical environments and consider other aspects such as manufacturing viability, and associated costs (King, 2004).

Container failure in the long term is unlikely to occur due to purely mechanical- or corrosion-related mechanisms but rather from a combination of plastic deformation and buckling following a period of corrosion during which the container wall thickness has been reduced and/or the material properties have been degraded. Mechanical loads can influence corrosion processes and corrosion processes can influence mechanical failure modes. For example, the general corrosion of the container material will reduce the wall thickness, leading to an increase in the probability of plastic collapse (King, 2017).

The main goal of Task 2 of ConCorD (Work Package 15) was to explore the potential of novel materials and processes for the optimisation of container performance. For the most promising novel materials, the planned experimental studies contributed to the understanding of corrosion/degradation processes. The work was organised according to the two main types of material classes: ceramic and metallic materials. In the case of ceramic materials, the experimental work was focused on studying materials and processes (deposition, sealing) for innovative solutions of ceramic containers and ceramic coatings on steel. For containers made of bulk ceramics, the key properties for long-term performance are fracture toughness and leaching/alteration. For thin coatings, a primary concern would be the presence of through-porosity or flaws. For metallic materials, the main aim of the experimental work was to study and consider the implementation of innovative solutions for metallic anti-corrosion coatings or optimised bulk metallic options. Studies focused on material development (alloy composition, coating technology) and initial corrosion tests to identify the benefit of these new container solutions.

The aim of this report is to provide a vision of the use of possible novel materials for HLW/SNF containers, based on the available literature data and the current results of the EURAD ConCorD WP.

2.1. Currently existing material solutions

There are several different nuclear waste disposal canister concepts proposed for adoption worldwide, their configuration depending mainly on the type of waste to be disposed of, the surrounding geological structure, and the material solution adopted to minimise the risk of loss of canister integrity. Copper (i.e. Sweden, Finland and Canada) and carbon steels (i.e. Belgium, France, Switzerland, Czech Republic, Slovakia, Hungary and Japan) are the container materials that have been traditionally considered for the disposal of SNF/HLW in countries with advanced disposal programs (see Table 1). The corrosion

EURAD (Deliverable n° 15.6) - Novel materials and processes for the optimisation of long-term container performance
Dissemination level: Public
Date of issue of this report: 06/05/2024

Page

behaviour of the types of containment systems typically envisaged in geological disposal is generally well understood, although, after many years of active research, areas of some uncertainty (typically covered by existing R&D programs) still exist. The understanding of degradation mechanisms and resulting durability estimates is particularly mature for disposal concepts envisaging the use of copper and carbon steels in conjunction with clay buffers (particularly bentonite) but also for concepts making use of concrete buffers/liners (Padovani, 2017).

EURAD (Deliverable n° 15.6) - Novel materials and processes for the optimisation of long-term container performance
Dissemination level: Public
Date of issue of this report: 06/05/2024

Page

Table 1. Currently existing canister materials and illustrative environmental conditions for various WMO repository designs (Gaggiano & Diomidis, 2023)

Country	Container materials and design and typical/minimal thickness	Buffer type, pH	Host rock	Groundwater
Belgium	Carbon steel container with cast iron insert	Portland cement, pH 13.5	Boom clay	Reducing $NaHCO_3$ waters, pH 8.5
Canada	Carbon steel member (30-47 mm) with copper coating (3 mm)	Bentonite, pH 7-8	Crystalline rock	Reducing Na-Ca-SO_4-Cl type water, saline, pH 5-8
			Sedimentary rock	Reducing Na-Ca-SO_4-Cl type water, highly saline, pH 6.3
Finland	Copper shell (50 mm) with massive cast iron insert	Bentonite, pH 7-8	Crystalline/granitic rock	Brackish Na-Cl to saline Na-Ca-Cl waters. Eh –300 mV, pH 7.5–8
France	Carbon steel container (65 mm)	Cementitious, pH~13	Callo-Oxfordian clay	Reducing Ca–Na–CO_3 waters, near-neutral pH
Japan	Carbon steel container (190 mm)	Compacted clay (pH 7-8)	Not determined	Not determined
Sweden	Copper shell (50 mm) with massive cast iron insert	Bentonite, pH 7-8	Crystalline/granitic rock	Dilute Na–HCO_3 waters, brackish Na–Ca–Cl waters and saline Ca–Na–Cl waters. Reducing Eh
Switzerland (Reference)	Forged carbon steel canister (140 mm)	Bentonite, pH 7-8	Opalinus clay	Reducing, near-neutral, Na–Cl waters
Switzerland (Alternative)	Carbon steel canister (120 mm) with copper coating (3 mm)	Bentonite, pH 7-8	Opalinus clay	Reducing, near-neutral, Na–Cl waters
UK (Variant 1)	Copper shell (50 mm) with massive cast iron insert	Bentonite, pH 7-8	Not determined	Assumed reducing
UK (Variant 2)	Carbon steel container (min 70 mm)	Bentonite, pH 7-8	Not determined	Assumed reducing

EURAD (Deliverable n° 15.6) - Novel materials and processes for the optimisation of long-term container performance
Dissemination level: Public
Date of issue of this report: 06/05/2024

Page

2.2.   Relevant requirements determining the material choice

Various factors need to be considered in the selection of alternative container materials. These factors can be divided between those determined by the material characteristics and the nature of the service environment (e.g., mechanical and corrosion resistance) and those determined by the broader requirements of the overall waste management program (e.g. minimum canister lifetime). In this context, on top of the choice of the material, the production route for the canister is also very important.

2.3.   Functional requirements

The most basic functional requirements of disposal canisters are to contain and isolate the spent fuel and high-level waste so that safety is maintained at a high level for people and the environment during fuel encapsulation, transport and handling of canisters, emplacement of canisters in the final repository and in terms of meeting the long-term performance requirements of the disposal system. The canister design achieves this by providing (Johnson et al., 2003):

- a **method of** containment of the waste that permits safe handling, interim buffer storage and emplacement in the repository;

- a **structural barrier** against the hydrostatic pressures and other mechanical forces that might compromise containment, by providing an absolute barrier to radionuclide release for the design lifetime of the canister;

- a **transport barrier** against contaminant release to the groundwater after eventual breaching, by inhibiting the transport of radionuclides through the breached part of the canister.

2.4.   Long-term performance requirements

The choice of a novel canister material will be influenced by the target canister's lifetime, which may be specified by a regulatory requirement or by a functional requirement to enable safe handling. Canister lifetime targets ranging from 1'000 to 100'000 years have been proposed in various national programs for high-level waste and spent fuel disposal. The broad range relates to different judgements made about the relative contributions to the safety of the different components of the disposal system. Having defined the target canister lifetime(s), there is then the need to select a canister material to meet that target for the given environment (Johnson et al., 2003) (King et al., 2010).

Containers will likely fail due to mechanical instability following a period of environmental degradation (i.e., corrosion damage). Therefore, both the mechanical integrity and the (general and localised) corrosion resistance are important.

The risks associated with mechanical integrity for novel canister materials can be divided into two sub-categories, one concerned with handling, and the second concerned with disposal. While the evaluation of mechanical integrity risks can be based on specific disposal load cases, their consideration in terms of mechanical handling normally needs to be more generic (Holdsworth et al., 2014).

In addition to good mechanical stability, novel container materials need to provide good general and localised corrosion resistance. Candidate advanced materials generally fall into one of two categories: corrosion allowance materials (e.g., steel) and corrosion-resistant materials (e.g., Ti-based and Ni-based alloys, copper). The prediction of the durability of the containers using advanced materials and the uncertainties associated with durability estimates, is a key input for the performance assessments (King et al., 2010).

EURAD (Deliverable n° 15.6) - Novel materials and processes for the optimisation of long-term container performance
Dissemination level: Public
Date of issue of this report: 06/05/2024

Page

2.5. Mechanical resistance

Mechanical failure modes are defined as any process that, in the absence of a corrosive environment, may lead to container failure. Failures can usefully be classified as resulting in either brittle fracture or ductile collapse (or some combination of the two) and, may be accelerated by exposure to the repository environment (King, 2014).

The risks associated with mechanical integrity can be divided in two sub-categories, one concerned with handling, and the second concerned with disposal. Load cases concerned with disposal can be relatively easy to formulate (since they depend on the specific disposal load cases) whereas those concerned with handling are not, since they depend on the specific canister design, handling, and emplacement method.

In the specific case of coatings, their long-term mechanical performance is strongly related to the presence of inherent porosity, macro defects and cracking due to internal stress or mechanical damage. Very thin coatings are notoriously difficult to apply uniformly, and without defects, on the surfaces of very large parts, in particular when the coating process involves containment to ensure well controlled environmental conditions (Holdsworth, 2018).

2.6. Corrosion resistance

In contrast to mechanical failure, it is not possible to eliminate all potential corrosion failure modes by appropriate container design. It is therefore accepted that the container will be subject to one or more forms of corrosion, which will ultimately determine the service life (King, 2014).

The form(s) of corrosion that could lead to canister failure will depend on both the material and the nature of the disposal environment. It is important to note that not all forms of corrosion will always occur because as the repository environment evolves so too will the corrosion behaviour of the canister. For a repository environment that evolves from initially warm and aerobic to cool and anaerobic in the long-term, rapid forms of localized corrosion will generally give way to slow uniform corrosion processes (King et al., 2010) (Holdsworth, 2014). The relevant corrosion processes considered for the evaluation of candidate/novel canister materials are the following:

- **General/Uniform corrosion**: it results in general loss of wall thickness but will typically not be life limiting as the canister is expected to fail by plastic collapse before penetration by corrosion. A simple method for predicting the lifetime of a container subject to general corrosion is to use an empirically measured corrosion rate (King, 2014) (King et al., 2010)

- **Localized corrosion**: Passive alloys, such as the Ni-based and Ti-based alloys, may be subject to localized corrosion which can occur, for example, in the form of pitting or stress corrosion cracking. These forms of corrosion consist of the preferential dissolution of the surface in discrete localised regions and tend to cause localized wall penetration, which could lead to failure before the plastic collapse of the canister. In localized corrosion, two stages can be identified, namely initiation and propagation. While it is necessary to know if a material is susceptible to the initiation of a local corrosion process, it is equally important to understand subsequent propagation characteristics and, for example, if the development of the process becomes self-arresting. In some cases, it is possible to demonstrate that localised corrosion processes will not initiate and that no localized penetration will occur (for example based on threshold potentials for initiation or using commonly accepted threshold temperatures for localized corrosion). It is also possible to calculate the extent of propagation and the time to completely penetrate the canister wall.

EURAD (Deliverable n° 15.6) - Novel materials and processes for the optimisation of long-term container performance
Dissemination level: Public
Date of issue of this report: 06/05/2024

Page

2.7. Impact on the geological barrier

The canister material should not adversely affect the performance of other barriers in the system. For example, chemical and physical interactions should not lead to the degradation of surrounding barriers in a way that could increase the rate of mass transport of radionuclides. Some processes that need to be considered include excessive temperatures, volume changes arising from corrosion product formation and excessive production of H_2 (Holdsworth, 2014).

3. Ceramic Materials and Coatings

Ceramics are classified as inorganic and non-purely metallic materials (in other words, they are not metals nor polymers). Very often, ceramics are divided into two categories: traditional ceramics and advanced (or technical) ceramics. The former includes objects like tiles, bricks, plates, and sanitary ceramics for instance, while the latter can be found in many, diverse fields such as microelectronics (diodes), automotive (sparkplugs), aeronautics (nose cones and brakes of airplanes), health (dental crowns), and nuclear energy (nuclear fuel) to cite a few important ones. The ability of ceramics to be used in so many advanced fields is related to the possibility of combining different compounds and tuning the material structure, to tailor their chemical and physical properties, for instance from highly insulating to superconducting. However, as ceramics are characterized by mixed ionic/covalent bonds, they generally exhibit common features: they are brittle, refractory, chemically stable, (usually) oxidation resistant, and hard.
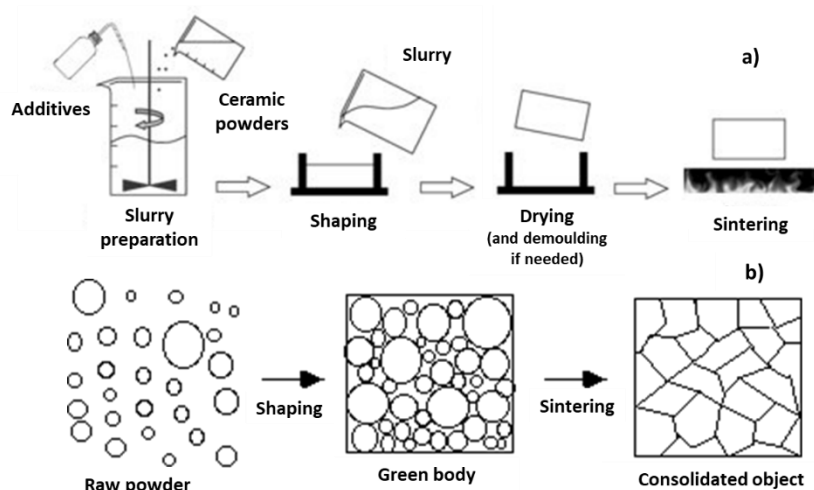
Figure 1. Illustrative representations of the different steps in the manufacturing of monolithic ceramics objects, a) at the macroscopic scale, and b) at the microstructure level.

To fabricate ceramics, many processes can be implemented, but they all rely on some common steps. First, preparation of the base material made of thoroughly blended (very) fine powders. For non-traditional ceramics, chemically prepared powders are used as starting materials; these synthetic powders are precisely controlled in terms of chemical compositions and particle size distribution. The second step is to form the ceramic particles into a desired shape in which the granular compact is controlled. This is accomplished by producing a slurry formed by the addition of water and/or additives such as binders and plasticizers to the powders, followed by a shape forming process that includes, e.g., extrusion, injection molding, and slip or tape or gel casting (Figure 1). This shaped product, named 'green body', is usually temporarily stored for drying. Then, it must undergo a heat-treatment at a relatively high temperature (roughly 1300–1800 °C) called sintering or sometimes, firing (note that a debinding pretreatment at a much lower temperature can be carried out before the sintering step). The high temperature allows the tiny grains of the individual ceramic components to fuse to form necks

leading to grains, and resulting in a rigid, dense (consolidated) object. It can be noted that a ceramic manufacturing process involves many steps (whose schematic representations are given in Figure 1, with a) showing the steps at the macroscopic scale, and b) displaying the microstructure evolution; the perfect control of these steps is not straightforward, leading to a certain complexity in achieving the desired material shape and properties, particularly if thick objects, or out of regular range properties are desired.

HLW containers must satisfy several requirements that can be gathered into one major obligation: being watertight over an adequate radioactive (or thermal power) decay period that can last centuries. This requirement is related to both mechanical and chemical durability throughout this period. The material used for the container must hence exhibit relevant mechanical and chemical resistance in the field conditions that can be aggressive (a few MPa of mechanical load, along with corrosive groundwater (alkaline or saline, at ~90 °C, water). Because of the complexity of the fabrication (particularly the drying step of the green body for thick pieces), and because of the usual intrinsic physical properties of ceramics (their brittleness is important to consider here), manufacturing a ceramic based HLW container constitutes a challenging task to address. Note that if one would consider ceramics for spent fuel containers, then the difficulty would be even larger, as the corresponding waste are generally much larger Furthermore, another issue to tackle is the sealing of the body and the lid of the container because traditional methods used for metals cannot be used for ceramics, as their melting temperature is too high. *Ad hoc* processes (which include both the heating method and the sealing material) must hence be developed.

These requirements apply to monolithic HLW ceramic containers. Another option is to develop a ceramic coating to prevent, or at least significantly limit, steel corrosion. In that case, the coating must (i) be waterproof, which requires a very low through porosity, (ii) strongly adhere to the steel substrate, and (iii) exhibit good wear resistance (if the container is not directly placed at the right location inside the cell, but pushed to its final place, as during this step, interactions with the cell liner or with the rock may damage the coating).

3.1. Ceramic containers

3.1.1. Alumina

The state of the art (Baroux, 2013) shows that ceramics are an attractive option owing to their high corrosion resistance and lack of gas formation during disposal (Holdsworth et al., 2014). Their fracture toughness (i.e., brittle nature) is however low in comparison to metals. In addition, in order to sustain the expected mechanical load in the repository, the thickness of the ceramic container wall should lie in the few cm range. Fabricating such thick, large ceramic parts is a technical issue to tackle; in addition, developing sealing processes (to seal the lid and the body of the containers) constitutes another technical issue that must be solved (Landolt et al., 2011).

The lack of interest within the ceramic community in the production of large ceramic pieces is mainly due to the fact that there is only a low demand for large-diameter ceramic pressure vessels from any other industrial sector. This makes their development difficult in the absence of investments. Part of Task 2 in ConCorD is in this sense a prospective task; in this project, focus has been given to the sealing process of ceramic parts using microwaves and a specially developed sealing material.

The recent work by Kelfayan (2019) allowed testing different glasses as sealing materials using a microwave heating process. This technology can promote a local and preferential heating of materials provided they exhibit a good coupling with the microwaves. Hence, the sealing material must be specifically designed to optimize such a good coupling. Sealing studies were initially realized on cylindrical alumina-based samples with a diameter of 40 mm, and a thickness of 10 mm. Such dimensions were chosen to be as representative as possible of those of ceramic containers (*i.e.*, wall thickness) to be sealed. The results showed that microwave heating is in principle suitable for sealing

EURAD (Deliverable n° 15.6) - Novel materials and processes for the optimisation of long-term container performance
Dissemination level: Public
Date of issue of this report: 06/05/2024

Page

ceramics, but the conclusions highlighted that an effort had to be made for the selection of the sealing materials themselves. In 2020, ConCorD task 2 proposed new intimate materials blends as sealing materials for alumina-based ceramic containers.

Initially, two methods were considered for the preparation of the blends: a modified Stöber process (Beck et al., 1992) (Stöber et al., 1968) and the hetero-aggregation method (Islan et al., 1995) (López-López et al., 2006). The idea here was to improve the microwave coupling of the sealing material through a structural modification at the nanoscale of its different constituents. For instance, the modified Stöber process was proposed to prepare core-shell particles for which the core and the shell differ by their ability to couple microwaves. It was assumed that it could be possible to derive benefit locally (*i.e.*, at the powder grain level) of the best-coupling material to get a localized, efficient, homogeneous, and fast heating process while keeping an overall blend formulation suitable for the sealing. Because of issues in terms of synthesis yield of core-shell particles leading to difficulties for large-scale production, the modified Stöber method was abandoned, and the studies only concentrated on the hetero-aggregation method as described hereafter.

The idea of hetero-aggregation is basically the same as that of core-shell structures, that is taking advantage of the addition to the sealing blend, at the local scale and in low quantity, of a material capable of strongly coupling the microwaves. The first tests were performed on a base sealing blend composed of α-alumina ultrafine powders and amorphous silica nano-powders. Hetero aggregation between these two types of powders was achieved through electrostatic interactions between particles of opposite charges in suspension at a suitable pH. Indeed, the particles may differ in their composition, shape, size and surface charge linked to pH (and/or ionic strength or use of specific adsorbed ionized additives). The case of hetero aggregation of particles with a high size asymmetry like the ones tested in ConCorD indeed allowed the formation of aggregates. Experimental parameters such as the size ratio, the relative concentration of particles, the pH and the ionic strength, could strongly modify that final aggregate structure, as well as the aggregation kinetics.

Figure 2a shows the granulometry of alumina and silica particles used in our study. The particles have a strong size difference. Moreover, there is a pH range, typically between 5.5 and 8, where Al_2O_3 and SiO_2 particles are electrostatically stabilised (*i.e.*, zeta potential over 25 mV in absolute value) with a surface charge of opposite polarity (Figure 2b) and for which the absolute zeta potential difference is maximized.
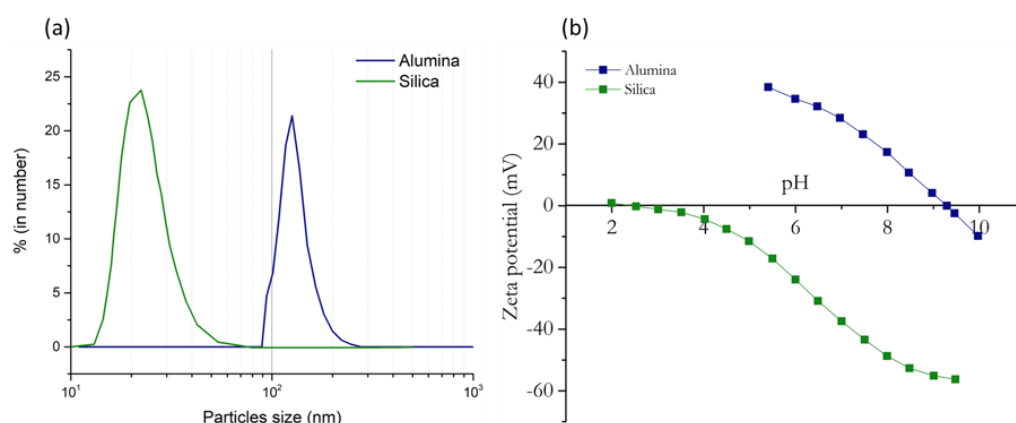
Figure 2. (a) Particle size distribution of Al_2O_3 and SiO_2 (b) Zeta potential of Al_2O_3 and SiO_2 particles.

The pH values in this range allow for an efficient hetero-aggregation between Al_2O_3 and SiO_2 particles. Thanks to IRCER's knowledge of this method (Tran et al., 2015) (Cerbelaud et al., 2009) (Cerbelaud et al., 2010) (Cerbelaud et al., 2018) (Cerbelaud et al., 2020) (Garcia-Perez et al., 2006) (Laganapan et

EURAD (Deliverable n° 15.6) - Novel materials and processes for the optimisation of long-term container performance
Dissemination level: Public
Date of issue of this report: 06/05/2024

Page

al., 2018) (Pagnoux et al., 2009), it was possible to obtain stable suspension of an Al_2O_3-SiO_2 system, which could be cast or coated on the sealing zone. In our study, the hetero-aggregated sealing blends were prepared using a slip-casting method to obtain materials in the form of cylindrical pellets of 10 mm in diameter and 3 mm in thickness. The microstructures of green bodies, shown in Figure 3, were composed of alumina particles homogenously decorated with silica nanoparticles. An illustration is also shown to schematize the hetero-aggregation phenomenon.
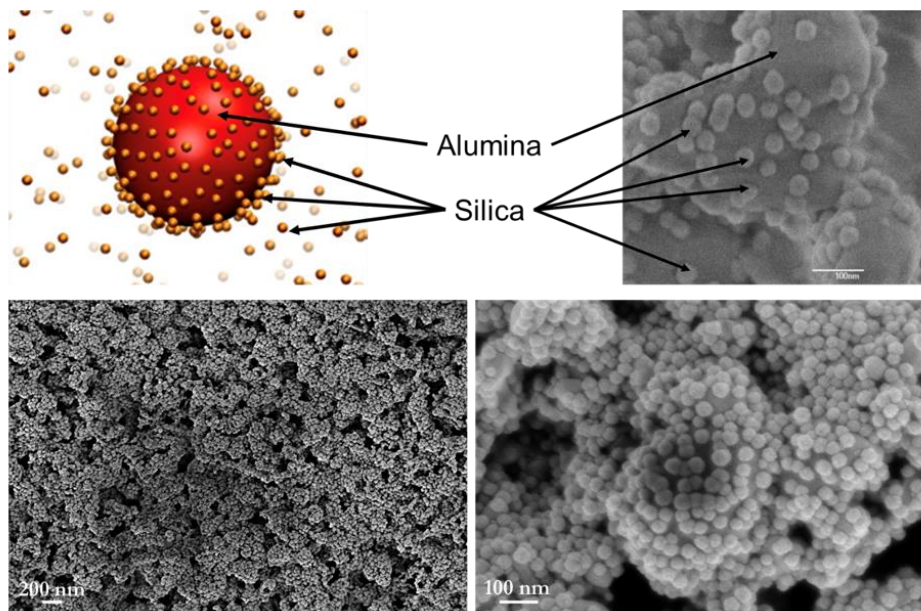
Figure 3. Illustration and SEM images of the Al_2O_3-SiO_2 hetero-aggregation phenomenon.

In order to improve the microwave coupling in the sealing material a microwave susceptor was added in the form of a nanoscale powder of silicon carbide (nano-SiC). A microwave susceptor is a material able to absorb electromagnetic energy and convert it into heat. The nano-SiC is a wide bandgap semiconducting material. Its dielectric properties enable it to absorb microwave energy. The aim here was then to homogeneously disperse the nano-SiC in the sealing material to allow for a favoured and homogeneous microwave heating. A potential explanation for this could be a "pinning" phenomenon of the electromagnetic field on tiny particles[1], but this hypothesis must still be confirmed. The nano-SiC powder presented an average size of around 33 nm (Figure 4a) and a behaviour in suspension close to that of silica with respect to the pH (Figure 4b). So, hetero-aggregation between the nano-SiC and alumina particles was possible.

---

[1] The electromagnetic field could be locally trapped at some small particles.

EURAD (Deliverable n° 15.6) - Novel materials and processes for the optimisation of long-term container performance
Dissemination level: Public
Date of issue of this report: 06/05/2024

Page
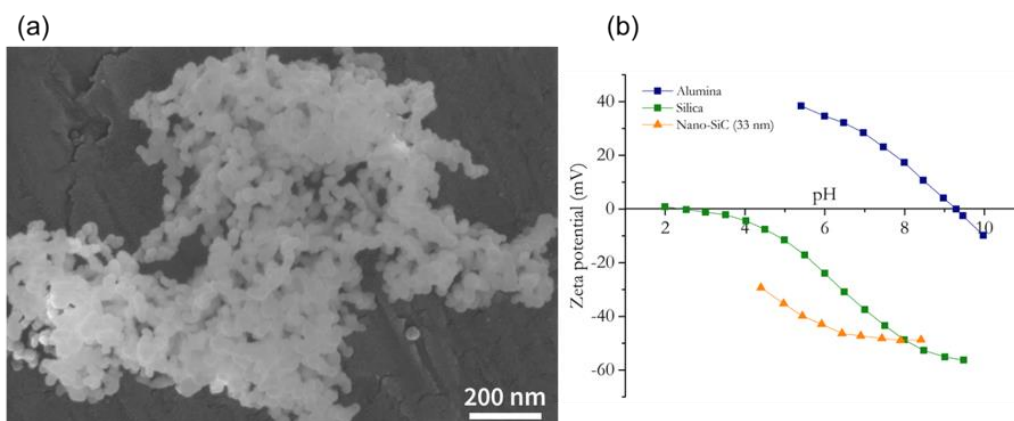
Figure 4. (a) SEM image of nano-SiC, (b) Zeta potential of Al_2O_3, SiO_2 and nano-SiC in water vs. pH.

The use of the nano-SiC was intended to optimize the microwave coupling, but a more general challenge dealing with the targeted application was to enhance the sintering kinetics and/or to lower the sintering temperature of the sealing material. There are basically two approaches to do that. The first approach consists of improving the powder reactivity itself by using fine starting powders and/or shaping the materials using colloidal routes, with the assistance of ultrasound for instance, to better eliminate agglomerates in the green materials afterwards. The second approach is to use sintering aids or additives. Additives in solid solutions can increase diffusion through defect creation and hence promote sintering. Moreover, additives forming a liquid phase can facilitate particle rearrangement and solution/reprecipitation phenomena. So, in this study, the choice was made to use simultaneously these two approaches.

In order to limit the sealing process temperature (to not alter the vitrified waste), the effect of the introduction of additives in the α-alumina powder was studied. Many oxides are good candidates for reducing the α-alumina sintering temperature by forming liquid phases, by themselves or in combination with other oxides. However, the addition of these sintering aids can also promote the formation of anisotropic grains and significantly affect the microstructure of alumina ceramics and their physico-chemical properties.

TiO_2 and CuO are mostly used as sintering aids for low-temperature sintering of alumina ceramics (around 1300-1400 °C as compared to 1500-1600 °C without aids). The sinter-aiding mechanism of the $CuO-TiO_2$ additive is generally ascribed to the formation of a limited substitutional solution and a eutectic phase, thus increasing ion vacancy concentration and atomic diffusion (Fu et al., 2016). In our case, to further improve this $CuO-TiO_2$ sintering aid, the addition of Bi_2O_3, with a low melting point (825°C), was attempted. With this new system, the temperature at which the liquid phase appears is decreased, hence promoting sintering at lower temperatures as well as densification through particle rearrangement. Moreover, like nano-SiC, Bi_2O_3 is an oxide well-known to be a good microwave susceptor (Balaji et al., 2009).

The first heating tests with microwaves, of the previously described blends prepared at IRCER-CNRS, were realized at EMSE in the summer of 2022. The tests were carried out in a microwave set-up with a 2.45 GHz single-mode cavity (Figure 5). This type of cavity allows for the study of the electric and magnetic fields effects independently from one another.

EURAD (Deliverable n° 15.6) - Novel materials and processes for the optimisation of long-term container performance
Dissemination level: Public
Date of issue of this report: 06/05/2024

Page
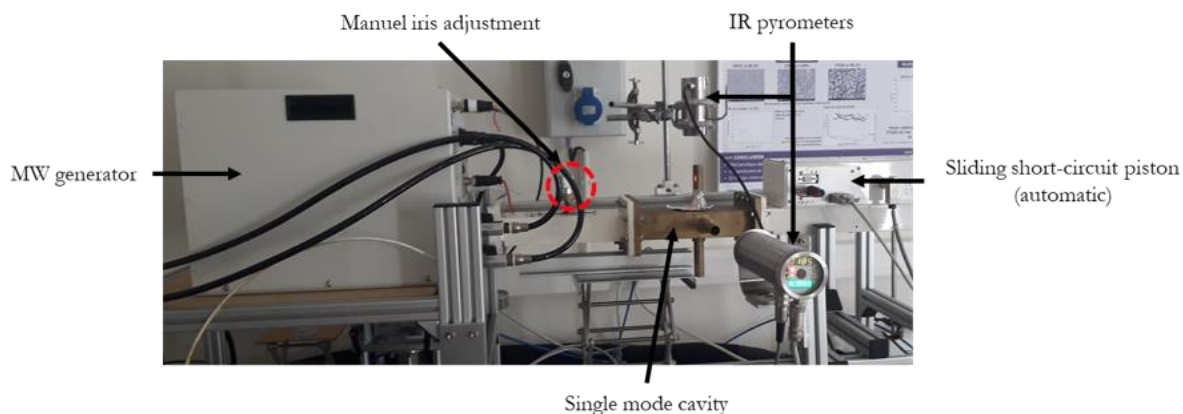
Figure 5. Microwave set-up.

The sample was placed in a single-mode cavity, on a sample holder designed to focus the electromagnetic field on the sample (Figure 6a). The cavity was equipped with two pipes, which allowed for the measurement of sample temperature along two directions using infrared (IR) pyrometers. The pyrometer, in the sample longitudinal axis, allowed for the recording of videos during the microwave tests (Figure 6b). This experimental set-up was controlled with an acquisition and control system allowing adjustment of the short-circuit piston position for resonance research and monitoring of the forward microwave power with an IPD module. However, the impedance adaptation via an iris was manually achieved. In practice, the operator had to minimize the reflected microwave power by adjusting the iris and short-circuit position, which could cause artefacts during the data acquisition.
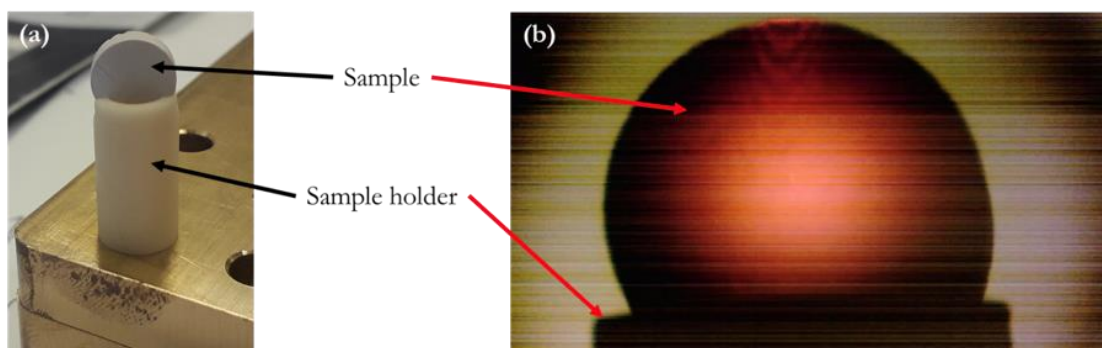
Figure 6. (a) picture of sample & holder, (b) screenshot during video recording of a microwave test.

The microwave tests of sealing materials were carried out by gradually increasing the power input on the sample, with power steps of 5 to 10 W, and 3 to 5 min holding time. It allowed stabilization of sample temperature and minimized the reflected power during the test. These first tests were limited to a maximum temperature of 1000 °C which was the detection limit of the IR pyrometers. The goal was to observe the influence of the composition of sealing materials on the microwave coupling.

The very first microwave tests were carried out on Al_2O_3-SiO_2 ceramic coupons. This first study focused on the influence of the amount of silica on microwave coupling in the sealing material. Figure 7a represents the temperature evolution of samples with different amounts of silica during the microwave heating. The heating behaviour of the samples is similar for the different tested compositions, with a notable sudden increase in the heating rate around 400 °C. However, the samples containing 59.8 and 69 vol% of SiO_2 exhibit a better heating efficiency. Indeed, these samples reach 400 °C in half the time needed for the sample containing 48.5 vol%. of silica. Moreover, Figure 7b shows that the temperature

EURAD (Deliverable n° 15.6) - Novel materials and processes for the optimisation of long-term container performance
Dissemination level: Public
Date of issue of this report: 06/05/2024

Page

of 400 °C is reached with a forward power of 80 W for the samples with the largest silica content, whereas a forward power of 120 W is needed for the sample with the lowest silica amount.
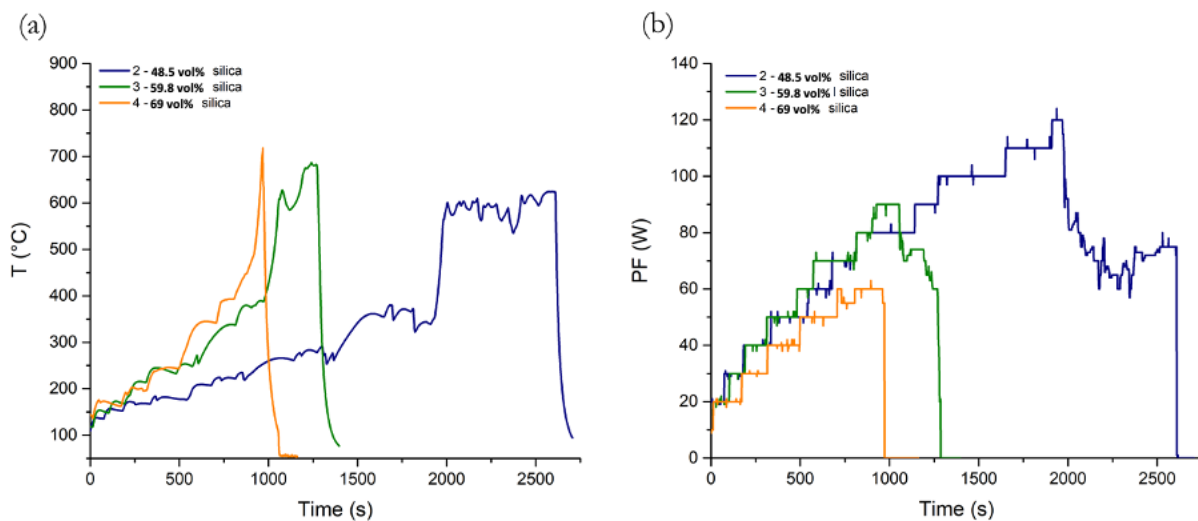
Figure 7. (a) Comparison of microwave coupling for samples containing different amounts of silica, (b) Corresponding forward power input during the microwave tests necessary to reach 400°C.

The improvement of the kinetics of the viscous sintering process in amorphous SiO_2 under microwave heating has already been studied in the literature (Eremeev et al., 2018). It was shown that the mass transport process in the amorphous phase is enhanced because of the microwave electromagnetic field. Thus, the viscous phase of SiO_2 in the Al_2O_3-SiO_2 system could appear at lower temperatures (400°C) than during conventional heating (800 °C). Therefore, the microwave coupling enhancement for samples 3 and 4 (with the highest silica content) is likely due to a fairly high amount of SiO_2 that makes the sample more reactive to the electromagnetic field, leading to a higher heating efficiency (especially between room temperature and 400°C).

The study continued with microwave heating of some modified Al_2O_3-SiO_2 systems. At first, Al_2O_3-SiO_2 formulations, with a fixed content of 48.5 vol.% of silica, and including low amounts, up to 2 vol.%, of nano-SiC were tested. Figure 8a shows a microwave coupling improvement when the amount of nano-SiC increases. The sudden drop in temperature for the sample containing 2 vol% of nano-SiC is due to the manual minimization of the reflected power during the microwave test. As the amount of SiO_2 is constant in all the samples, it is the presence of nano-SiC which makes the samples more reactive to the electromagnetic field, as revealed here by a higher heating efficiency (between 25 and 400 °C). Moreover, the power required to reach 400 °C is lower for samples containing nano-SiC, except for the one containing 0.5 vol%. of nano-SiC (Figure 8b).

EURAD (Deliverable n° 15.6) - Novel materials and processes for the optimisation of long-term container performance
Dissemination level: Public
Date of issue of this report: 06/05/2024

Page
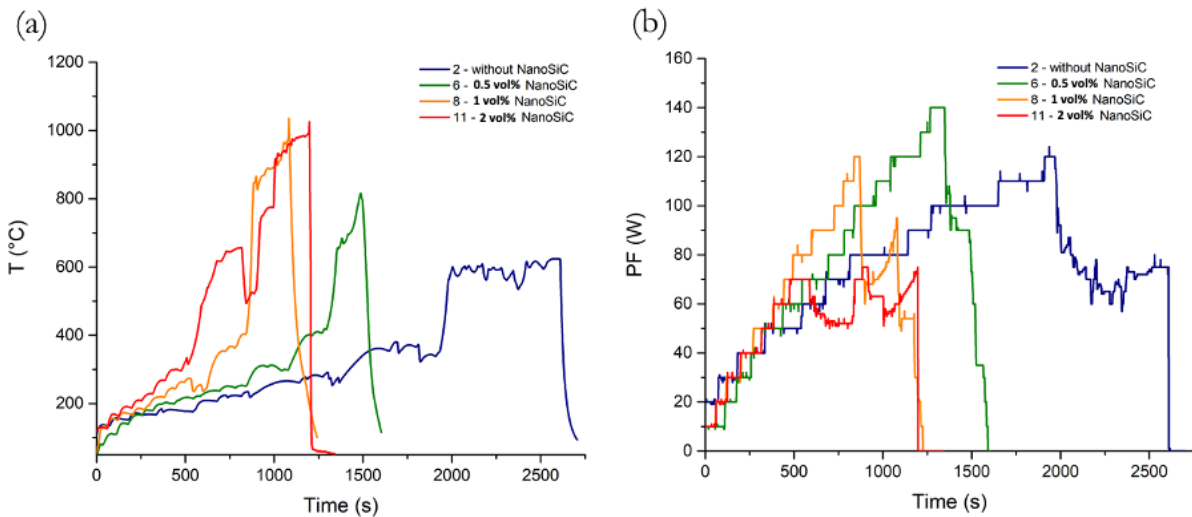
Figure 8. (a) Comparison of microwave coupling for samples containing different amounts of nano-SiC, (b) Corresponding forward power input during the microwave tests necessary to reach 400 °C.

These results obtained with the introduction of a very low amount of nano-SiC in the sealing material formulation can be considered as a real breakthrough in the optimisation of microwave coupling for such types of formulation. Indeed, the introduction of only 1 vol% of nano-SiC in a system containing 48.5 vol% of silica leads to a microwave heating reactivity that is similar to that of an Al_2O_3-SiO_2 system containing more than 59 vol% of SiO_2 without any nano-SiC. As the presence of silica is usually accompanied by lower mechanical and chemical resistance, decreasing its quantity is of real interest.

The following step was to study an Al_2O_3-SiO_2 system, with a fixed amount of 48.5 vol% of silica and with CuO-TiO_2 and Bi_2O_3 sintering additives. Figure 9a compares the microwave heating results between the basic Al_2O_3-SiO_2 system, the one modified with the sintering additives and the one with the further introduction of 1 vol.% of nano-SiC.
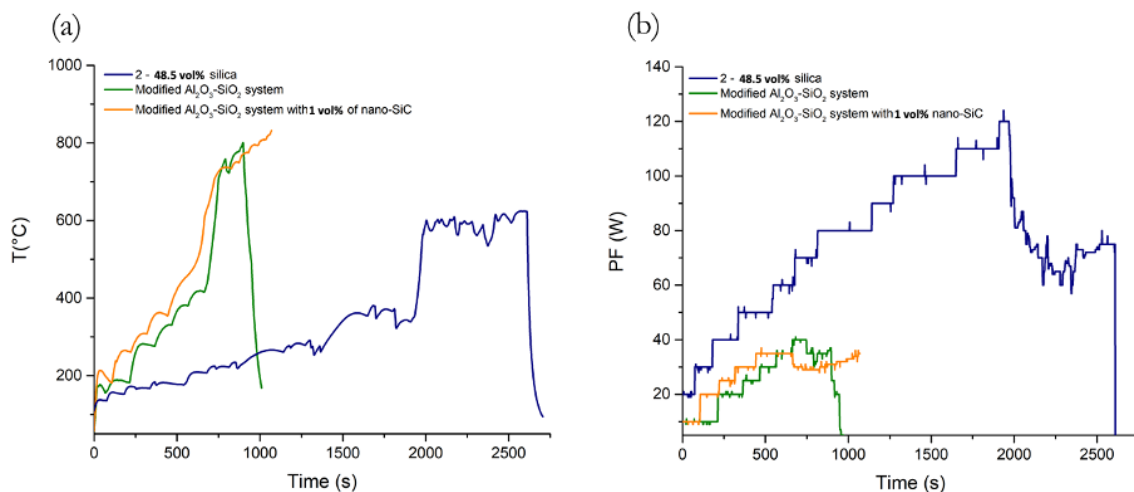
Figure 9. (a) Comparison of microwave coupling for samples with different compositions, (b) Corresponding forward power input during the microwave tests necessary to reach 400 °C.

The Al_2O_3-SiO_2 system modified with sintering aids exhibits an improved microwave coupling when compared to the simpler Al_2O_3-SiO_2 system (sample 2), similar to what was observed with the introduction of nano-SiC particles. The heating behaviour remains the same with a linear heating up to

about 400 °C, and then a controlled thermal runaway. Yet, the further addition of such nano-SiC does not seem to bring any additional improvement, but in the state of the art, the amount of nano-SiC introduced could still be optimized. A major difference in input power on modified systems can be observed in Figure 9b. Indeed, only 35 W is needed to reach 400 °C (as compared to 80 W without sintering aids). This result constitutes significant progress in optimising aluminosilicate sealing materials able to couple with microwaves at low temperatures with low input power. All microwave tests are summarised in Figure 10.
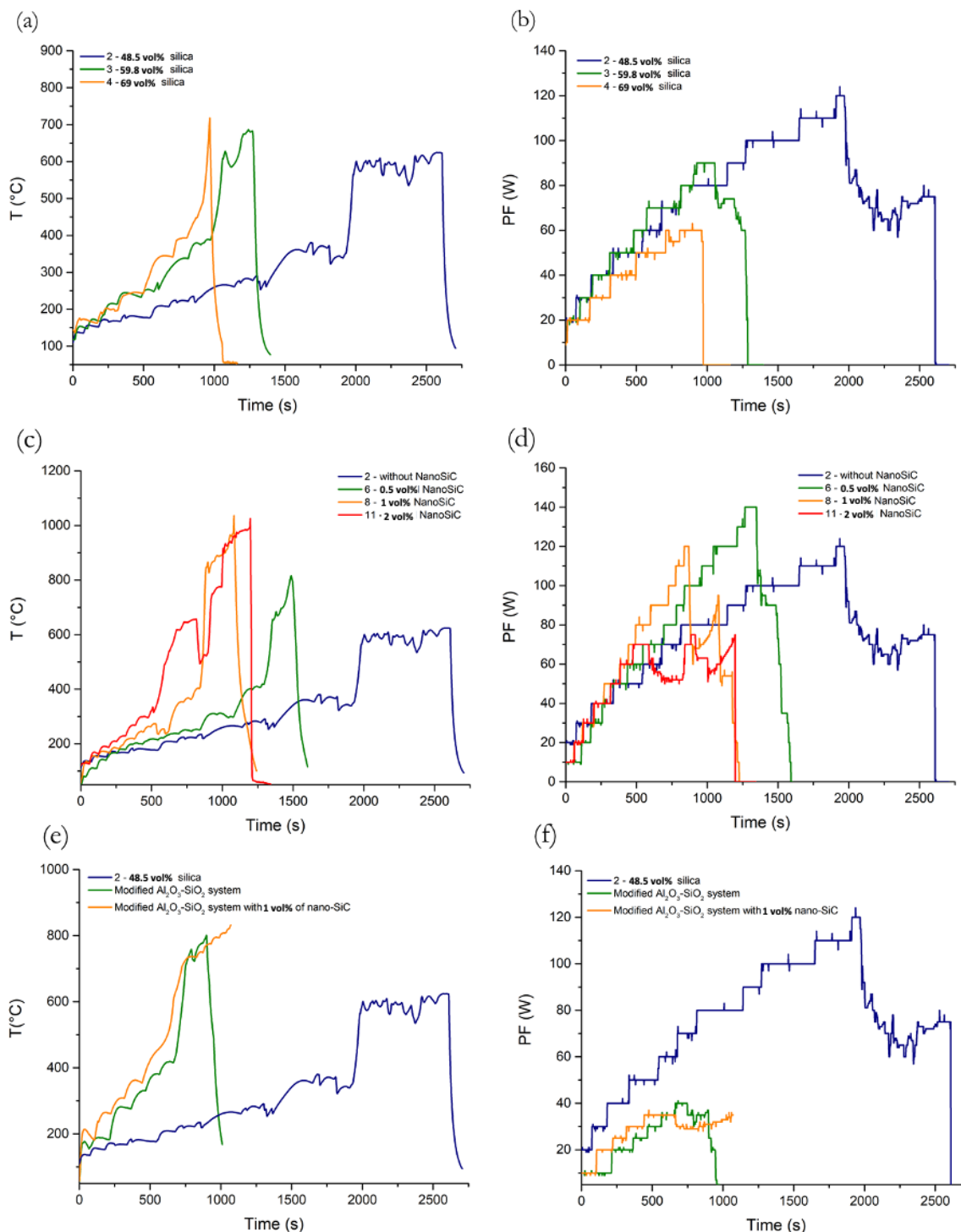
Figure 10. Overview of all microwave tests performed on Al₂O₃-SiO₂ systems (a) and (b), Al₂O₃-SiO₂ system with nano-SiC (c) and (d), modified Al₂O₃-SiO₂ system (e) and (f).

EURAD (Deliverable n° 15.6) - Novel materials and processes for the optimisation of long-term container performance
Dissemination level: Public
Date of issue of this report: 06/05/2024

Page

The next part of the study dealt with the sealing tests of two ceramic pieces and the further evaluation of the sealing mechanical properties. The first tests to make ceramic assemblies were conducted using a ceramic composed of 72 % Al_2O_3 – 24 % SiO – 1.61 % MgO – 1.29 % K_2O – 0.78 % Na_2O from supplier Porcelaine Pierre Asquié, Limoges (PPA). This ceramic composition used in past projects (Scelma, Noumeha 2015-2018) was successfully assembled with microwave heating. In these past studies, the sealing material was Alumino-Boro-Silicate glasses (Figure 11) in order to achieve sealing at a reasonable temperature (*i.e.*, < 700 °C).
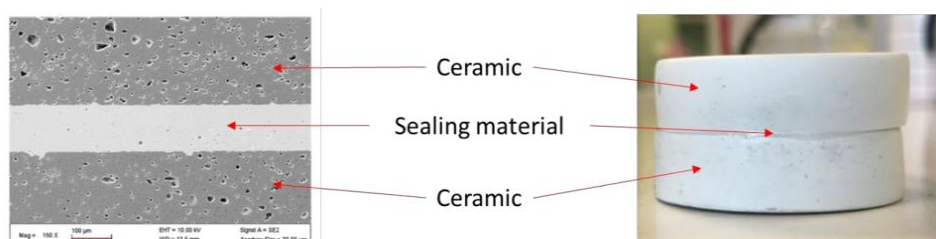
Figure 11. SEM observation of the sealing area (left) of ceramics sealed by alumino-boro-silicate glass (right).

From the several formulations of the new sealing material, differential scanning calorimetry (DSC) and sintering tests in a conventional oven were performed on compositions SiO_2-Al_2O_3, SiO_2-Al_2O_3 + nano SiC until 1400 °C. The results showed a very high stability of the new materials and a sintering temperature higher than 1400 °C which does not allow the densification of any formulations. Despite the addition of CuO, TiO_2 and Bi_2O_3 sintering additives in the basic composition to facilitate sintering, densification of the samples was not obtained in a conventional oven.

The densification can, however, be reached using microwave heating as the densification of some samples was observed. Figure 12 presents SEM and optical observation of a SiO_2-Al_2O_3 sample containing CuO, TiO_2 and Bi_2O_3 additives. Sintering of the sample is partial and inhomogeneous and it follows the temperature field produced during microwave heating. Thus, sintering is more advanced in the middle part of the sample than in the border and it can be at the origin of the appearance of cracks. Note that during the coupling test, temperature measurement was limited to 1000 °C due to the pyrometer capability (see Figure 10); yet, in some experiments, the temperature limit of the pyrometer was reached and the real temperature of the sample would exceed 1000 °C.
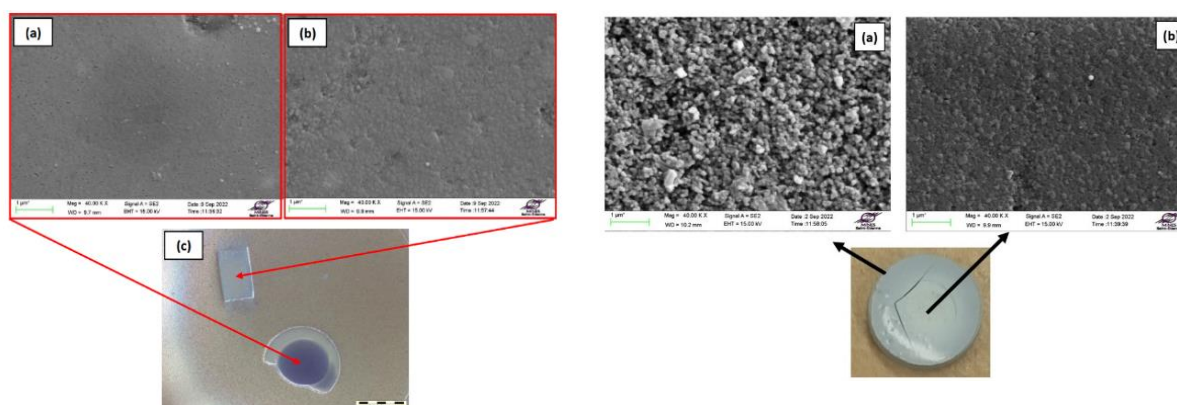
Figure 12. SEM observation of a SiO_2-Al_2O_3 sample containing CuO/TiO_2/Bi_2O_3 additives after a coupling test. Partial and inhomogeneous sintering is observed where the sintering of the central part of the sample is more advanced.

EURAD (Deliverable n° 15.6) - Novel materials and processes for the optimisation of long-term container performance
Dissemination level: Public
Date of issue of this report: 06/05/2024

Page

The fact that microwave heating produces sintering of material at a lower temperature is well known in the ceramics community and it is extensively discussed in the literature but a coherent explanation for it cannot be found to date, except for the issue related to temperature measurement by pyrometry (Zuo et al., 2014) (Zuo et al., 2015) (Sorrell et al., 1998) (Binner et al., 2007).

Due to the very high temperature needed to obtain densification of the new sealing material and to prevent the heating of the metallic container in the targeted application, it was decided to mix the newly developed material with a silicate glass (powder) which has a low melting temperature in order to make a composite material.

Composite materials were then obtained by mixing glass powder (Alumino-Boro-Silicate glasses) and the newly developed powders (Figure 13). The mixing ratio was determined by performing wetting tests which consisted of heating compacted samples (cylindrical samples of 8 mm diameter and 8 mm height) on ceramic pellets up to 1200 °C. The tests showed that the composite needs to contain at least 60 % glass to wet the ceramic. The melting temperature of the used glass is around 600 °C. For a composition containing nano-SiC, the formation of bubbles was observed. The bubble can be attributed to the reactivity of SiC at high temperatures that produce gases (Tixier, 2022) (Brossard et al., 2013).

Figure 13. Wetting test of composite materials. The left sample is composed of 60% glass-40 % SiO_2-AlO_2 blend, the middle sample is composed of 60% glass-40 % SiO_2-AlO_2-Bi_2O_3-CuO with nano SiC blend, and the right sample is composed of 50% glass-50 % SiO_2-AlO_2 blend.

Composite materials composed of 60%wt of glass and 40%wt SiO_2-Al_2O_3 blend are then considered to perform assembly tests by direct microwave heating in a single-mode cavity. First assembly tests were realized using ceramic disks of 5 mm height, and 40 mm diameter from PPA supplier. Powder of sealing material is deposited on one ceramic specimen side to cover its surface and another ceramic piece is laid over to form a ceramic/sealing-material/ceramic assembly. The heating procedure was to increase the sample temperature at 30 °C / min until 700-800 °C increasing microwave power from 50 W to 200 W. A temperature step of 20 min is then performed at the maximum temperature reached. Figure 14 presents the temperature evolution of the sample during a sealing test by microwave heating. The experimental setup to perform the assembly test using ceramics can be seen in Figure 15.

![eurad logo] European Joint Programme on Radioactive Waste Management

EURAD (Deliverable n° 15.6) - Novel materials and processes for the optimisation of long-term container performance
Dissemination level: Public
Date of issue of this report: 06/05/2024

Page
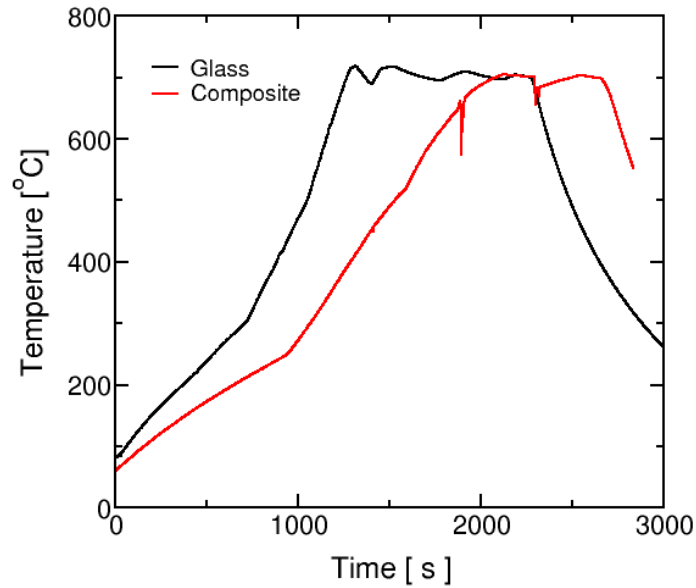
Figure 14. Evolution of sample temperature during sealing tests using glass and composite as sealing material.

Without insulators surrounding the assembly, fractures of the systems were systematically observed due to thermal gradients as heat is produced by the sample itself in transforming the electromagnetic field to heat (Zuo et al., 2014).
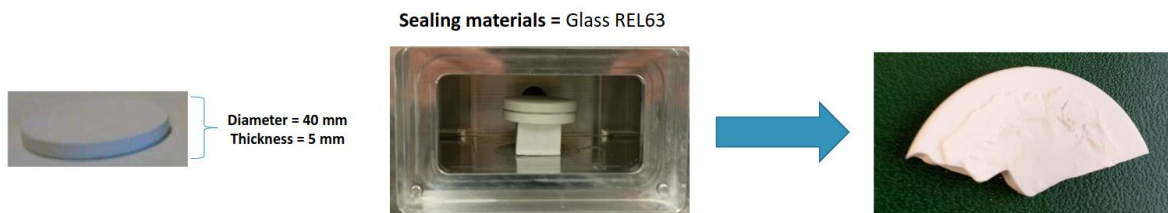
Figure 15. Experimental configuration to perform assembly test using ceramics.

An insulating box composed of commercial porous Al_2O_3-SiO_2 [2] was then used to prevent beaks of the assembly (Figure 16a). The insulating box is assumed to be transparent to microwaves (low value of the imaginary part of the permittivity). In such a configuration, it was possible to heat the assembly following the previous heating procedure. Despite the ceramics seeming to be sealed, optical observation of the cross-section of the assembly after heat treatment shows that the sealing area presents defects either using only glass (Figure 16b) or composite (Figure 16c) as sealing material.

---

[2] © RATH Altraform - https://www.rath-group.com/

EURAD (Deliverable n° 15.6) - Novel materials and processes for the optimisation of long-term container performance
Dissemination level: Public
Date of issue of this report: 06/05/2024

Page
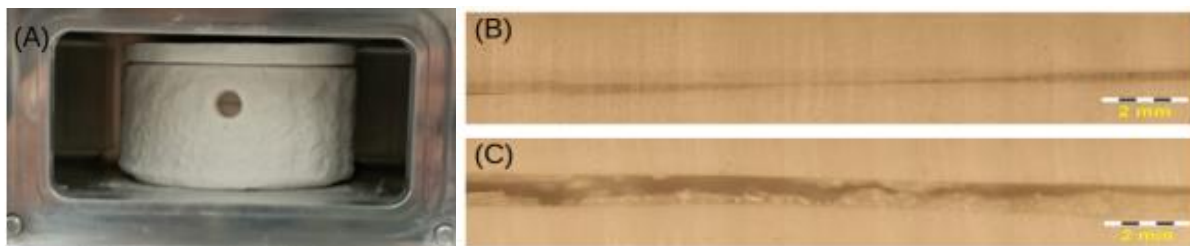
Figure 16. Insulating box inside microwave oven to avoid temperature gradient of the assemblies (a). Optical observation of the sealing area in cross-section using only glass as sealing material (b) and composite material (c).

A continuous sealing area is obtained using only glass, but porosity is observed also in this case (Figure 16b). A discontinuous sealed area is observed using composite as sealing material. These results show that process parameters such as the maximum temperature, the temperature step and/or the formulation of the sealing material need to be optimized. Indeed, the sealing zone must be continuous between the ceramics to be joined for mechanical and sealing reasons.

3.1.1.1. Results with new ceramic formulation

New results on the ceramics formulation and processes to make the ceramics showed that a purer alumina ceramic would make it possible to reduce the thickness of the ceramic canister by 1 to 2 cm. Based on this conclusion, new ceramic specimens were produced by sintering in a conventional oven using pure alumina powder (BA15). The new cylindrical ceramic samples were densified at 97%, their dimension is 16 mm in diameter and 10 mm in height.

The first sealing test using pure alumina ceramics and different sealing materials showed the absence of coupling and consequently the heating of the assembly. As mentioned by Zymelka et al. (2013), alumina does not absorb microwave energy efficiently at low temperatures and the use of a susceptor is recommended to engage the microwave coupling. Another point to mention is that despite coupling materials (glass, new sealing materials) being used to produce the assembly, no heating of the system was obtained. In the coupling tests, the samples were compacted powders. For assemblies, the powder is spread between the ceramic disks, and it is not compacted. The absence of heating suggests an effect of either the compaction or the thickness of the sealing material to obtain a microwave coupling with the sealing material.

3.1.1.2. Permittivity measurements

In parallel to performing microwave coupling tests and sealing tests by microwave heating, a setup was developed to measure the permittivity of materials as a function of the temperature. In the future, this device will help in the selection of materials for microwave applications at high temperatures. Indeed, few data exist concerning the dependence of dielectric properties (permittivity) with temperature (Komarov, 2012). The permittivity at microwave frequencies is indeed a quantity that is difficult to measure at elevated temperatures (Couderc et al., 1973) (Tinga et al., 1993) (Garcia-Baños et al., 2016) (Wu et al., 2019). Consequently, there is limited corresponding data in the literature (Wroe et al., 1996) (Baeraky, 2002) (Zhao et al., 2011) (Maniere et al., 2018).

The development of a device to measure the permittivity was performed at Saint-Etienne (Ganster et al., 2018). The system is composed of a 2.45 GHz single-mode resonant cavity. It allows heating the sample with microwaves and the qualification of resonance using a vector network analyser (VNA) to measure the scattering parameter s_{11}. The permittivity is deduced from microwave field disturbances (Waldron, 1960).

EURAD (Deliverable n° 15.6) - Novel materials and processes for the optimisation of long-term container performance
Dissemination level: Public
Date of issue of this report: 06/05/2024

Page

Figure 17 presents a schematic and a picture of the device. Labview software is used to control all the devices. Microwave heating and resonance measurements cannot be realized at the same time and they must be synchronized. A switching system is used to plug either the microwave source into the cavity or the VNA. A radiofrequency (RF) load is used for safety as when analyzing the resonance with VNA, the switching system redirects the microwave to the laboratory.
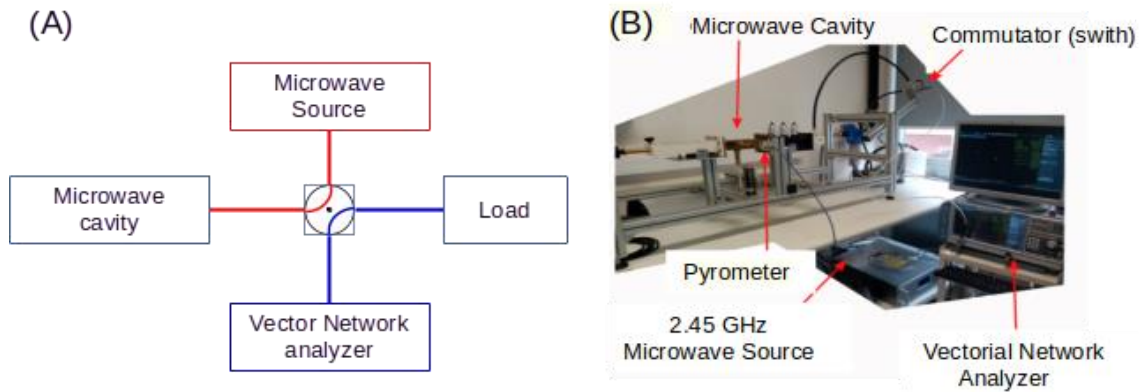
Figure 17. Schematic (a) and picture (b) of the device to measure the permittivity from the S_{11} parameter.

Resonance is measured by VNA which is a radiofrequency device that evaluates the S_{11} parameter needed to characterize the permittivity of a sample exposed to an electric field (Pozar, 1998). At a given frequency ν, S_{11} (ν) corresponds to the ratio S_{out} (ν) / S_{in} (ν), where S_{in} (ν) is a signal intensity emitted toward the resonator and S_{out} (ν) is the returning signal from the resonator at frequency ν. Figure 18 presents the S_{11} parameter when the resonant cavity is empty (black curve) and loaded with a sample (red curve). The minimum of the S_{11} curve indicates the resonant frequency. When the cavity is loaded with a sample, a shift of the S_{11} minimum occurs and the shape of the corresponding curve is changed.
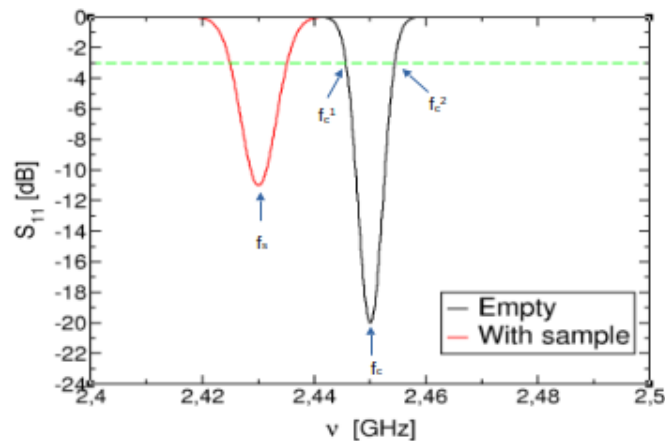
Figure 18. S_{11} signal of a 2.45 GHz empty cavity (black curve) and when a sample is placed in the field.

The permittivity can be derived using these equations:

$$\epsilon' = \alpha \frac{V_C}{2 V_S} \frac{f_C - f_S}{f_S} + 1$$

where fc and fs are the resonant frequencies of the cavity without and with samples, respectively. VC and VS are the volume of the cavity of the sample, respectively. And:

$$\epsilon'' = \alpha \frac{V_C}{4V_S}\left(\frac{1}{Q_S} - \frac{1}{Q_C}\right)$$

where Q_C and Q_S are resonance quality factors of the cavity without and with the sample, respectively. Q_C is a quality factor and is defined as the peak frequency (f_C) divided by the peak bandwidth (f_C^1-f_C^2), see Figure 18.

First experiments were conducted on SiC which couples easily with microwaves. Figure 19 presents the temperature of the sample for heating cycles of 3.5 s period (3 s of heating – 0.5 s for S_{11} measurement) at 200 W. The result shows a fast heating of the sample (after 3.5 s, 220 °C is reached) and that the equilibrium temperature of 420 °C is reached after 60 s. The corresponding resonant frequency is represented in Figure 19c.

An evolution of the resonant frequency is observed despite the fact that the temperature has reached a plateau. Longer tests and modelling of the experimental setup are under investigation to evaluate the thermal transfers from the sample to the sample holder and the effects on the resonance.
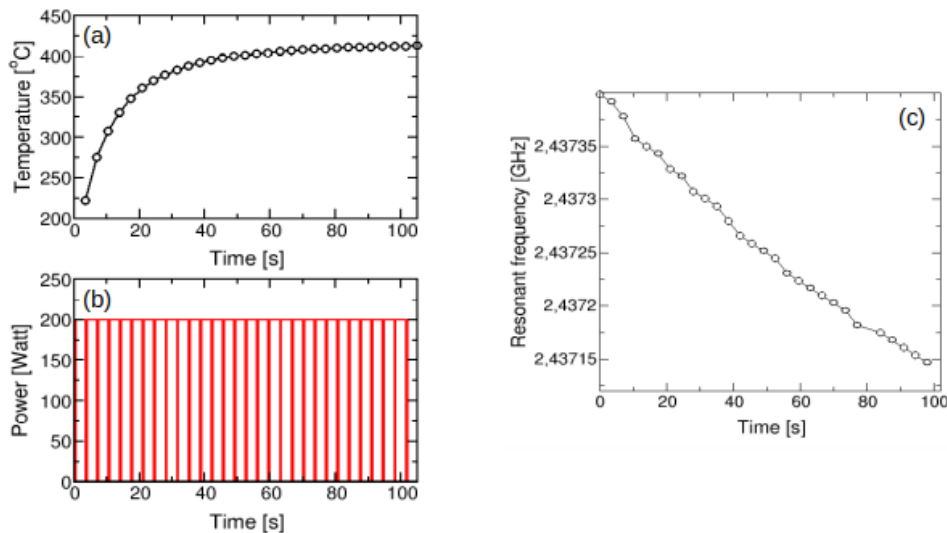
Figure 19. Temperature evolution of the SiC sample (a) during a heating cycle of 200 W power applied (b), and the corresponding evolution of the resonant frequency (c).

Real and imaginary parts of the SiC permittivity were derived and are represented in Figure 20. The real part is in good accordance with the literature (Ghorbel et al., 2023), while the imaginary part is underestimated. The set-up is now operational to evaluate the permittivity of any material and improvements are underway to achieve higher temperatures. Its use would be an advantage to test the microwave coupling and the determination of permittivity for simulation works.

EURAD (Deliverable n° 15.6) - Novel materials and processes for the optimisation of long-term container performance
Dissemination level: Public
Date of issue of this report: 06/05/2024

Page
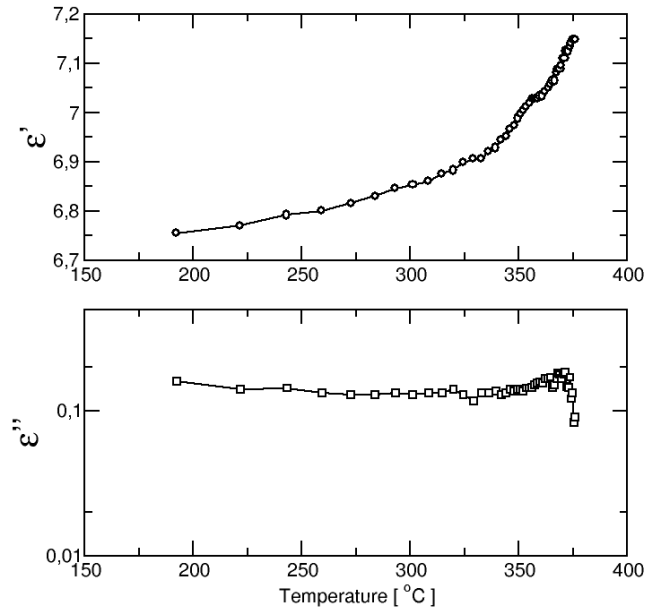
Figure 20. Temperature evolution of the real and imaginary parts of SiC permittivity.

3.1.2. SiC with Cr additives

In the literature, it has been shown that silicon carbide (SiC) is a viable material option for container fabrication (Holdsworth, 2013) (Knorr et al., 2008). Until recently, it was only feasible to manufacture large pieces out of SiSiC (silicon-impregnated silicon carbide) and RSiC (recrystallised silicon carbide). However, recent developments make it possible to produce larger pieces from conventional SSiC (sintered silicon carbide), Figure 21 (Kerber et al., 2013) and even high-strength grades of SSiC (Wötting et al., 2007).
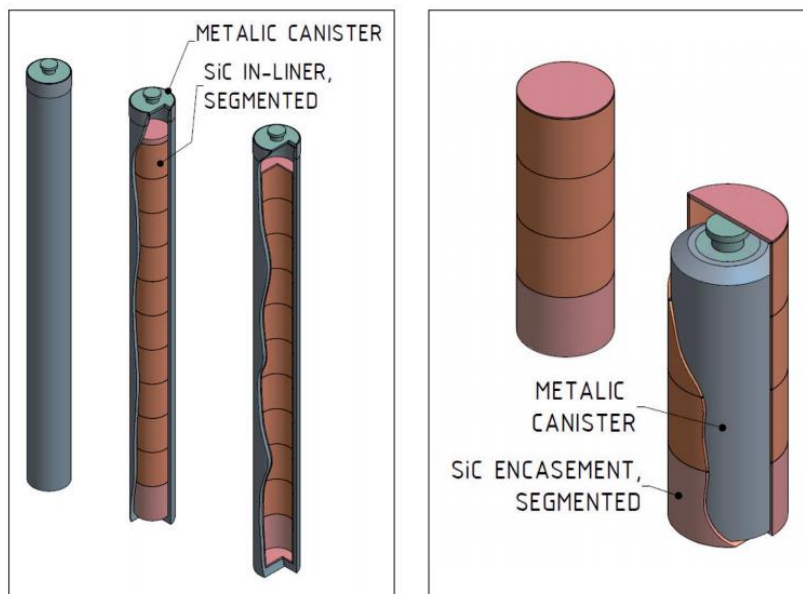
Figure 21. Proposed SSiC encasement solutions for (a) SF rod disposal, with a diameter of 430mm and height of 4980mm, and (b) VHLW disposal, with a diameter of 465mm and a height of 1,390mm (Kerber et al., 2013).

EURAD (Deliverable n° 15.6) - Novel materials and processes for the optimisation of long-term container performance
Dissemination level: Public
Date of issue of this report: 06/05/2024

Page

SiC can be a promising material for containers for disposal of SF/HLW in geological formations due to the fact it does not react with water and acids (up to 450 °C) and has high hardness (≈28 GPa). Nowadays the world's leading R&D centres make corrosion resistance tests of SiC (with or without various alloying additions) under conditions simulating various environmental conditions.

In 2018 two companies "General Atomics" and "Westinghouse Electric" conducted corrosion tests of modern fuel cladding made of SiC/SiC composites (under conditions of normal operation of water-cooled reactors BWR and PWR) (Deck et al., 2018). The composition of the liquid in the autoclave during the tests corresponded to different types of coolants (BWR/NWC and BWR/HWC water conditions: 290 °C at 7.2 MPa; PWR water conditions: 343 °C at 18.6 MPa); the tests were carried out for 3 months. The obtained results indicate that SiC has a high corrosion resistance; the authors calculated the dissolution rate of 1 μm per year, which is approximately 1% of the total thickness of the fuel cladding.

The positive effect of Cr on the corrosion resistance of SiC ceramics (Lobach et al., 2020) was experimentally shown under conditions simulating the inner environment of VVER-1000 reactor (350 °C at 16.8 MPa; H_3BO_3 – 3 g/dm^3; NH_3 – 3 mg/dm^3; KOH – 12.3 mg/dm^3). It is shown that doping of SiC with Cr decreases the dissolution rate of SiC(Cr) compared to SiC without additives, due to the formation of corrosion-resistant products (Cr_2O_3), which significantly affect the ability of SiO_2 films to passivate the surface of the samples. Also, it should be noted that the authors Lobach et al. (2018) showed the effect of Cr additives on the mechanical properties of SiC and found that doping of SiC with 0.5 %wt Cr leads to an increase in fracture toughness (K_{1c}) by (25 – 50)% (from 4.2 to 6.2 $MPa·m^{1/2}$) while maintaining a high level of hardness with a value of 28.0 GPa.

The results of scientific research indicate that SiC-based ceramics are promising materials both for fuel claddings and canisters for deep geological disposal (Lobach et al., 2020) (Deck et al., 2018) (Kerber et al., 2013). Also, it should be noted that the construction of SiC canisters consists of assembled sealed segments (Figure 21), since it is technically difficult to manufacture a monolithic canister construction with large dimensions. Therefore, despite the fact that the described lixiviation tests of SiC were carried out under severe conditions (T = 350°C, P = 16.8 MPa), there is a need to study the mechanisms of corrosion processes in the system (SiC - compound - SiC) under the conditions simulating geological disposal (T = 90°C), because the interconnection of SiC segments is an important and actual task, taking into account the conditions (corrosion and radiation exposure) of their usage. There are two most promising directions in the world for interconnecting SiC segments:

- the first one is the Laser joining method (Knorr et al., 2008), which is based on a combination of pure oxidic braze filler (trademark: CERALINK ®) and laser beam. The filler inside the joining zone is melted locally by using a laser beam. CERALINK ® shows an ideal wetting of the ceramic surface and high oxidization resistance. The ceramic joint surface does not need pre-treatments (no metallization). This paper indicates that the obtained joints are gas-tight, have high mechanical strength and have no cracks. Joining surfaces do not require preliminary treatment;

- the second direction is soldering based on various materials (for example, glass-ceramic). So, in the work of Wang et al. (2020) the joining scheme of SiC/SiC composites is given, where the material Y_2O_3-Al_2O_3-SiO_2 (YAS) was used. The authors consider that a reliable glass-ceramic joining with strong joints is obtained. Shear strength tests showed an increase in the strength of the joining with increasing soldering temperature; the maximum strength reached 51.7 MPa at a soldering temperature of 1400°C.

Research conducted at KIPT was devoted to optimizing the sintering process for the manufacture of composite materials based on SiC doped with Cr. The process of synthesis of SiC-based ceramic composites was performed using hot pressing.

SiC powder brand 440 NDP (Figure 22a) produced by the "Superior Graphite Co" (USA) was used to obtain SiC-based ceramic composites. According to the manufacturer's specifications, this powder is a

EURAD (Deliverable n° 15.6) - Novel materials and processes for the optimisation of long-term container performance
Dissemination level: Public
Date of issue of this report: 06/05/2024

Page

modification of α-SiC with an organic binder. To determine the main characteristics of the raw SiC powder, this material was characterised by means of SEM, EDS, XRD and DTA/TGA.

| (a) | (b) | (c) |
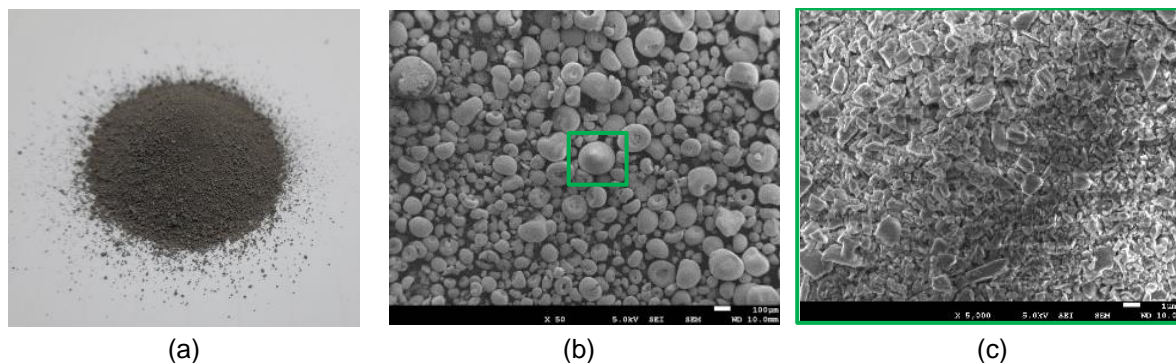
Figure 22. Appearance (a) and EM images (b, c) of the SiC powder.

Electron microscopic studies (Figure 22b) show that the powder consists of spherical agglomerates with an average size of 40 - 100 µm. In turn, the agglomerates are composed of particles with an average size of 440 nm (Figure 22c). EDS of the SiC powder shows that it consists of Si, C and a small amount of O, which indicates the purity of this powder (Figure 23).
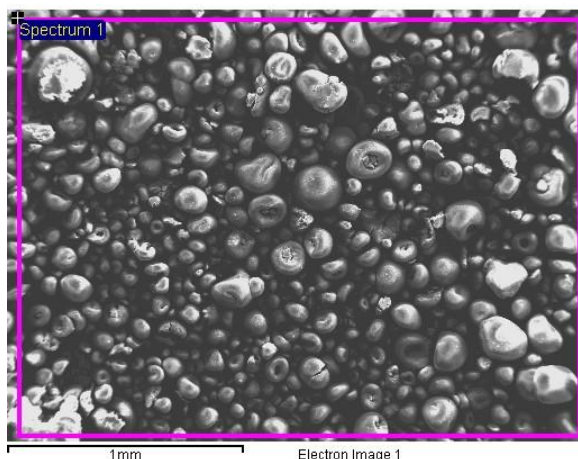
Element	Weight%	Atomic%
C K	46.91	65.36
O K	6.70	7.01
Si K	46.39	27.63
Totals	100.00	

Figure 23. EDS analysis of the raw SiC powder.

XRD analysis (Figure 24) showed that the silicon carbide powder is a single-phase material and consists of the hexagonal SiC-6H polytype (also called α-SiC, the most encountered SiC polymorph among over 250 known). No other phases were detected (within the sensitivity limit). Lattice parameters of the SiC-6H phase are: a = 3.081 Å; c = 15.118 Å. In addition, diffraction peak broadening is observed on the diffraction pattern, therefore, the Williamson-Hall (1953) method was applied to determine microstructural characteristics of SiC: microstrains and crystallites size (coherent scattering domain size). The estimated crystallite size of SiC-6H carbide is D = 52.5 nm while microstrains are insignificant.

EURAD (Deliverable n° 15.6) - Novel materials and processes for the optimisation of long-term container performance
Dissemination level: Public
Date of issue of this report: 06/05/2024

Page
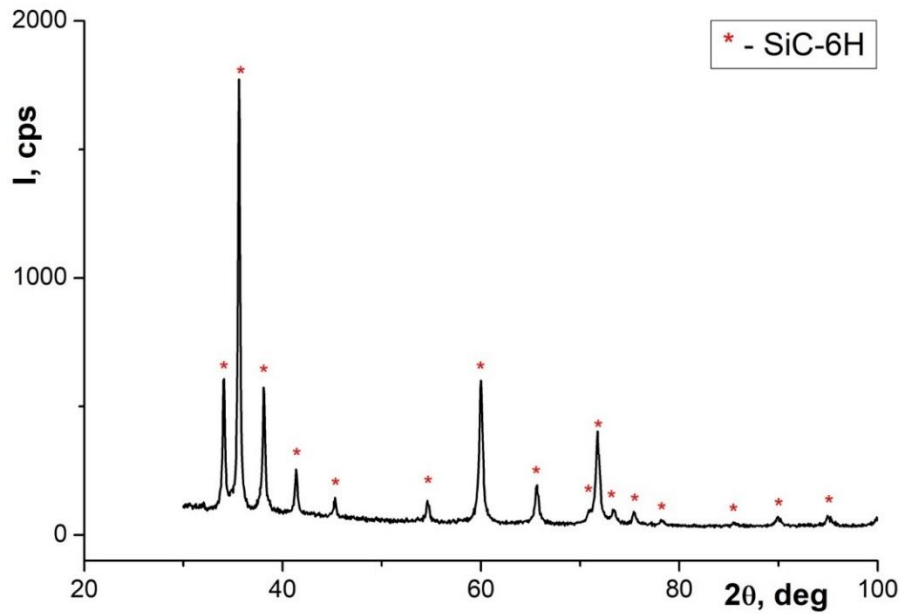
Figure 24. XRD pattern of the raw SiC powder.

The DSC/TGA curves of the SiC powder (Figure 25) suggest that in the temperature range of 25 - 400°C physical moisture (up to 150°C) and organic binder volatilize, which is confirmed by the weight loss on the TGA curve (~17%). The exothermic peak at 420 °C corresponds to the partial oxidation of SiC to SiO_2.
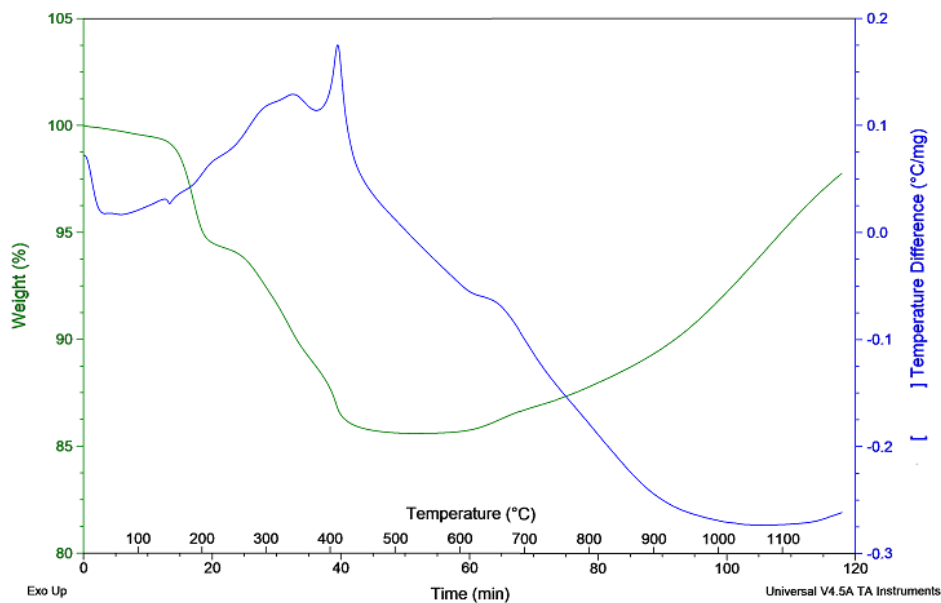
Figure 25. DSC/TGA curves of the raw SiC powder.

Manufacturing of SiC samples with Cr additives

Further, experiments were carried out using a mixture of SiC with Cr. The preparation of powder mixtures (with different Cr content) was carried out in the following steps:

EURAD (Deliverable n° 15.6) - Novel materials and processes for the optimisation of long-term container performance
Dissemination level: Public
Date of issue of this report: 06/05/2024

Page

1. Cr was added to the SiC powder, and the Cr content varied from 0.3 to 0.9 %wt (0.3% - 0.5% - 0.7% - 0.9 %).

2. Raw materials were mixed in a ball mill (container and balls - ZrO_2): V = 300 rpm, t = 3 h.

3. This mixture was dried at T = 90°C, t = 24 hours.

The powder mixture (SiC with Cr additives) was loaded into a graphite mold (Figure 26), which was subsequently placed in a laboratory hot pressing facility (Figure 27).
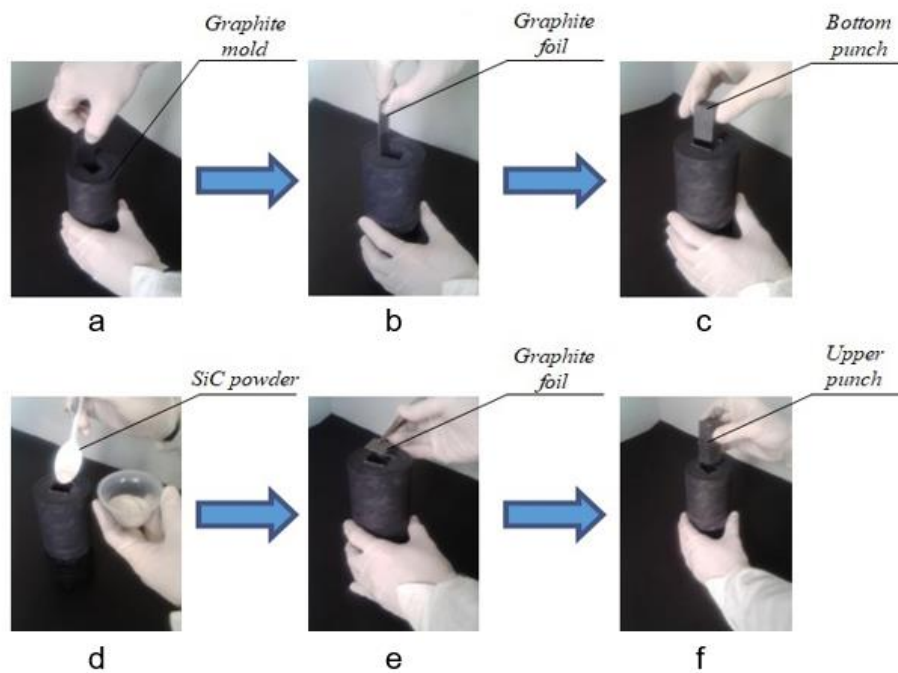
Figure 26. Preparation of the mold with SiC powder (a,b-mounting protective foil, c-placing bottom punch, d- filling of SiC powder into the mold, e-mounting protective foil, f- placing upper punch).

EURAD (Deliverable n° 15.6) - Novel materials and processes for the optimisation of long-term container performance
Dissemination level: Public
Date of issue of this report: 06/05/2024

Page

Figure 27. Laboratory HP facility for sintering ceramic materials.

Sintering was carried out in a temperature range of 1850 - 2100 °C, the time of exposure under pressure ranged from 10 to 45 min, and the heating rate and pressure were constant: 200°C/min and 40 MPa, respectively. The appearance of the obtained samples is shown in Figure 28.
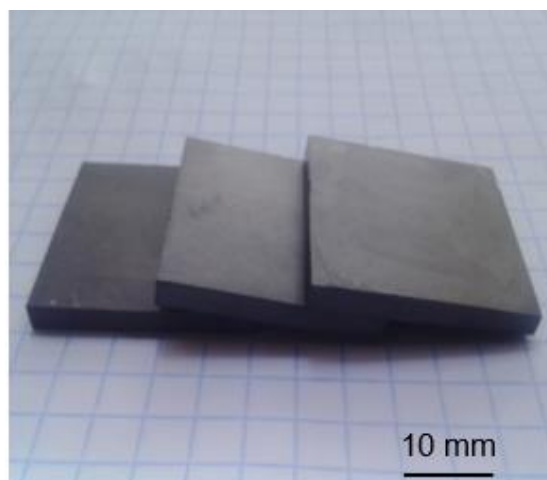
Figure 28. Obtained SiC(Cr) samples (25x25x4 mm).

EURAD (Deliverable n° 15.6) - Novel materials and processes for the optimisation of long-term container performance
Dissemination level: Public
Date of issue of this report: 06/05/2024

Page

The results of the density measurements (pycnometric method, results in Table 2) allow choosing the optimal parameters of the sintering process to obtain high-density SiC samples (up to 99.0 % from the theoretical density of pure SiC – 3.21g/cm³).

Table 2. Parameters/Characteristics of obtained samples

Samples	Measured density, g/cm³	From theoretical density of pure SiC,%
SiC (0 % Cr)	3.161	98.5
SiC (0.3 % Cr)	3.108	96.8
SiC (0.5 % Cr)	3.181	99.1
SiC (0.7 % Cr)	3.167	98.7
SiC (0.9 % Cr)	3.129	97.5

Optimal technological parameters for manufacturing of SiC are the following: T = 2050-2100°C, exposure time under pressure t = 30 min, pressure P = 40 MPa, heating rate v ~ 200°C/min. The choice of parameters is based on the results obtained in the work (Voyevodin et al., 2017) where a series of ceramic samples was produced to study the effect of the hot pressing (HP) on the formation of a high-density structure and on the physical and mechanical properties of SiC. The raw SiC powder was loaded into a graphite mold (Figure 26), after that simultaneous forming and sintering were carried out using the HP method. Based on the literature data, the following technological parameters were chosen: sintering was carried out in the temperature range of 1850 - 2100 °C, the temperature holding time under pressure was 10 - 45 minutes, the heating rate and pressure were constant (200 °C/min and 40 MPa, respectively).

The crystal structure and quantitative phase composition of SiC(Cr) samples were identified by X-ray diffraction (XRD) analysis using Cu-Kα radiation (DRON-4-07). Diffraction patterns of all studied samples are almost identical; for example, the DP of SiC (Cr) with the highest Cr content (0.9%wt Cr) is shown in Figure 29.
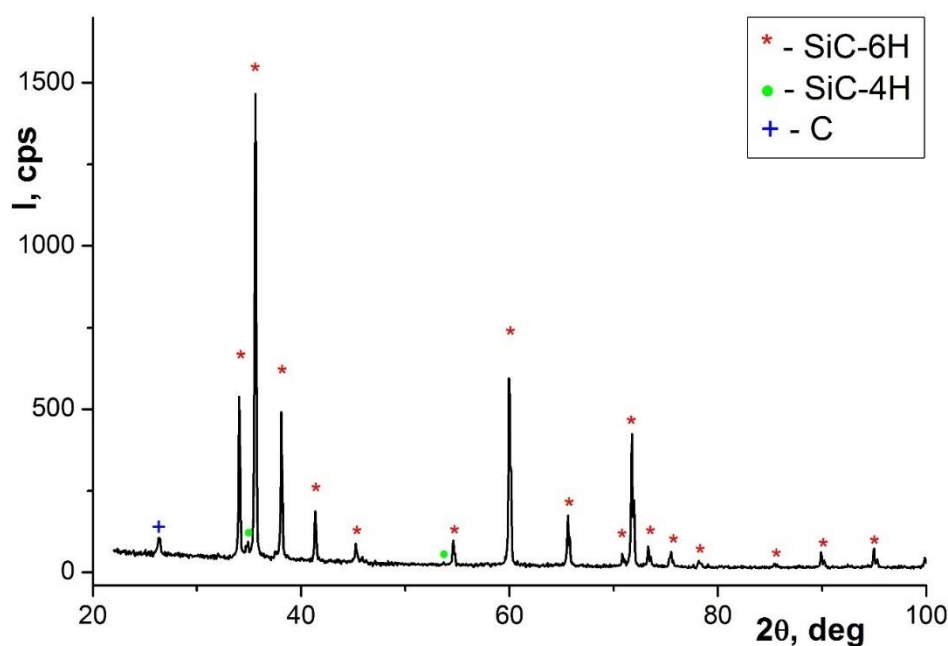
Figure 29. XRD patterns of SiC(Cr) sample with 0.9 wt.% chromium content

EURAD (Deliverable n° 15.6) - Novel materials and processes for the optimisation of long-term container performance
Dissemination level: Public
Date of issue of this report: 06/05/2024

Page

Analysis established the presence of 2 SiC polytypes (6H and 4H) in all samples, as well as a small amount of carbon C (see Table 3). The main constituent phase is SiC-6H (weight fraction is about 96%, lattice parameters: a = 3.080 Å; c = 15.112 Å). Since the raw powder is single-phase SiC-6H (Figure 24), it can be concluded that an insignificant amount of the SiC-4H polytype is formed during the hot pressing. It is important to point out that polytype modifications of SiC are identical in their physico-mechanical and electro-chemical properties. Therefore, a trace of SiC-4H polytype in the samples does not affect the sample properties. A small amount of carbon is detected on the surface of the samples due to their contact with the graphite mold. Also, it is important to note the absence of chromium Cr peaks on diffraction patterns (3 strongest Cr peaks are expected to be at 2θ angles of 44.39°, 64.58° and 81.73°). Chromium is a heavier element than silicon and carbon and has a higher "scattering capability" than SiC. Therefore, with a higher chromium content (0.9 wt.%) its diffraction peaks should be detected. On the other hand, chromium is a strong carbide-forming element and the absence of peaks related to chromium may indicate the formation of chromium carbides, the "scattering capability" of which is much less than that of chromium.

Table 3. Phase composition of the silicon carbide samples SiC(Cr) with different chromium content

%wt. Cr	Phase	Weight fraction, %wt	Lattice parameters, Å
0.3Cr	SiC-6H	94.5	a = 3.080; c = 15.113
	SiC-4H	2.4	a = 3.078; c = 10.061
	C	3.1	a = 2.46; c = 6.75
0.5Cr	SiC-6H	95.5	a = 3.080; c = 15.112
	SiC-4H	2.8	a = 3.079; c = 10.064
	C	1.7	a = 2.46; c = 6.71
0.7Cr	SiC-6H	94.0	a = 3.080; c = 15.114
	SiC-4H	2.3	a = 3.079; c = 10.061
	C	3.7	a = 2.46; c = 6.76
0.9Cr	SiC-6H	91.1	a = 3.080; c = 15.114
	SiC-4H	2.9	a = 3.079; c = 10.064
	C	6.0	a = 2.46; c = 6.75

3.1.2.1. Light Optical Microscopy

It was found that with an increase in the concentration of chromium, black dots appear in the structure of silicon carbide (Figure 30). Perhaps these are silicides or chromium carbides and carbon.

EURAD (Deliverable n° 15.6) - Novel materials and processes for the optimisation of long-term container performance
Dissemination level: Public
Date of issue of this report: 06/05/2024

Page

EURAD (Deliverable n° 15.6) - Novel materials and processes for the optimisation of long-term container performance
Dissemination level: Public
Date of issue of this report: 06/05/2024

Page

Figure 30. Structure of SiC samples with the different Cr content.

3.1.2.2. Raman spectroscopy

The studies were carried out using the device InVia, Renishaw, argon ion laser with a wavelength of 514 nm as an excitation source. The 6H–SiC polytype corresponds to a peak at a Raman shift of 767.5, 788.0 cm^{-1}. The addition of chromium leads to a broadening of these peaks, which may indicate the presence of an amorphous phase (Delobel et al., 2020) (Luo et al 2012) in the samples with 0.9 wt.% chromium content (Figure 31).

EURAD (Deliverable n° 15.6) - Novel materials and processes for the optimisation of long-term container performance
Dissemination level: Public
Date of issue of this report: 06/05/2024

Page
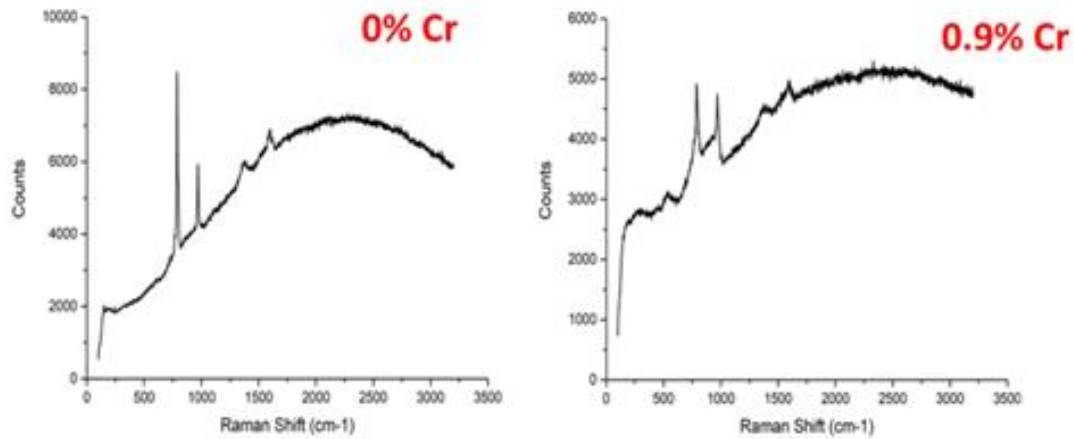
Figure 31. Raman spectroscopic analysis of SiC and SiC(0.9Cr).

3.1.3. Mechanical properties of SiC with Cr additives

3.1.3.1. Microhardness

The microhardness of the samples was measured by microhardness tester LECO LM700AT at a load of 200 g, with a holding time of 14 s. The results are presented in Figure 32. The pure silicon carbide sample has a microhardness of 22.8 GPa. Such a value of the microhardness for the silicon carbide synthesized by the HP method follows the known data from the literature, which are in the range of 20-26 GPa (Gouadec et al., 2007) (Pérez-Rodríguez et al., 1996).

Adding chromium to SiC increases the microhardness from 22.8 to 25.5 GPa. SiC with 0.5 wt% Cr additions has the highest hardness of 25.5 GPa (Figure 32). An increase in chromium concentration up to 0.9 wt% results in a decrease in SiC(Cr) microhardness to 21.7 GPa.
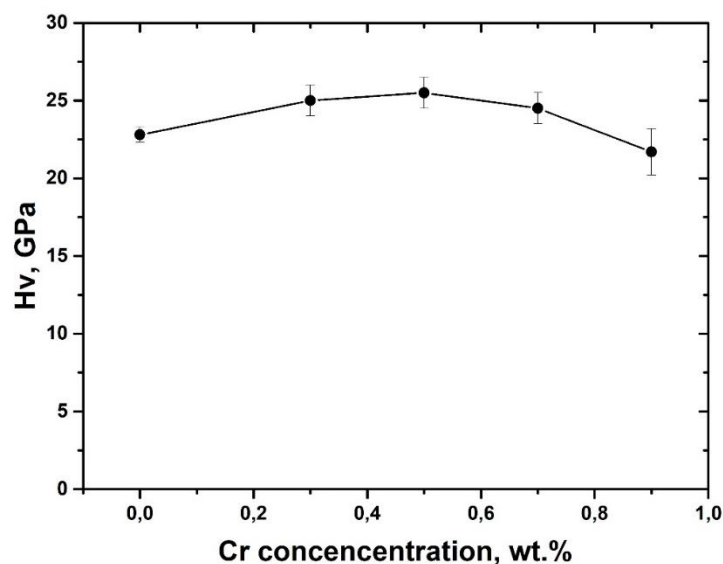
Figure 32. The microhardness vs. Cr concentration of studied SiC(Cr) samples

EURAD (Deliverable n° 15.6) - Novel materials and processes for the optimisation of long-term container performance
Dissemination level: Public
Date of issue of this report: 06/05/2024

Page

3.1.3.2. Nanohardness

Nanohardness of SiC(Cr) samples were determined by nanoindentation using the Nano Indenter-G200 system (Agilent Technologies, USA) equipped with Berkovich diamond tip. The depth of indentation was approximately 500 nm. The addition of chromium in the range of 0.3 to 0.7 wt.% increases the nanohardness compared to SiC without Cr additives (Table 4 and Figure 33).

Table 4. The values of nanohardness (H) and Young's modulus (E) of SiC samples with different Cr concentration.

№ sample of SiC	Cr, %wt	H, GPa	E, GPa
1	0	31±4	438.9±26
2	0.3	33.4±2.6	464.3±21
3	0.5	37.8±1	522±14
4	0.7	35.9±2.3	487.0±12
5	0.9	27±1.8	235.1±6
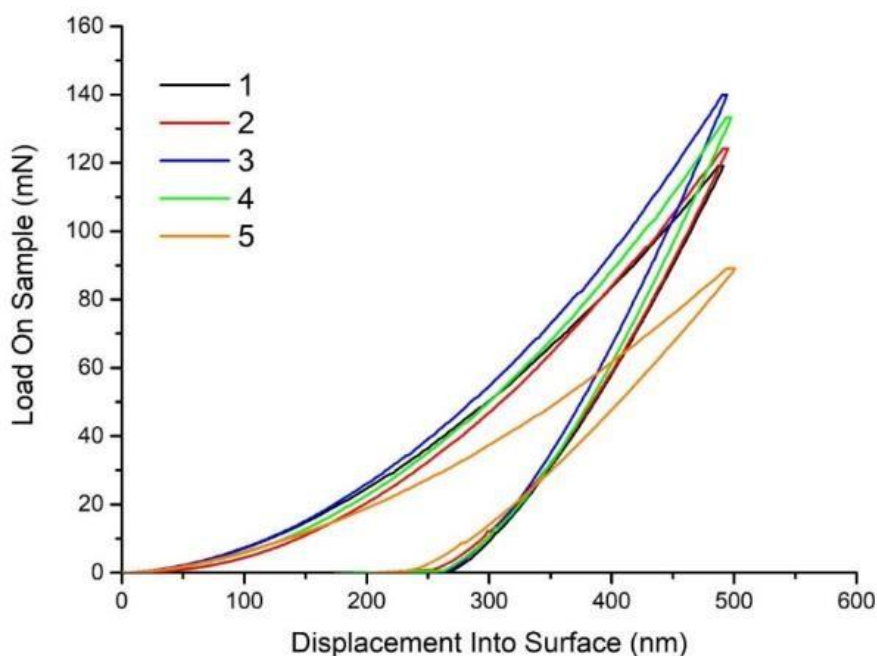
Figure 33. The load-unload curves vs. Cr concentration of studied SiC(Cr) samples.

The nanohardness of SiC with the addition of 0.5 %wt Cr is 37.8 GPa, while pure SiC has 31.0 GPa. Increasing the content of Cr to 0.9 %wt leads to a sharp decrease of nanohardness from 37.8 GPa to 27.0 GPa. The reduction of SiC nanohardness during chromium doping by more than 0.7 %wt can occur due to the formation of a number of phases: Cr_xSi_y and Cr_xC_y.

3.1.3.3. Long-term corrosion resistance

Samples of pure SiC and chromium (0.3%wt. and 0.5%wt.) doped SiC were tested for long-term corrosion resistance in distilled water at 90 °C. Corrosion tests were performed by keeping the samples in a container with distilled water and weighing them on an analytical balance after a certain period of

EURAD (Deliverable n° 15.6) - Novel materials and processes for the optimisation of long-term container performance
Dissemination level: Public
Date of issue of this report: 06/05/2024

Page

time. Before weighing, the samples were dried in dry air at 120 °C for 5 minutes. The results of the corrosion studies are shown in Figure 34.
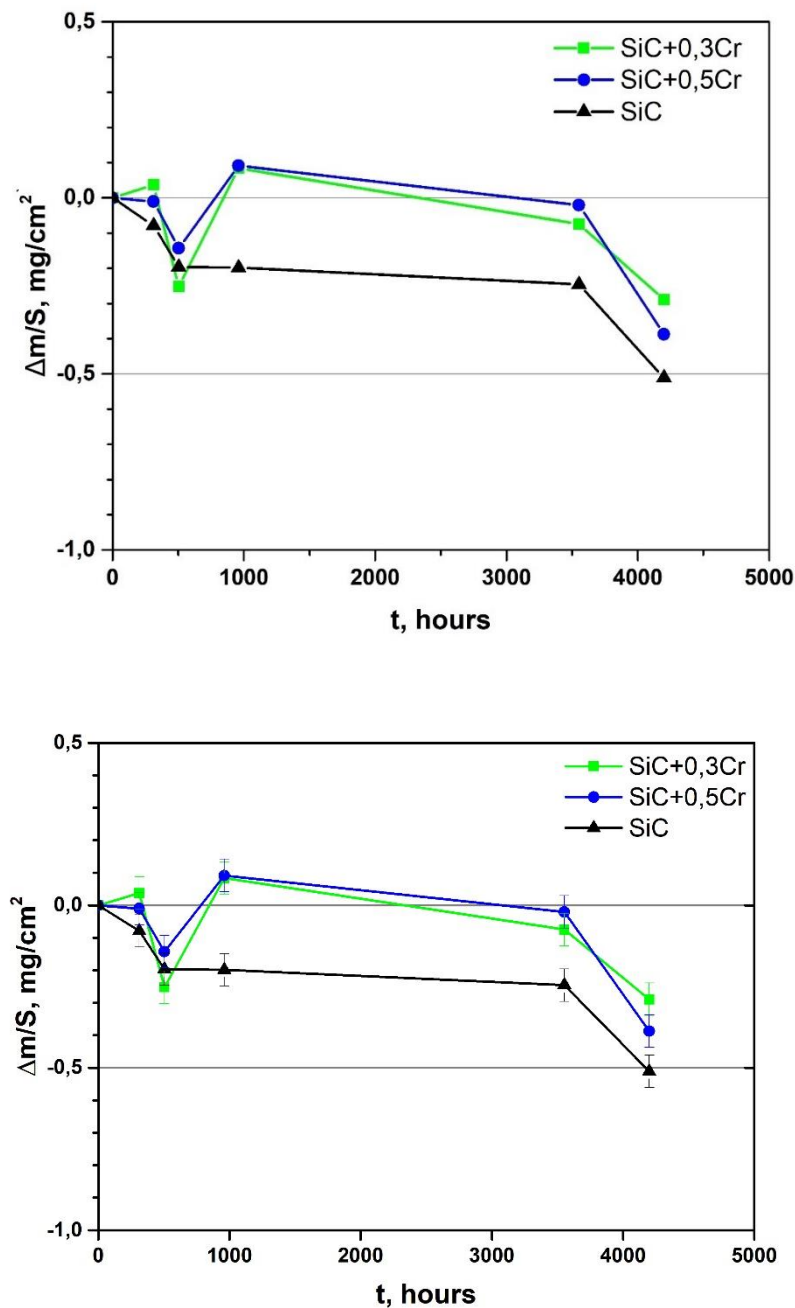
Figure 34. Changes in specific weight of SiC samples as a function of immersion time in distilled water at 90 °C.

As can be seen from Figure 34, silicon carbide samples dissolve in water in a non-monotonous manner, and in the first 600 hours there is a fairly rapid dissolution, then the process is somewhat slower, and after 3500 hours an acceleration of dissolution is again observed. Similar dissolution of silicon carbide was observed in water at a temperature of 350 °C and a pressure of 16.8 MPa (Terrani et al., 2015). SiC dissolution in autoclaves is also observed under different test conditions (Temperature 290-330 °C, Pressure 7-15 MPa, pH 5.6-7.2, oxygen (1.0 ppm O_2) and hydrogen (0.3 – 3.57 ppm H_2) concentration) (Lobach et al., 2020). The dissolution of SiC can reach 0.3 mg/cm² in 1440 hours at a water temperature

EURAD (Deliverable n° 15.6) - Novel materials and processes for the optimisation of long-term container performance
Dissemination level: Public
Date of issue of this report: 06/05/2024

Page

of 290 °C and an oxygen concentration of 1.0 ppm O_2. CVD SiC samples showed mass loss in the range of 0.01 - 0.03 mg/cm^2 for 40 hours at 300 °C and 8.5 MPa water (Suyama et al., 2019). The mechanism of oxidation and dissolution of SiC in the water of BWR and LWR reactors is described in detail in (Lobach et al., 2020). Below is an equation for hydrothermal corrosion of SiC in 300°C water (Terrani et al., 2015):

$$SiC + 2H_2O = SiO_2 + CH_4 \quad (1)$$

$$SiO_2 + 2H_2O = Si(OH)_4 \quad (2)$$
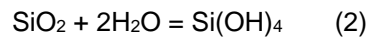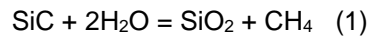
In other words, it was found that parts of the SiC samples were corroded by the formation of silica and the subsequent dissolution of silica in water.

The dissolution of chromium doped SiC samples in the initial test phase up to 500 h is similar to that of pure SiC (Figure 34). Thereafter, however, an increase in the mass of the Cr-doped samples and a significant delay in dissolution are observed between 500 and 3500 hours. This mass change is similar to the behavior of the alloyed samples when tested in water at 350 °C, but significantly different in time (Lobach et al., 2020). This is most likely due to the lower test temperature (90 °C) at which the formation of the protective chromium oxide film is much slower. After 3500 hours of testing, a recurring break in the weight change curve of the samples is observed. It is possible that the selected concentrations of chromium (0.3-0.9 wt%) are not sufficient to form a dense and continuous protective film of chromium oxide on the surface of SiC(Cr) samples. However, the dissolution of chromium-doped samples is slower than that of pure SiC only in the intermediate range of 500 to 3500 hours.

3.1.3.4. Summary

Optimization of technological parameters of SiC composite sintering was carried out. The optimal parameters of the sintering process for obtaining the high-density SiC samples were established (T = 2050°C; t = 30 min; P = 40 MPa; heating rate of 200 °C/min). SiC mixtures with Cr additives (from 0.3 to 0.9 %wt) were prepared. Visual inspection have shown that black dots appear in the silicon carbide structure with increasing chromium concentration, possibly, carbon, silicides or chromium carbides. According to Raman spectroscopy obtained SiC (Cr) samples belong to the polytype 6H-SiC. Silicon carbide samples with chromium concentration from 0.3 to 0.5 %wt have the highest microhardness (25 GPa) and nanohardness (37.8 GPa). Samples of pure SiC and chromium (0.3%wt. and 0.5%wt.) doped SiC were tested for long-term corrosion resistance in distilled water at 90 °C. The corrosion test results show that pure SiC samples are soluble in water. Chromium-alloyed samples dissolve at the early stage of the test, increase in weight at the intermediate stage, which may be due to the formation of protective films, and begin to dissolve again after 3500 hours of testing. The average dissolution rate of these materials is in the range of 0.095 to 0.16 μm per hour.

SiC can withstand high temperatures, making it suitable for environments where conventional materials may fail. Pure SiC exhibits solubility in water, but chromium-doped SiC has slightly higher corrosion resistance. The dissolution rate in water is quite low, not exceeding 0.16 μm/hour. SiC has high strength and hardness, which can lead to less material use and lighter containers. SiC is more expensive to produce and machine than conventional materials. Steel is susceptible to corrosion without proper coating or treatment, and is heavier than SiC, which can result in higher transportation costs. Copper has good corrosion resistance. Copper is also more expensive than low-alloy steel. Further research and development is needed to optimize the alloying and sealing methods of SiC for container applications and to fully evaluate its feasibility compared to traditional materials.

Ceramic-coated steel containers should improve the corrosion resistance of those containers, and reduce the $H_{2(g)}$ production. Therefore, the primary requirement of a ceramic coating applied to carbon steel (or cast iron) nuclear waste disposal canister is to prevent access of bentonite and/or clay pore water to the substrate *via* cracking or leaching for a period of a few hundred to a few (tens) of thousands of years, depending on the geological disposal facility concept. Ceramic coating solutions for SF/HLW

EURAD (Deliverable n° 15.6) - Novel materials and processes for the optimisation of long-term container performance
Dissemination level: Public
Date of issue of this report: 06/05/2024

Page

disposal canisters are less mature than metallic coatings. The main issues to be addressed are related to the inherent brittleness of ceramics, the mismatch of the coefficient of thermal expansion with the underlying steel, and the requirement for relatively large thicknesses and very low porosity. Nevertheless, yttria-stabilized zirconia or graded alumina and titania multilayer coatings appear to be promising options that require further development before their feasibility can be better assessed. Regardless of the ceramic coating material selected, methods for covering the lid-to-canister weld and repairing the coating would also need to be developed.

Physical Vapor Deposition (PVD) coatings provide good corrosion protection compared to coatings deposited by conventional spraying. Despite the lower thickness of PVD coatings, they have much lower porosity than coatings deposited by spraying. Another major advantage of PVD over electrochemical deposition is the environmental friendliness of the process.

3.1.4. CrN-based coatings

Chromium nitride (CrN) has proven to be one of the most successful and widely used PVD coatings in industry due to its high hardness, excellent wear resistance and remarkable stability against corrosion (Milošev et al., 1997). The CrN coating deposited on AISI 304 stainless steel has high corrosion resistance in 0.5M H_2SO_4 solution and 0.5M NaCl solution (Milošev et al., 1993). The CrN film with gradient structure design showed a lower coefficient of friction (COF) and wear rate than a single CrN layer under high load and frequency conditions, indicating a good potential to improve the anti-wear and anti-corrosion capabilities of pump valve pipes and hydraulic and power transmission systems in marine environments (Cen et al., 2018). The demand for high quality coatings in recent years has led to intensive research into the further development of the chromium-based coating family (Cedeno-Vente et al., 2021). Daub et al., (2015) provided a comparative analysis of the corrosion resistance of 2-4 µm thick CrN, TiAlN and AlCrN coated Zry-4 alloy. The CrN coating was shown to have better overall performance in both aqueous and steam environments. CrN coatings on the Stellite™ (cobalt-based alloy) samples showed excellent wear and corrosion resistance in high-temperature, high-pressure water with γ-rays of 100 Gy/h by 60Co source irradiation during testing (Kawana et al., 1996). The Co elution rate from stellite decreased drastically with film thickness, and it can decrease by about 4 orders of magnitude in CrN coatings with a thickness of 7 µm. This is the only publication we are aware of that has investigated the effect of γ-irradiation on the corrosion resistance of coatings. Chromium nitride coatings are promising for the corrosion protection of carbon steel, but additional studies are needed on the long-term corrosion processes in the simulation of geological disposal (T = 90°C).

The main goal of the KIPT research was both to optimize the process of obtaining ceramic CrN coatings on steel substrates by the PVD method and to prepare a batch of samples for corrosion testing.

3.1.4.1. Sample preparation

A set of ceramic CrN coatings was formed using unfiltered cathodic arc evaporation (CAE) in a Ukrainian industrial cathodic arc machine "Bulat-6". A vacuum arc plasma source with magnetic stabilization of a cathode spot was used. The cathodes used in the experiments were made of pure chromium. The arc current of the chromium cathode was I_{Arc} = 100±2A. Nitrogen gas (99.9% purity) was used in the chromium nitride deposition experiments. The thickness of the coatings obtained was ≈30 µm. In this case, the parameter that was changed was the substrate bias voltage from -50 to -300 V. The substrate bias voltage significantly affects the energy of the deposited particles and thus the composition of the structure and the properties of the coatings. The coatings were deposited on a low carbon steel substrate (see chemical composition in Table 5).

EURAD (Deliverable n° 15.6) - Novel materials and processes for the optimisation of long-term container performance
Dissemination level: Public
Date of issue of this report: 06/05/2024

Page

Table 5. Chemical composition of the low carbon steel (named as Steel 3 in Ukraine).

C	Si	Mn	Ni	S	P	Cr	N	Cu	As
0.14 - 0.22	0.15 - 0.3	0.4 - 0.65	0.3	0.05	0.04	0.3	0.008	0.3	0.08

The parameters of the chromium nitride coating deposition processes are given in Table 6. At least 10 samples were used for each deposition process for all types of studies.

Table 6. CrN coatings deposition conditions: arc current I, nitrogen pressure P_{N2} and bias voltage U_b.

Coating Deposition Process Number	Deposition Parameters		
	I, A	P_{N2}, Pa	Ub, V
CrN#1	100	1.8	-50
CrN#2	100	1.8	-150
CrN#3	100	1.8	-300

3.1.4.2. Analysis

XRD analysis of the coatings was carried out in Cu-Kα radiation (λ = 0.154187 nm) using X'Pert Pro diffractometer with 1D PIXcel detector. Phase identification was performed using the COD database. Estimation of microstructural characteristics (crystallite size D and microstrain ε) is based on integral breadth analysis. The coating structure was analyzed using Raman spectroscopy. The Raman spectra were recorded at room temperature using a micro-Raman system (InVia, Renishaw, UK) and a 514 nm argon ion laser as the excitation source. Scattered radiation was collected with ×50 microscope objective. Spectra were recorded in the range of 120–3300 cm^{-1} in several randomly selected points.

The corrosion resistance of the steel substrate and the substrate-coating systems was evaluated by potentiodynamic polarization tests using an Electrochemical Unit. The measurements were carried out in a conventional three-electrode cell with a sample acting as the working electrode. The active area of each sample was 1 cm^2. The reference electrode was a saturated calomel electrode (SCE, $Hg/Hg_2Cl_2/KCl$), and a platinum sheet was used as the counter electrode. The potentiodynamic polarization tests were conducted in 3 wt.% NaCl solution (pH=6.5), at room temperature (25 ± 1 °C).

Assessment of the surface morphology of the samples, within the corroded areas and those not treated with the corrosive medium, was performed by means of a Scanning Electron Microscope (SEM). The mechanical properties of the coatings were determined by nanoindentation using the Nano Indenter-G200 system (Agilent Technologies, USA) equipped with Berkovich diamond tip. The depth of indentation was approximately 500 nm.

The adhesion of CrN coatings was determined using the Daimler−Benz test under 1500 N load (Vidakis et al., 2003). In this test, a six-grade scale (HF1-HF6) indicates the level of adhesion of a coating: HF1−HF4 indicates good adhesion with small cracking or delamination of the coating in the surrounding of the crater, whereas HF5 and HF6 represent a poor adhesion with large coating delamination around the indented zone (Figure 35).

EURAD (Deliverable n° 15.6) - Novel materials and processes for the optimisation of long-term container performance
Dissemination level: Public
Date of issue of this report: 06/05/2024

Page
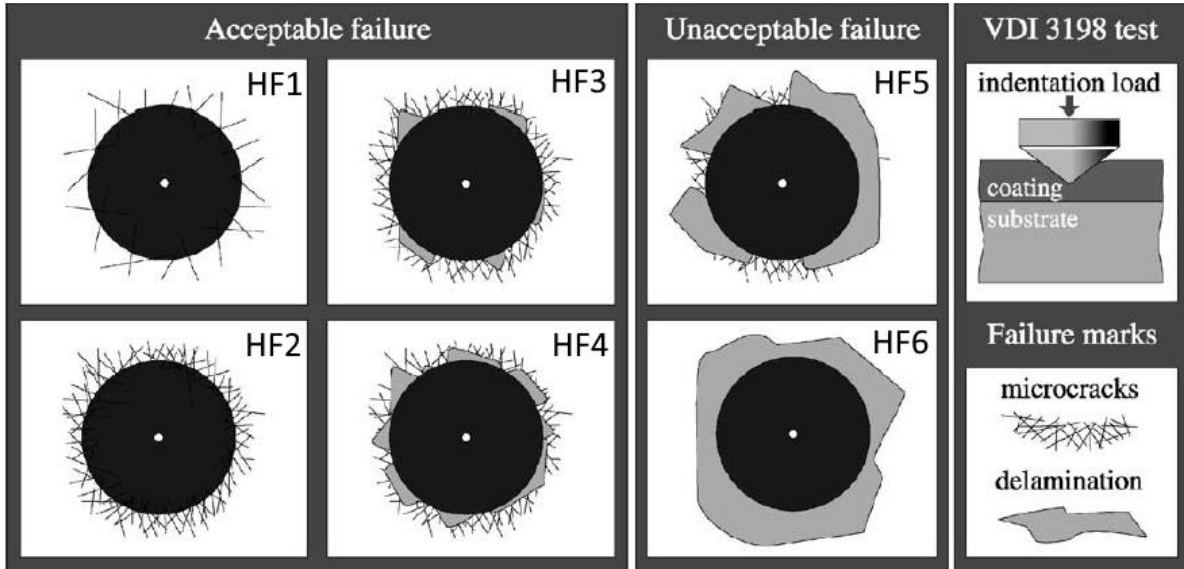
Figure 35. The principle of the VDI 3198 (Daimler−Benz) indentation test (Vidakis et al., 2003).

Structural analysis of the steel substrate-CrN coating system has been performed. XRD phase analysis showed that the substrate is ferritic steel (Figure 36a) with a lattice parameter a = 2.869 Å. It should be noted that diffraction peaks from the substrate are also present in the diffraction patterns of the analyzed coatings.

The positions of the diffraction lines in Figure 36b correspond to the data in the cards for CrN (ICDD 11-0065) and Cr_2N (ICDD 35-0803). Note that the diffraction lines are shifted to lower angles with respect to the equilibrium position of CrN, indicating macro stress. This is caused by increasing the substrate bias voltage, which can lead to changes in the phase composition of the coating as a result of sputtering and Cr_2N phase formation (Figure 36b for U_b = -300 V). Some lines are also broadened. This would indicate both grain refinement and the occurrence of micro stresses. Chromium nitride coatings #2 (Figure 36b) consist of strongly textured fcc CrN phase with preferred orientation {111}. The lattice parameter of chromium nitride CrN a = 4.186 Å is much more than the literature data (a = 4.148 Å), which may be due to the presence of residual stresses in the coating. The estimated microstructural characteristics of CrN coating are crystallite size D = 42.8 nm and strain ε = 3.25·10^{-3}.

a   *b*
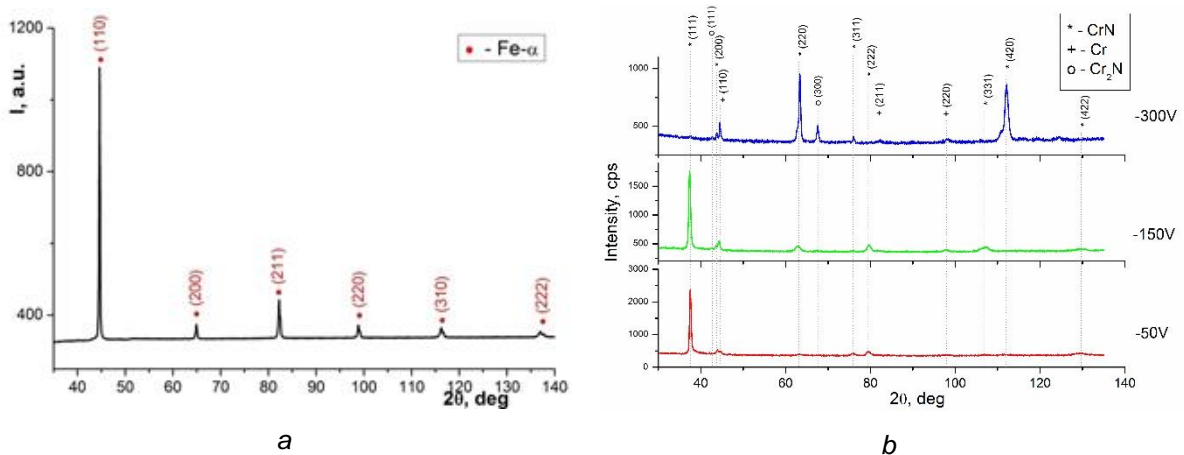
Figure 36. X-ray diffraction patterns of substrate Steel (a) and CrN coatings deposited under different bias potentials Ub (b).

EURAD (Deliverable n° 15.6) - Novel materials and processes for the optimisation of long-term container performance
Dissemination level: Public
Date of issue of this report: 06/05/2024

Page
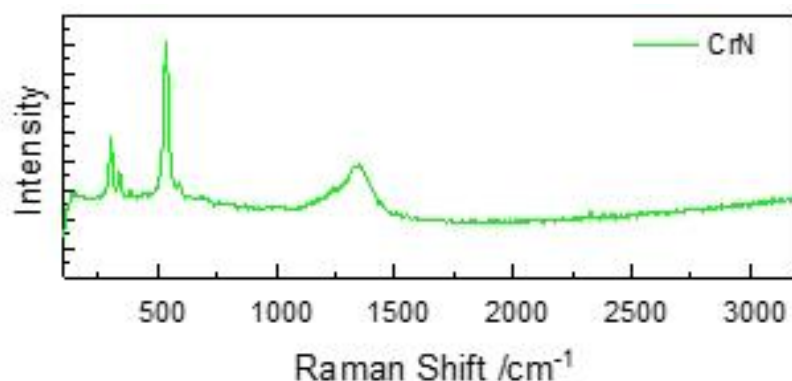
Figure 37. Raman scattering of CrN #2 coating on steel substrate.

For a sample coated with a CrN layer the narrow and well-resolved bands centered at 298, 340, 382 and 533 cm^{-1} confirm the presence of crystalline CrN phase (Figure 37) (Qi et al., 2013). Thus, chromium nitride coatings that were deposited by cathodic arc evaporation have a crystalline structure. Depending on the substrate bias potential, it is possible to change the phase composition of these coatings and the size of the crystallites. The structural characteristics and mechanical properties (hardness and elastic modulus) of thick chromium nitride coatings deposited on steel substrates are summarized in Table 7.

Table 7. CrN coatings: deposition conditions and results of the structural investigations composition, structural parameters and mechanical properties (hardness (H) and Young's modulus (E)).

Coating	Chemical composition, at%		Phase	Lattice parameter, nm	Grain size, nm	Ra, nm	H, GPa	E, GPa
	Cr	N						
CrN#1	48	52	CrN	0.41847	78	120	21	315
CrN#2	49	51	CrN	0.4186	43	98	23	320
CrN#3	53	47	CrN + Cr_2N	0.4187	67	82	24	340

Chromium nitride coatings have high adhesion to steel substrates, at the level (HF1-HF2) according to the scheme shown in Figure 35. with very small cracks in the coating around the crater (see Figure 38).
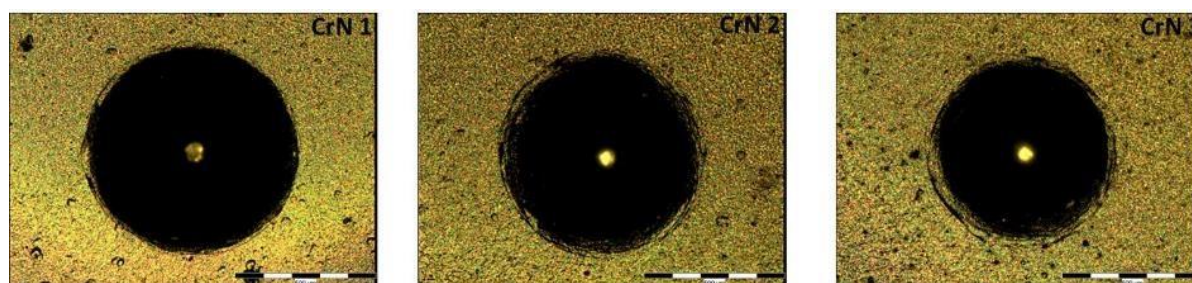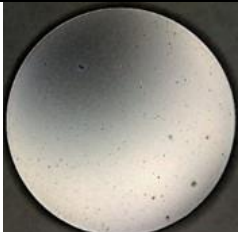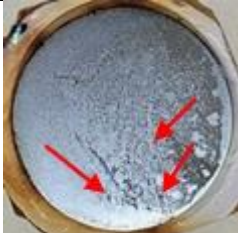
Figure 38. Images of failure modes after Rockwell C indentation for CrN coatings.

3.1.4.3. Long-term corrosion of samples with CrN coatings.

EURAD (Deliverable n° 15.6) - Novel materials and processes for the optimisation of long-term container performance
Dissemination level: Public
Date of issue of this report: 06/05/2024

Page

The corrosion resistance of coated steel samples was studied in a 3% NaCl deaerated solution at room temperature (20°C). The uncoated steel sample is intensively oxidized in the first 24 hours, the oxide on the surface of the sample is poorly bound and goes into solution. After a long exposure, the entire surface of the sample is covered with pitting and a thick layer of rust (Table 8, Steel 3).

Table 8. Photos of coated samples surface in the initial state and after corrosion testing at different immersion times.

Hours	Steel 3	CrN#1	CrN#2	CrN#3
0				
24				
296				

The CrN coated samples did not corrode even at the maximum immersion time. Only the first sample, CrN #1, shows traces of pitting associated with through-hole defects in the coating. Pits are marked with red arrows in the photo. The CrN #2 sample has the best protective properties. After 296 hours of testing, no traces of corrosion were found. Therefore, the chromium nitride coating deposited at a bias potential of -150 V and having the smallest crystallite size of 43 nm has the best corrosion resistance of the coatings investigated.

Additionally, the CrN #2 coating, which was deposited at a substrate potential of -150 V was investigated by electrochemical corrosion methods (open circuit potential and potentiodynamic polarization tests). The results of these studies are shown in Figure 39.

EURAD (Deliverable n° 15.6) - Novel materials and processes for the optimisation of long-term container performance
Dissemination level: Public
Date of issue of this report: 06/05/2024

Page

Figure 39. Open circuit potentials (OCPs) (a) and Tafel plots (b) recorded for the substrate and substrate-CrN coating systems during immersion in 3 wt.% NaCl solution.

As can be seen from Figure 39(a) the Open circuit potentials of bare steel and of the steel-coating system are significantly different. For bare steel, the potential is strongly negative (<-0.5 V). Chromium nitride coatings have a more positive potential (-0.1 V) that practically does not change during the exposure time, confirming their high corrosion resistance. The corrosion potential (E_{corr}) and corrosion current (I_{corr}) for the specimens were calculated from Tafel curves (Figure 39b). For steel and chromium nitride coated steel, the corrosion potentials are -548 and -187 mV and the corrosion currents are 29.6 and 0.85 μAcm^{-2}, respectively. The steel surface and coating were further investigated by SEM methods to determine the formation of pitting and corrosion products (Figure 40).

EURAD (Deliverable n° 15.6) - Novel materials and processes for the optimisation of long-term container performance
Dissemination level: Public
Date of issue of this report: 06/05/2024

Page
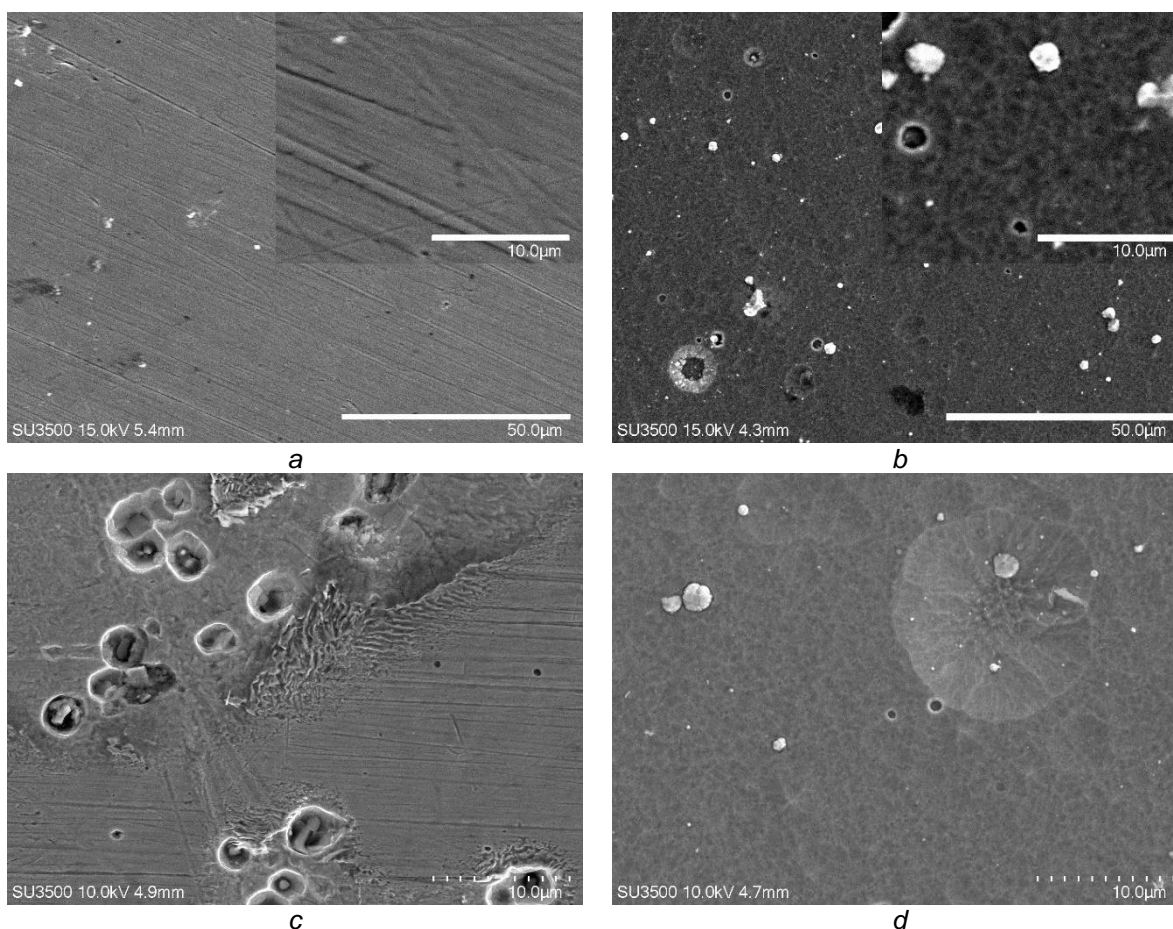
Figure 40. SEM micrographs of the Steel substrate (a, c) and with CrN #2 coatings (b, d), before (a, b) and after (c, d) potentiodynamic polarization tests.

In the initial state, the surface of the steel is smooth, and traces of polishing are visible (Figure 40a) on the surface of the coating along with visible macroparticles and craters (Figure 40b), which is characteristic of nitride coatings deposited by cathodic arc evaporation (Ovcharenko et al., 2015). After the potentiodynamic polarization tests, the steel surface shows traces of pitting corrosion, the size of pits is of the order of 5 μm in diameter (Figure 40c). At the same time, there are no pits on the surface of the CrN coating and the surface became smoother (Figure 40d).

3.1.4.4. Conclusion

The obtained research results confirm the high corrosion resistance at a temperature of 20 °C in a solution of 3% NaCl of thick coatings of chromium nitride deposited by cathodic arc evaporation on the surface of steel.

3.1.5. TiO$_2$ coatings

The most studied class of high hardness coatings formed by PVD methods (magnetron sputtering and cathodic arc evaporation) are titanium nitrides and carbides. Problems of synthesis of various metal oxides by vacuum arc method were discussed in the review (Tay et al., 2006). Earlier, KIPT specialists developed vacuum-arc nanostructured TiO$_2$-based coatings (structure - anatase) with controlled bactericidal activity for orthopaedic implants (Belous et al., 2013). The influence of the negative bias potential of the substrate has been studied by the authors (Belous et al., 2018). It is shown that titanium

EURAD (Deliverable n° 15.6) - Novel materials and processes for the optimisation of long-term container performance
Dissemination level: Public
Date of issue of this report: 06/05/2024

Page

coatings deposited in an oxygen medium at a pressure of 0.03 Pa represent a dispersed system of oxides, the composition of which depends on the magnitude of the bias potential on the substrate. The results of electrochemical measurements show that the current density characterizing the dissolution of steel coated with titanium nitrides and oxynitrides with a thickness of ~ 6 μm is up to 10 times lower than for uncoated steel in the range of corrosion potentials -0.5-0 V. With the increase of the coating thickness up to 12 μm, the samples corrode much slower, which correlates with the decrease of the coating porosity, where the density of the corrosive current decreases by 2 - 3 orders of magnitude. The highest corrosion resistance is observed in the samples with a layer thickness of ~12 μm, deposited from the oxygen-nitrogen mixture at an oxygen pressure $P_{O2} = 3 \times 10^{-2}$ Pa. These coatings provide high corrosion resistance of steel close to that of a pure titanium nitride coating in a 3% aqueous NaCl solution (Belous et al., 2018). The anodized and thermally oxidized Ti samples with TiO_2 coatings showed relatively high corrosion resistance in 4M HCl and 4M H_2SO_4 solutions at 100±5°C, and the passive current density values of the thermally oxidized samples were five orders of magnitude lower than that of the anodized titanium sample under the electrochemical test condition (Minhas et al., 2021). The corrosion protection provided by the conversion coating combined with TiO_2 coating on stainless steel in pure water and saline solution was quite good (Bamoulid et al., 2008). Corrosion test results showed that TiO_2 films deposited on $MgCa_2Zn_1Gd_3$ effectively protected this alloy from corrosion in Ringer's solution at 37°C (Kania et al., 2021). Although it is difficult to relate these qualitative electrochemical corrosion data to long-term storage performance, it can be assumed that titanium oxide coatings deposited by PVD methods are promising for corrosion protection of low-carbon steel containers. Additional studies are needed on the mechanisms of long-term corrosion processes in the TiO_2 coating-steel substrate system under conditions simulating geological disposal (T = 90°C).

The main objective of the KIPT research was to optimize the process of obtaining ceramic TiO_2 coatings on steel substrates by the Cathodic Arc Evaporation (PVD) method and to prepare a batch of samples for corrosion testing.

3.1.5.1. Sample preparation

A set of ceramic TiO_2 coatings was formed by unfiltered cathodic arc evaporation (CAE) in a Ukrainian industrial vacuum arc furnace "Bulat-6". A vacuum arc plasma source with magnetic stabilization of a cathode spot was used. The cathodes used in the experiments were made of pure titanium (99.9%). The arc current of the titanium cathode was $I_{Arc} = 90 \pm 2A$. Argon and oxygen gases (99.99% purity) were used in the titanium oxide deposition experiments. The thickness of the coatings obtained was ≈30 μm.

Stainless steel (SS 316L) and Steel 3 substrates with dimensions of Ø30 and h=3 mm and polished to a roughness of Ra = 0.02 μm were used as substrates for the deposition of the coatings. Titanium oxide coatings were deposited at 1.8 Pa (gas mixture O_2 + Ar) and at different bias potentials -50, -100 and -150V. A photograph of a titanium oxide-coated steel sample and an SEM image of the coating surface are shown in Figure 41.

EURAD (Deliverable n° 15.6) - Novel materials and processes for the optimisation of long-term container performance
Dissemination level: Public
Date of issue of this report: 06/05/2024

Page
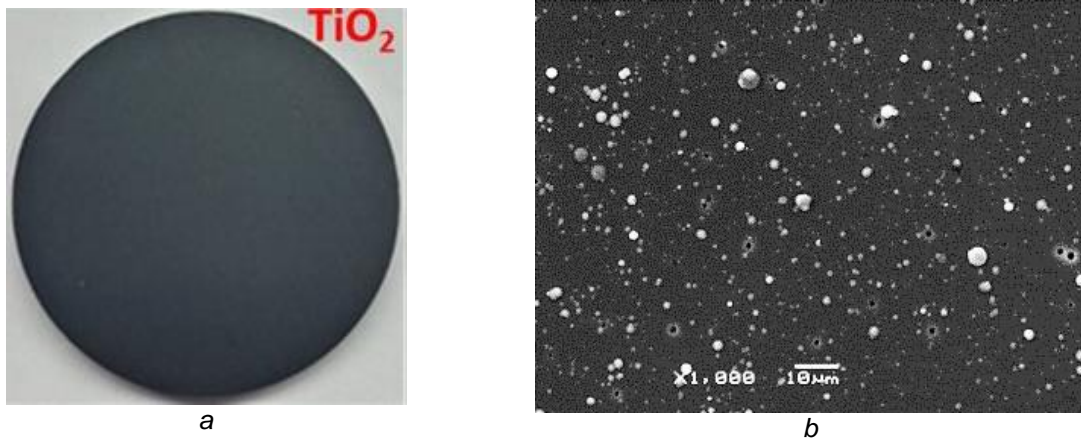
Figure 41. Photo of steel samples with ceramic coating (a) and SEM image of TiO$_2$ film surface (b).

As can be seen from the photograph (Figure 41a), the titanium oxide coating has a dark gray color with no delamination or macrocracking. The microscopic image (Figure 41b) shows microdefects on the surface caused by the presence of macroparticles, which is typical of the cathodic arc evaporation process. The results obtained by the micro-Raman system of the TiO$_2$ coating structure are shown in Figure 42. Multiple point measurements were taken on each sample.
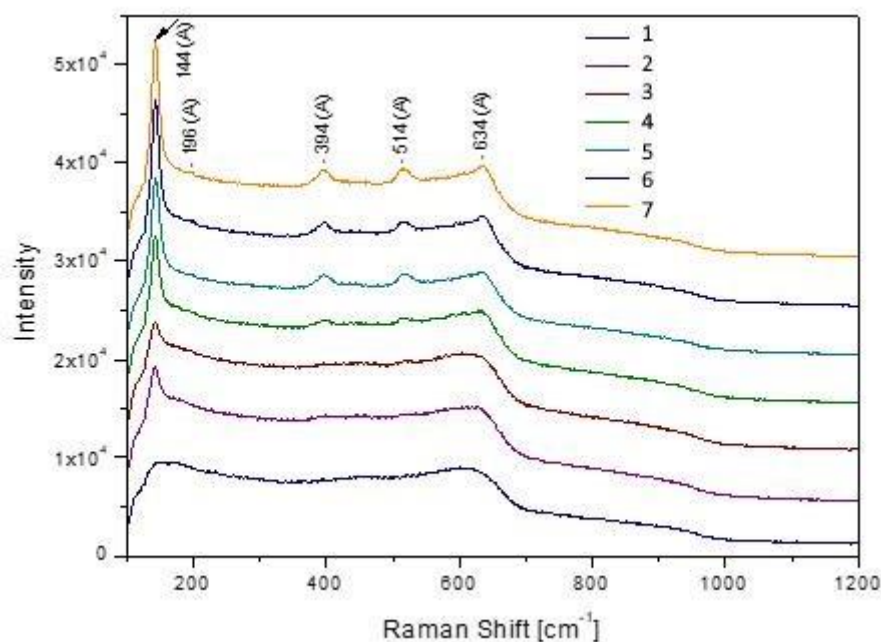
Figure 42. Raman spectra of TiO$_2$ coatings deposited at different bias voltages: -50 V (1-3); -100 V (4, 5) and -150 V (6, 7).

The TiO$_2$ coatings deposited at the substrate bias of -50 V are amorphous (1-3). Measurements at all three points confirmed this. A number of bands characteristic of the anatase crystalline form of TiO$_2$ were distinguished in the samples deposited at higher bias voltages of -100 (4, 5) and -150 V (6, 7). The bands at 144, 196, 394, 514 and 634 cm^{-1} are attributed to $E_{g(1)}$, $E_{g(2)}$, B_{1g}, A_{1g}, B_{1g} and $E_{g(3)}$ active anatase modes, respectively. Since the curves at the measurement points are very close in shape, two measurements were sufficient to determine the crystal structure of the TiO$_2$ coatings deposited at -100

EURAD (Deliverable n° 15.6) - Novel materials and processes for the optimisation of long-term container performance
Dissemination level: Public
Date of issue of this report: 06/05/2024

Page

and -150 V of the bias potential (Figure 42). The hardness (H) and elastic modulus (E) of the TiO_2 coatings are shown in Table 9.

Table 9. Mechanical characteristics: hardness (H) and Young's modulus (E) of the TiO_2 coatings.

Ubias, V	H, GPa	E, GPa
-50	6.4±1.0	155±10
-100	9.5±0.5	172±12
-150	12±1.0	183±15

As shown in Table 9 the bias voltage has a strong effect on the mechanical properties of titanium oxide coatings. As the bias voltage increases from -50 to -150 V, the hardness of the coatings increases from 6.4 to 12 GPa and Young's modulus increases from 155 to 183 GPa.

TiO_2 coatings have high adhesion to steel substrates, at the level (HF2) with very little cracking of the coating around the crater (Figure 43). Coatings deposited at -150 V have better adhesion (Figure 43b) than coatings deposited at lower bias voltages (Figure 43a).

a   b
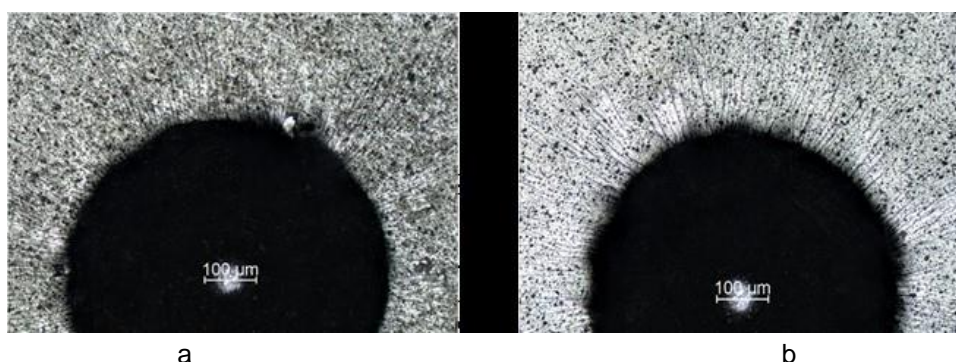
Figure 43. Photos of the imprints in the surface of TiO_2 films deposited at -50 V (a) and -150 V (b) after Daimler-Benz tests.

To evaluate the corrosion resistance of 316L steel substrates coated with TiO_2 coatings, potentiodynamic polarization tests (linear - Figure 44a and cyclic - Figure 44b) were performed using the Atlas 0531 Electrochemical Unit.
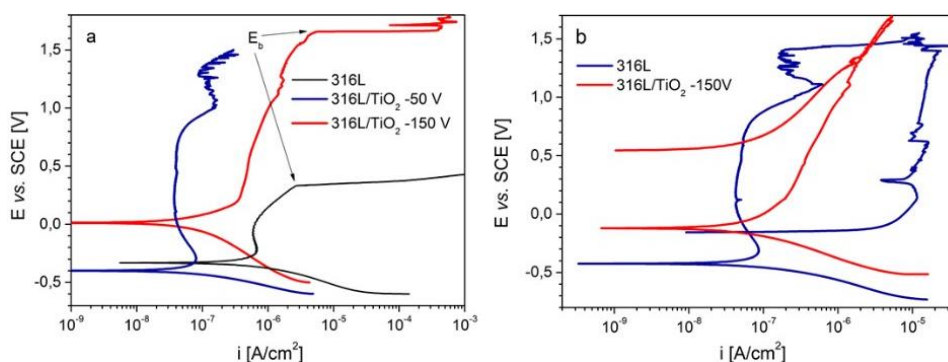
Figure 44. Results of corrosion studies for 316L steel substrate with TiO_2 coatings: linear polarization curves (a) and cyclic polarization curves (b).

EURAD (Deliverable n° 15.6) - Novel materials and processes for the optimisation of long-term container performance
Dissemination level: Public
Date of issue of this report: 06/05/2024

Page

Measurements were performed in a conventional three-electrode cell in an environment of 0.14 M NaCl solution, pH = 7.2. This corrosive environment was chosen only to compare the corrosion resistance of coatings deposited at different bias voltages on the substrate. The obtained polarization curves were used to estimate the corrosion potential (E_{corr}), corrosion current density (I_{corr}), polarization resistance (R_{pol}) and E_b – breakdown potential (or the pitting potential), the potential value at which the anodic current density increases rapidly due to a breakdown of the blocking/passive layerTable 10

Table 10. Corrosion characteristics of the TiO$_2$ coatings deposited on 316 L stainless steel substrates in the 0.14 M NaCl solution and on Steel 3 substrates in 3% NaCl solution.

Sample	E_{corr}, mV	i_{corr}, µA/cm^2	R_{pol}, Ωcm^2	Eb, V
316L	-301	3.00×10^{-1}	94×10^7	0.328
316L/TiO$_2$; -50 V	-409	1.34×10^{-1}	446×10^7	-
316L/TiO$_2$; -150 V	20	0.53×10^{-1}	900×10^7	1.664
Steel 3/TiO$_2$; -150 V	-33	0.815×10^{-1}	-	-

TiO$_2$ coatings deposited at -150 V bias potential have higher chemical stability (higher values of E_{corr} and R_{pol}; lower value of I_{corr}) and pitting corrosion resistance (no hysteresis loop in the cyclic polarization curve Figure 44b). Additionally, the corrosion resistance of these coatings was investigated on Steel 3 samples in 3% NaCl solution. The results of these studies are shown in Figure 45.

<center><i>a</i>   <i>b</i></center>
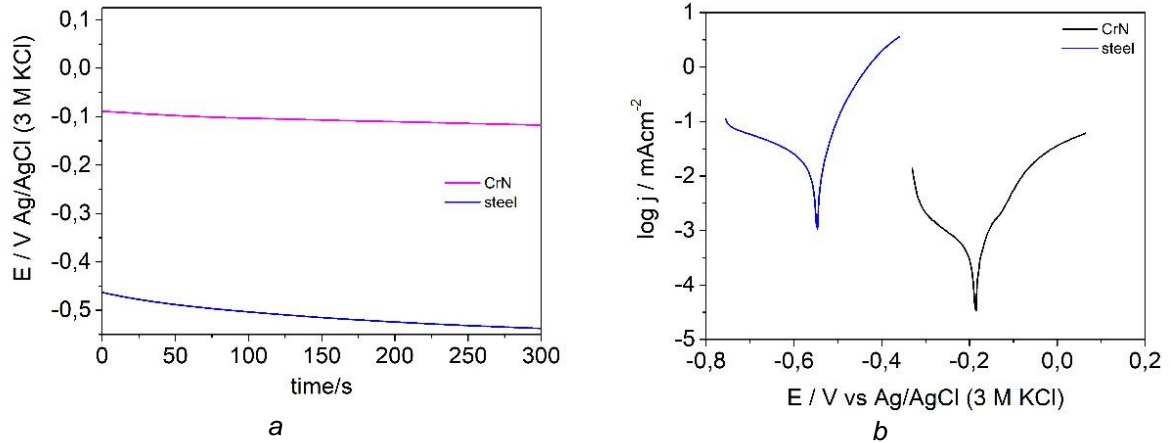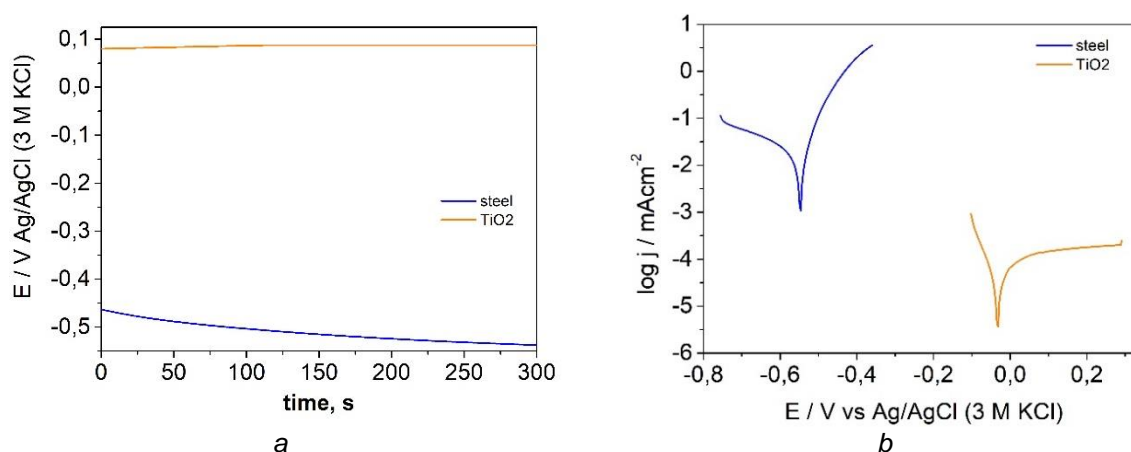
Figure 45. Open circuit potentials (OCPs) (a) and Tafel plots (b) recorded for the Steel 3 and Steel 3/TiO$_2$ coating systems during immersion in 3 wt% NaCl solution.

As shown in Figure 45a, the open circuit potentials of steel and coating differ significantly. Steel has a strongly negative potential (<-0.5 V). The titanium oxide coating has a positive potential of 0.1 V that remains constant during exposure, confirming its high corrosion resistance. The corrosion potential (E_{corr}) and corrosion current (I_{corr}) of the samples were calculated from Tafel curves (Figure 45b). For TiO$_2$-coated Steel 3, the corrosion potential is -33 mV, and the corrosion current is $0.815\cdot10^{-1}$ µA/cm².

It is important to note that the corrosion currents for this coating on stainless steel and on Steel 3 are very close in magnitude at $0.53\cdot10^{-1}$ and $0.815\cdot10^{-1}$ µA/cm², respectively. (Table 10) This may indicate the absence of through porosity in titanium oxide coatings on steel and stainless steel substrates.

The surface of titanium oxide coating on steel substrates was examined by SEM after deposition and after potentiodynamic polarization tests (Figure 46).

EURAD (Deliverable n° 15.6) - Novel materials and processes for the optimisation of long-term container performance
Dissemination level: Public
Date of issue of this report: 06/05/2024

Page
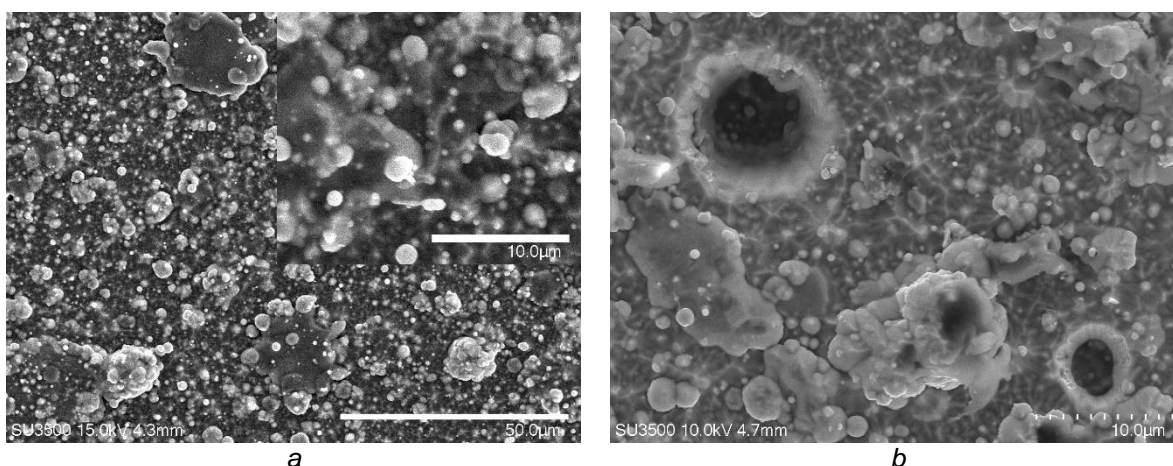
Figure 46. SEM micrographs of the Steel 3 substrate with TiO_2 coatings before (a) and after (b) potentiodynamic polarization tests.

As can be seen from the comparison of the SEM images of the coating surface in Figure 46, craters or pits appear in the coating after corrosion tests (Figure 46b). There are no corrosion products from the steel substrate in these pits, and they do not appear to be through-hole pits. A possible reason for the appearance of such pits after potentiodynamic testing could be the loss of macroparticles of cathode material. Macroparticles are generated at the cathode during the coating deposition process and are typically 0.1-10 µm in size. These macro particles may be embedded in the coating and may be present on the coating surface. They are typically weakly mechanically bonded to the ceramic coating material. The mechanical loss of these macro particles from the coating will lead to the formation of craters. Such craters do not penetrate the steel substrate, so 30 µm titanium oxide cathodic arc coatings provide a relatively high level of protection against corrosion of steel substrates in a 3% NaCl solution.

3.1.6.   Long-term corrosion resistance of ceramic CrN and TiO_2 coatings in water at 90°C

A furnace with a thermostat was specially prepared for long-term corrosion testing during 4200 hours on steel samples with ceramic coatings. The coatings were deposited on cylindrical Steel 3 samples. CrN and TiO_2 coatings were deposited at parameters selected from previous experiments: bias potential on the substrate -150 V, the thickness of coatings 30 µm. The samples were continuously rotated against the cathode for uniform coating deposition over the entire surface.

After deposition, the samples were weighed and placed in glass containers with deaerated distilled water. The containers with water were placed in a thermostat in which the temperature was maintained at 90 °C. To measure the change in weight of the samples, they were periodically removed and weighed. The test bench layout, sample drawing, and sample photos are shown in Figure 47.

EURAD (Deliverable n° 15.6) - Novel materials and processes for the optimisation of long-term container performance
Dissemination level: Public
Date of issue of this report: 06/05/2024

Page

Figure 47. Schematic diagram of thermostat (a), drawing of steel sample (b), photographs of Steel 3 samples (c) with CrN (d) and TiO$_2$ (e) coatings.

The results of the long-term corrosion studies of Steel 3 samples with CrN and TiO$_2$ in distilled water at 90 °C are shown in Figure 48.

Figure 48. Changes in the specific weight of Steel 3 samples with CrN and TiO$_2$ coatings as a function of immersion time in distilled water at 90 °C.

EURAD (Deliverable n° 15.6) - Novel materials and processes for the optimisation of long-term container performance
Dissemination level: Public
Date of issue of this report: 06/05/2024

Page

As can be seen in Figure 48, the steel sample has a high weight loss and dissolves intensely to form rust. The tests on the steel sample were terminated after 500 hours due to severe dissolution. A photograph of the steel sample after the test is shown in Figure 49a.

a   *b*   *c*
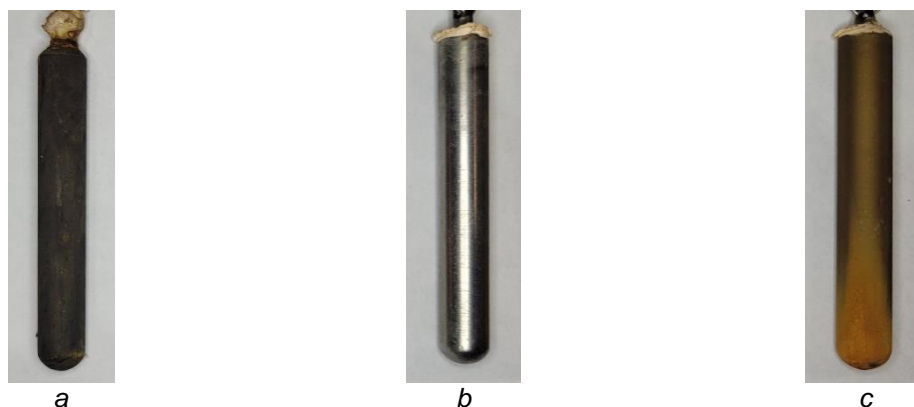
Figure 49. Photos of samples after testing: Steel 3 sample after 500 h (a); CrN coating (b) and TiO$_2$ coating (c) after 4000 h.

The TiO$_2$ coatings showed a slight weight loss in the first phase of the test up to 1000 hours (Figure 49). However, after 1000 hours, a sharp increase in weight loss was observed due to the appearance of through pitting on the steel substrate. The formation of rust stains on the surface and intense corrosion at the end of the sample were observed (Figure 49c). These coatings may need to optimize the architecture of the interface with the steel substrate to avoid pitting and porosity. CrN coatings show minimal weight change throughout the test period, indicating high corrosion resistance (Figure 49). No traces of pitting or rusting are observed on the CrN coating surface after 4000 hours of testing (Figure 49b).

3.1.6.1. Summary

The influence of bias potential on the structure and corrosion resistance of thick (30 µm) CrN coatings has been studied. The coatings have a crystalline structure, the crystallite sizes depend on the bias potential, the smallest crystallite size of 43 nm was obtained at a potential of -150 V. The coatings have high mechanical properties (H=23 and E=320 GPa) and good adhesion (HF1) to steel substrate. The CrN coating deposited under bias - 150 V with the smallest crystallite size of 43 nm has the best protective properties: after 296 hours of testing at 20 °C in 3% NaCl solution, no traces of corrosion were found. Electrochemical studies have shown that in this solution, the potential and corrosion current of the coating (E_{corr}= -187 mV, I_{corr}=0.85 µAcm^{-2}) is much lower than that of Steel 3 (E_{corr}= -548 mV, I_{corr}=29.6 µAcm^{-2}), and no traces of pitting corrosion have been found.

TiO$_2$ coatings deposited at -150 V bias potential have anatase structure, acceptable mechanical properties (H=12 GPa), higher chemical stability (higher values of E_{corr} and R_{pol}; lower value of I_{corr}) and resistance to pitting corrosion (no hysteresis loop in the cyclic polarization curve). For the TiO$_2$ coating, the corrosion currents on stainless steel and Steel 3 are very close in magnitude at $0.53 \cdot 10^{-1}$ and $0.815 \cdot 10^{-1}$ µA/cm2, respectively. The results of near-disposal tests on steel samples with CrN and TiO$_2$ coatings show that in water at 90 °C, the TiO$_2$ coatings show weight loss and pitting. The best result in terms of corrosion resistance is shown by the CrN coatings with minimal weight loss and no pitting on the surface. The data on the mechanical properties and corrosion resistance of cathodic arc ceramic coatings of CrN and TiO$_2$ indicate that single-phase CrN coatings with a thickness of at least 30 microns are the most promising for protecting low-alloy steel containers. The corrosion resistance of these

EURAD (Deliverable n° 15.6) - Novel materials and processes for the optimisation of long-term container performance
Dissemination level: Public
Date of issue of this report: 06/05/2024

Page

ceramic coatings can be further improved by creating multilayer structures such as CrN/CrON and Ti/TiO$_2$. The composition and structure of multilayer ceramic PVD coatings can be optimized to prevent the formation of porosity and significantly enhance their corrosion resistance. The use of low-alloy steel with ceramic coatings can be a less expensive alternative to copper in the manufacture of containers.

4. Metallic Materials and Coatings

4.1. Alternative copper grades: molecular dynamics and experimental performance assessment

VTT's work in the subtask "Alternative metallic materials" aimed to explore the viability of alternative copper grades for copper canisters, considering factors such as improved availability, corrosion resistance and lower cost. The work was mainly experimental in nature, but also included a brief modelling part aiming to support the understanding of the effects of hydrogen in copper. The term "copper" refers to a spectrum of alloys, whose material properties depend on dopants and impurities within the microstructure.

Advantages of copper include excellent mechanical properties and superior corrosion resistance, but its disadvantages are the high cost, particularly for highly pure grades, and the limited availability of those grades. Container materials typically require copper grades with a purity of ≥99.3% (w/w). The copper chosen in the KBS-3 concept must follow the standard EN 1976:2012 (UNS C10100), with additional stipulations for critical element/impurity concentrations, e.g., O <5 wt-ppm, P from 30-100 wt-ppm, H < 0.6 wt-ppm, and S< 12 wt-ppm (SKB, 2022).

Most approaches nowadays focus on adopting oxygen-free phosphorus-doped (OFE+P) copper as the container material but given ongoing optimization of the final concepts other copper grades should also be investigated. High conductivity phosphorous doped copper (HCP) is a potential candidate for a canister material due to its lower cost, greater availability, and use of recycled material. However, little is known about how this material behaves in anoxic repository conditions in contact with aggressive agents. This research focused on investigating the impact of impurities on corrosion properties of commercial copper alloys, OFE+P and HCP, in the Finnish disposal concept. The properties of the copper alloys examined in this study are compiled in Table 11.

Table 11. Composition and typical use of Cu-OFE+P and Cu-HCP copper alloys.

	Cu-OFE+P	*Cu-HCP*
Description	*Very pure, oxygen-free copper*	*Higher oxygen content (Cu 99.95 wt.%), low residual P content*
Composition	*Cu (min. 99.99 wt.%)* *Bi (< 5 wt-ppm)* *Pb (<5 wt-ppm)* *P (30-70 wt-ppm)* *O (<1 wt-ppm)*	*Cu (min. 99.95 wt.%)* *P (20-70 wt-ppm)* *O (30-40 wt-ppm)*
Typical use	*Current canister material in the Finnish national concept*	*Telecommunication cables, terminals, clad products, busbars, base plates for power modules, electrical conductors, pressure vessels*

4.1.1. Molecular dynamics modelling

The ambitious goal of the molecular dynamics modelling was to study the effect of hydrogen on the mechanical properties of Cu. Essential steps towards such modelling were taken. These included setting up models for a perfect Cu crystal, a Cu crystal with point defects, and polycrystalline Cu with a random set of grain sizes and orientations. In these systems, diffusion of atomic hydrogen was studied to check

EURAD (Deliverable n° 15.6) - Novel materials and processes for the optimisation of long-term container performance
Dissemination level: Public
Date of issue of this report: 06/05/2024

Page

that the transport properties of hydrogen can be estimated from simulations, and the effect of point defects and grain boundaries on the transport properties can be evaluated. The work did not attempt to assess the chemistry leading to formation of hydrogen on the Cu surface, nor the penetration of hydrogen into the bulk sample. Thus, all simulations were performed for bulk conditions. Different Cu grades were not explicitly considered, and all simulated systems consisted of pure Cu with hydrogen.

Although surface chemistry of hydrogen on Cu was not attempted in the current work, it was nevertheless seen as important to ensure it could be done in the future, making use of the work of this project. Furthermore, it was considered important to include the potential association/dissociation reactions of hydrogen in bulk Cu. For this reason, a force field was required that has the capability to describe the dissociation of the hydrogen molecule, as well as the recombination of two hydrogen atoms into a hydrogen molecule, when the hydrogen is inside a Cu lattice. Such force fields include the ReaxFF force field (van Duin et al., 2001), the COMB force field (Liang et al., 2013), and the Cu-H Bond-Order Potential (Zhou et al., 2015). After an evaluation of these options, we concluded that the Cu-H Bond-Order Potential (hereinafter BOP) was best suited for our purposes. This force field was available in the MD software LAMMPS (Thompson et al., 2022) which VTT is already familiar with.

The creation of a bulk face-centered-cubic (FCC) copper lattice using LAMMPS is simple, involving only a few lines in the input script. For bulk FCC copper, we verified the elastic constants C_{11}=176 GPa, C_{12}=125 GPa and C_{44}=82 GPa given in (Zhou et al., 2015) using a system of 4000 Cu atoms, and the appropriate script in the LAMMPS examples for measuring elastic properties. The creation of point defects in the lattice is also straightforward. Randomly removing 1% of Cu atoms yielded elastic constants of C_{11}=174 GPa, C_{12}=122 GPa and C_{44}=81 GPa, while removing 5% of Cu atoms yielded elastic constants of C_{11}=161 GPa, C_{12}=108 GPa and C_{44}=75 GPa.

The introduction of grain boundaries to the structure is more challenging due to the vast number of different possibilities. Creating a series of single, well-defined grain boundaries is relatively easy (Tschopp et al., 2015) but achieving a single system with a grain boundary structure that would resemble the grain boundary structure of a real polycrystalline material is practically impossible, as this implies a system with a very large (computationally prohibitive) number of atoms to accommodate all boundaries in appropriate proportions, as dictated by their energetics.

In practice, creation of moderate-size polycrystalline systems makes use of randomness. In the popular Voronoi tessellation method, a space containing a set of random points is divided into cells surrounding these points such that a segment of a cell boundary between two points is always equidistant from these two points. The cell volumes can then be filled with structures of a (randomly) chosen orientation. However, in the current work, we chose an approach based on melt solidification. First, a relatively large (500000 atoms) perfect crystal was created. It was subsequently heated to T=2000 K, which is well above the melting point T_m=1390 K for the BOP potential. After the system had completely melted, the temperature was brought again below the melting point, which resulted in the formation of a polycrystalline system.

Figure 50 presents the evolution of crystallinity as a function of time at two temperatures (600K, 800 K). Specifically, the quantity plotted is the fraction of atoms belonging to a FCC crystalline phase, as given by the Common Neighbor Analysis algorithm implemented in the Ovito software (Stukowski 2010). Following a rapid period (< 1 ns) of initial nucleation, the effect of temperature on the crystallinity, and crystallization rate is clearly observed, with a higher temperature corresponding to slower crystallization rate and higher crystallinity.

EURAD (Deliverable n° 15.6) - Novel materials and processes for the optimisation of long-term container performance
Dissemination level: Public
Date of issue of this report: 06/05/2024

Page
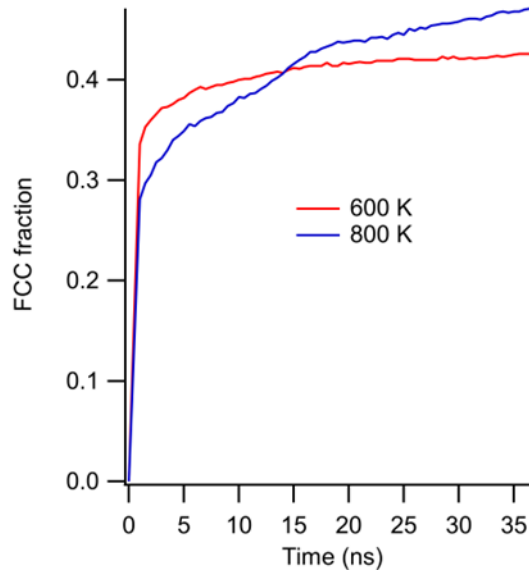
Figure 50. Time evolution of the FCC crystalline phase during melt solidification.

Figure 51 shows visualizations of the polycrystalline structures. It is observed that the FCC crystallites (green) are somewhat bigger in the 800K case. The red portions are designated as the hexagonal close-packed (HCP) phase by the common neighbour analysis (CNA) algorithm, and they may correspond to glide planes in the FCC structure. The HCP phase represents about 15% of all atoms. The rest (grey) is classified as "other" by the CNA, and it contains the grain boundaries. Obviously, using a higher temperature would have resulted in yet larger crystallites, and likely more well-defined grain boundary regions, but the process would have been too slow to observe computationally, as a larger system would have been required to accommodate the larger crystallites. The structures shown in Figure 51 may be thought to represent "worst-case" scenarios when considering the effect of grain boundaries on hydrogen diffusion.
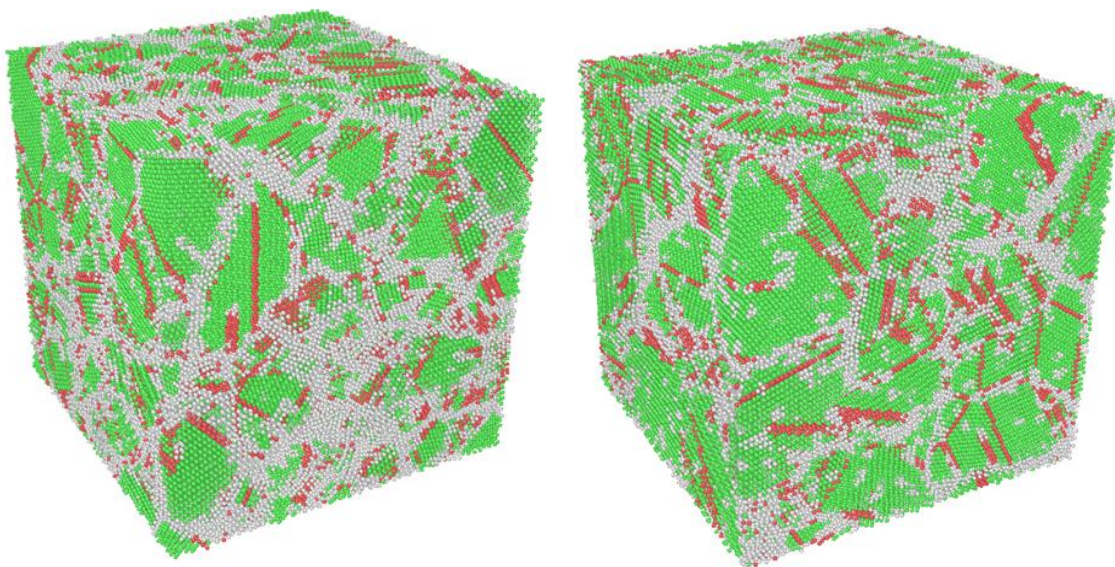
Figure 51. Polycrystalline Cu structures from melt solidification at 600 K (left), 800K (right).

EURAD (Deliverable n° 15.6) - Novel materials and processes for the optimisation of long-term container performance
Dissemination level: Public
Date of issue of this report: 06/05/2024

Page

The diffusion of hydrogen was studied in a single crystal and two polycrystalline systems by randomly inserting hydrogen atoms into the structure at a concentration of 1%. This concentration is much higher than the true hydrogen uptake of copper, but it is used for computational reasons. True hydrogen concentrations of the order of ppm would mean a single hydrogen atom in a structure of 500000 copper atoms. Observing the diffusion of a single atom for diffusion, while possible, would lead to extremely poor statistics, as well as spending most of the computational resources on the movement of copper atoms. It is expected that a concentration of 1% is high enough to provide meaningful statistics on diffusion, but low enough so that interactions (and possibly reactions) between hydrogen atoms do not affect the results.

The diffusion of hydrogen atoms was determined by recording the Mean Square Displacement (MSD) in the temperature range 300-1000 K as a function of time, and computing the diffusion constant from the slope of the MSD(t) curve according to

$$\langle \bar{r}^2(t) \rangle = \frac{1}{N} \sum_N [\bar{r}(t) - \bar{r}(0)]^2 = 6Dt$$

where N is the number of hydrogen atoms, and D is the diffusion constant. At each temperature, the simulation was run until a clear linear dependence of the MSD on time was observed and the slope of the curve could be accurately determined.

The simulated diffusion constants are plotted in Figure 52 together with a line fitted to a compilation of experimental results (Magnusson et al., 2017). Simulations were performed for a perfectly crystalline FCC Cu, as well as for the two polycrystalline Cu structures shown in Figure 51. All simulated diffusion constants are slightly below experimental ones. As expected, diffusion is slowest in the perfect FCC crystal. The atomic disorder due to grain boundaries increases the diffusion constant, and it is noted in particular that the structure produced by melt solidification at 600K containing smaller crystallites and wider grain boundaries yields the fastest diffusion. However, the effect of grain boundaries is perhaps surprisingly small, considering that diffusion along grain boundaries is often thought to be dominating, as the defects in grain boundaries generally provide more free volume for diffusion. On the other hand, the tendency of hydrogen to be trapped in Cu lattice defects is well known (Ganchenkova et al., 2014), but traps not involving impurities (such as oxygen) are shallow and should not be effective at temperatures above 500K. The current simulations were not designed to analyse hydrogen trapping in detail.
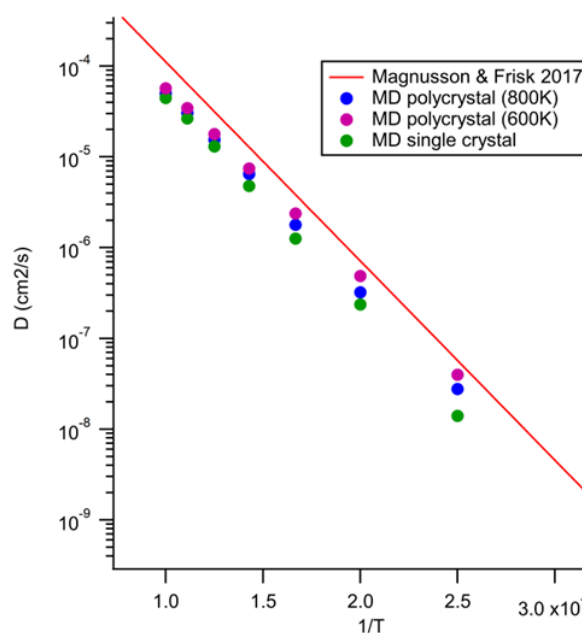
Figure 52. Experimental and simulated diffusion constant for hydrogen atoms.

4.1.2. Experimental approaches

The corrosion behavior of copper canisters is linked to the repository environment evolution, which is divided into four stages or phases and correlates with the mechanical evolution properties relevant to the global warming climatic scenario. VTT's experimental contribution addresses the fourth phase identified by Posiva on the repository lifetime evolution (Posiva, 2021). The expected evolution of the canister in a KBS-3 repository environment proceeds as presented in Table 12:

Table 12. Qualitative description of the repository lifetime (Posiva, 2021).

	Environmental conditions	Loading and deformation mechanisms / Temperature
Initial State / Phase 1	Atmosphere in encapsulation facility and hot cells Residual stress from canister fabrication and sealing.	Handling loads elastic deformation / Increased temperature from welding and from radiogenic heating
Early evolution (0 to 10,000 years) (phases 2-3)	Initially aerobic due to trapped atmospheric O_2, transitioning to anoxic conditions Initially unsaturated, transitioning to saturated Pore-water salinity increases as buffer becomes saturated with saline/brackish groundwater Possible asymmetric loading from uneven buffer swelling, transitioning to isostatic loading of 4-14 MPa due to buffer swelling and hydrostatic pressure No near-field microbial activity due primarily to low water activity/high swelling pressure/lack of space in buffer	Buffer even and uneven swelling; Limited plastic deformation in copper Plastic strains in the copper shell / Initial increase in canister temperature to a maximum of 95 °C after 10-20 years, followed by gradual cooling
Remaining temperature period (10,000 to 49,000 years) (phase 4)	Anoxic Saturated Sulfide present in groundwater and produced by microbial activity at locations away from the canister surface Isostatic load of 4-14 MPa due to buffer swelling and hydrostatic pressure, with the possibility of a minor asymmetric component if the rock contour in the deposition hole is uneven Buffer porewater equilibrated with saline/brackish groundwater No near-field microbial activity due primarily to low water activity/high swelling pressure/lack of space in buffer	Buffer even and uneven swelling; limited copper shell plastic deformation and creep Plastic strains in the copper shell / Temperature throughout repository decreases to ambient after a few tens of thousands of years
Next permafrost and glaciation period (49,000 to 79,000 years) (phase 4)	Anoxic Increased hydrostatic load due to formation of ice sheet Possible intrusion of dilute glacial melt water to repository depth Redox buffering by host rock consumes any intruding O_2 No near-field microbial activity due primarily to low water activity/high swelling pressure/lack of space in buffer	High isostatic loading, plastic deformation and creep; Copper shell compressed against insert with creep and plastic strains; Permanent bending deformation and plastic strains in the insert Rock shear loading, plastic deformation in the insert / Fully cooled repositories, temperature is governed by ambient conditions

EURAD (Deliverable n° 15.6) - Novel materials and processes for the optimisation of long-term container performance
Dissemination level: Public
Date of issue of this report: 06/05/2024

Page

	Anoxic Repeated glacial cycles resulting in periodic increases in hydrostatic load Erosion of bentonite in a limited number of deposition holes resulting in: Higher sulfide flux Possibility of microbial activity in deposition hole and biofilm formation Absence of buffer swelling pressure Increasing likelihood of shear displacement in some deposition holes	Subsequent glacial cycles and rock shear events Copper shell compressed against insert with creep and plastic strains; Permanent bending deformation and plastic strains in the insert / Fully cooled repositories, temperature is governed by ambient conditions
Long-term evolution up to 10^6 years (phase 4)		

Ammonia (NH_3) can be introduced to the canister environment during the construction of the repository (residues from explosives), by human or microbial activities or by the gas-phase radiolysis of atmospheric N_2 (King et al., 2010). If ammonia exists in the repository, there is a possibility that it could rapidly migrate to the surface of the canister via the unsaturated buffer. When in contact with copper, it acts as a corrosive agent, breaking the protective oxide layer on the surface when the corrosion potential and interfacial pH values exceed the Cu_2O/CuO equilibrium line on a Pourbaix diagram (Figure 53 (Posiva, 2021) (King, F. 2021). The disruption of the passive layer can cause the initiation and propagation of cracks in the material under tensile stress.

However, only the presence of SCC agents cannot induce cracking; it is essential to transport these species in sufficient quantities to the canister surface. When the near field becomes saturated, the slow diffusive transport through compacted buffer will restrict the movement of dissolved ammonium ions (Posiva, 2021). Ammonium ions have the potential to transform into ammonia gas in unsaturated conditions and quickly diffuse to the canister surface. The dissolution of $NH_3(g)$ could produce an aqueous ammonium environment if the canister surface is wet (Posiva, 2021). Nevertheless, additional requirements for cracking still need to be met, such as the existence of tensile stress, a sufficiently positive E_{corr} value, and an acceptable interfacial pH (Figure 53).

Elucidating the pitting potential of copper is a good approximation to narrow down the conditions (potential, pH, or mechanical stress) that could trigger stress corrosion cracking (SCC) on copper alloys. Conceptually, at the fourth phase, the canister in contact with anoxic groundwater (at ambient temperature) will experience a potential window between -390 to -500 mV vs. saturated calomel electrode (SCE) and pH between 7 and 9 (blue dashed rectangle in Figure 53) (King, F. 2021). According to Figure 53, the critical potential for stress crack corrosion (SCC) to occur is sensitive to pH. Moreover, the potential at which SCC of copper in ammonia occurs is related to the oxidation state of copper and has been observed only above the Cu_2O/CuO - oxidation potential (King, 2021).

EURAD (Deliverable n° 15.6) - Novel materials and processes for the optimisation of long-term container performance
Dissemination level: Public
Date of issue of this report: 06/05/2024

Page
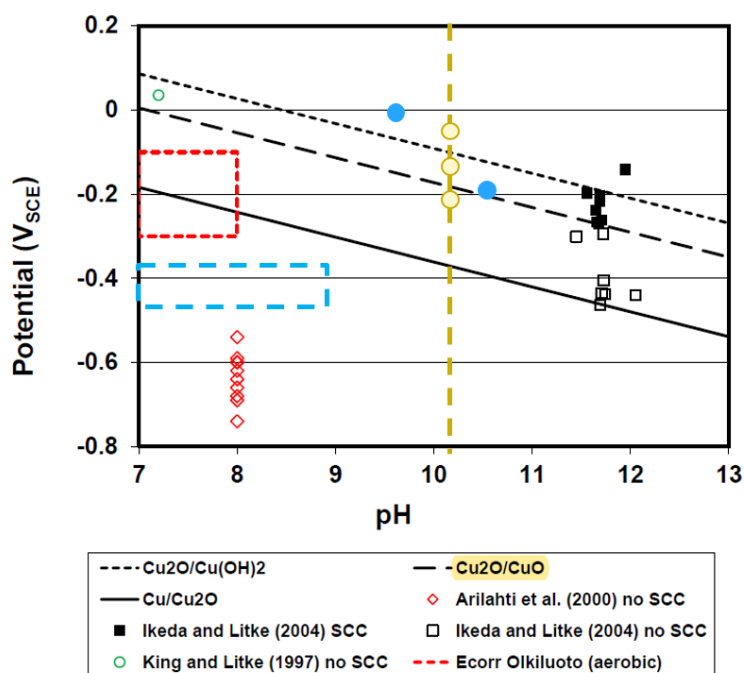
Figure 53. Pourbaix diagram adapted from previous works (King, F. 2021) where the pitting potentials obtained by potentiodynamic polarization curves were added in blue dots.

The current literature available on SCC of copper by ammonia is not conclusive on the critical concentration of ammonia and the type of chemical precursor to be used. Detailed site investigation studies indicated that 3 mg/l and 1.1 mg/l of ammonia were found at at Hästholmen (Finland) and Olkiluoto (Finland), respectively (Anttila et al., 1999a) (Anttila et al., 1999b). In this study, we set a relatively higher concentration (100 mg/l) to narrow down the conditions that trigger SCC of copper in ammonia-containing simulated groundwater under anoxic conditions. The breakdown of the passive layer was investigated by polarizing 1 cm² Cu specimens from –100 mV to +1200 mV at a scan rate of 0.167 mV/s and cut-off current density of 0.1 mA/cm². Potentiodynamic polarization tests were performed in a five-necked flat-bottom flask containing three deaerated solutions, each prepared with a different ammonia precursor, resulting in different pHs: (i) $(NH_4)_2SO_4$, pH 7.7; (ii) NH_4Cl, pH 8.0; and (iii) NH_4OH, pH 10.4.

Figure 54a shows a decrease in corrosion current density of almost one order of magnitude in the potentiodynamic curves of higher pHs. This can be explained by the presence of a more homogeneous oxide layer, formed at a higher pH, confirmed by the visual inspection of the samples after the analysis (Figure 54b). The reddish-brown layer found on the polarized Cu in the presence of NH_4OH (Figure 54b) corresponds to the formation of Cu_2O (Hoar et al., 1971) due to the local anodic reaction:

$$2Cu + H_2O \rightarrow Cu_2O + 2H^+ + 2e^-$$
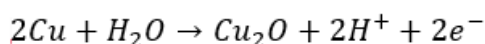
Conversely, there is a shift of the corrosion potential towards more positive values, from -377 mV to -278 mV as the pH decreases. This feature can be justified by the effect of the pH on the cathodic process driven by different counterions. The open circuit potential (OCP) values vs. Ag/AgCl (where oxidation and reduction reactions occur at the same rate) for the three measurements are -275 mV (pH 7.7), -311 mV (pH 8.0), and -368 mV (pH 10.4). This sets the pH 10.4 within the oxidation range of Cu to $Cu(NH_3)_2^+$ followed by precipitation to Cu_2O (Hoar et al., 1971):

$$2Cu(NH_3)_4^{2+} + 6H^+ + H_2O + 2e^- \rightarrow Cu_2O + 8NH_4^+$$

EURAD (Deliverable n° 15.6) - Novel materials and processes for the optimisation of long-term container performance
Dissemination level: Public
Date of issue of this report: 06/05/2024

Page
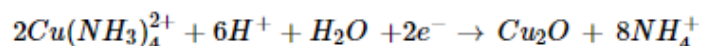
These types of complexes are stable in neutral and alkaline solutions and, in this particular case, they are formed due to the excess of ammonia (Radmehr et al., 2014). The reactions correspond to the passive (green) and transpassive (orange) regions, visible in the anodic branch at pH 10.4.
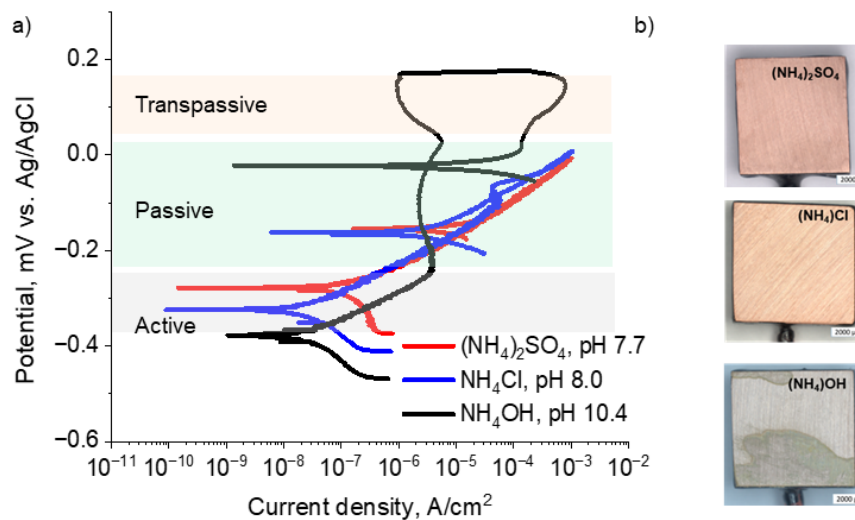
Figure 54. a) Potentiodynamic polarization curves of the groundwater containing 100 mg/l of three different ammonia precursors highlighting active, passive and transpassive regions; b) stereoimages of the copper samples after the measurements.

The resulting pitting potentials of samples with the hysteresis that indicate the passive layer breakdown (10 and 100 mg/L of NH_4OH) were plotted over the comparative Pourbaix diagram (Figure 53) as blue dots. Given the more alkaline conditions induced by 100 mg/l of NH_4OH at pH 10.4 and the visible surface oxidation, we chose this precursor for the three-month autoclave experiment. To compensate the absence of oxygen in the autoclaves and induce a comprehensive oxidation state of the copper, three potentials (-200 mV, -125 mV and -50 mV vs. SCE, yellow dots in Figure 53) were constantly applied to the U-bend samples sorted into three racks. They correspond to Cu_2O, CuO and $Cu(OH)_2$ oxidation states, respectively, based on the assumption that the thermodynamically stable phases are formed. The potential values were defined based on the earlier results reported by King (2021), where it is expected to achieve the threshold of SCC at the highest anodic potential (-50 mV).

The experiments were performed for two different copper grades, more specifically, oxygen-free phosphorus-doped (OFE+P) and high conductivity phosphorous copper (HCP), obtained in two different deformation states (flat and bent). In addition to the manufacturing process's cold work, we bent the rectangular specimens (150 mm × 15 mm × 3 mm) to 180° u-bends to induce deformation stresses considerably higher than in the disposal loads. The number of samples and their labelling are described in Table 13.

Following a three-month immersion, micro indentation tests (Vickers hardness VH1) were conducted. The results indicate that all samples had mean values ranging from 57.5 to 60.9, however it is important to note that the phosphorus-doped Cu-OFP samples (1D and 1D4) had somewhat higher values. All values are in agreement with the hardness range (40 to 65) suggested by the manufacturer (Aurubis Finland Oy[3] - datasheets 2022).

EURAD (Deliverable n° 15.6) - Novel materials and processes for the optimisation of long-term container performance
Dissemination level: Public
Date of issue of this report: 06/05/2024

Page

Table 13. Composition and deformation state of the six samples employed in this study. Vickers hardness (HV1) mean values and standard deviation obtained for the mass loss samples after immersion.

Sample name	Composition	Deformation state	Vickers hardness VH1
AP	Cu-HCP	Flat	57.5 ± 5.2
1A	Cu-HCP	Bent	57.9 ± 2.5
1B	Cu-HCP	Bent	58.5 ± 2.8
1D	Cu-OFE+P	Flat	60.8 ± 1.9
1D4	Cu-OFE+P	Bent	60.9 ± 2.0
1D5	Cu-OFE+P	Bent	58.2 ± 0.5

The received material was subjected to metallographic sectioning resulting in samples used for hydrogen uptake analysis (6 specimens of each alloy), mass loss tests (6 specimens of each alloy), U-bends (triplicates, summing up to 54 samples), and 1 specimen of each alloy for electrochemical assays. Prior to immersion, the surfaces were polished using silicon carbide paper grade #500 followed by cleaning with acetone and ethanol. Figure 55 depicts the 3D design and mounting of the racks containing the U-bends as well as the mass loss samples, right after their placement in the bottom of the autoclave. A saturated Ag/AgCl 0.5 M KCl was used as the reference electrode for the electrochemical tests and a stainless-steel mesh as the counter electrode (CE), ensuring an area ratio to the working electrodes higher than 10.
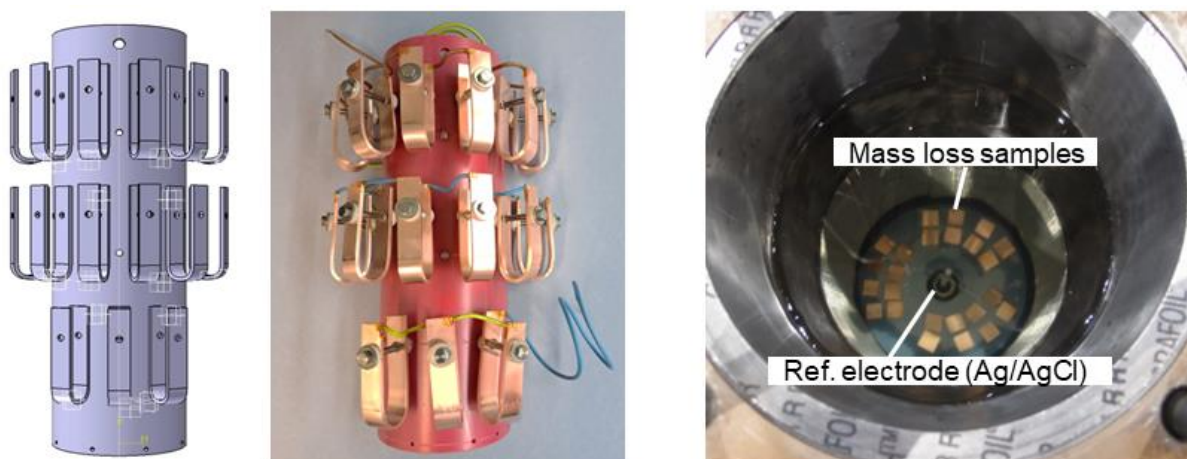
Figure 55. 3D design and mounting of the sample racks with the U-bends; top view of the autoclave right after the addition of groundwater containing 100 mg/l NH_4OH. At the bottom, mass loss samples and the reference electrode (Ag/AgCl (0.5M KCl)) can be observed.

All tests were carried out at room temperature in simulated groundwater deaerated by nitrogen purging (5N N_2) to which 100 mg/l of ammonia hydroxide was added. The chemical composition of the simulated groundwater is presented in Table 14. The pH and ammonia concentration of the autoclave were weekly monitored using a UV-vis spectrophotometer (Hach Lange) and a test kit ammonia Hach LCK302. Additions of NH_4OH were made to keep the pH value around 10 – 10.4 and ammonia concentration between 90 and 130 mg/l.

EURAD (Deliverable n° 15.6) - Novel materials and processes for the optimisation of long-term container performance
Dissemination level: Public
Date of issue of this report: 06/05/2024

Page

Table 14. Chemical composition of the simulated groundwater.

	K	Ca	Cl	Na	SO$_4$	Br	HCO$_3$	Mg	Sr	Si	B	F	Mn	PO$_4$	lactate
mg/L	54.7	280	5274	3180.2	595	42.3	13.7	100	8.8	3.1	1.1	0.8	0.2	0.1	1

The samples were examined using a light optical microscope (LOM) and scanning electron microscopy (SEM) after immersion in autoclaves. The Vickers hardness HV1 of the copper specimens (mass loss and U-bends) was measured employing a Struers DuraScan 20 at different spots of the prepared cross-sections. The corrosion rates were determined based on mass loss results and H-uptake was measured using the hot melt extraction method. Electrochemical impedance spectroscopy (EIS) involves applying an alternating current (AC) voltage to the system and measuring the resulting current response. Since AC voltage varies sinusoidally over time, the root mean square (V_{RMS}) voltage is often used because it provides a measure of the effective voltage applied to the system over time. In our measurement setup, a potential of 10 V_{RMS} was applied after measuring the open circuit potential (OCP) stability for 2 minutes. The frequency was varied between 10 kHz and 1 mHz to measure EIS using a PalmSens4 Potentiostat. Polarization resistance values over time were calculated by fitting the EIS curves using an electrical equivalent circuit (EEC) with the PSTrace 5.9 software provided by PalmSens®. Raman analysis of the U-bends was carried out using a Cora 5001 Fiber from Anton Paar® scanning the top of the samples from -400 cm^{-1} to 3500 cm^{-1} to elucidate differences in chemical composition.

Energy dispersive X-ray spectroscopy (EDS) was performed to investigate indirectly, via chemical composition, the oxidation state of the outer surfaces of U-bend samples after immersion using a Thermo Scientific UltraDry Silicon Drift X-ray detector connected to a Zeiss Merlin field emission scanning electron microscope (FESEM). The microstructure and grain size of the six samples were determined by etching the cross-sections and the images acquired in a reverse light stereomicroscope. Copper surfaces were investigated by SEM of the plain top surfaces of the U-bends, cross sections and by focused ion beam (FIB), as a tool to analyse the depth of the surface features. Three Wenking potentiostats model LB 81 applied constant potentials (-200 mV, -125 mV and -50 mV vs. Ag/AgCl) to the U-bends sorted into three racks containing 18 samples (each) connected by copper wires, which correspond the stable phases displayed in Figure 53: Cu_2O, CuO and $Cu(OH)_2$, respectively.

4.1.2.1. Electrochemical analysis

The six samples were investigated by EIS tests performed weekly to assess their electrochemical behaviour over time when immersed in simulated groundwater containing ammonia. The tests were conducted over a three-month period, and Figure 56 displays the Nyquist and Bode plots after 3, 45, and 79 days. The comparative analysis shows that all alloys present a similar behaviour with no significant variation of impedance values observed in the period, indicating that the passive oxide layer formed on the surface of the samples is stable under the studied conditions.

EURAD (Deliverable n° 15.6) - Novel materials and processes for the optimisation of long-term container performance
Dissemination level: Public
Date of issue of this report: 06/05/2024

Page
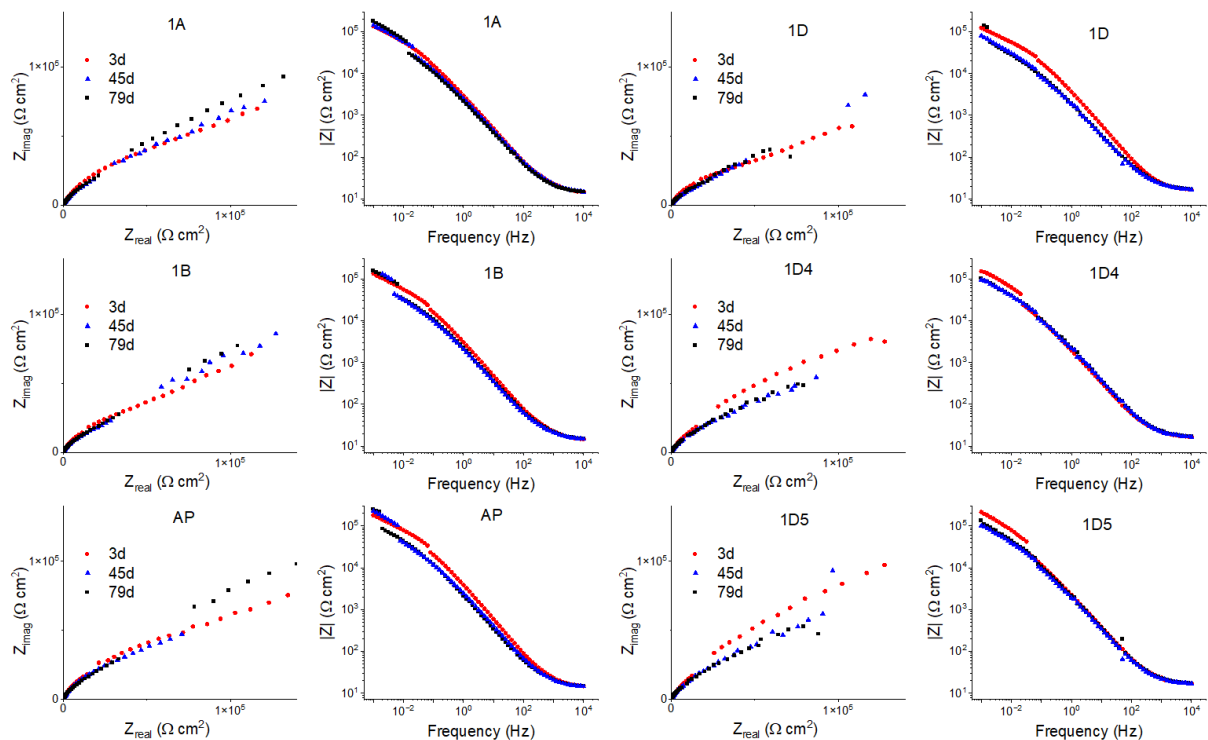
Figure 56. Nyquist and Bode plots of the copper alloys 1A, 1B, AP, (Cu-HCP) and 1D, 1D4 and 1D5 (Cu-OFE+P) after 3, 45 and 79 days of immersion in simulated groundwater containing 100 mg/l NH$_4$OH.

One of the most used models to fit EIS data is the simplified Randles cell. It consists of a charge transfer resistance (R$_{ct}$) in parallel with a double layer capacitor (CPE$_{dl}$), added to the solution resistance (R$_s$) (Loveday et al., 2004). It is worth noting that charge transfer resistance (R$_{ct}$) and polarization resistance (R$_p$) are different properties. The impedance that charge transfer encounters at electrode-electrolyte interfaces is known as polarization resistance (R$_p$). It arises when an external voltage pushes the electrode potential out of equilibrium, prompting electrochemical processes to transfer negative charges, leading to current flow (Loveday et al., 2004). However, when studying simple redox reactions, R$_{ct}$ and R$_p$ can be considered the same because they can be modelled with a simple resistance. Information on the polarization resistance of the samples was extracted by fitting the impedance results using an electrical equivalent circuit (EEC) or simplified Randles (Figure 57). The EEC was composed of solution resistance (R$_s$) in series with one time constant (R$_{ct}$ + CPE$_{dl}$).
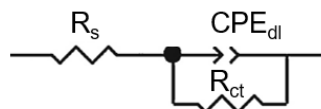
Figure 57. Electrical Equivalent Circuit composed of one time constant (R-CPE) used to fit the EIS data.

Figure 58 depicts the Rp values for both materials, oxygen-free phosphorus-doped (OFP+P) and high conductivity phosphorous copper (HCP). The time evolution of Rp of Cu-HCP (Figure 58, left) presents values between 100 and 200 kΩ cm^2 with up spikes in the line trend. These spikes might have been triggered by different reasons e.g., noisy EIS data, presence of oxidizing substances (nitrite, nitrate, or other water components) that deliver oxygen for corrosion, or even some small variation of oxygen in the solution that resulted in redox reactions on the Cu surfaces, however, there are no relevant variations in terms of corrosion behavior. The oxygen free alloys (Figure 58, right) show, in particular for 1D4 and

EURAD (Deliverable n° 15.6) - Novel materials and processes for the optimisation of long-term container performance
Dissemination level: Public
Date of issue of this report: 06/05/2024

Page

1D5 (bent deformation state), higher R_p in the first month of immersion, with values between 200 and 350 kΩ cm². After this period, their Rp decreases and remains similar to 1D until the end of the immersion. This suggests that the bent OFE+P alloys have increased corrosion resistance in ammonia environments but solely at the initial stages of immersion. Figure 58b depicts stereomicrographs of the electrochemical samples after immersion. Notably, a significant change in oxidation state, likely due to redox reactions, is evident in samples 1B, AP, and 1D while 1A underwent the formation of large and deeper pits. This could partially explain the higher R_p observed for the bent OFE+P, but further investigation is necessary to understand their decrease in Rp after one month of immersion.
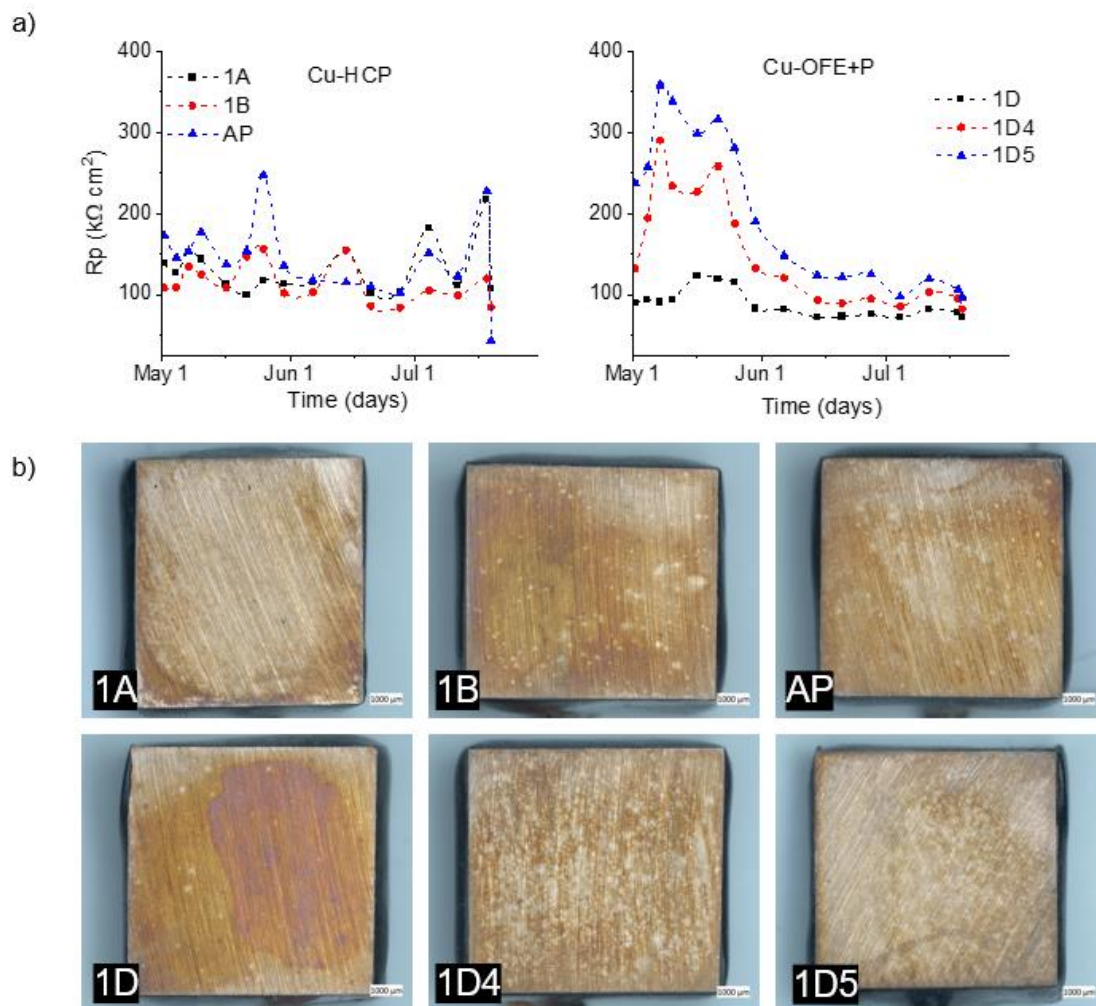
Figure 58.a) Time evolution of polarization resistance values after fitting the EIS results using one time constant for Cu-HCP (left) and Cu-OFE+P (right); b) Stereomicrographs of the six samples after immersion in ammonia-containing simulated groundwater with ammonia as an aggressive agent for three months.

Mass loss samples were placed in the bottom of the autoclaves and left until the opening after three months. Right after opening the autoclaves, the samples were rinsed with ethanol and placed in a desiccator. A deoxidizing procedure (also known as pickling) was carried out by immersing the specimens and the reference (non-immersed sample) in a solution containing 500 ml H_2O + 500 ml HCl (37%) + 3.5 g hexamethylenetetramine for 5 minutes. They were subsequently rinsed with ethanol, dried and weighed on an analytical scale which offers a readability of up to 0.00001 grams. This procedure was repeated until the weight loss was stable allowing the calculation of the corrosion rate (CR) in µm/year using Equation 1 (ASTM G 31-72):

EURAD (Deliverable n° 15.6) - Novel materials and processes for the optimisation of long-term container performance
Dissemination level: Public
Date of issue of this report: 06/05/2024

Page

$$CR = \frac{(K \times W_{loss})}{(A \times t \times d)}$$

Where K is a constant that defines the units for the corrosion rate (8.76×10^7 for µm/year), W_{loss} is the equivalent weight in grams, t is the time of exposure in hours (2088), d is the density of Cu (8.94 g/cm^3) and A is the surface area of the sample in cm^2. Mean corrosion rate values and standard deviations obtained for replicates are shown in Figure 59. The small range of CR values between 0.2 and 0.4 µm/year and large standard deviations of AP and 1D5 suggest that all alloys corrode similarly.
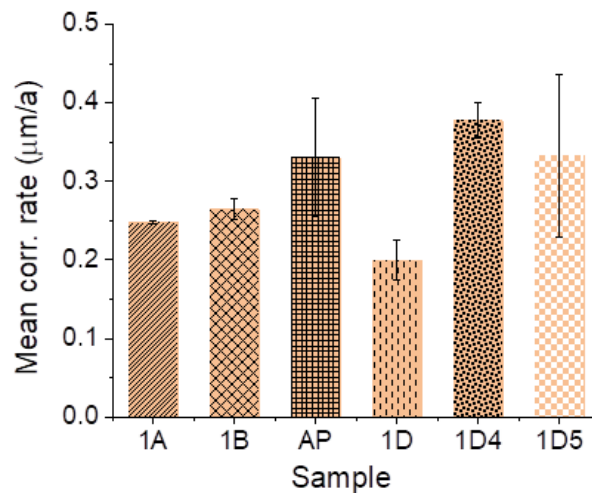
Figure 59. Mean corrosion rate values and standard deviations for the six copper alloys calculated with the weight losses after the pickling procedure.

4.1.2.2. Hydrogen uptake and copper hardness

Species such as halides, ammonia, carbonate ion, and phosphates can form complexes with Cu(I) and Cu(II) and activate copper thermodynamically. In the thermal power industry, ammonia significantly corrodes copper alloys in steam surface condensers due to the formation of soluble complexes such as ($Cu(NH_3)_2^{2+}$ and $Cu(NH_3)^{2+}$) (Macdonald et al., 2012). Hydrogen gas can be produced at the surface of copper by a sequence of reactions that occur when it is exposed to anoxic conditions and excess of ammonia. At the anode, copper metal oxidizes to release copper ions into the solution:

$$Cu \rightarrow Cu^{2+} + 2e^-$$
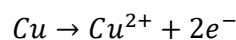
At the cathode, ammonia is reduced and hydrogen gas is produced:

$$6NH_3 + 6e^- \rightarrow 3NH_2^{\mp}3H_2$$
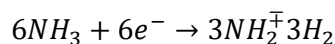
Overall, the global cell reaction can be represented as follows:

$$\left(Cu + 2NH_3 + 2H^+ = Cu\left(NH_3\right)_2^{2+} + H_2 \right)$$
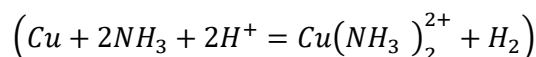
Several authors (Forsström et al, 2020) (Macdonald et al., 2012) studied hydrogen uptake in the presence of sulfides and they report that a fraction of H$_2$ can ingress the copper structure through grain boundaries and dislocations. Despite the low concentration of hydrogen gas in the borehole (theoretically ~10^{-6} M (Macdonald et al., 2012)) and the low concentration of ammonia in the repository to trigger the reactions above described, it is relevant to investigate hydrogen uptake in the studied conditions.

Six specimens of each alloy (75 x 55 x 15 mm) were immersed for the purpose of determining the H uptake into the copper structure. After opening the autoclaves, the samples were immediately polished

EURAD (Deliverable n° 15.6) - Novel materials and processes for the optimisation of long-term container performance
Dissemination level: Public
Date of issue of this report: 06/05/2024

Page

slightly using silicon carbide #220 to remove the oxide layer, rinsed with milli-Q water, ethanol and dried with hot air blow. They were then immersed in liquid nitrogen and transported to the laboratory for analysis. Hot melt mass spectroscopy (HMMS) was employed to determine the average values of hydrogen concentration in different samples before and after immersion. The results in wt.ppm are depicted in Figure 60, top left corner. An interesting behaviour was observed for sample 1D (Cu-OFE+P) with an almost two-fold in H concentration before immersion (in comparison to other specimens before immersion), but the low value (2.1 ppm) remains nearly insignificant to propagate cracks on copper (Lynch 2012). After the three months of immersion, all samples revealed lower values than before immersion, varying between 0.5 and 0.9, indicating that no hydrogen uptake occurred in the studied period.

The grain size of the samples was investigated along with a detailed examination of their integrity through stereo microscopies of cross sections after the etching, confirming the absence of grain boundary corrosion (Gubner et al, 2006). Figure 60 (top right corner) presents the mean grain sizes in μm calculated according to the ASTM E112 – 2010 using the intercept method. The determination consists of dividing the total length of the intercept line by the number of grains cut by the lines multiplied by the magnification. The obtained values are in good agreement with the tabulated grain size numbers from the standard. Although there might be a correlation between the highest hydrogen uptake value after immersion with the smallest grain size (sample 1A), further correlations are rather difficult to establish. The absence of hydrogen uptake during these tests might be associated with the low concentration (or non-formation) of H_2 under anoxic conditions or the temperature of the tests (H_2 solubility in copper increases only above about 600 °C (Magnusson et al., 2017)). The atmospheric pressure of the tests also limits the solubility of H_2 compared to disposal "in-situ" conditions (hydrostatic pressure of about 4 MPa at the repository depth but it can increase up to 40 MPa during periods of glaciation (Posiva, 2021)). In addition, the stereo images acquired in a reverse light show that the grain boundaries of all samples were not degraded across the thickness during the three months.

EURAD (Deliverable n° 15.6) - Novel materials and processes for the optimisation of long-term container performance
Dissemination level: Public
Date of issue of this report: 06/05/2024

Page
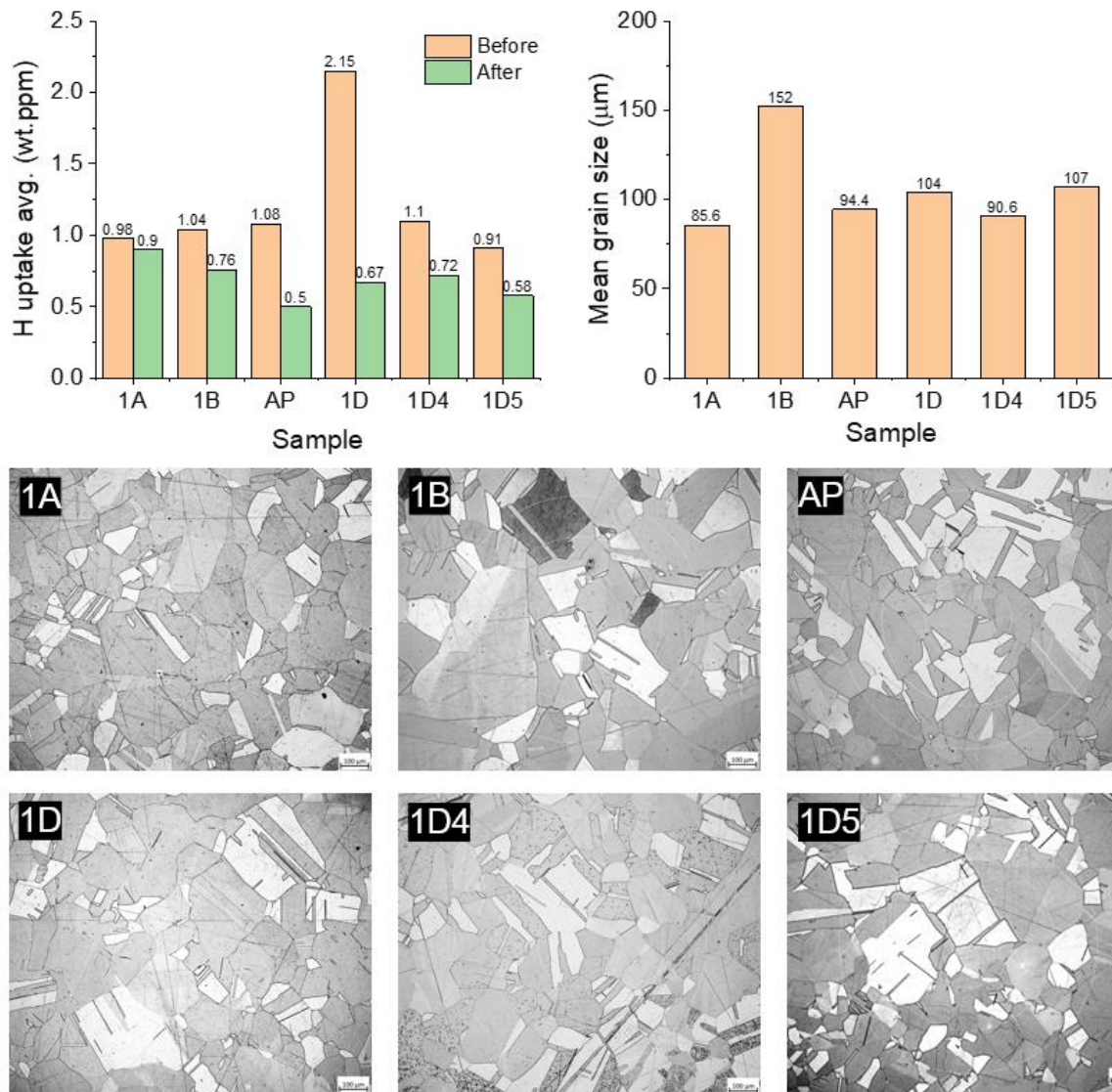
Figure 60. Average hydrogen concentration values before (orange) and after (green) immersion in ammonia-containing simulated groundwater; Mean grain size (top right corner) and stereo microscopies of cross sections after the etching.

Vickers Hardness profiles were obtained using a microindenter to record ten measurements in different positions of U-bend cross-sections. The results (Figure 61) deviate from the as-received samples, presented in Table 13. Overall, all values are higher than the as-received materials (57 to 60 HV) because of the plastic deformation. The results show that the 180° bending process induces stress, leading to differential hardness across the cross-section: the inner surface exhibits higher hardness values compared to the intermediate layer and outer surfaces, consistently observed across all U-bends. A horizontal comparison of the values reveals a hardness gradient from the top towards the sides, corroborating the decrease in hardness at the highest tension point.

EURAD (Deliverable n° 15.6) - Novel materials and processes for the optimisation of long-term container performance
Dissemination level: Public
Date of issue of this report: 06/05/2024

Page
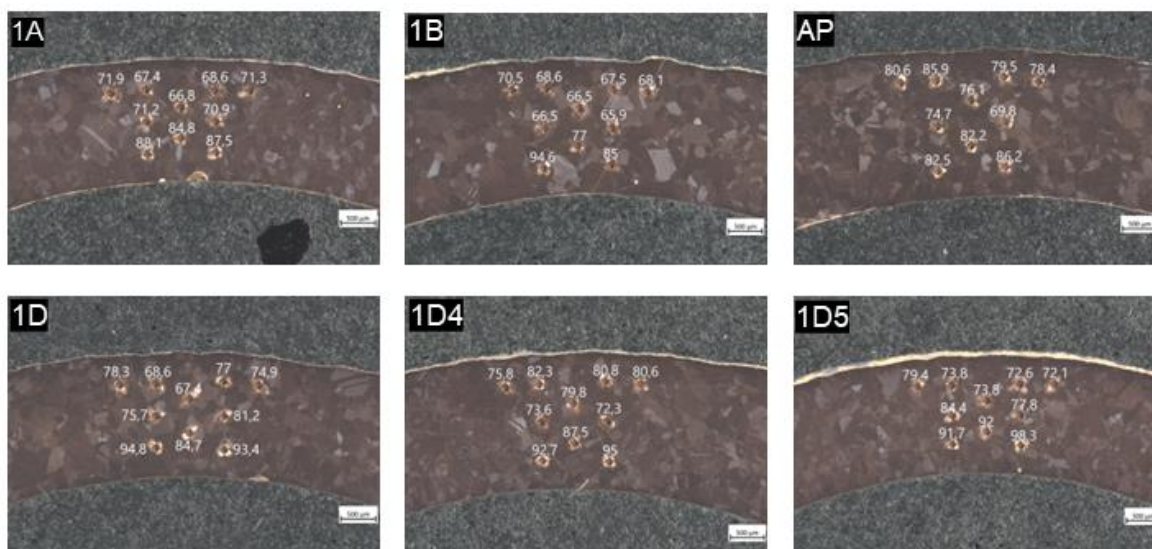
Figure 61. Stereomicrographs of Cu U-bends cross-sections after three of months immersion with the Vickers hardness measurements HV1 in different spots.

4.1.2.3. Chemical composition

Raman spectra were recorded for the exposed and non-exposed Cu-OFE+P (samples 1D) and Cu-HCP (samples AP). Non-immersed surfaces were stored in a desiccator. One specimen per potential applied was studied: AP2 and 1D2 (-200 mV), 1D4 and AP5 (-125 mV) and 1D9 and AP9 (-50 mV). A clear attenuation in signal intensity can be observed in Figure 62 for the samples after immersion which might be related to the more amorphous nature of the oxide layer formed on the surfaces. No shifts were observed for the different potentials applied. The broad peak around 762 cm^{-1} could be attributed to Cu$_2$O while the one at 890 cm^{-1} is characteristic of Cu(OH)$_2$ (Galbiati et al, 2017). Nonetheless, further surface analysis by EDS, reported in Figure 63, is necessary to identify specific changes in elemental composition.

EURAD (Deliverable n° 15.6) - Novel materials and processes for the optimisation of long-term container performance
Dissemination level: Public
Date of issue of this report: 06/05/2024

Page
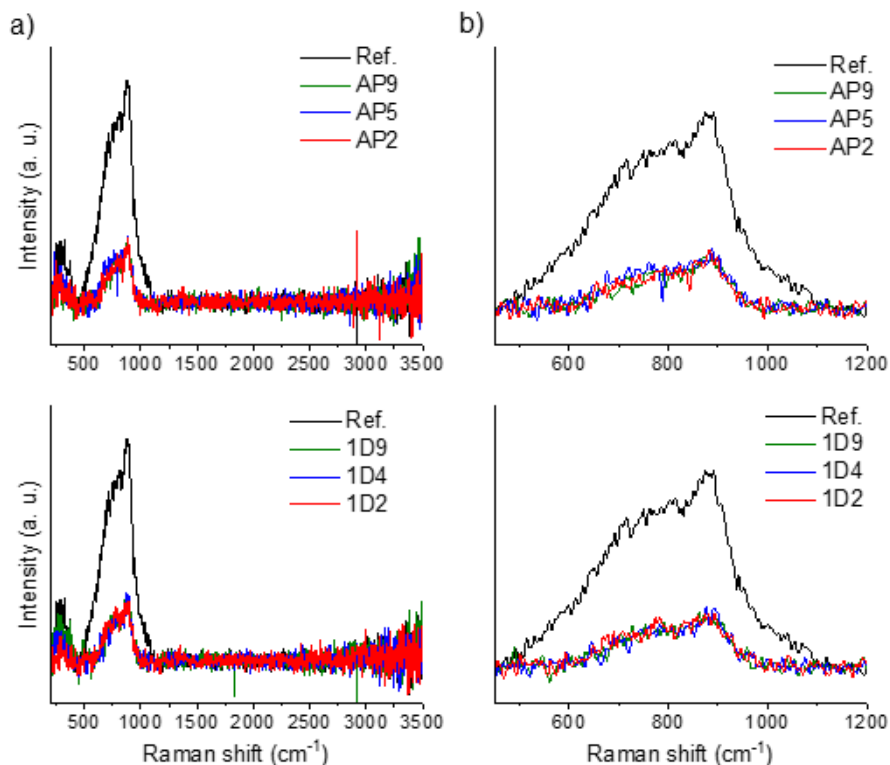
Figure 62. Raman spectra recorded on top U-bends copper specimens before (reference) and after immersion in ammonia containing groundwater for three months. Left: full spectra, right: magnified peaks in the range 450 to 1200 cm^{-1}.

The results of the EDS point analysis performed on the copper U-bends before and after immersion are presented in Figure 63 and the corresponding semi-quantitative values, in Table 15. The spectra reveal that the reference specimen (non-immersed) consists of 99.6 wt.% Cu and 0.4 wt.% O. Carbon has been disregarded in the analysis due to surface contamination. These numbers confirm the formation of an oxide layer on Cu exposed to the air even before immersion.
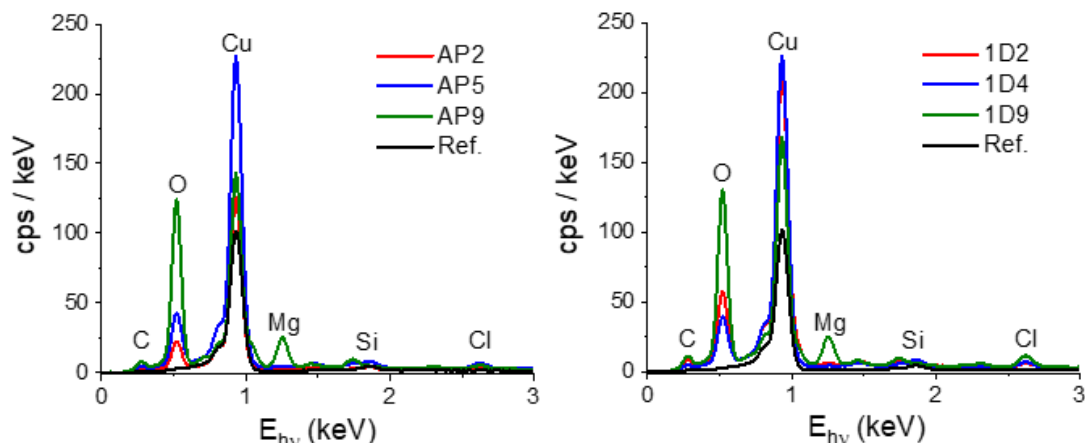
Figure 63. EDS spectra of reference (non-immersed) and immersed Cu samples. The semi-quantitative results of the EDS analyses are listed in Table 15.

The oxygen peak variations seen in Figure 63 may indicate that applying more anodic potentials causes a larger level of copper oxidation. When -200 mV was applied to the U-bends (AP/2, 1D/2), the Cu/O ratio varied between 3 and 6. For the samples where -125 mV was applied (AP/5, 1D/4), the Cu/O ratio

EURAD (Deliverable n° 15.6) - Novel materials and processes for the optimisation of long-term container performance
Dissemination level: Public
Date of issue of this report: 06/05/2024

Page

is approximately 5, while for the samples with -50 mV (AP/9, 1D/9), the Cu/O ratio is between 1 and 2. Elements such as Si, Cl and Mg were also detected in some samples, which can be associated with groundwater elements (Table 14).

Table 15. Semi-quantitative EDS elemental composition of Cu-OFE+P (samples 1D) and Cu-HCP (samples AP) before (reference) and after immersion in ammonia-containing groundwater for three months. Values are represented in Wt.%.

Wt.%	O	Si	Cl	Cu	Mg	Cu/O
Reference	0.4	-		99.6	-	-
AP/2	13.7	-	1.8	84.5	-	6.1
AP/5	16.1	-	1.8	81.8	0.2	5.0
AP/9	36.3	1.6	0.8	56.1	5.1	1.5
1D/2	20.5	-	1.3	76.8	1.4	3.7
1D/4	15.9	1.2	1.4	81.5	-	5.1
1D/9	26.7	1.1	2.2	60.3	9.6	2.2

4.1.2.4. Visual inspection and cross-sectional analysis

After removing the samples from the autoclaves, the specimens were visually inspected. A reference non-immersed sample is included in Figure 64 (left) for comparison. While the application of -200 mV yielded a brownish layer, -125 mV resulted in a reddish colour and -50 mV produced a blueish coloration, characteristics of the increasing oxidation state of copper. This agrees with the EDS results presented in Figure 63 and with the semi-quantitative values shown in Table 15.
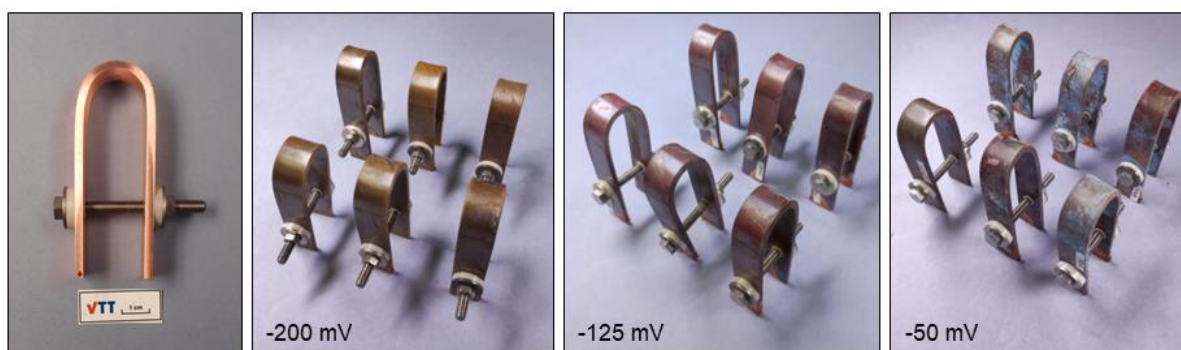
Figure 64. From left to right: Copper U-bend sample before immersion; three sets of six samples after 3 months immersed in simulated groundwater with 100 mg/l NH_4OH having constant potential applied (-200 mV, -125 mV and -50 mV vs. SCE, respectively).

Microscopic inspection using a stereomicroscope and SEM demonstrated the absence of surface defects when -200 and -125 mV vs. SCE were applied to the U-bends. However, the samples under -50 mV showed the presence of small density of surface defects in SEM. Such small features (Figure 65 and Figure 66) are challenging to investigate by plan view SEM and therefore additional investigations were performed for the cross-section and by utilizing a focused ion beam (FIB) to make a local micro-section of the defects.

EURAD (Deliverable n° 15.6) - Novel materials and processes for the optimisation of long-term container performance
Dissemination level: Public
Date of issue of this report: 06/05/2024

Page
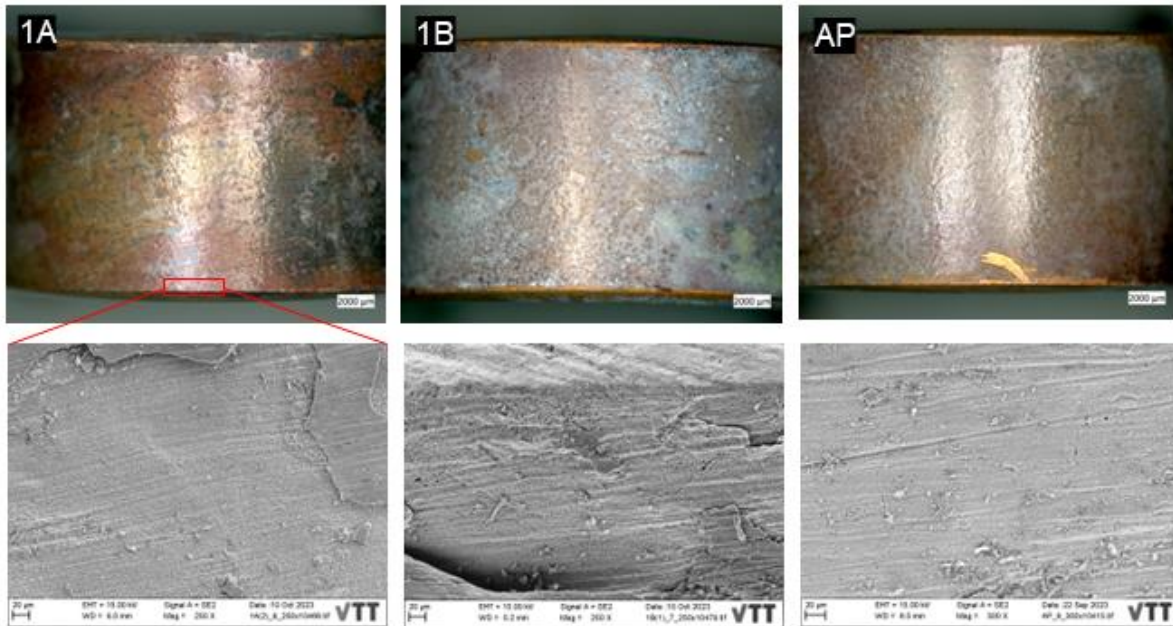
Figure 65. Stereomicrograph of the U-bends 1A, 1B and AP (Cu-HCP) and SEM images of the curved edge where small features suggest the formation of intergranular surface defects.
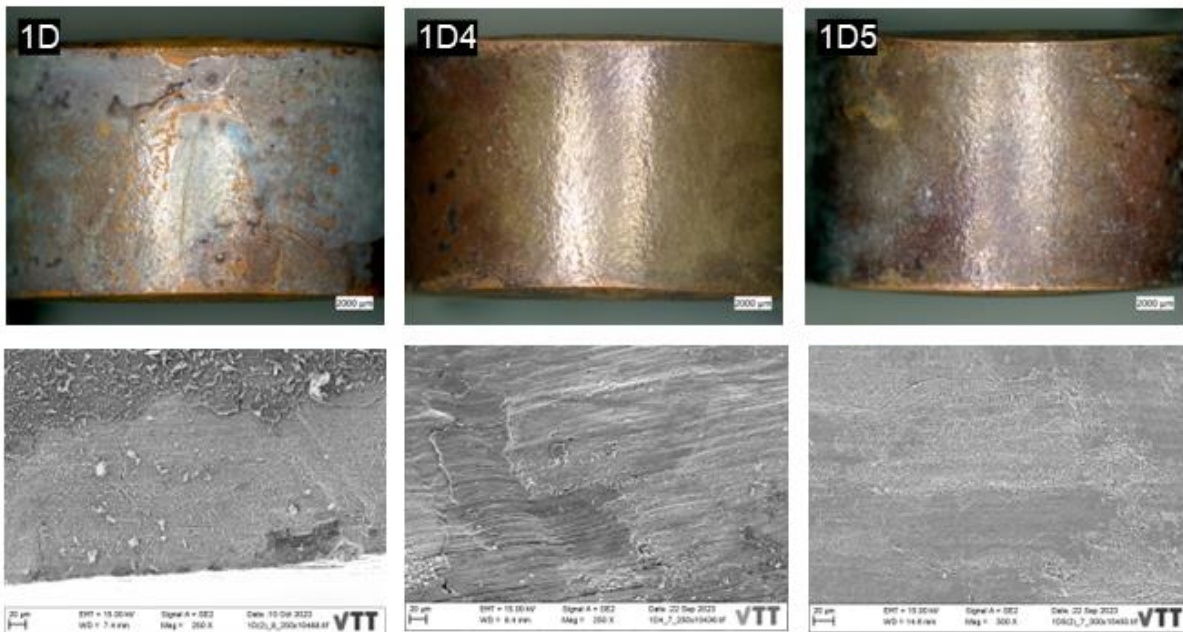
Figure 66. Stereomicrograph of the U-bends 1D, 1D4 and 1D5 (Cu-OFE+P) and SEM images of the curved edge where small features suggest the formation of intergranular surface defects.

Cross-sections of the samples were prepared using metallographic methods and the resulting materials were embedded in epoxy resins for SEM analysis. Figure 67 displays the interface metal/resin where the oxide layer and the presence of surface defects can be observed for all samples. The images prove that although defects about 1 µm thick were formed on the oxide film, very few of them reached the underlying metal. In fact, the crack mechanisms on copper have been a topic of debate in previous research. While evidence for cracks of pure copper has been observed by some researchers under anoxic conditions (phase 4, Table 12) (Ikeda et al., 2011), there are controversies in the scientific community about the features reported. It is unclear if they correspond to SCC (Suzuki et al., 1981)

EURAD (Deliverable n° 15.6) - Novel materials and processes for the optimisation of long-term container performance
Dissemination level: Public
Date of issue of this report: 06/05/2024

Page

(Becker et al., 2020) or intergranular corrosion followed by the opening of the grain boundaries by excessive plastic strain (Taxen et al., 2018) (Taxen et al., 2019) (King et al., 2010). In this research, the possible mechanism of defect formed on both alloys is likely tarnish rupture, depending upon the break of the oxide layer to reveal the underlying metal (Fujimoto et al., 2021) (King, F. 2021).
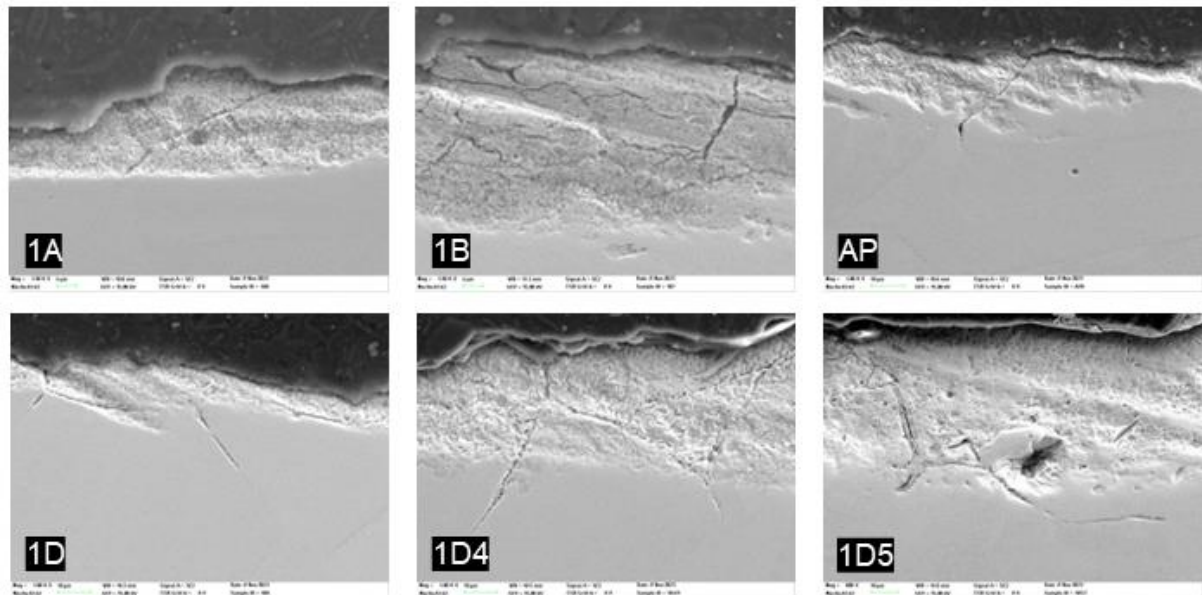
Figure 67. Cross-sectional images of Cu U-bends after three months of immersion in ammonia-containing groundwater with application of -50 mV.

By employing FIB, we created micro-sections of the defects to acquire additional insights. Figure 68 illustrates that the surface defects on two different areas of sample 1D/9 (Cu-OFE+P) correspond solely to the oxide layer without reaching the bulk of the underlying substrate. As previously suggested by the cross sections, these high-resolution images confirm that the maximum depth of the defects is about 1 µm.
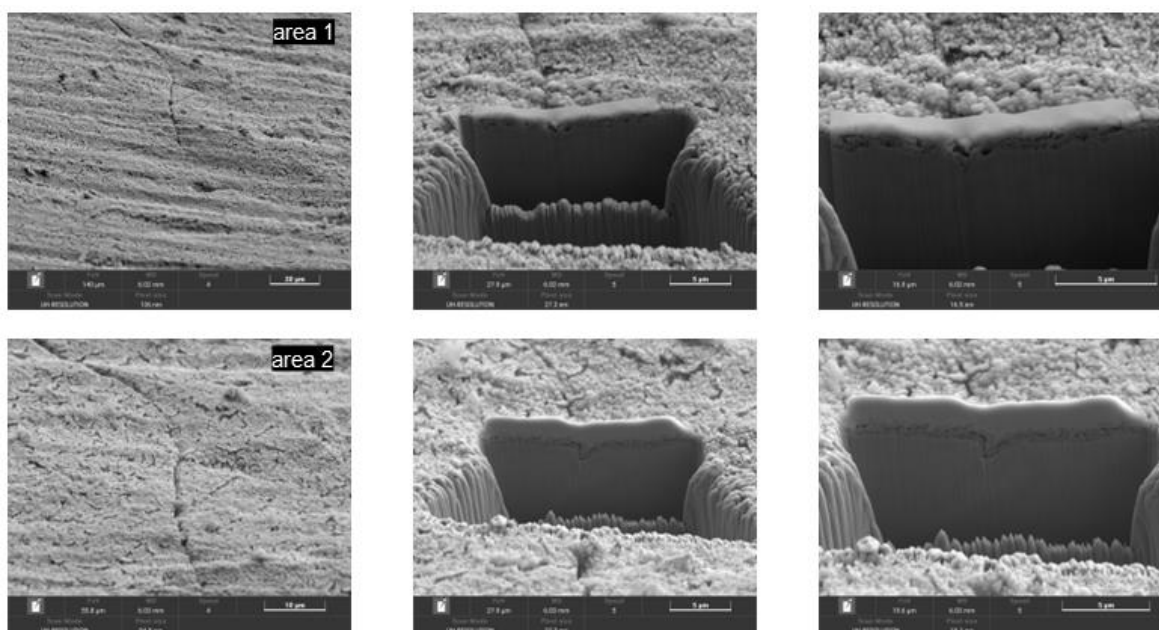
Figure 68. FIB micro cross sections of sample 1D/9 (Cu-OFE+P) imaged by FEG-SEM.

The sample AP/9 (Cu-HCP) in Figure 69 presents similar features to those observed in Figure 68. Here a slightly deeper surface defect is observed, penetrating around 4 µm into the bulk. Nevertheless, the FIB analysis indicates that these defects are fully oxidized. Altogether, the images show that a porous oxide layer ranging from 1 to 40 µm is formed on the surface of OFE+P and Cu-HCP samples after autoclave immersion for 3 months in simulated groundwater (pH 10 – 10.4, 100 mg/L of ammonia added) at room temperature. The propagation length of the surface defects is only 1–5 µm indicating that the oxide layer delays their propagation and acts as a protective barrier for corrosive species (Dinu et al. 2013). Notwithstanding, the mechanisms of surface defect formation are open questions for future studies.
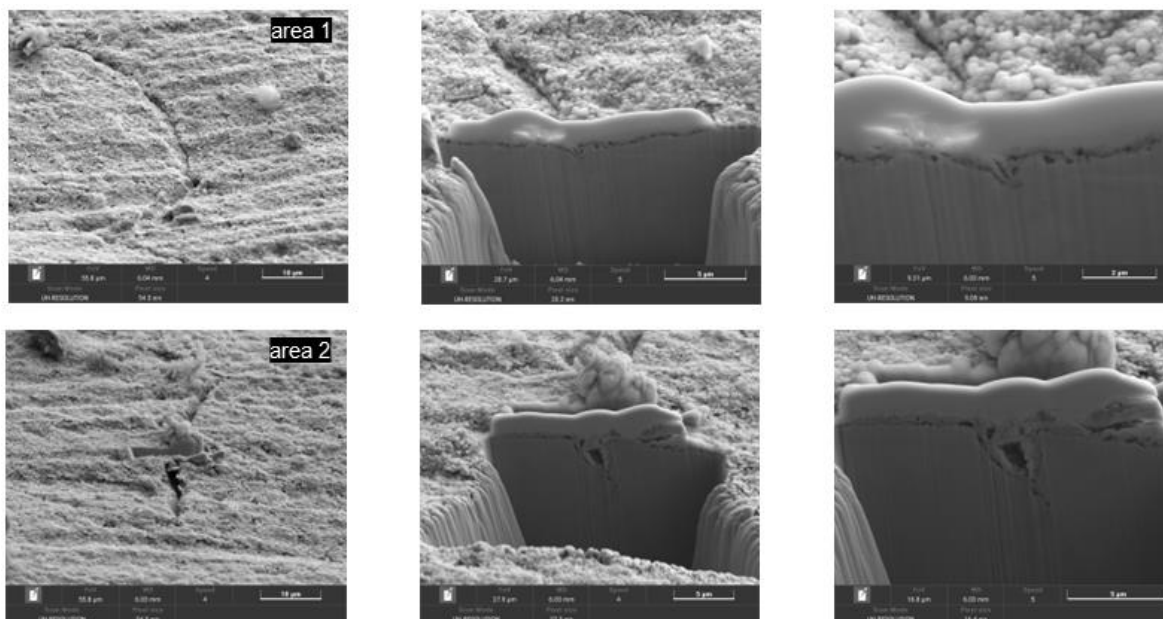
Figure 69. FIB micro cross sections of sample AP/9 (Cu-HCP) imaged by FEG-SEM.

4.1.2.5. Conclusions

A 3-month autoclave experiment with ammonia-containing simulated groundwater under anoxic conditions (ammonia and pH disturbed fourth phase), yielded data about OFE+P and HCP copper. More specifically, the electrochemical behaviour of the alloys was elucidated, along with their corrosion rate, hydrogen uptake, and information on the SCC of highly stressed U-bends at different potentials. The results showed similar electrochemical behaviour for all the alloys after one month of immersion. While OFE+P copper initially exhibited higher R_p values, which is interpreted to be a signal of higher corrosion resistance, the average polarization resistance and corrosion rates for the 3-month immersion test showed very similar behaviour for HCP. The reason behind the higher initial R_p values was not assessed in detail but they might be related to the different rolling parameters during the sample manufacturing. Hydrogen uptake measurements revealed that the copper grain size (85–152 µm) did not correlate with the intake of hydrogen; in fact, no hydrogen uptake was observed in this environment because of the low temperature of the test or non-formation of H_2 in anoxic circumstances.. Applying different potentials to the U-bends resulted in various oxidation states, with the highest anodic potential (-50 mV vs. SCE) leading to the highest oxidation of copper ($Cu(OH)_2$) showing a distinctive blueish layer. Small surface defects were observed in both OFE+P and HCP specimens after this exposure. These defects were, however, blunt in nature, covered with oxide, and their formation mechanism requires further work. These observations point out that HCP copper performed equally well as compared to OFE+P in NH_3 containing groundwater. While the results are encouraging, it is noted that several other aspects (such

EURAD (Deliverable n° 15.6) - Novel materials and processes for the optimisation of long-term container performance
Dissemination level: Public
Date of issue of this report: 06/05/2024

Page

as creep properties or alternative environments, e.g., sulfides) need to be taken into account before HCP can be considered as an alternative canister material.

4.2. Metallic coatings

Titanium, chromium and copper are well-known materials for corrosion protection (Ahmad, 2006). Metallic coating resistant to corrosion will be deposited on a steel container to significantly reduce the corrosion of the steel, and hence the gas production.

Good protective properties of Cr coatings have been demonstrated under normal operating conditions: autoclave tests in PWR and BWR simulated media (Wei et al., 2019) (Brachet et al., 2015). PVD deposited chromium coatings are being intensively investigated for the protection of zirconium alloy fuel cladding. The high corrosion resistance of chromium in water makes it promising for use as a coating for steel containers.

The use of copper as an external container corrosion barrier has been considered for many years by many national nuclear waste management research programs, including those in Sweden and Finland, and by the Canadian Nuclear Waste Management Organization (NWMO) (Keech et al., 2014). In the Canadian program, NWMO, the copper coating methods are still under development and the exact composition and property requirements of the copper have not yet been established.

Candidate titanium coating solutions for application to carbon steel canisters for nuclear waste disposal are immune to microbially induced corrosion (MIC).

Open issues for the use of titanium, chromium, and copper as protective coatings on steel substrates are the following: corrosion resistance in water, the thickness required to eliminate through-porosity, the effect of through-porosity and irradiation on corrosion resistance, mechanical properties (hardness and adhesion to the steel substrate).

Titanium alloys are known to be immune to MIC (King, 2020). They also exhibit extremely low general corrosion rates, high resistance to corrosion under irradiation, and certain alloys are also immune to localized forms of corrosion (Hua et al., 2005). Titanium coatings deposited by PVD methods have been studied mainly by electrochemical methods (Zhou, 2012). Titanium coatings have better corrosion resistance in both corrosive media (0.5 N NaCl and 0.5 N Na_2SO_4 + 0.1 N H_2SO_4) than uncoated steel (Zhujmg et al., 1991). Hydrogen absorption as a result of general anaerobic corrosion under disposal conditions will occur. However, such processes are generally predictable and long canister life can be expected with confidence.

No corrosion resistance study of titanium, copper and chromium PVD coatings on carbon steel under specific nuclear repository environmental conditions has been published to date. The research into alternative processes to chromium plating is focused on finding new surface technologies based on more environmentally friendly processes, such as Physical Vapor Deposition (PVD) (Bijalwan et al., 2022).

Processes for manufacturing metallic (Ti, Cr and Cu) coatings on various steel substrates by physical vapor deposition (PVD) method are proposed by KIPT. PVD processes are well developed at KIPT, optimization of the working mode of the coating production process was carried out taking into account the chemical composition of metal substrates considered as container material. The main attention was paid to the production of test specimens of coatings (Ti, Cr and Cu) and the study of their behavior under corrosion conditions.

The processes for the deposition of metallic (Ti, Cr, Cu) coatings on steel substrates by PVD (cathodic arc evaporation (CAE) and magnetron sputtering (MS)) methods were optimized to achieve high deposition rates. The principal schemes of deposition processes by MS and CAE are given in Figure 70.

EURAD (Deliverable n° 15.6) - Novel materials and processes for the optimisation of long-term container performance
Dissemination level: Public
Date of issue of this report: 06/05/2024

Page

<center>a   b</center>
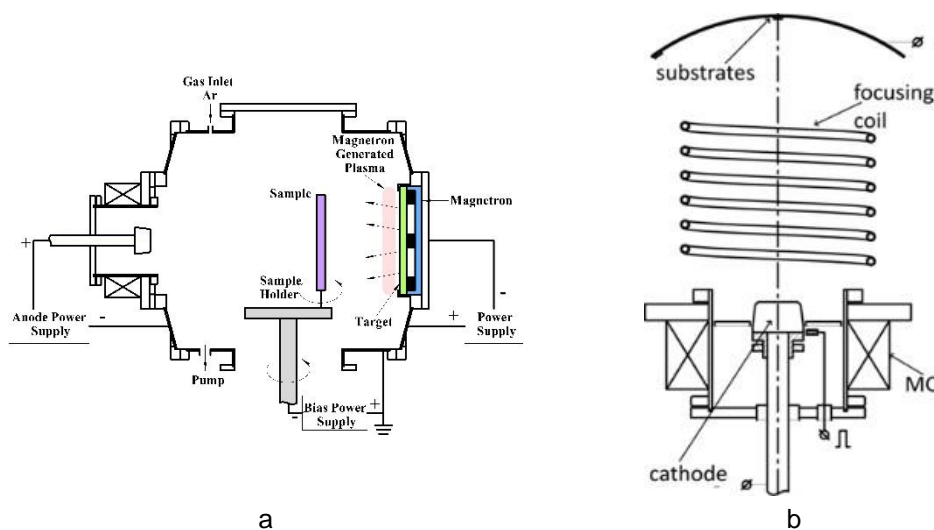
Figure 70. Scheme of coatings deposition on steel substrate by MS (a) and CAE (b) processes.

Rectangular copper and titanium plates (180×90 mm) with a thickness of 5 mm were used as targets for the magnetron. The magnetron was powered by a direct current source. The additional magnetic field coil provided increased ion bombardment of the coating surface and increased deposition rate (Figure 70a).

Deposition of metal coatings by cathodic arc evaporation was carried out using a source with magnetic stabilization (MC - magnetic coil) of the cathode spot. The cylindrical cathodes (Ø 60 mm, height 45 mm) were made of titanium, copper and chromium. The cathode materials used for coating deposition were 99.9% pure. To increase the coating deposition rate, an additional plasma focusing system was specially installed (Figure 70b). This system (focusing coil) allows to increase the deposition rate of coatings several times as compared to the conventional method.

A cylinder with an inner diameter of 500 mm and length of 500 mm was the vacuum chamber of the system. Steel substrates, 20 mm in diameter and 3 mm thick with the chemical composition the same as in Table 16 were used. They were polished using abrasive silicon carbide paper to a roughness Ra of about 0.02 µm. The substrates were chemically degreased and ultrasonically cleaned in a hot alkaline bath for 10 min and dried in warm air. After cleaning, they were mounted on a planetary rotating holder with a rotation speed of about 30 rpm.

The substrate-cathode distance was about 300 mm. In the first step of coating deposition, the chamber was evacuated to a pressure of 2×10^{-3} Pa. Substrates were ion etched with copper, chromium or titanium ion bombardment by applying a DC bias of −1300 V for 3 min. The arc current was 90 A for all coatings. Metallic coatings (Cu, Cr and Ti) were deposited in a high vacuum (3×10^{-3} Pa). During deposition, the substrate temperature was about 400 °C.

XRD analysis of the coatings was carried out in Cu-Kα radiation (λ = 0.154187 nm) using X'Pert Pro diffractometer with 1D PIXcel detector. The corrosion resistance of the steel substrate and the substrate-coating systems was evaluated by means of potentiodynamic polarization tests using the Electrochemical Unit. The measurements were carried out in a conventional three-electrode cell with a sample acting as the working electrode. The active area of each sample was 1 cm^2. The reference electrode was a saturated calomel electrode (SCE, Hg/Hg$_2$Cl$_2$/KCl), and a platinum sheet was used as the counter electrode. The potentiodynamic polarization tests were conducted in 3 wt% NaCl solution (pH=6.5), at room temperature (25 ± 1 °C).

Assessment of the surface morphology of the samples, within the corroded areas and those not treated with the corrosive medium, was performed using a scanning electron microscope (SEM).

EURAD (Deliverable n° 15.6) - Novel materials and processes for the optimisation of long-term container performance
Dissemination level: Public
Date of issue of this report: 06/05/2024

Page

4.2.1. Copper

As a result of the optimization of CAE processes of metal coating deposition, deposition rates for copper are increased up to 15 µm/h. Cu coatings were deposited on low carbon steel substrate (chemical composition of Steel 3). Copper coatings up to 30 µm thick have been deposited using different parameters of the Cathodic Arc Evaporation (Cu1-3) and Magnetron Sputtering processes (Cu MS). The deposition conditions and properties of the Cu coatings are given in Table 16 and photographs of the obtained samples are in Figure 71.

Table 16. Deposition conditions and properties of Cu coatings obtained by MS (Cu MS) and CAE (Cu 1-3) processes.

Coating	Deposition parameters			Chemical composition, at.%		Thickness, µm	Grain size, nm	Ra, nm	H, GPa
	I, A	PAr, Pa	Ub, V	Cu	O				
Cu1	100	0.05	-25	99	<1	32	228	220	0.91
Cu2	100	0.05	-50	99	<1	31	559	298	0.93
Cu3	100	0.05	-300 P*	99	<1	33	350	282	0.84
Cu MS	5	0.5	-50	98	2	32	97	129	0.9

P* - pulsed negative substrate bias voltage (f=20 kHz, d=20%).

a   b   c   d

Figure 71. Photos of the steel samples with deposited metallic Cu coatings with thickness up to 30 µm under different parameters of the deposition processes by MS (a) and CAE (b, c, d)

As can be seen from Table 16, copper coatings deposited by the cathodic arc method have a rather low amount of impurities (<1 at.%) and a sub-microcrystalline grain size (228-559 nm). Coatings deposited by the magnetron method have a slightly higher level of impurities (~ 2 at.%) and the size of the crystallites is in the range of 97 nm. The main impurity in the coatings is oxygen, which comes from the residual atmosphere of the vacuum chamber. The difference in oxygen content between the cathodic arc and magnetron sputtered coatings can also be explained by the presence of impurities in the technically pure argon required for the magnetron sputtering process. Since copper coatings deposited by magnetron sputtering have higher levels of impurities, further studies focused on coatings deposited by cathodic arc evaporation.

The copper coating deposited by cathodic arc evaporation consists of the Cu phase with lattice parameter a = 3.6151 Å and preferred orientation {111}. Diffraction peaks of copper are sharp, indicating a coarse-grained state (Figure 72).

EURAD (Deliverable n° 15.6) - Novel materials and processes for the optimisation of long-term container performance
Dissemination level: Public
Date of issue of this report: 06/05/2024

Page
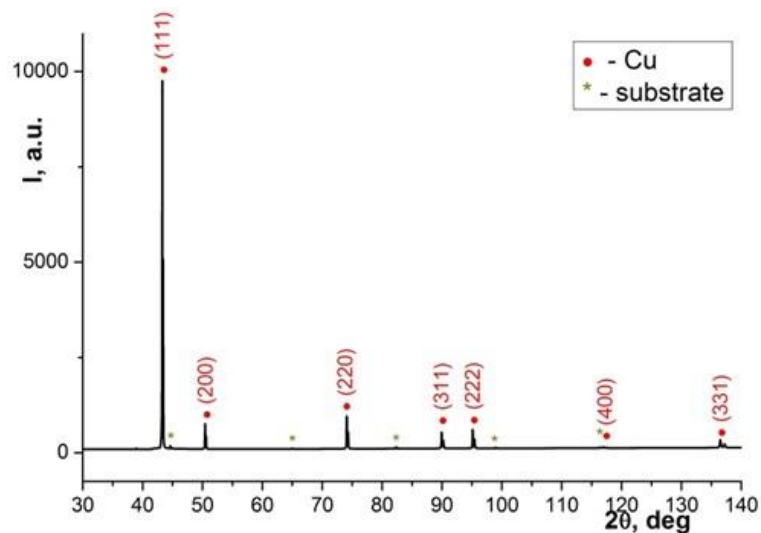
Figure 72. X-ray diffraction pattern of a steel substrate with Cu coating.

Adhesion of Cu coatings obtained by MS and CAE processes was determined using the Daimler−Benz test and results are presented in Figure 73.
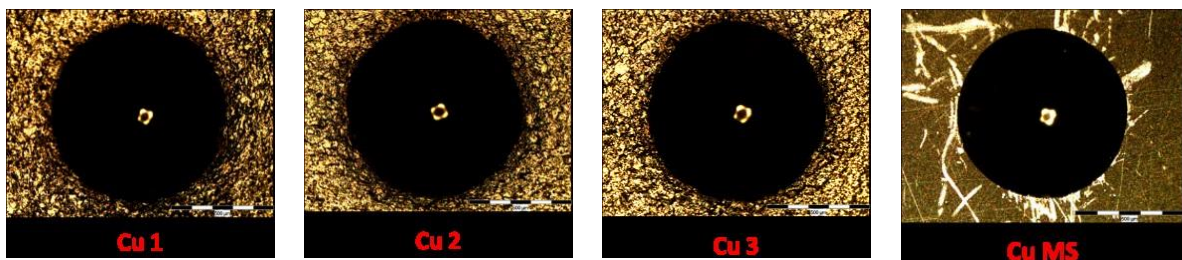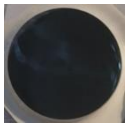
Figure 73. Photographs of the surfaces of Cu coatings after Daimler−Benz test.

Cu coatings have high adhesion to steel substrates, at the level (HF1–HF2) without any cracking of the coating in the surrounding of the crater. Light microscopy images of the surface of coatings deposited by cathodic arc evaporation show a developed grain structure (Figure 73 Cu1-3), while the surface of coatings deposited by magnetron sputtering is smoother and darker (Figure 73 Cu MS).

The long-term corrosion test in 3% NaCl at 20°C of the steel samples (Steel 3) with Cu coatings was performed and the results are presented in Table 17.

EURAD (Deliverable n° 15.6) - Novel materials and processes for the optimisation of long-term container performance
Dissemination level: Public
Date of issue of this report: 06/05/2024

Page

Table 17. View of Steel 3 and coated samples after long-term corrosion with various durations of testing.

Hours	Steel 3	Cu, 5 µm	Cu, 15 µm	Cu1, 30 µm	Cu2, 30 µm	Cu3, 30 µm	Cu, MS 30
0							
144							
296							

The results of corrosion tests showed that the steel specimens corroded intensively (Table 17). Corrosion pits appear on the surface of magnetron sputtered copper coatings after 144 hours of testing, and their number and size increase after 296 hours of testing. These coatings were not investigated further due to their low corrosion resistance.

The influence of the thickness effect of copper coatings can be clearly seen in the example of coatings with thicknesses of 5, 15 and 30 µm deposited by cathodic arc evaporation (Table 17). The 5 µm coatings show pitting after 144 hours of testing, the 15 µm coatings show pitting after 296 hours of testing, and the 30 µm coatings show no pitting on the coating surface. The influence of bias potential on corrosion resistance is not so obvious, but the best surface quality with complete absence of corrosion products is observed for the coating deposited at -50 V bias potential (Cu2). Further research has focused on this Cu2 coating.

4.2.2. Titanium

Cathodic arc evaporation PVD process has outstanding potential to deposit corrosion-resistant coatings with relatively dense structures (Charrier et al., 1997). Titanium and titanium alloys are widely used for corrosion protection because they offer high chemical resistance against various corrosive media due to a dense self-sealing oxide layer (Zhou, 2012) and have been considered as candidate canister materials for the disposal of spent fuel in a number of countries (King, 2020). Titanium coatings deposited by cathodic arc evaporation at optimal parameters have 1.25 times higher mechanical properties than bulk titanium (Klimenko et al., 2022).

Due to their high corrosion resistance, titanium coatings are used to protect various non-corrosion-resistant metals and alloys (Zhang et al., 2005) (Aksenov et al., 2012) (Chang et al., 1989) (Boyda et al., 2008). For example, a dense titanium coating with a thickness of about 10 µm was successfully deposited on the surface of magnesium and the results of electrochemical polarization proved that Mg corrosion current density decreased by an order of magnitude (Zhang et al., 2005). Titanium coatings were also successfully used to protect such corrosive materials as uranium (Aksenov et al., 2012) and its DU-0.75Ti alloy [14] and Sm-Co magnetic alloy (Boyda et al., 2008). The Ti film showed better corrosion resistance than TiN and a stable passive area during 7 days of immersion in Ringer's solution on 316L stainless steel (Wathanyu et al., 2020). Protection capabilities against corrosion of various types of low-alloy steels by titanium coatings deposited by cathodic arc evaporation were studied (Zhujmg et al., 1991) (Creus et al., 1997) (Creus et al., 2000).

EURAD (Deliverable n° 15.6) - Novel materials and processes for the optimisation of long-term container performance
Dissemination level: Public
Date of issue of this report: 06/05/2024

Page

The purpose of this work was to study the effect of the bias potential on the structure and corrosion resistance of titanium coatings for the protection of steel 3 from corrosion in environments with a high content of chloride ions. During the deposition different DC bias voltage (-50, -100, -150, -200 V) were applied to the substrate.

4.2.3. Composition, structure and morphology

SEM images of the surface and cross sections of samples with coatings deposited on the substrate at various bias potentials are presented in Figure 74. The surface morphology is typical for coatings obtained by cathodic arc evaporation (Anders, 2008). The coatings have a dense homogeneous cellular structure with availability of cathode material macroparticles of different sizes from a few to 10 µm (Figure 74, left column). Spots of delamination, cracks and open porosity are not observed. Most macroparticles are present on the surface of the sample deposited at a bias potential of -50 V (Figure 74b). With an increase in the bias potential of the substrate to -200 V, a gradual decrease in the quantity of macroparticles is observed and the surface of the coatings becomes more uniform (Figure 74, c-h). A decrease in the number of macroparticles on the surface of coatings with an increase in the negative potential of the substrate is usually explained by the reflection of a negatively charged macroparticle in the electric field of the substrate (Keidar et al., 1999).

The images of cross sections of samples (Figure 74, right column) show a dense, uniform, compact structure of the coatings with a small number of defects caused by the action of the abrasive during grinding. As a result of grinding, the coatings are not destroyed and do not exfoliate from the substrate. It should be noted that the average ion energy and substrate temperature were used in the synthesis of coatings corresponding to zone 2 in the diagram of A. Anders structural zones (Anders, 2010), which is characterized by a columnar coating structure with growing grains from the substrate to the surface. Columns in such coatings are clearly seen on microscopic images of the cross sections of samples obtained by chipping after cooling in liquid nitrogen (Suliali et al., 2022). The columnar structure on the cross sections obtained by us is practically not visible, which indicates a strong bond between the grains in the obtained coatings. The thickness of the coatings deposited at different values of the bias potential differs little and is in the range of 18 – 21 µm. According to the EDX analysis, all coatings are 99% titanium and contain a small amount of oxygen and carbon impurities (Figure 75). The images show a transition diffuse zone between the coating and the substrate, which improves adhesion. As the potential increases, the thickness of the transition zone increases from 0.3 to 2.0 µm, which can be explained by the enhancement of radiation-stimulated diffusion processes. It is believed that the collision of high-energy ions and plasma atoms with a substrate causes an increase in the concentration of vacancies on its surface, which leads to an increase in the solubility of alloying elements and an acceleration of the diffusion process (Wang et al., 2018).

a

b

EURAD (Deliverable n° 15.6) - Novel materials and processes for the optimisation of long-term container performance
Dissemination level: Public
Date of issue of this report: **06/05/2024**

Page
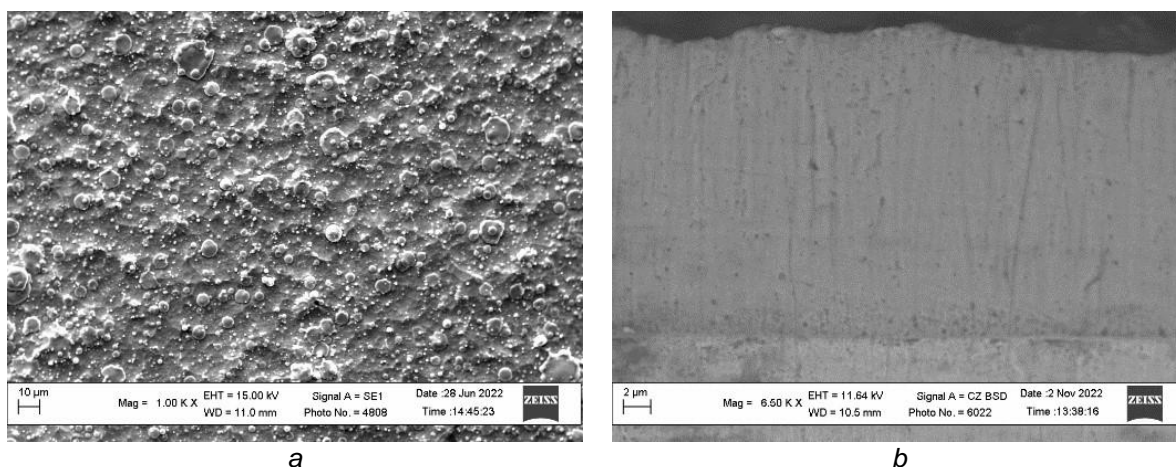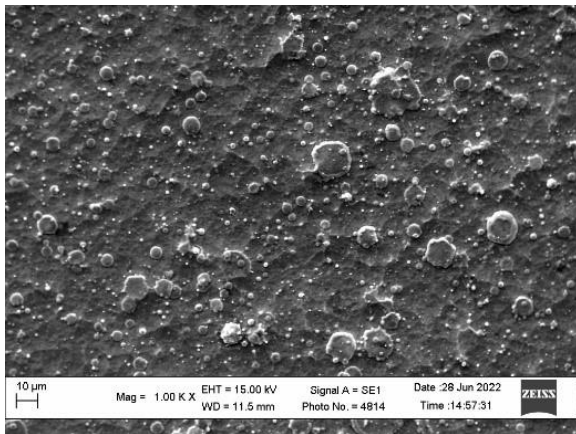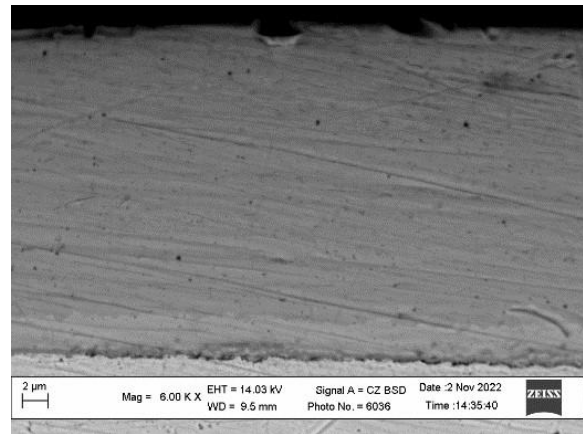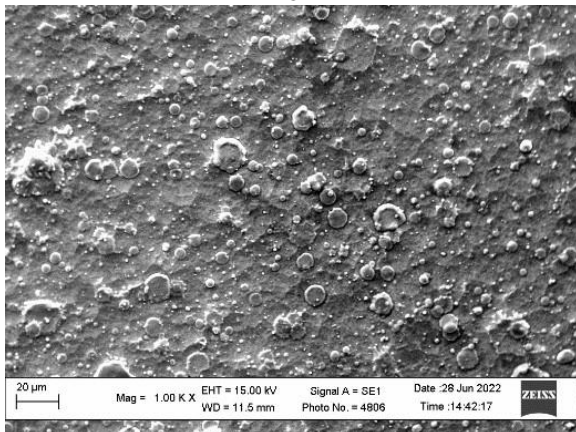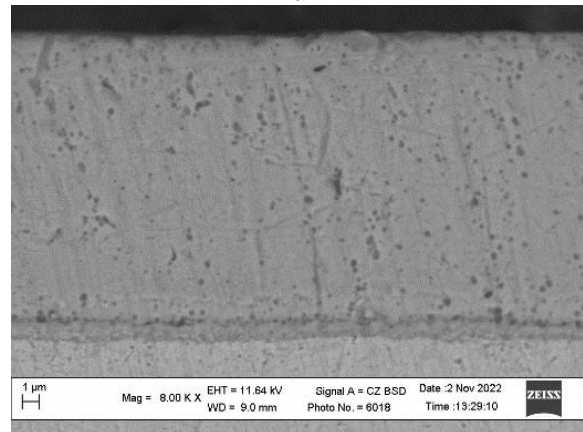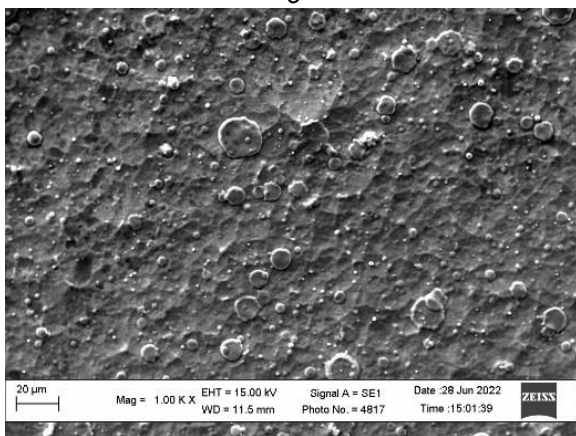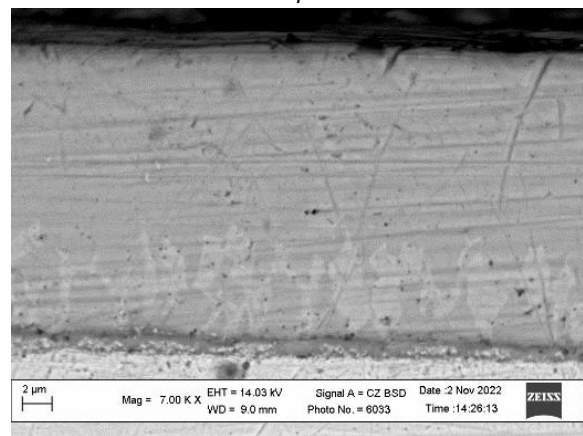
Figure 74. SEM images of the surface (left column) and cross sections (right column) of Ti-coatings deposited at different values of the bias potential: 50 V (a, b); 100 V (c, d); 150 (e, f); 200 V (g, h).

EURAD (Deliverable n° 15.6) - Novel materials and processes for the optimisation of long-term container performance
Dissemination level: Public
Date of issue of this report: 06/05/2024

Page
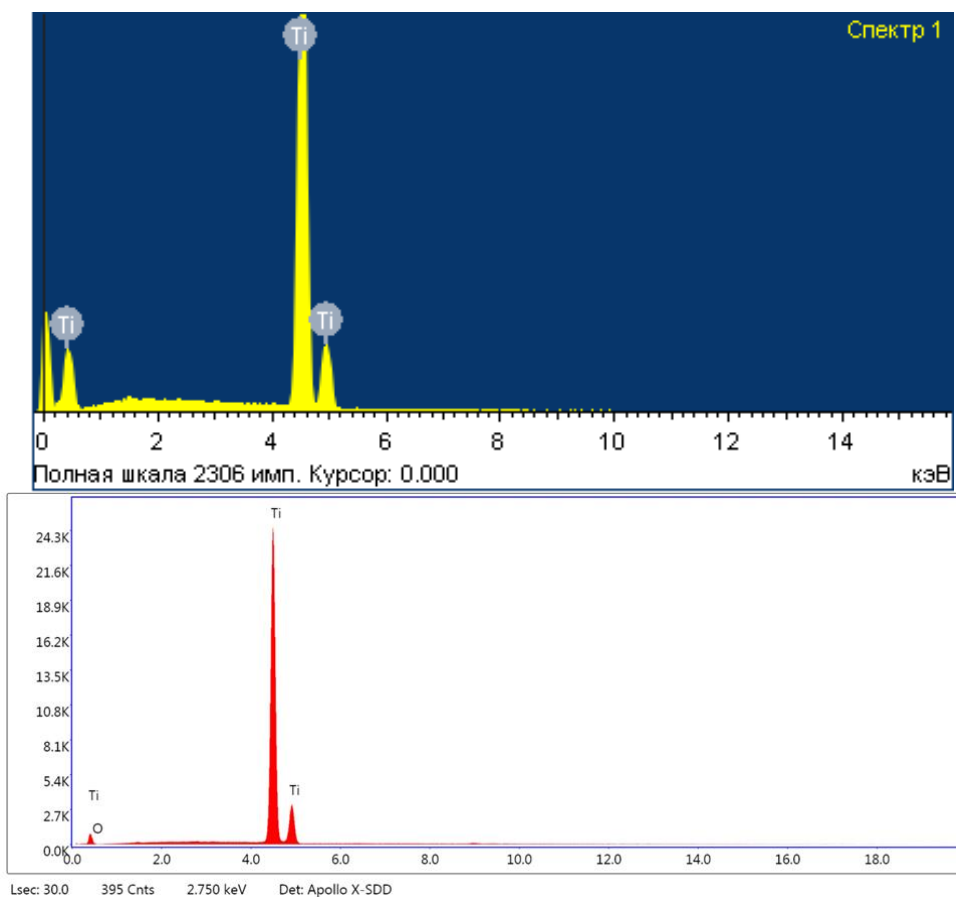
Figure 75. EDX analysis of the titanium coating deposited by CAE method (Two different types of analyzers are used to confirm that the impurities in the Ti coatings are at the limit of detection).

X-ray diffraction patterns of samples with coatings deposited at different values of the bias potential on the substrate are presented in Figure 76. The analysis shows that only one crystalline phase -α-Ti with a hexagonal close-packed (HPC) crystal lattice is found in all coatings. The diffraction curves contain all the peaks characteristic of the α-Ti structure, however, the ratio of the integral intensities of the diffraction lines varies depending on the potential and somewhat differs from the tabulated data obtained for a non-textured powder sample (JCPDS [44–1294]). According to these data, the line (101) at 40.2° is the most intense for α-Ti with a random orientation of crystallites. The most intense is the line (002) near 38.5°on the diffraction pattern of the coating obtained at a potential of 50 V and a potential of 200 V - the line (110) near 63.0°. It is known that α-Ti ion-plasma coatings deposited from flows of high-energy particles are characterized by the formation of a texture (Dellasega et al., 2021). The analysis of the texture of the deposited coatings was carried out by calculating the texture coefficients. The calculation results are presented in Figure 77.
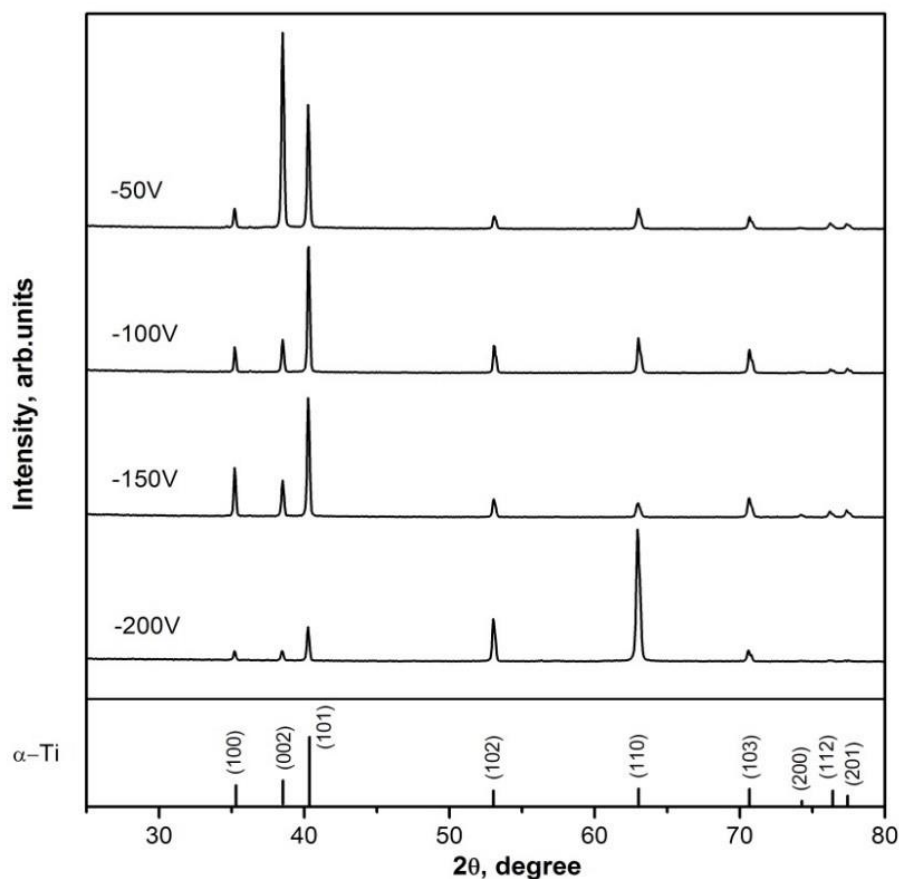
Figure 76. X-ray diffraction patterns of coatings obtained at different values of the bias potential on the substrate. The lines in the hatched diffraction pattern represent the α-Ti peaks according to JCPDS [44–1294].
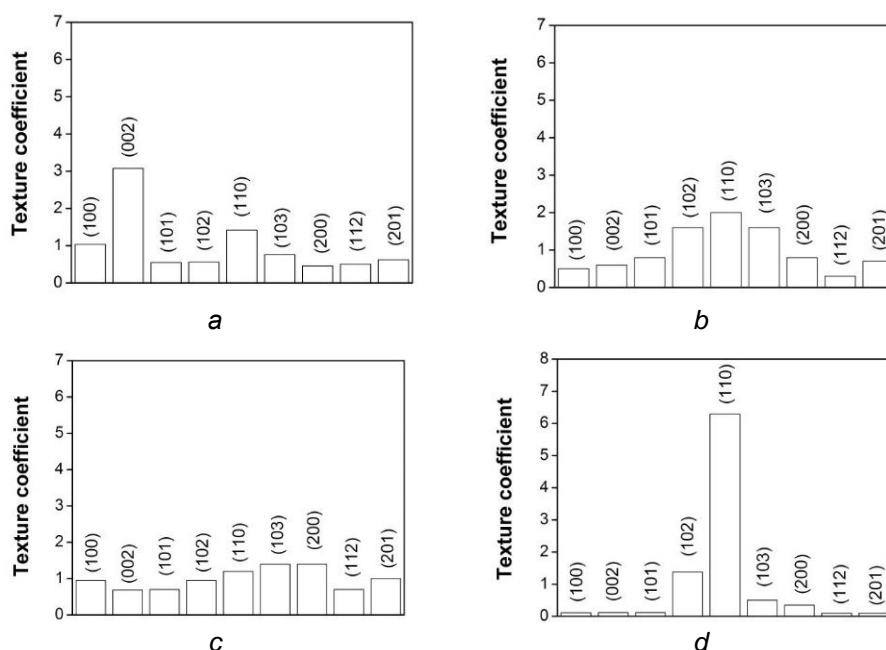
Figure 77. Texture coefficients for α-Ti coatings obtained at different values of the constant bias potential on the substrate: 50 V (a); 100 V (b); 150 (c); 200 V (d).

EURAD (Deliverable n° 15.6) - Novel materials and processes for the optimisation of long-term container performance
Dissemination level: Public
Date of issue of this report: 06/05/2024

Page

The texture is poorly pronounced in the coatings deposited at a potential of 100 and 150 V. The texture coefficients for all reflections have close values. As the bias potential decreases or increases, the predominant orientation becomes more pronounced. At a low potential of 50 V the growth of crystallites is most likely, which are oriented by close-packed planes of (001) type parallel to the surface, as evidenced by the increase in the texture coefficient for (002) compared to other reflections, however, the texture in this case is not sufficiently perfect. The most textured is the deposited coating at a potential of 200 V. The texture reflection coefficient (110) reaches 6.3 for it, which is much higher than other values. Thus, most of the crystallites are oriented so that the hexagonal prism formed by Ti atoms lies in the coating plane, i.e., close-packed crystallographic planes (001) are oriented perpendicular to the surface. It should be noted that, in contrast to the intensity, a change in potential has practically no effect on the width of diffraction lines. The crystallite size in all coatings is close to 160 nm according to the estimate using the Scherrer formula.

The parameters of the α-Ti crystal lattice in the direction normal to the coating surface were determined based on the angular position of the diffraction peaks on the θ-2θ diffractograms. The parameter of α-Ti crystal lattice for all coatings is 0.2950 nm, which corresponds to the tabled value for this phase. Another lattice parameter - c gradually increases with increasing substrate potential in the range of 50–200 V from the tabled value of 0.4684 nm to 0.4693 nm (Figure 78). Such an increase is associated with an increase in the crystal lattice deformation under the effect of more energetic titanium ions forming the coating. Bombardment of the growing coating surface by accelerated plasma ions causes compaction of coatings, generation of defects and residual compression stresses (Manova et al., 2010).
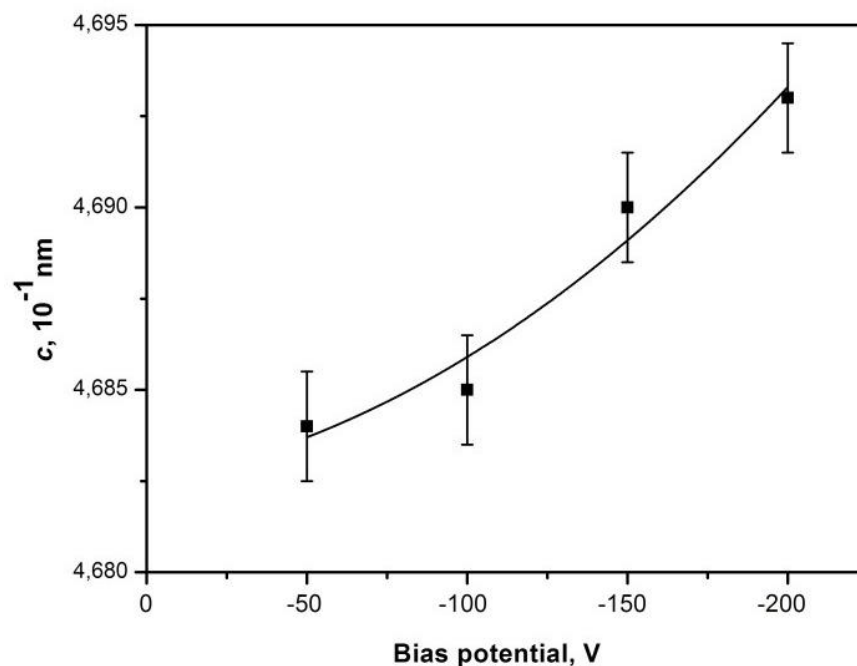
Figure 78. The effect of a constant bias potential on the parameter of the α-Ti crystal HCP lattice in coatings.

4.2.3.1. Hardness of the titanium coatings

The results of microhardness measurements on a sample of uncoated steel St.45 and samples with Ti coatings are shown in Figure 79. The change in bias potential on the substrate during deposition has

little effect on the hardness of the coatings in the range of 4.5 and 5.5 GPa. The values obtained are much higher than the hardness of commercially pure bulk titanium (1.8 GPa) (Nagaraj et al., 2023). There are few reports on the hardness of pure titanium PVD coatings. Hardness in the ranges of 2 to 8.5 GPa, depending on the conditions of the deposition processes, is discussed in (Kottfer et al., 2016). The increase in hardness is largely associated with a decrease in grain size in the coatings and the formation of a nanostructured state (Cavaleiro et al., 2007).
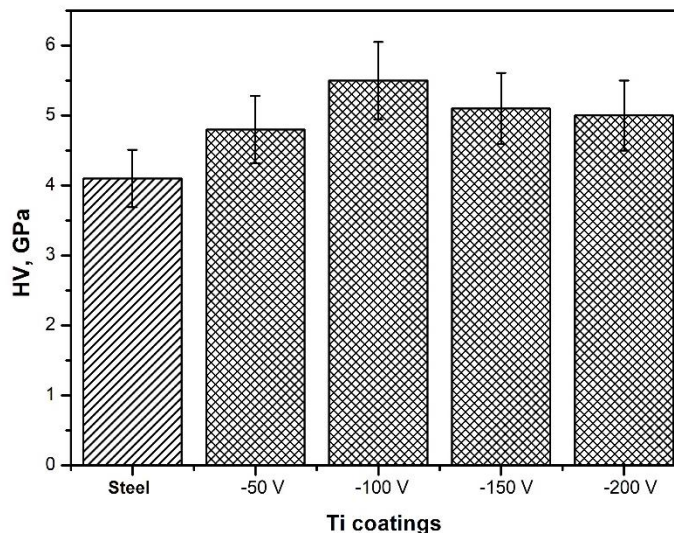
Figure 79. Microhardness of uncoated steel samples and Ti-coated samples deposited at different bias potentials.

As a result of optimization of CAE processes of metal coating deposition, deposition rates for titanium are increased up to 40 µm/h. Ti coatings were deposited on low carbon steel substrate. Titanium coatings up to 50 µm thick were obtained with different parameters of deposition processes by cathodic arc evaporation and magnetron sputtering. The deposition conditions and properties of the Ti coatings, as well as the samples obtained, are given in Table 18 and Table 19.
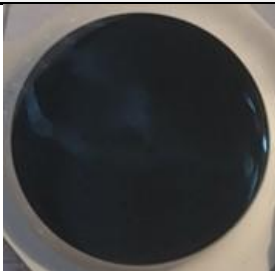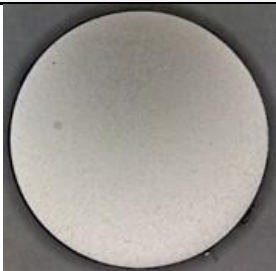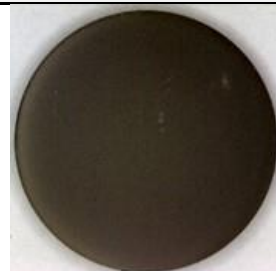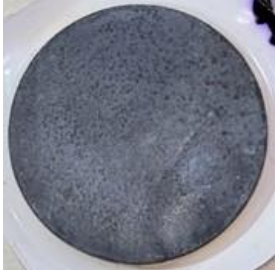
Table 18. Deposition conditions and properties of Ti coatings obtained by MS and CAE processes.

Coating	Deposition parameters			Chemical composition, at.%		Thickness, µm	Grain size, nm	Ra, nm	H, GPa
	I, A	PAr, Pa	Ub, V	Ti	O				
Ti CAE	100	0.05	-100	99	<1	53	350	582	4.5
Ti MS	5	0.5	-50	98	2	52	97	103	4.9

Long-term corrosion in 3% NaCl at 20°C of steel samples (Steel 3) with Ti coatings has been studied.

EURAD (Deliverable n° 15.6) - Novel materials and processes for the optimisation of long-term container performance
Dissemination level: Public
Date of issue of this report: 06/05/2024

Page

Table 19. View of Steel 3 and Ti coated samples after long-term corrosion with different test durations.

Hours	St.3	Ti CAE	Ti MS
0			
144			
296			

The steel sample is intensely oxidized after a long exposure; the entire surface of the sample is covered with a thick layer of rust. Samples coated with Ti do not corrode even at maximum immersion time in the solution. Ti coating deposited by MS has poor corrosion resistance, pits are observed on the surface. This may be due to porosity and poor adhesion of the coating.

4.2.4. Chromium

The application of protective heat and corrosion resistant coatings by physical deposition methods is an effective way to increase oxidation resistance (Idarraga-Trujillo et al., 2013) (Kim et al., 2013) (Kuprin et al., 2015). The choice of chromium as a protective coating is due to its exceptionally high oxidation resistance (Nymar et al., 2023), high thermal conductivity (93.9 W/mK), and low activation. Chromium coatings with a thickness of 5-10 µm significantly reduce the oxidation rate of pure zirconium in water at 360 °C (Ma et al., 2023). As a result of the optimization of CAE processes of metal coating deposition, deposition rates for chromium are increased up to 30 µm/h.

Cr coatings were deposited on a low carbon steel substrate. Chromium coatings up to 30 µm thick were obtained by various parameters of deposition processes by cathodic arc evaporation. Deposition conditions and properties of the coatings and samples obtained are given in Table 20 and Figure 80.

EURAD (Deliverable n° 15.6) - Novel materials and processes for the optimisation of long-term container performance
Dissemination level: Public
Date of issue of this report: 06/05/2024

Page

Table 20. Deposition conditions and properties of chromium coatings obtained by CAE processes.

Coating	Deposition parameters			Chemical composition, at%		Thickness, μm	Grain size, nm	Ra, nm	H, GPa
	I, A	P_{Ar}, Pa	U_b, V	Cr	O				
Cr1	100	0.05	-50	99	<1	32	228	160	4.2
Cr2	100	0.05	-300 pulsed	99	<1	31	559	138	4.3
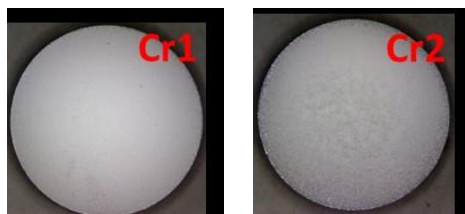
Figure 80. Deposited metallic Cr coatings with thickness up to 50 μm processed by CAE.

The adhesion of Cr coatings was determined using the Daimler-Benz test and the results are shown in Figure 81.
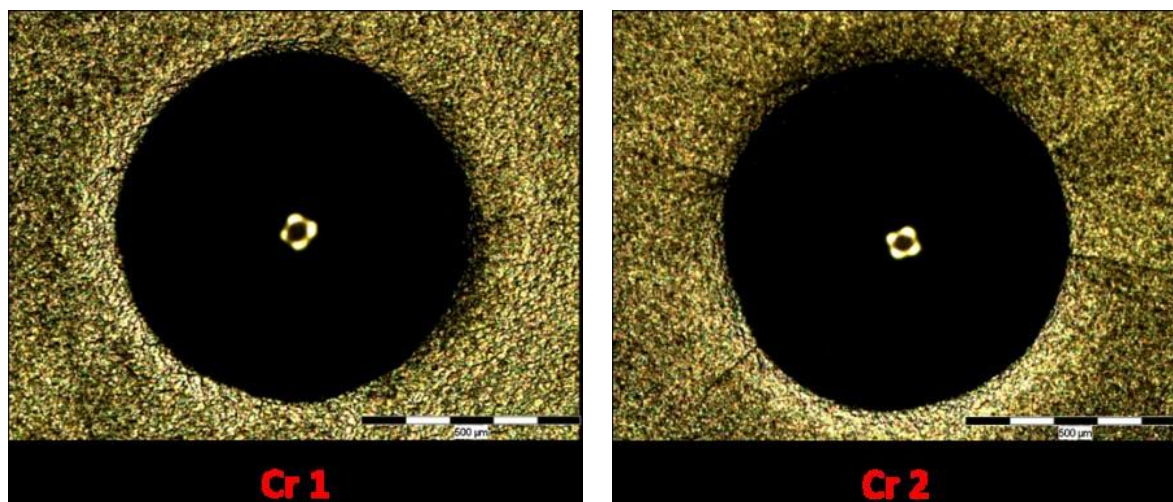
Figure 81. Photographs of the surfaces of Cr coatings after Daimler−Benz test

It was found that Cr coatings have high adhesion to steel substrates, at the level (HF1-HF2). The long-term corrosion in 3% NaCl at 20°C of steel samples (Steel 3) with Cr coatings was estimated (Table 21). The steel specimen is intensively oxidized, after a long exposure, the entire surface of the specimen is covered with pitting and a thick layer of rust at the time when the Cr-coated samples do not corrode even at the maximum test time in solution.

EURAD (Deliverable n° 15.6) - Novel materials and processes for the optimisation of long-term container performance
Dissemination level: Public
Date of issue of this report: 06/05/2024

Page

Table 21. View of Steel 3 and Cr coated samples after long-term corrosion with different test durations.

Hours	St.3	Cr 1	Cr 2
0			
144			
296			

The steel specimen is intensively oxidized, after a long exposure the entire surface of the specimen is covered with a thick layer of rust at the time when the Cr-coated samples do not corrode even at the maximum test time in solution.

The chromium-coated sample Cr 1 has a smoother surface, and no cracks were observed on its surface during the adhesion tests. This is most likely due to the lower bias potential (-50 V) at which the coating was deposited and consequently the lower level of internal stresses. Therefore, further corrosion studies were conducted with chromium coatings deposited at a substrate bias potential of -50 V.

In addition, the corrosion resistance of the uncoated Steel 3 sample and samples with metallic Cu, Ti, and Cr coatings were determined by electrochemical characterization in a 3.5 wt% NaCl solution at 20ºC. The results of these tests are shown in Figure 82.
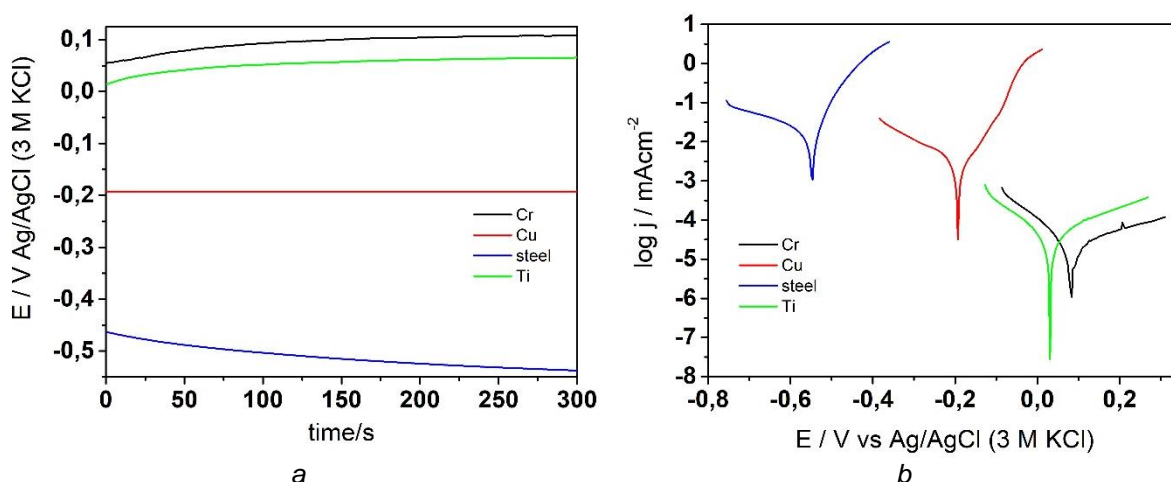
Figure 82. Open circuit potentials (OCPs) (a) and Tafel plots (b) for the Steel 3 substrate and Steel 3 with coatings during immersion in 3 wt% NaCl solution.

EURAD (Deliverable n° 15.6) - Novel materials and processes for the optimisation of long-term container performance
Dissemination level: Public
Date of issue of this report: 06/05/2024

Page

As shown in Figure 82a, the open circuit potentials of steel and coatings differ significantly. Steel 3 has a strongly negative potential (<-0.5 V), indicating low corrosion resistance. The titanium and chromium coatings have a positive potential of 0.05 and 0.1 V, respectively, which remains constant during exposure, confirming their high corrosion resistance. For the copper coatings, this potential is -0.2 V. The corrosion potential (E_{corr}) and corrosion current (I_{corr}) of the samples were calculated from Tafel curves (Figure 82b) and are summarized in Table 22.

Table 22. Electrochemical parameters characterizing the corrosion processes of Steel 3 substrate and Steel 3 with coatings in 3 wt% NaCl solution.

Sample	E_{corr} / mV	I_{corr} / μAcm^{-2}
steel	-548	$3,0 \times 10^1$
Cu	-194	$1,7 \times 10^0$
Ti	31	$9,7 \times 10^{-2}$
Cr	82	$2,6 \times 10^{-2}$

The highest corrosion potential and lowest corrosion current are for the chrome coating and quite close values for the titanium coating. This may indicate the absence of through porosity in titanium, chromium and cooper coatings on steel substrates. The surface of metallic coatings on Steel 3 substrates was investigated by SEM after deposition and after potentiodynamic testing (Figure 83).

a

b

c

d

EURAD (Deliverable n° 15.6) - Novel materials and processes for the optimisation of long-term container performance
Dissemination level: Public
Date of issue of this report: 06/05/2024

Page

e	*f*
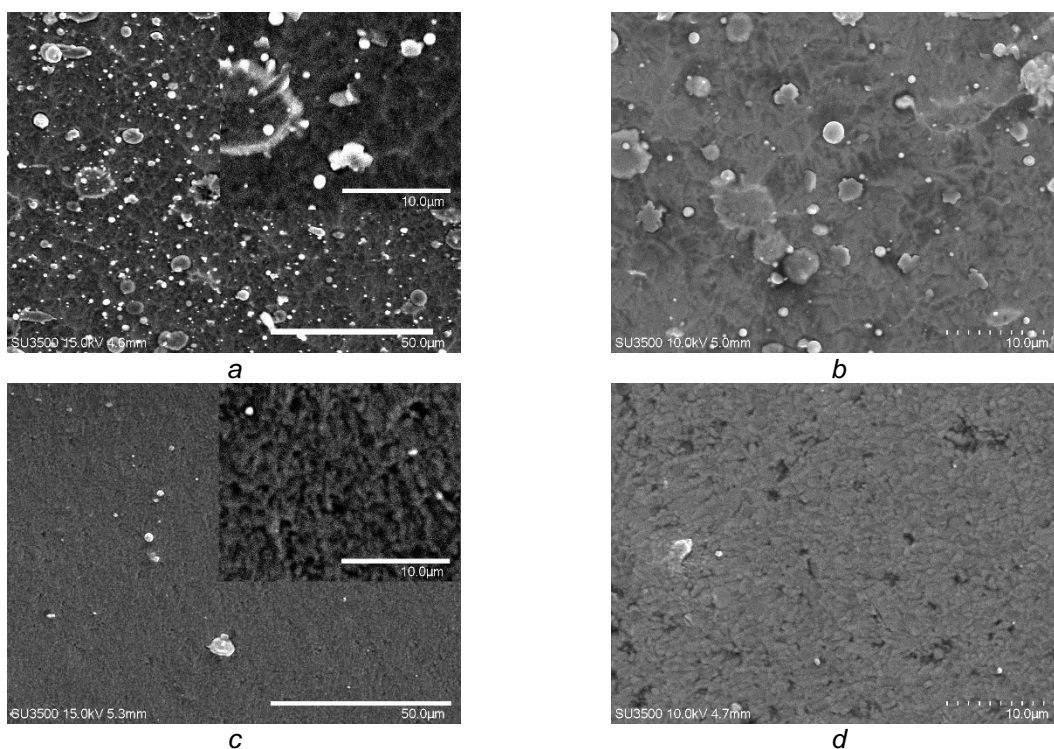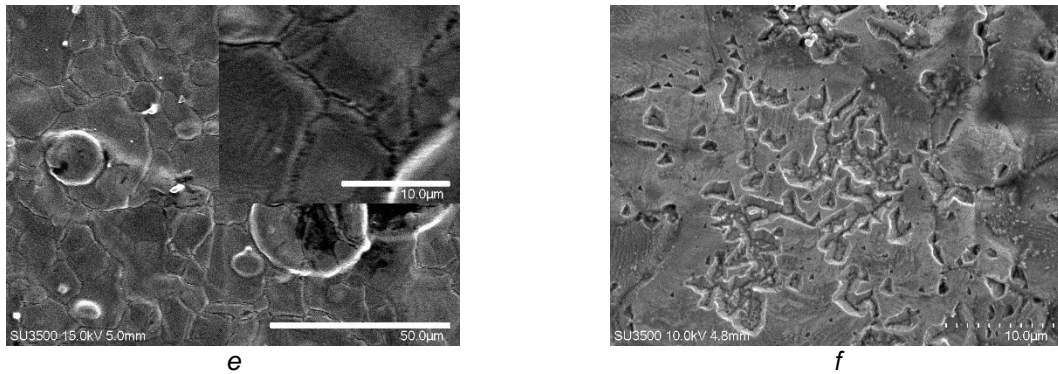
Figure 83. SEM micrographs of Steel 3 with Ti (a, b), Cr (c, d) and Cu (e, f) coatings: initial (a, c, e) and after (b, d, f) potentiodynamic corrosion tests.

As can be seen from the comparison of the SEM images of the surfaces of the coating in Figure 83, no craters or pits appear in the Ti and Cr coatings after corrosion tests. The effect of smoothing the surface of the coatings is observed due to the dissolution of small particles of cathode material that are weakly bonded to the coating (Figure 83b, d). Titanium and chromium coatings deposited by CAE provide sufficient corrosion protection for steel substrates in a 3% NaCl solution. Only the surface of the copper coating showed surface defects in the form of pits, most likely due to the dissolution of the copper coating (Figure 83f).

4.2.4.1. Long-term corrosion resistance of metallic coatings in water at 90°C.

A furnace with a thermostat was specially prepared for long-term corrosion testing of steel samples with metallic coatings. The coatings were deposited on cylindrical steel samples. Cu, Cr and Ti coatings were deposited at parameters selected from previous experiments: bias potential on the substrate -50 V for Cu and Cr, -100 V for Ti and thickness of coatings 30 µm. The samples were continuously rotated against the cathode for uniform coating deposition over the entire surface.

After deposition, the samples were weighed and placed in glass containers with distilled water. The containers with water were placed in a thermostat in which the temperature was maintained at 90 °C. To measure the change in weight of the samples, they were periodically removed and weighed. The samples photos are shown in Figure 84.

a	*b*	*c*
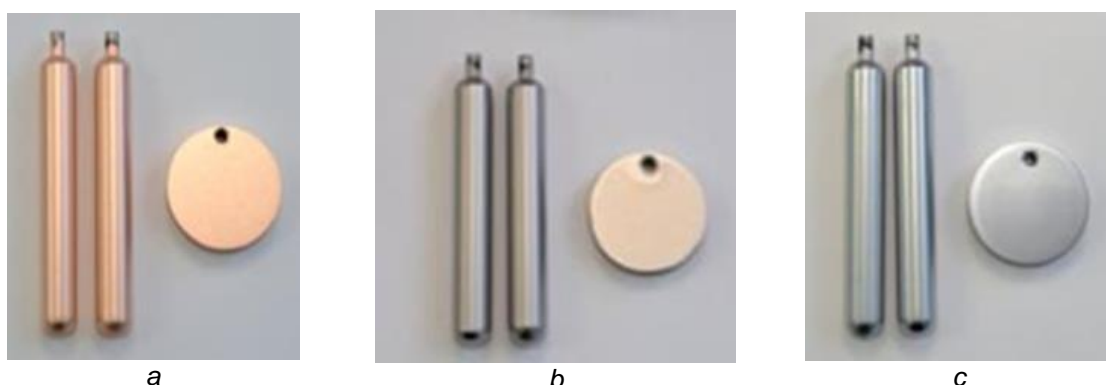
Figure 84. Photographs of the steel samples with Cu (a), Ti (b) and Cr (c) coatings.

The results of the long-term corrosion tests (4200 hours) of steel samples with Cu, Ti and Cr coatings in distilled water at 90 °C are shown in Figure 85.

EURAD (Deliverable n° 15.6) - Novel materials and processes for the optimisation of long-term container performance
Dissemination level: Public
Date of issue of this report: 06/05/2024

Page
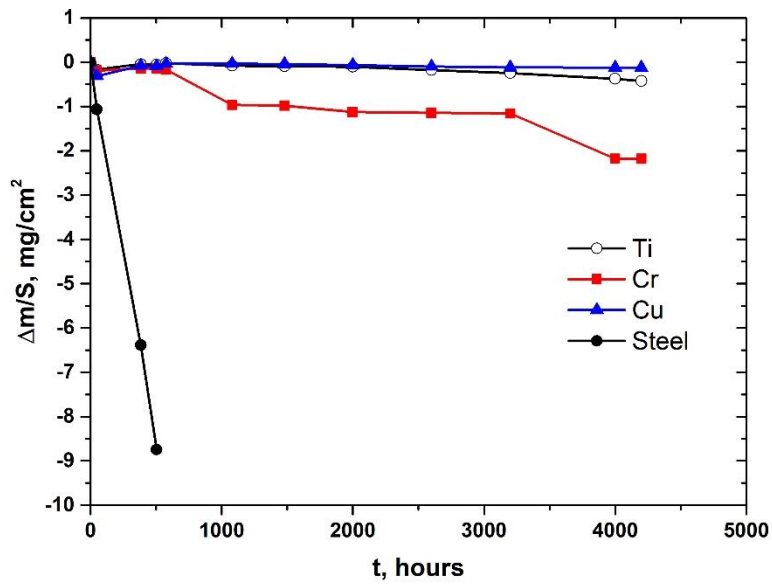
Figure 85. Changes in specific weight of steel samples with Cu, Ti and Cr coatings as a function of immersion time in distilled water at 90 °C.

As can be seen in Figure 85, the steel sample has a high weight loss and dissolves intensely to form rust. The tests on the steel sample were terminated after 500 hours due to severe dissolution. A photograph of the steel samples with coatings after the test is shown in Figure 86.

| a | b | c |
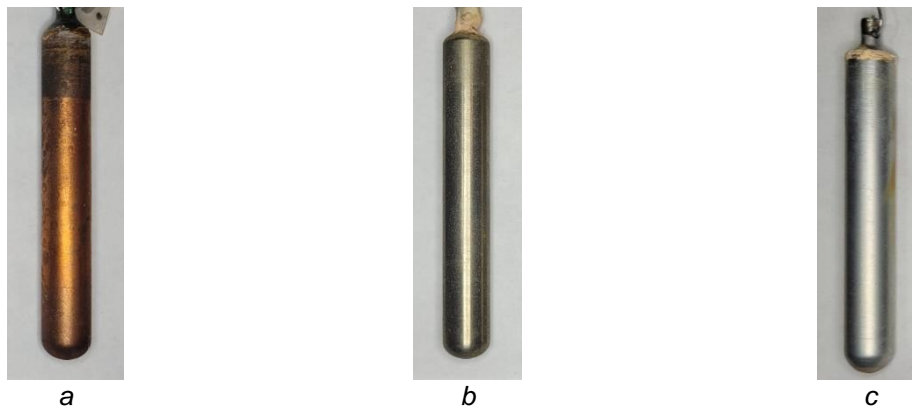
Figure 86. Photos of the steel samples with coatings after testing: Cu (a); Ti (b) and Cr coating (c).

The Cr coating showed a slight weight loss in the first phase of the test up to 1000 hours (Figure 85). However, after 1000 hours, an increase in weight loss was observed due to the appearance of continuous small pits on the steel substrate. The formation of rust patches on the surface of the specimen was observed (Figure 86c). These coatings may need to optimize the architecture of the interface with the steel substrate to avoid pitting and porosity.

Ti and Cu coatings show minimal weight change throughout the test period, indicating high corrosion resistance (Figure 86a and Figure 86a). However, some traces of pitting or rusting are observed on the surface of the Ti coating after 3000 hours of testing (Figure 86b).

EURAD (Deliverable n° 15.6) - Novel materials and processes for the optimisation of long-term container performance
Dissemination level: Public
Date of issue of this report: 06/05/2024

Page

4.2.4.2. Summary

The influence of the bias potential on the structure and properties of titanium coatings deposited by cathodic arc evaporation has been studied. The deposited Ti coatings have good mechanical properties and high adhesion to steel substrates. Electrochemical corrosion tests have shown that coatings deposited at a bias potential of -100 V have the best corrosion resistance. Ti, Cu and Cr coatings deposited by CAE with a thickness not less than 30 µm have excellent corrosion resistance (no pitting) in 3% NaCl after electrochemical testing.

Ti, Cr and Cu coatings deposited by CAE on steel substrates underwent long-term corrosion testing (4200 hours) near disposal conditions (water, T= 90 °C). The Cr coating showed weight loss and small pits. Optimization of the interface with the steel substrate to avoid pitting and porosity may be required for these coatings.

Ti and Cu coatings show minimal weight change throughout the test period, indicating high corrosion resistance. However, some pitting and traces of rusting are observed on the surface of the Ti coating after 3000 hours of testing.

4.2.5.   New copper/alumina composite coatings

This part of Task 2 focused on the elaboration and characterization of metal-matrix composite (MMC) coatings produced by cold spray (CS) technology and intended to act as a corrosion barrier for HLW containers against ground water in deep geological disposal facilities. The concept of manufacturing a dual-shell container with a copper coating for corrosion protection directly on the steel structure was raised to avoid the drawbacks related to classical manufacturing approaches including machining/forging and adjustment issues with waste container which could arise with rigid cylinders of copper (Lee et al., 2011) (Keech et al., 2014) (Legoux, 2014).
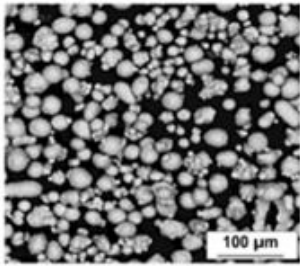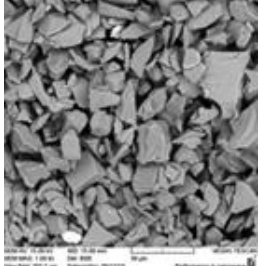
The main interest in metal copper for this application lies in its thermodynamic stability in anoxic ground water to secure core steel HLW container for extremely long periods of time (Andersson, 2002) (Raiko et al., 1996). It is among the main materials proposed as nuclear waste canister materials. Moreover, this CS technology allows deposition of thick coatings, several millimetres, directly on the surface of the steel container, and welding joint can be covered by copper after welding steel cover. The addition of Al_2O_3 ceramic particles in the process is motivated by the fact that denser deposits are obtained when Al_2O_3 ceramic particles are added to the coating, compared to pure copper coatings. The densification of deposits through the "hammer" effect of ceramic particles contributes both to reducing the porosity rate and increasing the binding forces of cohesion and adhesion between copper particles, with ceramic particles helping to fill the voids between the particles. This results in a decrease in the active surface area of the material in corrosive environment. Furthermore, the presence of pores can contribute to increasing the sensitivity to localized corrosion through coupling effects related to differences in dissolved oxygen concentration between the interior of the pores and the external environment (Maev et al., 2008) (Shkodkin et al., 2006) (Koivuluoto et al., 2010) (Hassani-Gangaraj et al. 2015).

  Materials produced by cold spray present defects such as porosity and decohesion between particles. Previous studies at EMSE (Bensaïd, 2024) showed that an optimal proportion of 30 vol.% of SiC particles made it possible to minimize porosity for a given set of process parameters (nature of carrier gas, temperature, pressure, distance between tracks). This set of parameters have been re-used to elaborate composite Cu-Al_2O_3 coatings and two nozzle displacement speeds were tested. After optimization of the cold spray technology parameters for the copper/alumina composite coatings, mechanical testing and corrosion studies were performed. The results are compared to those of both wrought copper alloys and pure cold spray copper coating. This work also focused on the synergy between material deformation and the corrosion of the coatings, particularly in the vicinity of porosity defects.

EURAD (Deliverable n° 15.6) - Novel materials and processes for the optimisation of long-term container performance
Dissemination level: Public
Date of issue of this report: 06/05/2024

Page

4.2.5.1. Materials

The composite cold spray coatings studied are produced from a mixture of powders Cu+32vol.%Al_2O_3. Pure cold spray coatings are produced with the same Cu powder while pure wrought copper is produced by cold crucible melting process and submitted to thermomechanical treatments. Their chemical composition is indicated in Table 23.

Table 23. Chemical composition of powders and wrought copper, and particle sizes

Materials	Chemical composition	Particle size		
Cu powder	99.97wt%	16.3-18.3 μm		
Al_2O_3 powder	99.95wt%	35 μm		
Wrought Cu	99.99wt%	-		

Cu powder Al_2O_3 powder

4.2.5.2. Elaboration of cold spray coating coupons

The influence of cold spray projection speed, combined with the projection angle, plays a determining role in the quality and efficiency of the deposition process. The projection speed ensures kinetic energy to the particles that changes adhesion to the target surface. The projection angle, adjusted by tilting the nozzle, can influence the interaction of the particles with the surface and provide flexibility of control to adapt the process to the specific needs of the application. Thus, two different projection strategies were studied during this work: the slow one corresponding to a low nozzle movement speed of 20 mm/s, and a fast strategy with a 40 mm/s scanning speed constituting multiple variable thick layers, both resulting in a coating of about 10 mm thickness. The construction strategy plays on the profitability of the process through the speed of production of the coating, but also with regard to the quality of the deposit.

Before spraying, the surface of the substrates is sandblasted with 12 mesh alumina abrasive particles in order to increase the roughness and the surface of contact, which allows the projected particles to better anchor on the surface. The carrier gas used is nitrogen, raised to 35 bars and 500°C. The spraying distance is 40 mm, and the inter-track distance 4 mm. Figure 87 shows an example of a composite Cu coating deposited on a steel substrate.
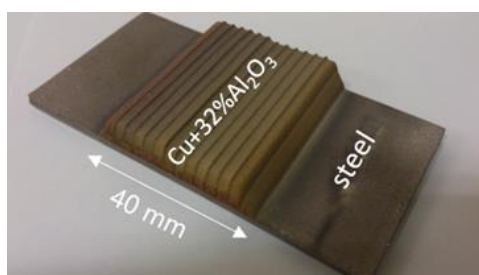
Figure 87. Composite cold spray coating coupon (Cu+32vol.%Al_2O_3).

4.2.5.3. Microstructure analysis

Cold spray coatings microstructures were analysed in detail at different scales, with optical microscopy Olympus GX51, SEM observations, EDX and EBSD analysis with a Zeiss Supra 55 VP microscope operating at 20 kV. Porosity and defects density were determined using a set of SEM images

EURAD (Deliverable n° 15.6) - Novel materials and processes for the optimisation of long-term container performance
Dissemination level: Public
Date of issue of this report: 06/05/2024

Page

representatives of the coating at different levels and orientations in the thickness, using ImageJ software for image analysis. Additional Archimedes measurements have also been realized to assess the open porosity of the samples.

4.2.5.4. Mechanical characterization

The mechanical properties (YS, UTS, A%) of the coatings and wrought Cu were determined using compression tests carried out at room temperature and at strain rate of 2.10^{-3} s^{-1} on a Schenck Uniaxial press. Figure 88 shows a sample of 4 mm and 6 mm in height placed on the piles of the press with a double layer Teflon tape wrapped over to limit friction. Only the direction perpendicular to the substrate surface was tested in this study as it is the one which presents the weakest mechanical properties, and is therefore the most conservative (Bensaïd, 2024).
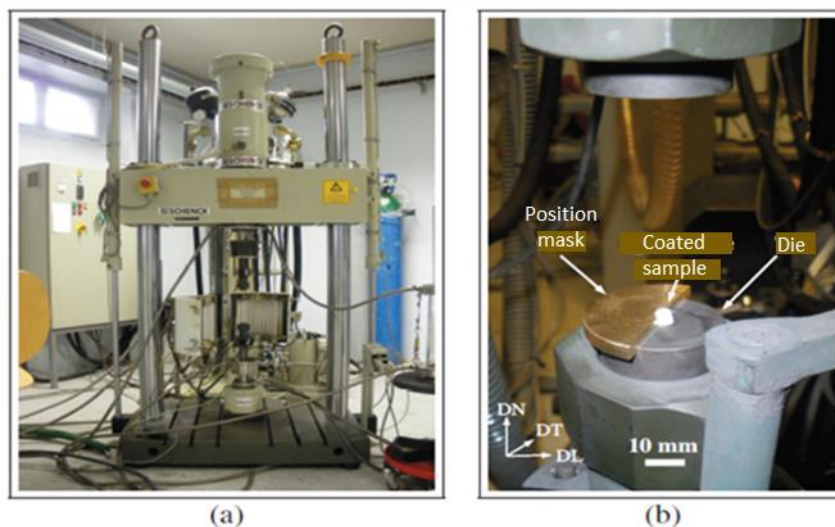
Figure 88. Compression machine for mechanical testing on cold sprayed coatings.

Creep tests were also performed at room temperature and 90°C on the same machine. Loadings applied were the YS and about 120% YS.

4.2.5.5. Electrochemical measurements and corrosion characterization

The corrosion behaviour was characterized by electrochemical methods using a Voltalab PGP201 potentiostat of Radiometer Analytical S.A. Company. Potentiodynamic experiments and open circuit potential (OCP) measurements were performed in a conventional type three electrodes cell, using a saturated calomel reference electrode deported into a cooled compartment via a Luggin capillary probe, a Pt foil counter electrode and the wrought Cu, pure CS copper, or CS Cu-32%Al_2O_3 coatings for working electrode. The polarization curves were carried out at a speed of 0.1 mV/sec from OCP-30mV to +200mV/SCE. The samples are left at free potential (OCP) before launching the polarization curves until stabilization after 24 hours. The test solution corresponds to the synthetic groundwater environment of the Bure site (named solution 1 by ANDRA); the composition is given Table 24. The test temperature was 90°C; the environment was deaerated by a continuous flow of an Ar/CO_2 mixture, maintaining pH at 6.6.

EURAD (Deliverable n° 15.6) - Novel materials and processes for the optimisation of long-term container performance
Dissemination level: Public
Date of issue of this report: 06/05/2024

Page

Table 24. Chemical composition of synthetic groundwater.

					Concentration (mmol/kgw)					
Cl	SO4	Na	K	Ca	Mg	Si	Sr	Al	Fe	DIC (HCO3)
35.10	14.96	40.78	0.705	9.554	4.106	0.352	0.208	0.00024	0.0508	5.732

To properly control the solution preparation and pH, an anaerobic glove box under a flow of argon was used (Figure 89a, Figure 89b). The environmental conditions of the corrosion tests that were targeted were anaerobic, however subsequent measurements of the oxygen content in the medium with an Orbisphere probe revealed a residual oxygen content of about 50 to 100 ppb. The presented results are therefore representative not of the long-term anoxic conditions of underground disposal, but rather of the transitional phase in the first years of disposal.

(a)   *(b)*   *(c)*
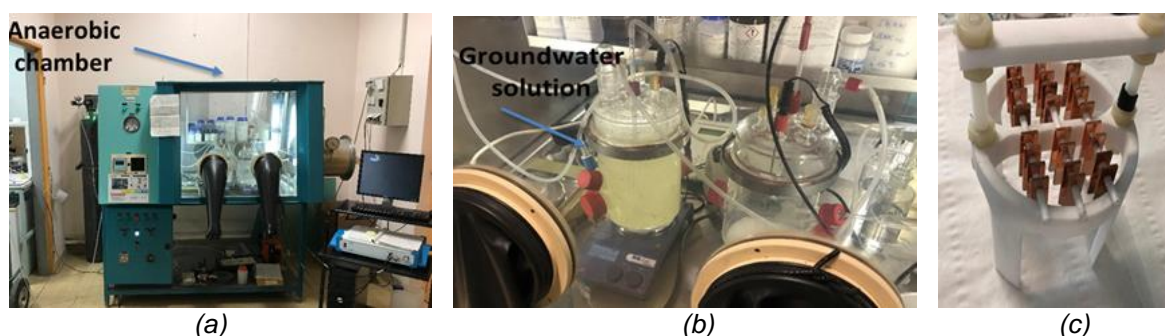
Figure 89. (a) Anaerobic glove box, (b) three-electrode cells in the glove box, (c) sample mounting support for long-term corrosion tests.

Long-term exposure tests have also been performed in groundwater environment in separate corrosion cells to determine corrosion rate by mass loss measurements on the three materials, composite $Cu+32vol.\%Al_2O_3$ and pure Cu cold sprayed coatings and wrought Cu. Tests were launched for a period of six months with samples taken regularly from the corrosion cells (Figure 89c). EDS, XRD and μ-Raman spectroscopy analysis were performed to characterize the corrosion products and oxides on the surface and inside surface defects.

Weight loss measurements were performed with a precision balance (resolution up to 0.1 mg). The masses of the specimens were measured before and after the tests. This first measurement gives the mass of the specimen with eventually the deposited scale. The scale was removed with successive cleaning steps according to standard practice. During each step, the sample is cleaned in distilled water and weighted, so that a curve plotting the mass loss, Δm vs time, can be built. Initially, the curve is linear, while it deviates for longer exposure times. The last point before such deviation is taken to measure the corrosion rate according to the following expression:

$$CR\ (\mu m/y) = \frac{Mass\ Cu\ lost\ (g).365\left(\frac{days}{y}\right).10^4(\mu m/cm)}{Surface\ exposed\ (cm^2).\rho_{Cu}\left(\frac{g}{cm^3}\right).immersion\ days}$$

4.2.5.6. Microstructure of the coatings

Figure 90 shows a metallographic cross section taken with an optical microscope indicating the heterogeneous distribution of porosity in the composite cold spray coating "low strategy" (deposition speed of 20 mm/s). Over approximately half the thickness of the deposit (total thickness of 7 mm), the

EURAD (Deliverable n° 15.6) - Novel materials and processes for the optimisation of long-term container performance
Dissemination level: Public
Date of issue of this report: 06/05/2024

Page

material is relatively dense with a homogeneous distribution of porosity from the steel substrate, grey at the bottom of the image, to mid-thickness. Above, one observes on the contrary strings of larger pores separating the successive lines deposited during the cold spray process. These zones of higher porosity density correspond to the overlap areas between deposition lines. For the same target coating thickness, the choice of a faster deposition speed reduces the thickness of the intermediate layers while increasing their number. Figure 90(b) shows the effect that the height of a layer can have on the profile of one deposition line. The angle formed by the direction of projection of the powder with the tangent to the surface has an effect on the anchoring of the grains of the powder. The greater this angle, the more grains are ejected or bounce out of the compaction zone and thus leave a greater number of porosities.

The compaction of previous layers by the deposit of the following layer is added to this effect. The thinner these layers are, the easier it is to compact and fill the porosities of the previous layer by plastic deformation of copper grains. Nevertheless, the overlap zones between lines of deposition remain the source of more porosity. Thus, by adopting the "fast strategy" overlap zones are multiplied and therefore the porosity defects with them. The whole challenge is to avoid the formation of porosity strings which weaken the material and reduce its mechanical properties.

(a)   *(b)*
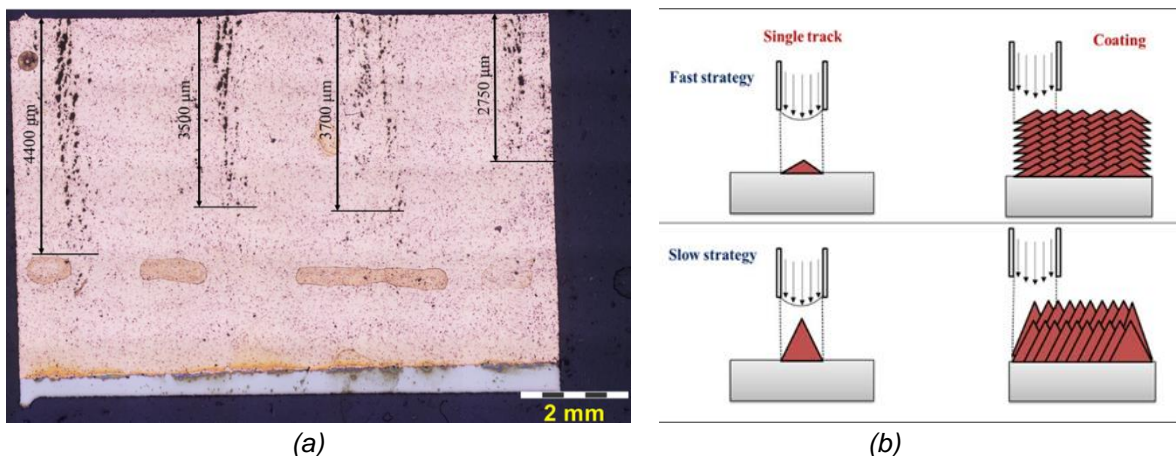
Figure 90. (a) Light microscope image of the cross-section of the composite cold spray coating (slow strategy: deposition speed of 20 mm/s) perpendicular to the deposition direction. The steel substrate is in grey at the bottom. (b) Effect of the speed deposition of the cold spray coating on the angle of incidence of the powder flow with the surface.

On the two metallographic sections, Figure 91, parallel to the surface of the coating, we clearly observe the presence of these strings of large pores on the one hand close to the surface of the coating, while on the other closer to the steel substrate, the distribution is homogeneous. The spread of these strings of porosity is approximately 1 mm and the distance which separates them corresponds approximately to the interline distance of 4 mm configured in the process.

EURAD (Deliverable n° 15.6) - Novel materials and processes for the optimisation of long-term container performance
Dissemination level: Public
Date of issue of this report: 06/05/2024

Page

(a)   *(b)*
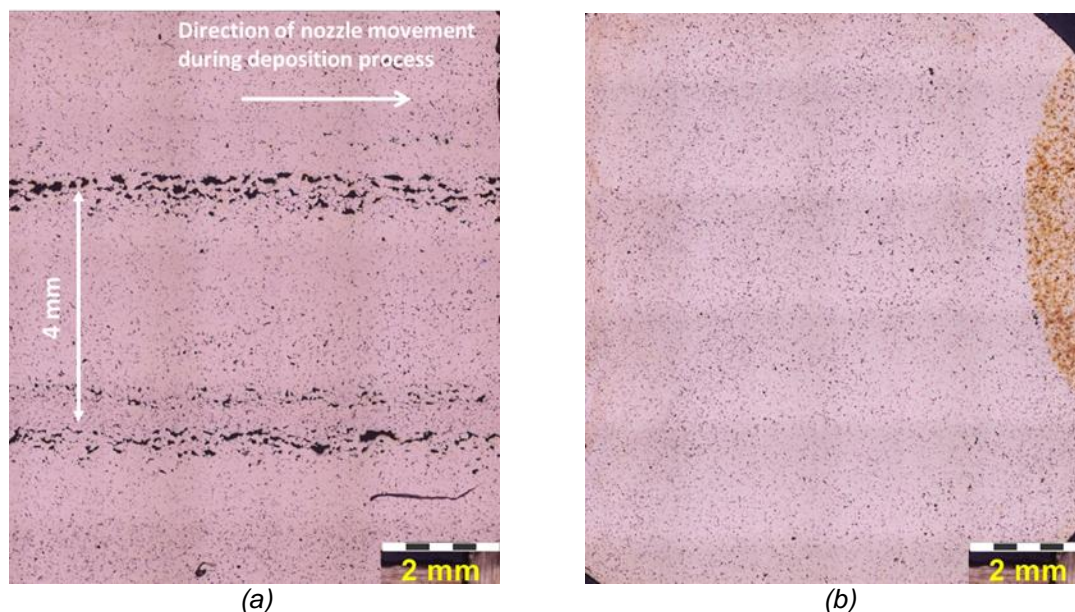
Figure 91. Light optical microscope images of a metallographic cross-section in a plane parallel to the surface of the coating (a) at the top, (b) at the bottom of the coating (composite cold spray coating using slow strategy: deposition speed of 20 mm/s).

At a finer scale, the SEM images of the pure Cu cold spray and Cu+32%Al$_2$O$_3$ composite cold spray in Figure 92 show the different pore morphologies in the coating. In the overlap zones between deposition lines, the size of the pores between the Cu/Cu particles and Cu/Al$_2$O$_3$ particles can reach one hundred micrometers, while between these zones, the coating is significantly denser but with persistent porosity which manifests itself by a lack of cohesion between particles, and/or filling during the plastic deformation of the Cu particles. The pores are nevertheless much smaller. No marked difference distinguishes these three coatings, apart from the fraction of alumina particles in the composite cold spray.

EURAD (Deliverable n° 15.6) - Novel materials and processes for the optimisation of long-term container performance
Dissemination level: Public
Date of issue of this report: 06/05/2024

Page
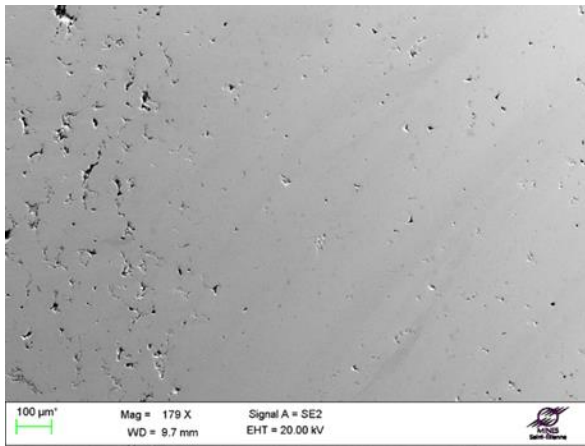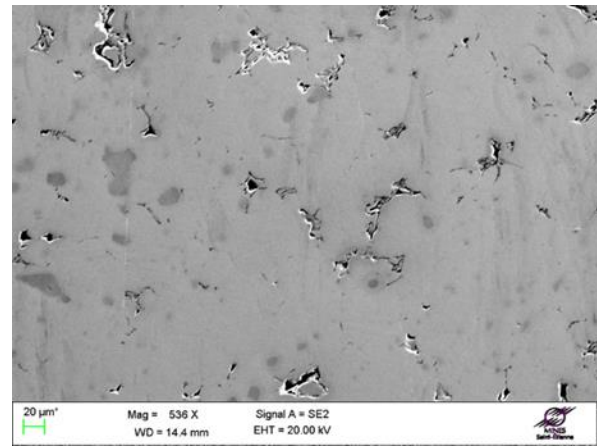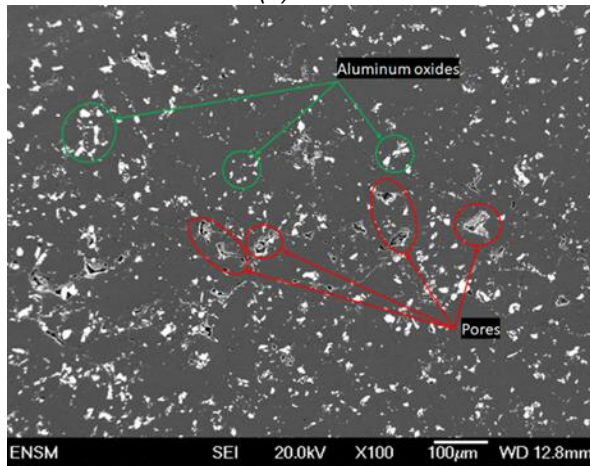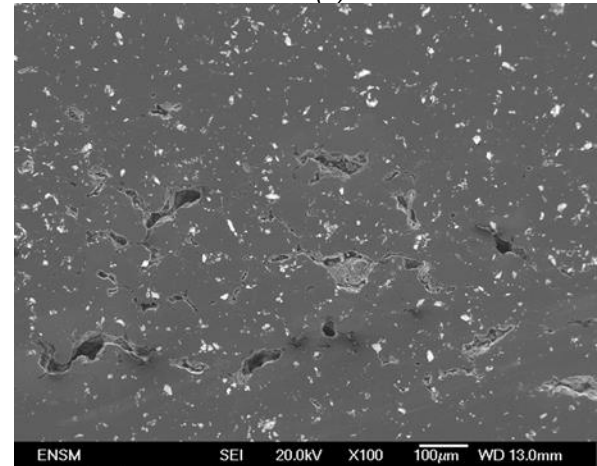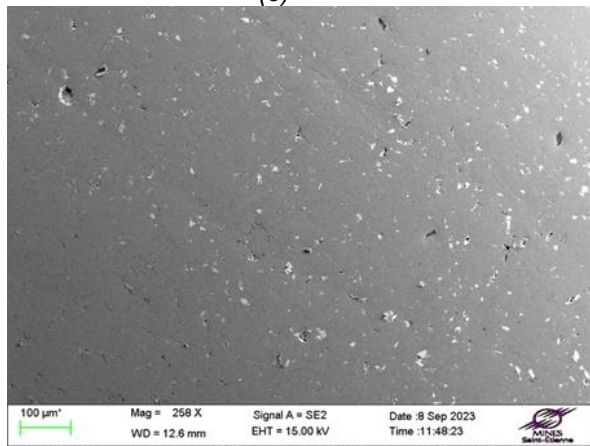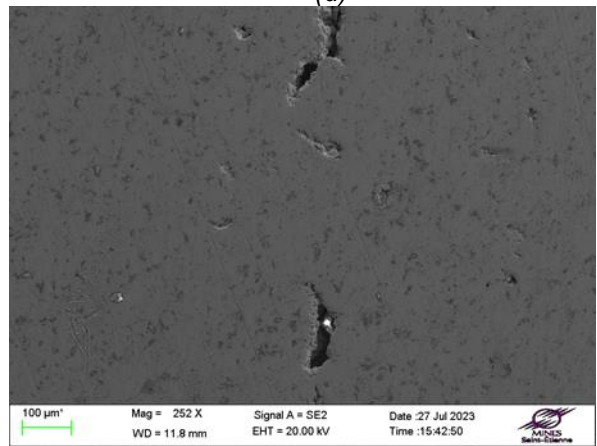
Figure 92. SEM images of metallographic sections. Pure Cu cold spray coating: (a) strings of pores (left side of the image), and intertrack zone of deposition. (b) Zoomed view of the high porosity zone. Composite cold spray coating (slow strategy: deposition speed of 20 mm/s): (c) Alumina particles in white and pores in black. (d) Large pores in the overlap zone between two deposition lines. Composite cold spray coating (fast strategy: deposition speed of 40 mm/s): (e) General view outside the overlap zone. (f) Large pores in the overlap zone between two deposition lines.

However, measuring the pore density by image analysis on a set of images representative of the different zones presents interesting differences. Table 25 gives the measured values for each of the materials. Fraction of alumina particles evaluated with the same method is also reported.

EURAD (Deliverable n° 15.6) - Novel materials and processes for the optimisation of long-term container performance
Dissemination level: Public
Date of issue of this report: 06/05/2024

Page

Table 25. Quantification of the alumina fraction and porosity rate.

Materials	Surface percentage of Al_2O_3 particles	Surface percentage of pores
Pure Cu cold spray coating	-	5.86%
Composite Cu+32vol.%Al₂O₃ (low strategy – 20 mm/s)	4.60%	1.28% (2.47% in the overlap zones)
Composite Cu+32vol.%Al₂O₃ (fast strategy – 40 mm/s)	3.66%	0.98% (3.31% in the overlap zones)
Wrought Cu	-	0

The content of alumina particles is fairly constant at a level of around 4%, which is very low considering 32vol.% in powder mixture. As a first approximation, the rate of particles in the final coating can be directly linked to the quantity of Al_2O_3 projected, but also to the ability of the particles to rebound upon contact with the deposit. This rebound capacity naturally depends on the energy dissipated by the impact with the ductile metallic matrix of copper but also on the anchoring potential associated with the penetration of Al_2O_3 into the matrix or the interaction with a copper particle impacting the coating at the same place and at the same time (Moridi et al., 2014) (Zakaria, 2014) (Hussain et al., 2009).

The porosity remains similar between the two composite cold spray coatings, around 1 to 1.30%. However, it is lower than that of pure Cu cold spray. These results are consistent with those obtained in the literature (Bensaïd, 2024). The increase in the content of ceramic particles generates greater deformation of the particles upon impact and thus allows them to more easily adhere to the surface of the deposit. The anchoring and hammering effect of the Al_2O_3 particles on those of copper plays an important role with respect to porosity.

Figure 93 presents the EBSD microstructural observations in IPF (Inverse Pole Figure) mode conducted on the composite Cu+32vol.%Al₂O₃ and pure Cu cold spray coatings. In both cases, we can observe grain refinement at the interfaces between splats. On the contrary, the core of the splats consists of larger grains. The colour gradient within these grains indicates plastic deformation associated with the impact. The microstructures appear to be more deformed at the interfaces between splats, as evidenced by the difficult indexing (black points) at the interfaces between splats and the much greater colour gradient at the core of deformed powders. Although these analyses remain qualitative, these results show that impact loading induces severe plastic deformation. Regarding the Al_2O_3/Cu interfaces, significant grain refinement is also observed, which is consistent with a mechanism of severe plastic deformation by impact.

Cold spray process can also involve static and dynamic recrystallization mechanisms linked both to the spray temperature if it is high enough and the self-heating of the copper due to severe plastic deformation and a high strain rate, thus facilitating the nucleation of small grains at this location.

EURAD (Deliverable n° 15.6) - Novel materials and processes for the optimisation of long-term container performance
Dissemination level: Public
Date of issue of this report: 06/05/2024

Page
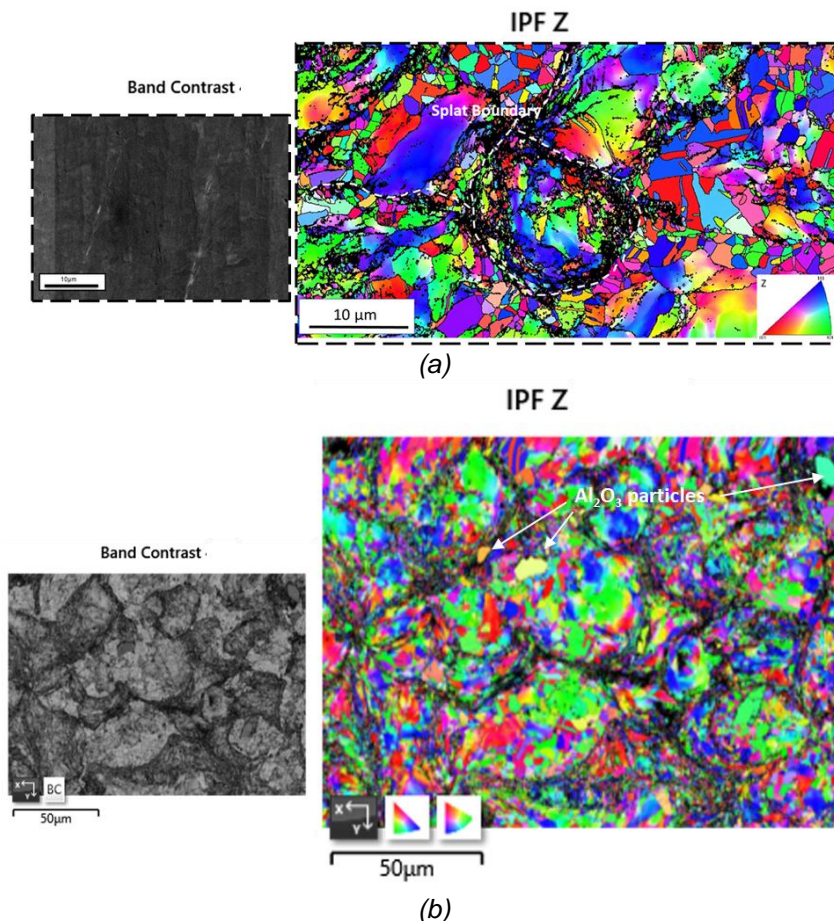
Figure 93. (a) EBSD mapping of pure Cu cold spray coating; (b) EBSD mapping of composite Cu+32vol.%Al₂O₃ cold spray coating (slow strategy).

4.2.5.7. Mechanical properties

The addition of ceramic particles to metal powder is a well-known process to improve deposition efficiency in cold spray process (particle anchoring and adhesion, decreased porosity). Yu et al. (2017) showed in the case of an Al 5056/SiCp coating, that an optimal content favoured the interactions between the aluminium matrix and the harder SiC particles, while beyond that, the interactions occurred rather between the SiC particles and therefore reduce the efficiency of the deposition.

Other authors have shown that the addition of ceramic particles also contributes to increasing the mechanical properties of the coatings, including both yield strength and tensile strength (Bensaïd, 2024) (Kumar et al., 2017).

Figure 94, taken from (Bensaïd, 2024), shows compression curves σ_{true}-ε_{true} of three composite Cu+xvol.%SiC cold spray coatings containing 10vol.%, 20vol.% and 30vol.% of SiC in the initial powder, and corresponding after deposit to respectively 3.00wt.%, 3.46wt.% and 5.49wt.% SiC in the coating. The curves of pure copper specimens (99.99%) wrought and annealed for 1 hour at 500°C are also reported. These results show a strong effect on ceramic particles on yield strength and ultimate tensile strength which can be increased by more than 70 MPa. All the coatings exhibit noticeable hardening, consistent with the behaviour of poorly strain-hardened copper. Compared to annealed copper of the same purity, where the strain hardening rate is significantly higher, or to extruded copper, composite coatings show an intermediate strain hardening rate and an apparent ductility that increases as the ceramic particle content rises.

EURAD (Deliverable n° 15.6) - Novel materials and processes for the optimisation of long-term container performance
Dissemination level: Public
Date of issue of this report: 06/05/2024

Page
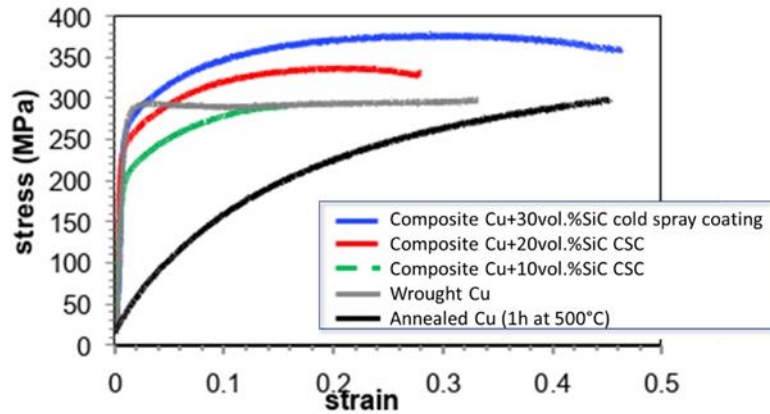
Figure 94. Stress-Strain curves of composite Cu+xvol.%SiC and pure massive Cu wrought and annealed 1h at 500°C (Bensaïd, 2024).

Compression test results from this study are shown in Figure 95. The compression curves of the composite Cu+32vol.%Al$_2$O$_3$ cold spray coatings, fast and slow strategy, are compared to that of pure copper cold spray coating. As expected, mechanical properties are increased with the addition of ceramic particles, however with a reduced ductility compared to the results of (Bensaïd, 2024), if we consider the plastic deformation at UTS. The mechanical properties of the materials studied is summarized in

Table 26.
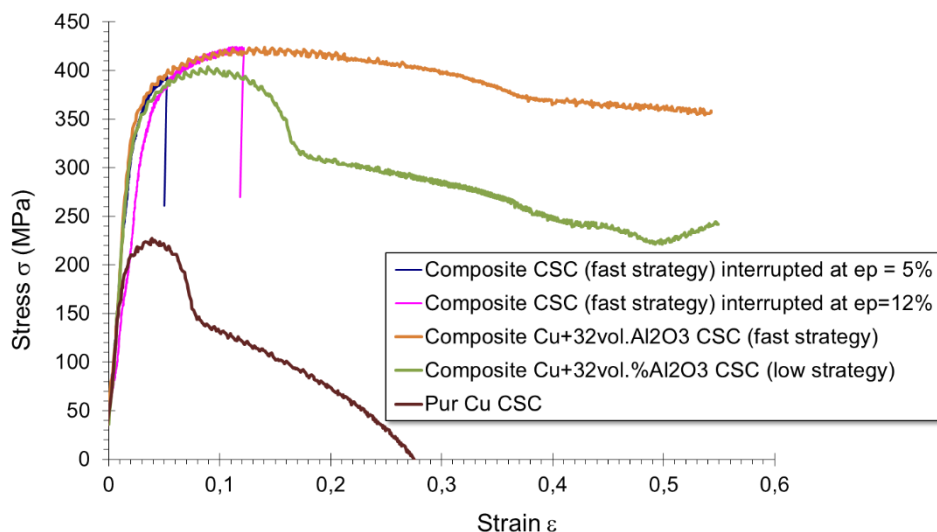
Figure 95. Stress-Strain compression curves of pure Cu cold spray coating and composite Cu+32vol.%Al2O3, fast and low strategy, cold spray coatings. Two tests on composite CSC were interrupted at 5% and 12% of plastic deformation.

EURAD (Deliverable n° 15.6) - Novel materials and processes for the optimisation of long-term container performance
Dissemination level: Public
Date of issue of this report: 06/05/2024

Page

Table 26. Mechanical properties of composite Cu+32vol.%Al$_2$O$_3$ cold spray coatings, pure Cu CSC and wrought and annealed pure Cu.

Materials	Yield strength (MPa)	UTS (MPa)
Pure Cu CSC	180	230
Composite Cu+32vol.%Al$_2$O$_3$ CSC (fast strategy)	330	420
Composite Cu+32vol.%Al$_2$O$_3$ CSC (slow strategy)	320	400
Wrought pure Cu	250	300
Annealed pure Cu (1 hour at 500°C)	25	-

The behaviour of the coatings beyond the UTS reflects damage different from a conventional tensile test on solid material. The presence of porosity leads to early shearing of the specimens in compression via localization of the deformation associated with the decohesion of Al$_2$O$_3$ particles and the presence of pores in the coating. Figure 96 shows a macroscopic view of the specimens from the two tests interrupted at 5% and 12% plastic deformation and the one carried out until rupture, corresponding to the composite CS coatings (fast strategy). One can observe the presence of an already large crack which therefore began before the plastic deformation of 5%. Cracks then progress with deformation, as observed on the specimen interrupted at 12% plastic deformation. The height of 6 mm of specimens including the part of coating which contains the strings of large pores, crack initiation is facilitated.

Analysis of the fracture surface on the broken specimen brought some interesting results (Figure 97), the first being the low Al$_2$O$_3$ content of 1,4% (surface fraction) which suggests that the alumina particles indeed reinforce the coating leading to fracture preferentially in Al$_2$O$_3$ particles poor regions. Copper particle boundaries can also be easily observed indicating that there are weak interfaces in the coating. Moreover, no signs of significant ductile deformation prior to fracture have been noticed.
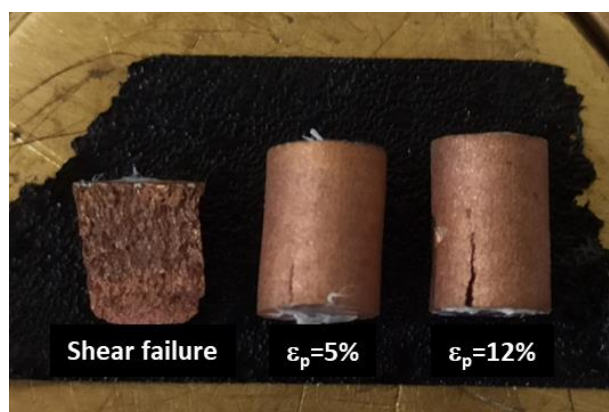
Figure 96. Specimens corresponding to composite Cu+32vol.%Al$_2$O$_3$, fast strategy, in Figure 95. Specimens from left to right: stressed until rupture, up to ep=5% and ep =12%.

EURAD (Deliverable n° 15.6) - Novel materials and processes for the optimisation of long-term container performance
Dissemination level: Public
Date of issue of this report: 06/05/2024

Page
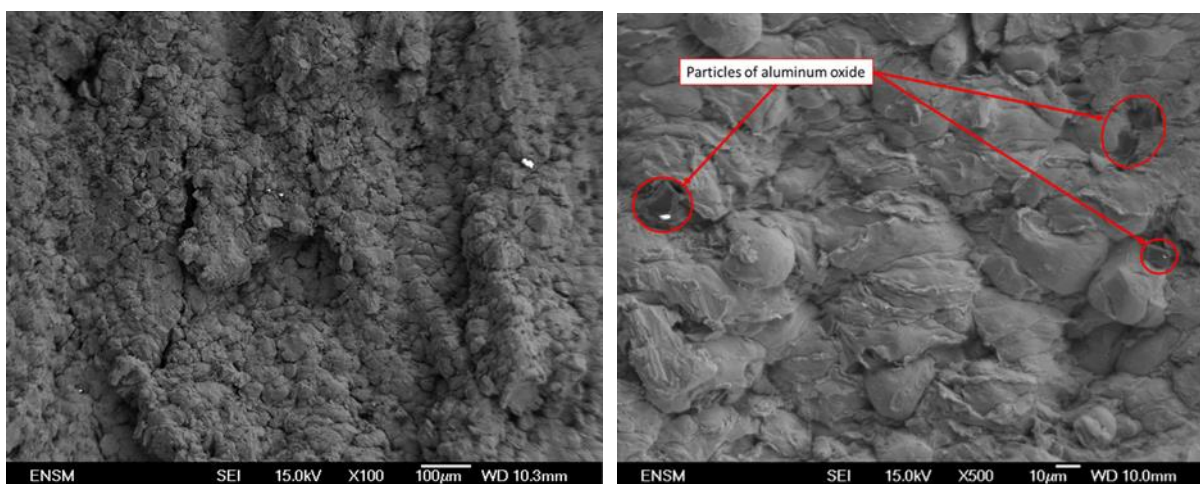
Figure 97. SEM images of the fracture surface on the broken specimen of the composite Cu+32vol.%Al$_2$O$_3$, fast strategy. General view on the left, enlarged view on the right.

4.2.5.8. Electrochemical behaviour

All electrochemical polarization tests were carried out on samples taken from the dense part of the coatings, in the first 3 mm of thickness in the coating from the steel substrate. Figure 98 presents the polarization curves of the materials in synthetic groundwater at 90°C. They show that cold-sprayed coatings, with or without ceramic particles, exhibit the same electrochemical behaviour as wrought solid copper. The corrosion potential values for the four materials are between -300 mV/SCE and -280 mV/SCE, this difference may be due to a slight variation in pH between these experiments, varying from 6.4 to 6.48. Although the currents remain low on the anodic branch at around +50 mV polarization ($i_a <$ 50 µA/cm^2), the shape of the curve clearly shows an active type of behaviour, without a passivity plateau. Beyond these values, a clear increase in the dissolution current is observed. This ultimately corresponds to the environmental conditions verified after testing where a residual oxygen content of approximately 50 ppb was measured, as indicated previously, while the target conditions were anoxic.
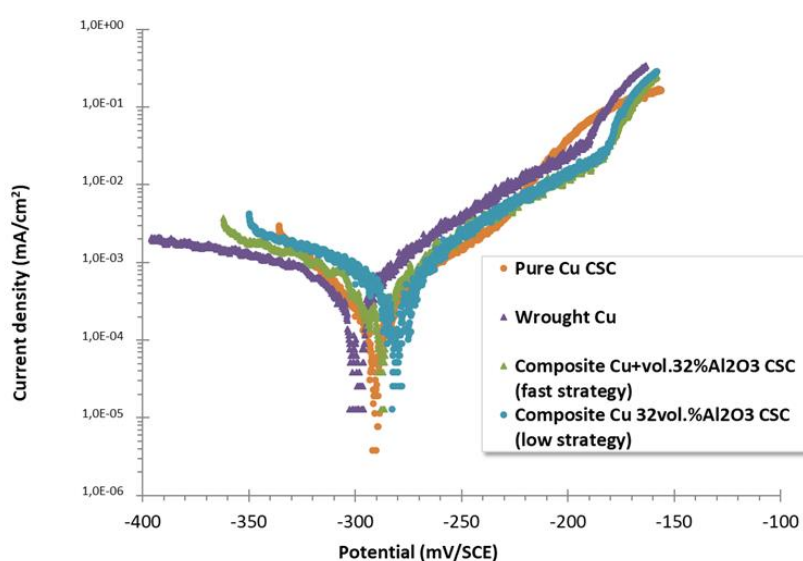
Figure 98. Potentiodynamic polarization curves of pure Cu cold spray coating and composite Cu+32vol.%Al$_2$O$_3$ CSC, low strategy and fast strategy, and pure wrought Cu in synthetic groundwater at 90°C and about 50 ppb dissolved O$_2$ content.

For purposes of comparison between materials, the Tafel method was applied to determine corrosion rates. Table 27 reports the calculated values. No noticeable difference is observed between the four materials. Corrosion rates are of the order of magnitude of 10 µm per year. Pure wrought copper appears to show slightly higher polarization resistance than cold spray coatings.

Table 27. Corrosion characteristics of pure Cu CSC, composite Cu+32vol.%Al$_2$O$_3$ CSC and wrought pure copper in synthetic groundwater at 90°C, 50 ppb O$_2$.

Material	Ecorr (mV/SCE)	Icorr (µA/cm^2	Rp (k Ω.cm^2)	Corrosion rate (µm/y)
Wrought Cu	-300	0.70	22.1	12.8
Pure Cu CSC	-290	0.69	15.6	12.7
Composite Cu+32vol.%Al$_2$O$_3$ CSC (low strategy)	-280	0.65	17.5	12.1
Composite Cu+32vol.%Al$_2$O$_3$ CSC (fast strategy)	-288	0.76	18.7	14.0

4.2.5.9. Long-term corrosion resistance

Long-term corrosion resistance has been assessed with immersion tests of materials for a maximum duration of six months. Composite Cu+32vol.%Al$_2$O$_3$ slow and fast strategy cold spray coatings (nozzle speed of respectively 20 mm/s and 40 mm/s), pure Cu CSC, and wrought Cu were tested in synthetic groundwater at 90°C and 50-100 ppb dissolved O$_2$. Table 28 shows optical images of some specimens after different durations of immersion. At this scale, one observes characteristic surfaces of uniform corrosion for all the materials with some mineral deposits, particularly for the longest durations of six months. The effects of corrosion on cold spray deposit samples reveal successive lines induced by the deposition process.

Table 28. Optical images of samples after long-term corrosion tests in synthetic groundwater at 90°C.

Materials (nozzle speed)	Cu-32%Al$_2$O$_3$ (20 mm/s)	Cu-32%Al$_2$O$_3$ (40 mm/s)	Cu-32%Al$_2$O$_3$ (40 mm/s)	Cu-32%Al$_2$O$_3$ (20 mm/s)
Sample images after corrosion tests				
	Sample #1	Sample #2	Sample #3	Sample #2
Immersion time	53 days	87 days	107 days	110 days

Materials (nozzle speed)	Wrought Cu	Wrought Cu	Pure Cu CSC (20 mm/s)	Pure Cu CSC (20 mm/s)
Sample images after corrosion tests				
	Sample #2	Sample #3	Sample #2	Sample #3
Immersion time	120 days	180 days	120 days	180 days

EURAD (Deliverable n° 15.6) - Novel materials and processes for the optimisation of long-term container performance
Dissemination level: Public
Date of issue of this report: 06/05/2024

Page

At higher magnification, Figure 99 shows SEM images of the surfaces. The composite CSC surfaces shown in Figure 99a and Figure 99b for different exposure durations in groundwater exhibit at this scale again uniform corrosion. The inter-particle boundaries do not appear to be more susceptible to corrosion insofar as no more pronounced corrosion mark is discernible in these zones. Likewise, areas with strings of porosities do not indicate any localized corrosion within the cavities.
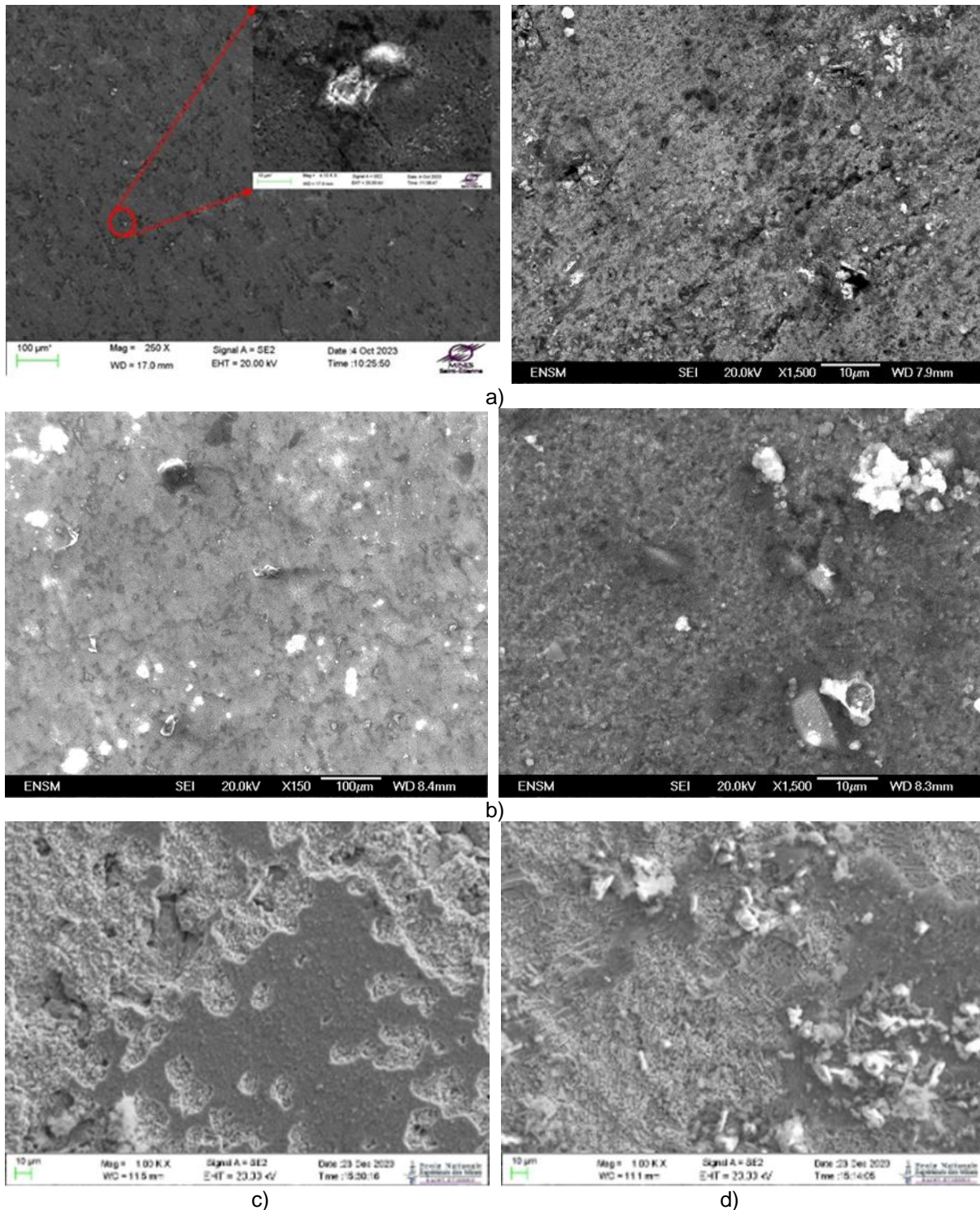
Figure 99. SEM images of a) Composite Cu-32vol.%Al_2O_3 CSC after 53 immersion days (left: general view with magnification on mineral scale, right: inter-particles boundaries); b) Composite Cu-32vol.%Al_2O_3 CSC after 87 immersion days corresponding respectively to speed deposition of 20 (left

EURAD (Deliverable n° 15.6) - Novel materials and processes for the optimisation of long-term container performance
Dissemination level: Public
Date of issue of this report: 06/05/2024

Page

side) and 40 mm/s (right side); c) Pure Cu CSC after 120 immersion days, and d) wrought Cu after 120 immersion days.

EDS surface analysis of the sample reported in Figure 100 shows the presence of very fragmentary mineral deposits and corrosion products including chlorides and sulphates, if one refers to the chemical elements identified. As indicated in (Tournassat, 2017), where the results of thermodynamic equilibrium calculations with PHREEQ between species in this solution give a theoretical saturation index of calcite equal to 0 and that of gibbsite equal to 0.69, the measured salt concentration values may be slightly lower and lead to undersaturation of the calcite. Ultimately, we do not observe any covering of the surface of the samples by a scale deposit, but simply scattered islands that could correspond to gypsum.
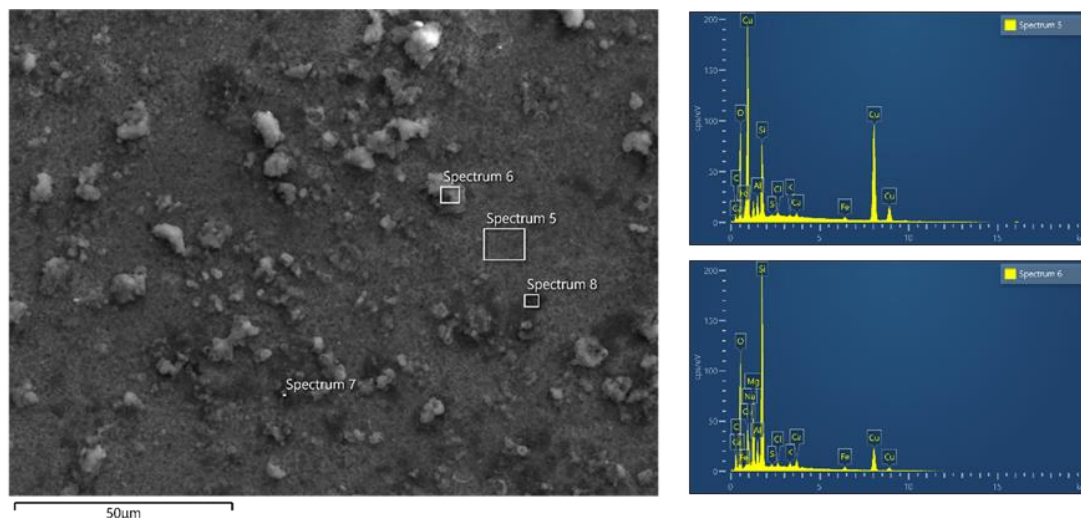
Figure 100. EDS analysis of the surface of composite Cu+32vol.%Al_2O_3 cold spray coating after 107 days in synthetic groundwater at 90°C.

XRD analysis of composite cold spray coating surfaces after cleaning in the ultrasonic bath only reveals the presence of an adherent Cu_2O oxide after immersion tests, as shown in Figure 101 for composite cold spray coating fast strategy. The nature of other corrosion products and possible mineral scaling observed on the surface of the samples just after immersion tests could not be identified by the analysis.

These results are confirmed with Raman analysis on composite cold spray coatings after 110 days of immersion in synthetic groundwater. Raman spectra shown in Figure 102 indicates several peak corresponding to both CuO, Cu_2O, and $CaSO_4$ (gypsum).

EURAD (Deliverable n° 15.6) - Novel materials and processes for the optimisation of long-term container performance
Dissemination level: Public
Date of issue of this report: 06/05/2024

Page
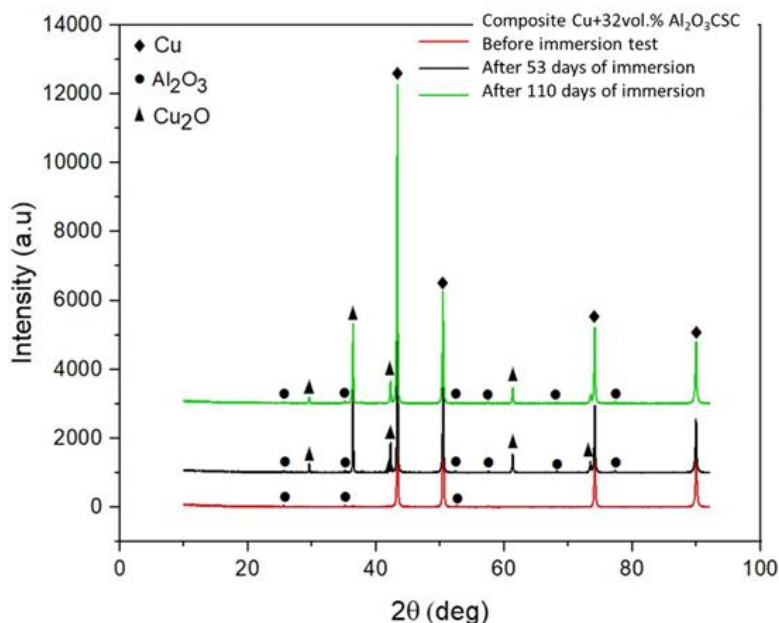
Figure 101. XRD analysis of composite Cu+32vol.%Al$_2$O$_3$ cold spray coating (fast strategy) surface after 0, 53 and 107 days of immersion in synthetic groundwater.
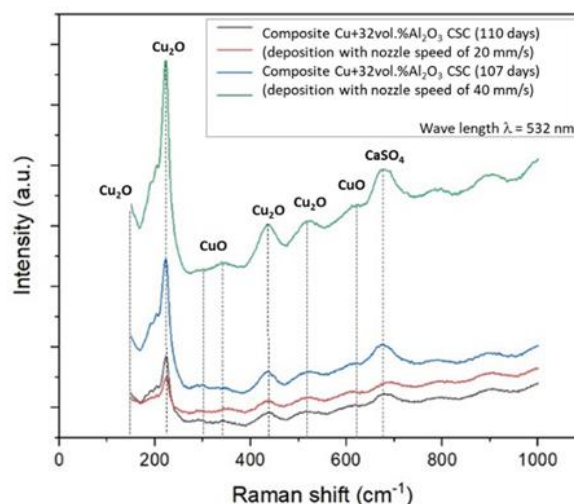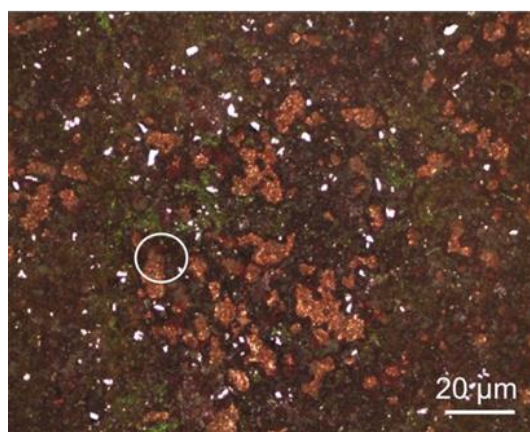
(a) (b)

Figure 102. a) Optical image of composite Cu+32vol.%Al$_2$O$_3$ (low strategy) after 110 days of immersion in groundwater (the white circle corresponds to the Raman analysis zone on the spectrum on right side). b) Raman spectra of composite cold spray coatings.

Figure 103 presents the mass losses of materials vs. time measured at the end of the long-term immersion tests. All the measurements seem to follow the same progression between the wrought pure copper and the cold spray coatings, both pure Cu CSC and composite Cu+32vol.%Al$_2$O$_3$. The measurements concerning composite cold spray coatings present a relatively large dispersion, the two highest points corresponding to the "fast strategy" one. The cause is not clearly identified, but it could come from the preparation of the samples during the final weighing at the time of cleaning in the ultrasonic bath, where some particles could have become detached.

EURAD (Deliverable n° 15.6) - Novel materials and processes for the optimisation of long-term container performance
Dissemination level: Public
Date of issue of this report: 06/05/2024

Page
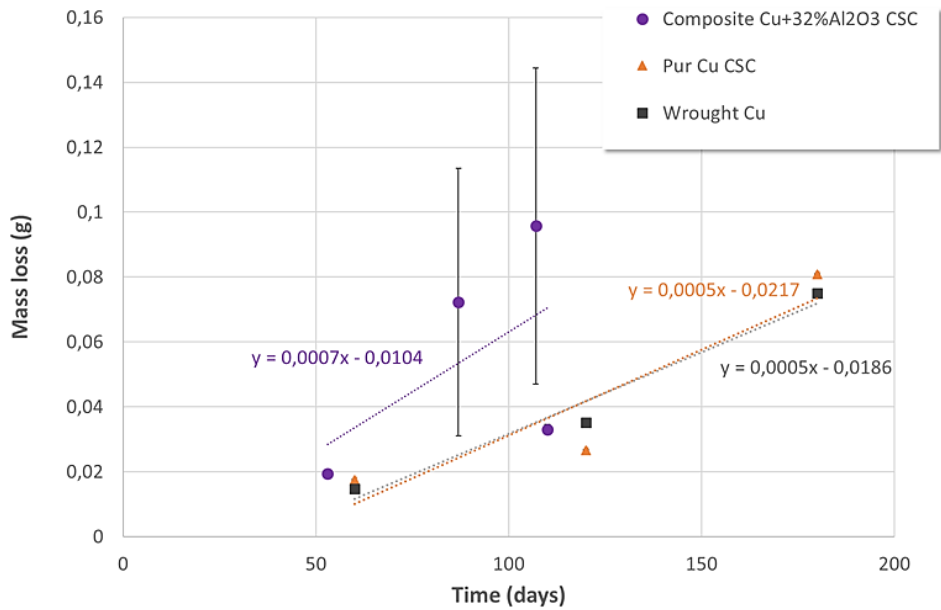
Figure 103. Corrosion mass loss in synthetic groundwater at 90°C vs time.

The corrosion rates calculated according to the expression given in paragraph §4.2.5.5 are reported in Table 29. These results show that the corrosion rates are of the same order of magnitude for all materials, from 13 µm/y to 47 µm/y. As we observed during the weigh-ins, the fast strategy composite CSC coating presents a higher corrosion rate, approximately more than twice, contrary to what is expected. These results are consistent with the corrosion rates determined via potentiodynamic polarization curves.

Table 29. Corrosion rates vs. Immersion time in synthetic groundwater at 90°C and 50-100 ppb dissolved O_2.

Materials	2 months (53-60 days)	3-4 months (87-120 days)	6 months (180 days)
Wrought Cu	14 µm/y	16 µm/y	23 µm/y
Pure Cu CSC	17 µm/y	13 µm/y	26 µm/y
Composite Cu+32vol.%Al203 CSC (low strategy)	21 µm/y	17 µm/y	-
Composite Cu+32vol.%Al203 CSC (fast strategy)	-	47 µm/y	-

4.2.5.10.   Creep behaviour

Creep tests were conducted on composite Cu+32vol.%Al_2O_3 (fast strategy) cold spray coating only insofar as it exhibits the best mechanical strength and ductility during compression tests. Nevertheless, its low tensile mechanical strength prevented the creep tests in the tensile direction on the originally intended 4x4 mm section specimens, due to the presence of highly detrimental porosity clusters. Therefore, creep tests were conducted in laboratory air on the same specimens as the compression tests, i.e., cylindrical specimens with a height of 6 mm and a diameter of 4 mm.

Figure 104 shows the creep curves conducted at three different constant stresses: 350 MPa, 300 MPa, and 260 MPa, corresponding to 106%YS, 90%YS, and 80%YS respectively (YS=330 MPa). For the two highest stresses, all three stages of creep, primary, secondary, and tertiary, are observed, with these two tests leading to coating failure in 25 minutes and 70 minutes for 350 MPa and 300 MPa respectively. The corresponding creep rates are 4.8 10^{-5} s^{-1} and 7.8 10^{-6} s^{-1}.

These results are consistent with numerous authors in the literature, where a natural decrease in creep rate with applied stress is observed (Paoletti et al., 2022) (Henderson et al., 1998) (Jenkins et al., 1950). However, the measured rates here are still lower than those obtained for annealed pure OFHC copper. Furthermore, studies on the effect of pre-strain on copper before creep testing show that the creep rate tends to decrease (Jenkins W.D., 1950). This suggests that the strain-hardened state resulting from the cold spraying of coatings enhances resistance to creep. The general trend is for the degree of plastic deformation and creep rate in the second steady-stage to decrease as the rate of loading and history strain was increased.
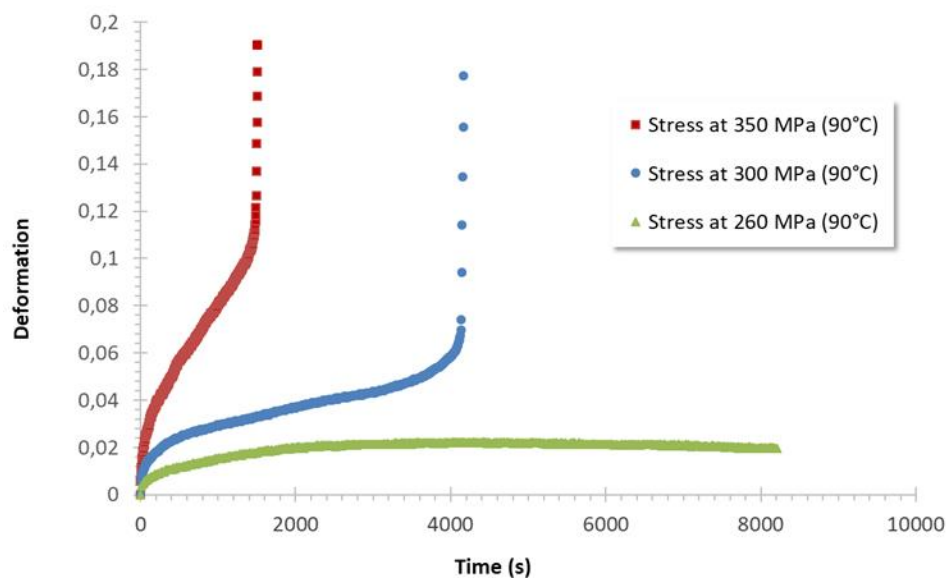
Figure 104. Creep curves of the composite Cu+32vol.%Al₂O₃ cold spray coating at 90°C in air.

4.2.5.11. Conclusions

The study of Cu+32vol.%Al₂O₃ composite coatings deposited by the cold spray process focused on the microstructure of the deposits, their mechanical properties, corrosion resistance, and creep resistance. Microstructure analysis, for a given set of process parameters (gas temperature of 500°C, nitrogen gas nature, spray distance of 40 mm, gas pressure of 35 bar, deposition line spacing of 4 mm), and two deposition speeds (20 mm/s and 40 mm/s named low and fast strategy) investigated, showed little effect of this speed on porosity. A low porosity is observed within the deposition lines while the overlap zones of the deposition lines exhibit significantly higher porosity, ranging from 2.47% to 3.31%. The EBSD analysis revealed a gradient of plastic deformation within the copper particles between the peripheral zones and the core of the particles. This results from both an increased effect of hammering by the ceramic particles and the phenomenon of recrystallization of the copper matrix. However, no crystallographic deformation texture is induced by this process

Mechanical properties evaluated under uniaxial compression show a behaviour similar to that of wrought copper, with a yield strength close to approximately 320-330 MPa. Nevertheless, the apparent strain hardening rate is significantly lower, and the maximum strength exhibits dispersion among the different tests conducted. This result arises from the presence of porosities, which tend to close during compression and contribute to reducing the strain hardening rate. Damage to the deposits beyond the ultimate tensile strength results in the fracture of specimens along zones of high porosity density, namely, the overlap of deposition lines. Ultimately, these defects govern the mechanical strength of the deposits beyond a loading exceeding the yield stress.

The electrochemical behaviour characterized in synthetic groundwater at 90°C representative of Bure in France, through dynamic polarization tests, shows no significant difference between tests on wrought

EURAD (Deliverable n° 15.6) - Novel materials and processes for the optimisation of long-term container performance
Dissemination level: Public
Date of issue of this report: 06/05/2024

Page

copper and composite cold spray coatings. The corrosion rates extracted from the curves using the Tafel method are in the range of 12 to 14 µm/year. However, these corrosion rates are relatively high compared to those expected in anoxic environments for copper. The anodic branches of the polarization curves indicate that the materials are in an active state.

The corrosion rate measurements by mass loss during immersion tests under these same test conditions for a maximum duration of 6 months show values in the range of 10 to 50 µm/year. Examination of the sample surfaces by X-ray diffraction and Raman analysis mainly reveals the predominant presence of copper oxide Cu_2O, along with some islands of gypsum $CaSO_4$.

The creep tests at 90°C intended for tensile loading could not be conducted due to very low mechanical strength in this mode of loading. Failure occurs rapidly by decohesion along the strings of porosities in the overlap zones of deposition lines. Consequently, these tests were carried out in compression under air at 90°C. The creep behaviour was characterized for three stress levels: 85%, 100%, and 115% of the yield strength. For the two highest loadings, the three phases of primary creep, steady-state creep, followed by final rupture, are observed. The steady-state creep rate is greater with higher stress levels. Creep at 85%YS shows, after the primary creep phase, a stable level of deformation as long as the deformation does not exceed 4% plastic strain.

No test in a corrosive environment could be conducted under compression to study the effect of dissolution on these creep rates. A specific setup needs to be developed.

EURAD (Deliverable n° 15.6) - Novel materials and processes for the optimisation of long-term container performance
Dissemination level: Public
Date of issue of this report: 06/05/2024

Page

5. Conclusions and future outlook

The ambition of Task 2 of ConCorD was to explore the potential of novel materials and processes for the optimisation of long-term container performance. For the most promising novel materials, experimental studies were designed to contribute to the understanding of their long-term corrosion/degradation behaviour.

The work within this task was organised according to the two main types of materials which are ceramic and metallic. In the case of ceramic materials, the experimental work was focused on studying materials and processes (deposition, sealing) for innovative solutions of bulk ceramic containers and ceramic coatings. For containers made of bulk ceramics, the key properties for long-term performance are fracture toughness and leaching/alteration. For thin (ceramic or metallic) coatings, a primary concern is the presence of porosity or flaws. For bulk metallic materials, the main aim of the experimental work was to study and consider the implementation of innovative solutions for metallic anti-corrosion coatings or optimised bulk metallic options. Studies focused on material development (alloy composition, coating technology) and initial corrosion tests to identify the benefit of these new solutions. The main objectives of Task 2 have been fulfilled and the main project achievements can be summarized as follows:

- New alumina-base (core-shell) materials were developed for the sealing of bulk ceramic (alumina) containers by means of microwave heating. The main result was the never-before achieved improvement in microwave coupling, enabling rapid heating. This should limit the increase in temperature at the inner side of the container during the sealing process in real conditions. The new sealing formulations also satisfy the required mechanical and leaching resistance specifications.

- The optimal parameters for the sintering of high-density silicon carbide were determined. Silicon carbide showed good mechanical and corrosion resistance properties for its potential use as bulk ceramic containers. In particular, the addition of 0.3% Cr in the material formulation was found to further improve the corrosion resistance of silicon carbide, under the tested conditions.

- Experiments conducted in anoxic ammonia-containing simulated groundwater provided valuable insights into the corrosion behavior of oxygen-free phosphorus-doped copper (OFE+P) and high conductivity phosphorus-doped copper (HCP) as container materials. The study revealed their electrochemical properties, corrosion rate, hydrogen uptake, and stress corrosion cracking (SCC) tendencies in U-bends under different potentials. Defects observed in the copper specimens were blunt and covered with oxide and require further investigation into their formation mechanism. Despite this, HCP copper showed comparable performance to OFE+P in ammonia-containing groundwater. Although these results are promising, additional considerations, particularly regarding creep and hardness properties, in addition to different SCC-promoting agents, are required before HCP can be considered a viable alternative material for canisters.

- Several ceramic (CrN and TiO_2) and metallic (Ti, Cu, and Cr) coatings were produced by means of cathodic arc evaporation with thicknesses up to 30 µm. Among the ceramic coatings, CrN showed the best result in terms of corrosion resistance, with minimal weight loss and no pitting on the surface. Among the metallic coatings, Ti and Cu coatings showed the best corrosion performances under the tested conditions, with minimal weight change throughout the test period, indicating high corrosion resistance, even though some traces of pitting or rusting were observed on the surface of the Ti coating after 3000 hours of testing.

- The study of a novel Cu + 32vol.% Al_2O_3 composite coatings deposited by the cold spray process focused on the microstructure of the deposits, their mechanical properties, corrosion resistance, and creep resistance. Mechanical properties evaluated under uniaxial compression show a behaviour similar to that of cold-worked solid copper. The electrochemical behaviour of this coating, studied at 90°C in a synthetic, quite corrosive medium, shows no significant difference between tests on solid copper and composite cold spray deposits.

EURAD (Deliverable n° 15.6) - Novel materials and processes for the optimisation of long-term container performance
Dissemination level: Public
Date of issue of this report: 06/05/2024

Page

Beyond the above-listed impactful results, a few additional benefits of the ConCorD Task 2 are worth mentioning. First, ConCorD has brought several partners together, and there is now a solid base for future collaborative work. Second, the partners involved in the Task developed skills, and improved processes and methods in a field that was not dealt with since a few decades (particularly the topic of ceramic materials for the disposal of HLW). Third, several technical solutions have been tested, and the most relevant ones start to be identified for further R&D work. The EURAD-2 InCoManD WP will definitely capitalize on all of those benefits. Many challenges must be tackled in the future regarding the development of novel materials for containers. These include the elaboration of thick, bulk ceramic materials, the sealing of large ceramic parts, the deposition of adherent, porous-free and corrosion-resistant coatings, to name the most important ones. In future research, the different materials considered within Task 2 of ConCorD will need to be further improved and qualified. Particular attention should be paid to the improvement and (mechanical) qualification of bulk metallic and ceramic materials (e.g., Cu, SiC and Al_2O_3) including the *ad hoc* material supply for the sealing. The ceramic and metallic coatings considered should be further qualified, especially in terms of adherence and porosity level. Comparative corrosion resistance of single and multi-layer PVD (metallic and/or ceramic) coatings could be performed.

New silico-aluminate materials containing a low weight fraction of nano-SiC (a few %) were developed for sealing bulk ceramic (alumina) containers by microwave heating. This should also limit the increase in temperature at the inner side of the container during the sealing process in real conditions. However, the mechanism for this enhanced coupling efficiency is still under debate. The intrinsic nature of SiC is likely one good reason for that, but it is not the only one. We suspect that the coupling efficiency is further enhanced by the pinning of the electromagnetic field on the nanoparticles. Future studies will then focus on generalising this strategy to other formulations while introducing at the nanoscale low amounts of a strong coupling material into the formulation of a less coupling material. Indeed, even if nano-SiC is extremely efficient in terms of microwave coupling, its oxidation during the sealing process is detrimental to reach the specifications in terms of mechanical properties and leaching resistance. Additional work on the formulation of the sealing material, targeting a fully oxide formulation, will then be necessary for the future exploitation of the know-how acquired in ConCorD.

Regarding sealing tests of ceramics, results show the importance of limiting thermal gradients during the process to avoid fracture of the ceramics by using thermal insulators. Despite that, a direct coupling of the sealing material has been achieved, tests on ceramic - sealing material - ceramic assemblies revealed the importance of materials inside the oven. Heating selectivity is shown, and the ceramic formulation has to be considered for coupling initiation and successful sealing. For pure alumina ceramic, which is a low coupling material, coupling with the sealing material does not initiate in assembly configuration. For a better understanding of the process, future works need to focus on the modelling of the process in order to understand the heating selectivity and to design future experiments. It would require a systematic determination of the permittivity of materials exposed to microwaves in function the temperature.

In ConCorD Task 2, no work dealt with the fabrication of thick, bulk alumina-base ceramic parts. Yet, in addition to SiC, those materials remain relevant (first of all for economical reasons), and R&D activities focusing on this main challenge should be carried out. Probably the best option would be pure alumina to be used for its potential high mechanical strength and chemical resistance.

Future work on alternative bulk copper grades should focus on determining the thresholds for stress corrosion cracking (SCC) of different copper alloys that can be considered advanced canister materials. These thresholds are related either to the chemical environment, mechanical loading, or material state of the final disposal canister. A clarified set of conditions for canister materials under repository conditions can be experimentally verified at VTT facilities to better understand the mechanisms of defect formation. For this purpose, an autoclave exposure to ammonia or other SCC promoting agents (e.g., sulfides) in groundwater with varying pHs (e.g., 10 to 12) and temperatures (up to 95 °C) is suggested as a follow-up of ConCorD. In addition, efforts will be made to better understand threshold stress and

EURAD (Deliverable n° 15.6) - Novel materials and processes for the optimisation of long-term container performance
Dissemination level: Public
Date of issue of this report: 06/05/2024

Page

the effect of hardness in different environmental conditions, especially on creep. The work is expected to provide an important set of data for optimizing the canister material selection.

VTT plans to use both existing and newly developed testing and characterization methods to determine the aspects that influence SCC in copper. Among these, a recently installed Xe plasma-focused ion beam (PFIB) allows precise sample preparation and state-of-the-art analyses, such as 3D tomography and 3D-Electron Backscatter Diffraction (EBSD). Additionally, the forthcoming Kelvin probe force microscopy (KPFM) and the Time-of-Flight Secondary Ion Mass Spectrometry (ToF-SIMS) will provide powerful tools to scan surface features, create potential maps and provide elemental analyses beyond the current capabilities.

The main goal on metallic and ceramic coatings during the ConCorD project was the qualification and improvement of previously selected innovative materials, as well as the development of methods for their manufacture to prevent or protect the container from corrosion and guarantee sufficient resistance to mechanical damage during handling. Future research can be carried out in two directions, focusing on bulk SiC material and on corrosion protective coatings:

(i) Improvement and (mechanical and corrosion) qualification of the bulk ceramic materials, e.g., pure and Cr doped SiC, and development of joining process for SiC-based ceramic parts by brazing with complex metallic and ceramic fillers;

(ii) Further development and technological advancement of coating deposition techniques (PVD) selection and qualification (adhesion, porosity, corrosion resistance) of a few relevant coating materials, including metallic, ceramic and composites of those such as CrN/CrON, Ti/TiO$_2$, Ti/Cu and associated potential multilayers.

The study on alumina copper cold spray coatings has shown that the addition of alumina particles improves both the adhesion of the deposit, its density and its mechanical properties, without altering its corrosion behaviour. The quality of the deposit can be influenced by numerous parameters of the cold spraying process. Those chosen in this study were based on laboratory experience, only the deposition speed having been studied. However, we have seen that a different nozzle scanning strategy could further improve the deposits, and in particular eliminate the formation of pore strings and thus obtain better mechanical properties in traction. Future research can be carried out on post-deposition heat treatments which can also improve the mechanical and microstructural properties. Indeed, annealing can significantly improve the cohesive forces between metal particles and increase the ductility of the coating due to the activation of restoration and recrystallization phenomena.

EURAD (Deliverable n° 15.6) - Novel materials and processes for the optimisation of long-term container performance
Dissemination level: Public
Date of issue of this report: 06/05/2024

Page

References

Ahmad, Z. (2006). Principles of Corrosion Engineering and Corrosion Control. Butterworth-Heinemann, p. 672.

Aksenov, A.A., Andreev, A.A., Belous, V.A., Strel'nitskij, V.E., Khoroshikh. V.M. (2012). Vacuum arc: plasma sources, deposition of coatings, surface modification. Kiev: "Naukova Dumka", 727 p. (in Ukrainian).

Anders, A. (2008). Cathodic Arcs: From Fractal Spots to Energetic Condensation. New York: Springer Inc., 540 p.

Anders, A. (2010). A structure zone diagram including plasma-based deposition and ion etching. Thin Solid Films, 518, p. 4087–4090.

Anttila, P., Ahokas, H., Front, K., Hinkkanen, H., Johansson, E., Paulamäki, S., Riekkola, R., Saari, J., Saksa, P., Snellman, M., Wikström, L., Öhberg, A. (1999a). Final disposal of spent nuclear fuel in Finnish bedrock – Hästholmen site report. POSIVA 99-08.

Anttila, P., Ahokas, H., Front, K., Hinkkanen, H., Johansson, E., Paulamäki, S., Riekkola, R., Saari, J., Saksa, P., Snellman, M., Wikström, L., Öhberg, A. (1999b). Final disposal of spent nuclear fuel in Finnish bedrock – Olkiluoto site report. POSIVA 99-10.

ASTM G31-72 (2004). Standard Practice for Laboratory Immersion Corrosion Testing of Metals, Annual Book of ASTM Standards, American Society for Testing and Materials.

Baeraky, T.A. (2002). Microwave measurements of the dielectric properties of silicon carbide at high temperature. Egypt. J. Solid. 25, 263-273.

Balaji, S., Mutharasu, D., Sankara Subramanian, N., Ramanathan, K., (2009). A review on microwave synthesis of electrode materials for lithium-ion batteries. Ionics, 15(6), pp. 765-777. doi: 10.1007/s11581-009-0350-4.

Bamoulid, L., Maurette, M.M., Caro, D.D., Guenbour, A., Bachir, A.B., Aries, L., Hajjaji, S.E., Benoît-Marquié, F., Ansart, F. (2008). An efficient protection of stainless steel against corrosion: Combination of a conversion layer and titanium dioxide deposit. Surface & Coatings Technology, 202, 5020-5026.

Baroux, C. (2013). Summary report of the preliminary feasibility study for ceramic HLW overpacks (2007-2012). Andra CG.NT.ASCM.13.0004.

Beck, J.S., Vartuli, J.C., Roth, W.J., Leonowicz, M.E., Kresge, C.T., Schmitt, K.D., Chu, C.T., Olson, D.H., Sheppard, E.W., Mccullen, S.B., Higgins, J.B., Schlenker, J.L. (1992). A new family of mesoporous molecular sieves prepared with liquid crystal templates. Journal of the American Chemical Society, 114, 10834-10843. doi: 10.1021/ja00053a020.

Becker, R., Forsström, A., Yagodzinskyy, Y., Hänninen, H., Heikkilä, M. Sulphide-induced stress corrosion cracking and hydrogen absorption in copper exposed to sulphide and chloride containing deoxygenated water at 90°C (2020). Swedish Radiation Safety Authority.

Belous, V.A., Khoroshikh, V.M., Nosov, G.I., Leonov, S.A., Komar, A.A., Ovcharenko, V.D., Kuprin, A.S., Reshetnyak, E.N., Kholomeev, M.G., Radchenko, V.A., Dedukh, N.V., Malishkina, S.V., Leont'eva, F.S., Nikol'chenko, O.A., Samoylova, K.M. (2013). Development of Ion-Plasma Technology of Deposition of the Nanostructure Bactericidal Coatings on Orthopaedic Implants and Fixative Devices. Production of Pilot Samples for Verification of their Use in Clinic. Nauka ta Innovacii, 9, 46-60. doi.org/10.15407/scin9.06.046.

Belous, V.A., Lunyov, V.M., Kuprin, A.S., Bortnitskaya, M.A., (2018). Structure and properties of TiOx and TiNxOy coatings formed in vacuum arc plasma fluxes. Problems of Atomic Science and Technology, 118, pp. 297-299.

EURAD (Deliverable n° 15.6) - Novel materials and processes for the optimisation of long-term container performance
Dissemination level: Public
Date of issue of this report: 06/05/2024

Page

Bensaïd, Z. (2024). Thesis under preparation: Durability of composite Cold Spray Coatings for nuclear waste storage, EMSE, within the framework of Ed Sis 488 and Mines Saint-Etienne.

Binner, J., Vaidhyanathan, B., Wang, J., Price, D., Reading, M., (2007). Evidence for Non-Thermal Microwave Effects Using Single and Multimode Hybrid Conventional/Microwave Systems. Journal of Microw. Power Electromagn. Energy, 42, p. 4763.

Bijalwan, P.K., Pathak, A.S., Bhagat, A.N., Dan, A. (2022). A review on physical vapor deposition-based metallic coatings on steel as an alternative to conventional galvanized coatings. Journal of Coatings Technology Research, 19(2), p. 403–438.

Bovda, O.M., Bovda, V.O., Chen, C.H., Garkusha, I.E., Leonov, S.O., Onischenko, L.V., Tereshin, V.I., Tortika, O.S. (2008). PVD Ti coatings on Sm-Co magnets. Problems of Atomic Science and Technology, 2008, (17), Issue 1, p. 189–191.

Brachet, J.C., Saux, M.L., Flem, M.L., Urvoy, S., Rouesne, E., Guilbert, T., Cobac, C., Lahogue, F., Rousselot, J.L., Tupin, M., Billaud, P., Hossepied, C., Monsifrot, E. (2022). On-going studies at CEA on chromium coated zirconium based nuclear fuel claddings for enhanced accident tolerant LWRS fuel. In Proceedings of the Top Fuel, Zurich, Switzerland, 13–19 September 2015, pp. 13-19.

Brossard, J.M., Prigent, P., Poirier, J., (2013). High temperature corrosion of oxide bonded silicon carbide refractory lining in WtE facilities. Journal of the European Ceramic Society, 33(11), pp. 2065-2072. https://doi.org/10.1016/j.jeurceramsoc.2013.02.015.

Cavaleiro, A., de Hosson, J. T. (Eds.). (2007). Nanostructured coatings. Springer Science & Business Media. 568 p.

Cedeño-Vente, M.L., Manriquez, J.A., Mondragón-Rodríguez, G., Camacho, N., Gómez-Ovalle, A.E., González-Carmona, J., Alvarado-Orozco, J.M., Espinosa-Arbelaez, D.G. (2021). Application of a transmission line model to evaluate the influence of structural defects on the corrosion behavior of arc-PVD CrN coatings. Ceramics International, 47, pp. 20885-20899.

Cen, S., Lv, X., Xu, B., Xu, Y., (2018). The Effect of Gradient Bias Design on Electrochemistry and Tribology Behavior of PVD CrN Film in a Simulative Marine Environment. Materials, 11, pp. 1753-16.

Cerbelaud, M., Aimable, A., et Videcoq, A. (2018). "Role of Electrostatic Interactions in Oil-in-Water Emulsions Stabilized by Heteroaggregation: An Experimental and Simulation Study". Langmuir, vol. 34, no 51, p. 15795-15803. doi: 10.1021/acs.langmuir.8b02922.

Cerbelaud, M., Muñoz, M., Rossignol, F., et Videcoq, A. (2020). "Self-Organization of Large Alumina Platelets and Silica Nanoparticles by Heteroaggregation and Sedimentation: Toward an Alternative Shaping of Nacre-Like Ceramic Composites". Langmuir, vol. 36, no 13, p. 3315-3322. doi: 10.1021/acs.langmuir.0c00170.

Cerbelaud, M., Videcoq, A., Abélard, P., Pagnoux, C., Rossignol, F., et Ferrando, R. (2008). "Heteroaggregation between Al2O3 Submicrometer Particles and SiO2 Nanoparticles: Experiment and Simulation". Langmuir, vol. 24, no 7, p. 3001-3008. doi: 10.1021/la702104u.

Cerbelaud, M., Videcoq, A., Abélard, P., et Ferrando, R. (2009). Simulation of the heteroagglomeration between highly size-asymmetric ceramic particles. Journal of Colloid and Interface Science, vol. 332, no 2, p. 360-365. doi: 10.1016/j.jcis.2008.11.063.

Cerbelaud, M., Videcoq, A., Abélard, P., Pagnoux, C., Rossignol, F., et Fernando, R. (2010). Self-assembly of oppositely charged particles in dilute ceramic suspensions: predictive role of simulations. Soft Matter, vol. 6, no 2, p. 370-382. doi: 10.1039/B908671D.

Chang, F., Levy, M., Jackman, B., Nowak, W.B. (1989). Assessment of corrosion resistant coatings for a depleted U-0.75 Ti alloy. Surface and Coatings Technology, 39–40(Part 2), p. 721-731.

EURAD (Deliverable n° 15.6) - Novel materials and processes for the optimisation of long-term container performance
Dissemination level: Public
Date of issue of this report: 06/05/2024

Page

Charrier, C., Jacquot, P., Denisse, E., Millet, J.P., Mazille, H. (1997). Aluminium and Ti/Al multilayer PVD coatings for enhanced corrosion resistance. Surface and Coatings Technology, 90(1–2), p. 29-34.

Couderc, D., Giroux, M., Bosisio, R.G. (1973). Dynamic high temperatura microwave complex permittivity measurements on samples heated via microwave absorption. J. Microwave Power, 8, 69.

Creus, J., Idrissi, H., Mazille, H. (1997). Galvanic corrosion behaviour of mild steel, Al, and Ti in 3%NaCl solution: application to PVD coatings on steel substrate. Surface Engineering, 13(5), p. 415-419.

Creus, J., Mazille, H., Idrissi, H. (2000). Porosity evaluation of protective coatings onto steel, through electrochemical techniques. Surface and Coatings Technology, 130, p. 224-232.

Daub, K., Van Nieuwenhove, R., Nordin, H., (2015). Investigation of the impact of coatings on corrosion and hydrogen uptake of Zircaloy-4. Journal of Nuclear Materials, 467, pp. 260-270.

Deck, C.P., Khalifa, H.E., Shapovalov, K.S., (2018). SiC-SiC Composite Cladding Development for Accident Tolerant Fuel. Transactions of the American Nuclear Society, 118, pp. 1305-1308.

Dellasega, D., Mirani, F., Vavassori, D., Conti, C., Passoni, M. (2021). Role of energetic ions in the growth of fcc and ω crystalline phases in Ti films deposited by HiPIMS. Applied Surface Science, 556, 149678.

Delobel, F., Lemonnier, S., D'elia, R., Cambedouzou, J., (2020). Effects of density on the mechanical properties of spark plasma sintered β-SiC. Ceramics International, 46, pp. 13244-13254.

Dinu, A., Chicinas, I., Abrudeanu, M., Velciu, L., Ionescu, D., Stanciulescu, A. (2013). Stress corrosion cracking initiation of oxidized Incoloy 800 in caustic environment. Romania.

EN 1976:1988. Copper and copper alloys – Cast unwrought copper products.

Eremeev, A.G., Egorov, S.V., Sorokin, A.A., Bykov, Yu.V., Rybakov, K.I., (2018). Apparent viscosity reduction during microwave sintering of amorphous silica. Ceramics International, 44(2), pp. 1797-1801. doi: 10.1016/j.ceramint.2017.10.113.

Forsström, A., Becker, R., Hänninen, H., Yagodzinskyy, Y., Heikkilä, M. (2020). Sulphide-induced stress corrosion cracking and hydrogen absorption of copper in deoxygenated water at 90°C. Materials and Corrosion. doi:10.1002/maco.202011695.

Fu, Y., Shen, P., Hu, Z., Sun, C., Guo, R., et Jiang, Q. (2016). "The role of CuO–TiO2 additives in the preparation of high-strength porous alumina scaffolds using directional freeze casting". J Porous Mater, vol. 23, no 2, p. 539-547, April. doi: 10.1007/s10934-015-0107-6.

Fujimoto, S. Tsuchiya, H. Ogawa, S. Iida, Y. Taniguchi N. (2021) Stress corrosion cracking of copper in swollen bentonite simulating nuclear waste disposal environment. Materials and Corrosion 72, 333–338. https://doi.org/10.1002/maco.202011878.

Gaggiano, R. Diomidis. N. (2023). 3.2.3 Containers using advanced materials (Novel Containers), Domain Insight (EURAD).

Galbiati, M., Stoot, A.C., Mackenzie, D.M.A., Bøggild, P., Camilli, L. (2017). Real-time oxide evolution of copper protected by graphene and boron nitride barriers. Scientific Reports, 7(1), 39770. doi:10.1038/srep39770.

Ganchenkova, M.G., Yagodzinskyy, Y.N., Borodin, V.A., Hänninen, H. (2014). Effects of hydrogen and impurities on void nucleation in copper: simulation point of view. Philosophical Magazine, 94(31), 3522-3548. https://doi.org/10.1080/14786435.2014.962642.

Ganster, P., Kalfayan, G., Tran, G., Meunier, C., Goeuriot, D., Texier-Mandoki, N. (2018). Réalisation d'assemblages verres/céramique par chauffage micro-ondes : Propriétés mécaniques et diélectriques. Conference Matériaux 2018, Strasbourg.

Garcia-Baños, B., Catalá-Civera, J.M., Peñaranda-Foix, F.L., Plaza-González, P., Llorens-Vallés, G. (2016). In Situ Monitoring of Microwave Processing of Materials at High Temperatures through Dielectric Properties Measurement. Materials, 9(5), 349.

Garcia-Perez, P., Pagnoux, C., Rossignol, F., et Baumard, J.-F. (2006). Heterocoagulation between SiO2 nanoparticles and Al2O3 submicronparticles; influence of the background electrolyte. Colloids and Surfaces A: Physicochemical and Engineering Aspects, vol. 281, no 1-3, p. 58-66, June. doi: 10.1016/j.colsurfa.2006.02.018.

Ghorbel, I., Ganster, P., Moulin, N., Meunier, C., & Bruchon, J. (2023). Direct microwave heating of alumina for different densities: experimental and numerical thermal analysis. Journal of the American Ceramic Society, p. 1-13.l

Gouadec, G., Colomban, Ph., (2007). Raman Spectroscopy of Nanomaterials: How Spectra Relate to Disorder, Particle Size and Mechanical Properties. Progress in Crystal Growth and Characterization of Materials, 53(1), pp. 1-56.

Gubner, R., Andersson, U., Linder, M., Nazarov, A., Taxén, C. (2006). Grain boundary corrosion of copper canister weld material. Technical report TR-06-01, SKB.

Hassani-Gangaraj, S. M., Moridi, A., Guagliano, M. (2015). Critical review of corrosion protection by cold spray coatings. Surface Engineering, 31(11), 803–815.

Henderson, P.J., Sandström, R. (1998). Low temperature creep ductility of OFHC copper. Material Science and Engineering: A, 246(1-2), 143-150.

Hoar, T.P., Podesta, J.J., Rothwell, G.P. (1971). Reactions of Cu and brasses in ammoniacal sulphate solutions. Corrosion Science, 11, 231-239.

Holdsworth, S.R. (2013). Ceramic Material Solutions for Nuclear Waste Disposal Canisters. NAGRA report NAB12-45.

Holdsworth, S.R. (2014). Feasibility evaluation study of candidate canister solutions for the disposal of spent nuclear fuel and high-level waste-A status review. NAGRA report NAB14-90.

Holdsworth, S.R. (2018). Alternative Coating Materials as Corrosion Barriers for SF and HLW Disposal Canisters. NAGRA report NAB18-19.

Holdsworth, S., Graule, T., et Mazza, E. (2014). "Feasibility evaluation study of candidate canister solutions for the disposal of spent nuclear fuel and high-level waste – a status review, NAB 14-90". Wettingen: National Cooperative for the Disposal of Radioactive Waste.

Hua, F., Mon, K., Pasupathi, P., Gordon, G., Shoesmith, D. (2005). A review of corrosion of titanium grade 7 and other titanium alloys in nuclear waste repository environments. Corrosion, 61, 987–1003.

Hussain, T., Mc Cartney, D.G., Shipway, P.H., Zhang, D. (2009). Bonding mechanisms in cold spraying: the contributions of metallurgical and mechanical components. Journal of Thermal Spray Technology, 18, 364-379.

Idarraga-Trujillo, I., Le Flem, M., Brachet, J.-C., Le Saux, M., Hamon, D., Muller, S., Vandenberghe, V., Tupin, M., Papin, E., Monsifrot, E., Billard, A., Schuster, F. (2013). Assessment at CEA of coated nuclear fuel cladding for LWRS with increased margins in LOCA and beyond LOCA conditions (Conference Paper) LWR Fuel Performance Meeting, Top Fuel., 2, p. 860-867.

Ikeda, B.M. Litke, C.D. Kwong, G. Stress Corrosion Cracking of Pure Copper under Possible Nuclear Fuel Waste Management Conditions, ECS Trans 33 (2011) 25–34. https://doi.org/10.1149/1.3557749.

Islam, A. M., Chowdhry, B. Z., et Snowden, M. J. (1995). Heteroaggregation in colloidal dispersions. Advances in Colloid and Interface Science, vol. 62, no 2-3, p. 109-136, December. doi: 10.1016/0001-8686(95)00276-V.

EURAD (Deliverable n° 15.6) - Novel materials and processes for the optimisation of long-term container performance
Dissemination level: Public
Date of issue of this report: 06/05/2024

Page

Japan Nuclear Cycle Development Institute. (2000). Project to Establish the Scientific and Technical Basis for HLW Disposal in Japan. H12 Report, JAEA.

Jenkins, W.D., Digges, T.G. (1950). Creep of High-Purity Copper. Journal of Research of the National Bureau of Standards, 45(2), August.

Johnson, L.H., King, F. (2003). Canister Options for the Disposal of Spent Fuel. Nagra Technical Report NTB 02-11.

Kalfayan, G., (2019). Procédé d'assemblage par chauffage micro-ondes à température modérée d'un matériau céramique alumino-silicaté pour surconteneur de déchets radioactifs. Thesis, Université de Lyon. Available at: https://tel.archives-ouvertes.fr/tel-03537034.

Kania, A., Szindler, M.M., Szindler, M., (2021). Structure and corrosion behaviour of TiO2 thin films deposited by ALD on a biomedical magnesium alloy. Coatings, 11, pp. 70-84.

Kawana, A., Ichimura, H., Iwata, Y., Ono, S., (1996). Development of PVD ceramic coatings for valve seats. Surface and Coatings Technology, 86-87, pp. 212-117.

Keech, P.G., Vo, P., Ramamurthy, Chen, S., J. Jacklin R., Shoesmith D. W. (2014). Design and development of copper coatings for long term storage of used nuclear fuel. Corrosion Engineering, Science and Technology, 49:6, 425-430, doi:10.1179/1743278214Y.0000000206.

Keidar, M., Aharonov, R., Beilis, I.I. (1999). Influence of an electrical field on the macroparticle size distribution in a vacuum arc. J. Vac. Sci. Technol. A, 17(5), p. 3067-3073.

Kerber, A., Knorr, J., (2013). SiC encapsulation of high level waste for long-term immobilization. Atw. Internationale Zeitschrift fuer Kernenergie, 58, pp. 8-13.

Kim, H., Kim, I., Jung, Y., Park, D.J., Park, J.Y., Koo, Y. (2013). High-temperature oxidation behavior of Cr-coated zirconium alloy. (Conference Paper) LWR Fuel Performance Meeting, Top Fuel., p. 842-846.

King, F. (2020). Canister Materials for the Disposal of Nuclear Waste. In: Comprehensive Nuclear Materials. 2nd Edition. Elsevier.

King, F. (2014). Predicting the Lifetimes of Nuclear Waste Containers. JOM, 66, 526–537. doi.org/10.1007/s11837-014-0869-3.

King, F., Shoesmith, D.W. (2010). Nuclear Waste Canister Materials, Corrosion Behaviour and Long-term Performance in Geological Repository Systems. In: Ahn, J., Apted, M.J. (Eds.), Geological Repository Systems for Safe Disposal of Spent Nuclear Fuels and Radioactive Waste. Woodhead Publishing, pp. 379–420.

King, F., Lilja, C., Pedersen, K., Pitkaenen, P., Vaehaenen, M. (2010). An Update of the State-of-the-art Report on the Corrosion of Copper Under Expected Conditions in a Deep Geologic Repository. Technical Report TR-10-67, SKB, p. 12.

King, F., Newman, R. (2010) Stress corrosion cracking of copper canisters, Stockholm.

King, F. (2021). Assessment of the Stress Corrosion Cracking of Copper Canisters. Posiva working report, Olkilouto, p. 12.King, F. (2013). Container materials for the storage and disposal of nuclear waste. Corrosion, 69, 986e1011.

King, F. (2014). Durability of High Level Waste and Spent Fuel Disposal Containers-an overview of the combined effect of chemical and mechanical degradation mechanisms. AMEC Nuclear UK Limited (AMEC).

King, F. (2017). Nuclear waste canister materials: corrosion behaviour and long-term performance in geological repository systems. Chapter in: Geological Repository Systems for Safe Disposal of Spent Nuclear Fuels and Radioactive Waste. Eds. Apted, M.J., Ahn, J. Elsevier Ltd: 365-408.

EURAD (Deliverable n° 15.6) - Novel materials and processes for the optimisation of long-term container performance
Dissemination level: Public
Date of issue of this report: 06/05/2024

Page

Klimenko, I.O., Marinin, V.G., Bortnitskaya, M.A., Kuprin, A.S. (2022). Cavitation and erosion resistance of vacuum arc Ti, Ti-Al, Ti-Zr and Ti-Ni coatings. Problems of Atomic Science and Technology, 140(4), p. 38–43.

Koivuluoto, H., Vuoristo, P. (2010). Effect of powder type and composition on structure and mechanical properties of Cu+Al2O3 coatings prepared by using low-pressure cold spray process. Journal of Thermal Spray Technology, 19(5), 1081–1092.

Komarov, V.V. (2012). Handbook of dielectric and thermal properties of materials at microwave frequencies. Artech house.

Knorr, J., Lippmann, W., Reinecke, A-M., Wolf, R., Kerber, A., Wolter, A., (2008). SiC encapsulation of (V)HTR components and waste by laser beam joining of ceramics. Nuclear Engineering & Design, 238, pp. 3129-3135.

Konishi, H. (2007). Selective separation and recovery of copper from iron and copper mixed waste by ammonia solution. ISIJ Int., 36, 520.

Kottfer, D., Ferdinandy, M., Kaczmarek, L., Trebuňa, P., Hvizdoš, P. (2016). The Study of Selected Properties of Ti EB PVD Coating Deposited Onto Inner Tube Surface at Low Temperature. Arch. Metall. Mater., 61(1), p. 67–74.

Kumar, S., Reddy, S.K., Joshi, S.V. (2017). Microstructure and performance of cold sprayed Al-SiC composite coatings with high fraction of particles. Surface and Coatings Technology, 318, 62-71.

Kuprin, A.S., Belous, V.A., Bryk, V.V., Vasilenko, R.L., Voyevodin, V.N., Ovcharenko, V.D., Tolmachova, G.N., Kolodiy, I.V., Lunyov, V.M., Klimenko, I.O. (2015). Vacuum-arc chromium coatings for Zr-1Nb alloy protection against high-temperature oxidation in air. Problems of Atomic Science and Technology, 96(2), p. 111 – 118.

Laganapan, A., Cerbelaud, M., Ferrando, R., Tran, C. T., Crespin, B., et Videcoq, A. 2018. Computer simulations of heteroaggregation with large size asymmetric colloids. Journal of Colloid and Interface Science, vol. 514, p. 694-703. doi: 10.1016/j.jcis.2017.12.071.

Landolt, D., Davenport, A., Payer, J.H., Shoesmith, D.W. (2011). A Review of Materials and Corrosion Issues Regarding Canisters for Disposal of Spent Fuel and High-Level Waste in Opalinus Clay. ChemInform, 42.

Lee, M.S., Choi, H. J., Choi, J. W., Kim, H. J. (2011). Application of Cold Spray Technique to the underground disposal copper canister and its corrosion properties. Nuclear Engineering and Technology, 43, 557-566. doi.org/10.5516/NET.2011.43.6.557.

Legoux, J.G. (2014). Development of cold spray coating for nuclear waste storage container application. EUCOSS 2014, Paris, May 26th.

Liang, T., Shan, T.-R., Cheng, Y.-T., Devine, B.D., Noordhoek, M., Li, Y., Lu, Z., Phillpot, S.R., Sinnott, S.B. (2013). Classical atomistic simulations of surfaces and heterogeneous interfaces with the charge-optimized many body (COMB) potentials. Materials Science and Engineering: R: Reports, 74(9), 255-279. https://doi.org/10.1016/j.mser.2013.07.001

Lobach, K., Kupriiyanova, Y., Kolodiy, I., Sayenko, S., Shkuropatenko, V., Voyevodin, V., Zykova, A., Bykov, A., Chunyayev, O., Tovazhnyanskyy, L., (2018). Optimisation of properties of silicon carbide ceramics with the use of different additives. Functional Materials, 25(3), pp. 496-504.

Lobach, K.V., Sayenko, S.Y., Shkuropatenko, V.A. Voyevodin, V. M., Zykova, H. V., Zuyok, V. A., Bykov, A. O., Tovazhnyans'kyy L. L., Chunyaev, O. M. (2020). Corrosion Resistance of Ceramics Based on SiC under Hydrothermal Conditions. Mater Sci 55, 672–682. https://doi.org/10.1007/s11003-020-00358-5.

EURAD (Deliverable n° 15.6) - Novel materials and processes for the optimisation of long-term container performance
Dissemination level: Public
Date of issue of this report: 06/05/2024

Page

Lobach, K.V., Kuprin, O.S., Sayenko, S.Y., Voyevodin, V.M., Kolodiy, I.V., (2020). Research and Development of Novel Materials for Accident Tolerant Fuel Cladding of Nuclear Reactors. East European Journal of Physics, (4), pp. 75-83. https://doi.org/10.26565/2312-4334-2020-4-10.

López-López, J. M., Schmitt, A., Moncho-Jordá, A., et Hidalgo-Álvarez, R. (2006). Stability of binary colloids: kinetic and structural aspects of heteroaggregation processes. Soft Matter, vol. 2, no 12, p. 1025. doi: 10.1039/b608349h.

Loveday, D., Peterson, P., Rodgers, B. (2004). Evaluation of Organic Coatings with Electrochemical Impedance Spectroscopy. Part 1: Fundamentals of Electrochemical Impedance Spectroscopy. JCT CoatingsTech, 46-52, August.

Luo, X., Goel, S., Reuben, R.L., (2012). A quantitative assessment of nanometric machinability of major polytypes of single crystal silicon carbide. Journal of the European Ceramic Society, 32, pp. 3423–3434.

Lynch, S. (2012). Hydrogen embrittlement phenomena and mechanisms. Corrosion Reviews, 30, 105–123.

Ma, H., Zhang, H., Hu, L., Li, S., Zhang, J., Zhang, W., Sun, R., Yao, M., Xue, J., Ren, Q., Liao, Y. (2023). Corrosion behavior of Cr-coated zirconium alloy cladding in LiOH/H3BO3-containing water at 360 ℃. Corrosion Science, 222, 111386.

Macdonald, Digby D., Sharifi-Asl, Samin, Engelhardt, George R., Urquidi-Macdonald, Mirna (2012). Issues in the corrosion of copper in a Swedish high level nuclear waste repository (SSM--2012-11). Sweden.

Maev, R.G., Leshchynsky, V. (2008). Introduction to Low Pressure Gas Dynamic Spray: Physics & Technology. Wiley-VCH, Weinheim.

Magnusson, H., Frisk, K. (2017). Diffusion, Permeation and Solubility of Hydrogen in Copper. J. Phase Equilib. Diffus. 38, 65–69. https://doi.org/10.1007/s11669-017-0518-y.

Manière, C., Lee, G., Zahrah, T., Olevsky, E.A. (2018). Microwave flash sintering of metal powders: From experimental evidence to multiphysics simulation. Acta Materialia, 147, 24-34.

Manova, D., Gerlach, J.W., Mandl, S. (2010). Thin Film Deposition Using Energetic Ions. Materials, 3, p. 4109-4141.

Milošev, I., Navinšek, B., (1993). Corrosion properties of selected Cr-based hard and protective coatings. Surface and Coatings Technology, 60, pp. 545-548.

Milošev, I., Strehblow, H.H., Navinšek, B., (1997). Comparison of TiN, ZrN and CrN hard nitride coatings: electrochemical and thermal oxidation. Thin Solid Films, 303, pp. 246-254.

Minhas, B., Dino, S., Zuo, Y., Qian, H., Zhao, X., (2021). Improvement of Corrosion Resistance of TiO2 Layers in Strong Acidic Solutions by Anodizing and Thermal Oxidation Treatment. Materials, 14, pp. 1188-13.

Moridi, A., Hassani-Gangaraj, S.M., Guagliano, M., Dao, M. (2014). Cold spray coating: review of material systems and future perspectives. Surf. Eng., 30(6), 369-395.

Nagaraj, M., Neelakantan, S. (2023). Correlation of microstructure and bio-tribocorrosion behavior of equal channel angular pressed pure titanium. Materials Today Communications, 35, 106078.

Nyman, J., Junaid, M., Sarius, N., Birch, J., Kahl, S., Högberg, H. (2023). Substrate bias effects on cathodic arc deposited Cr coatings. Results in Materials, 19, 100450.

Nuclear Energy Agency. (2003). Engineered Barrier Systems (EBS): Design Requirements and Constraints, NEA-EC Joint Workshop Proceedings, Turku, Finland, 26-29 August 2003, OECD, Paris, ISBN 92-64-02068-3.

EURAD (Deliverable n° 15.6) - Novel materials and processes for the optimisation of long-term container performance
Dissemination level: Public
Date of issue of this report: 06/05/2024

Page

Ovcharenko, V.D., Kuprin, A.S., Tolmachova, G.N., Kolodiy, I.V., Gilewicz, A., Lupicka, O., Rochowicz, J., Warcholinski, B., (2015). Deposition of chromium nitride coatings using vacuum arc plasma in increased negative substrate bias voltage. Vacuum, 117, pp. 27-34.

Padovani, C., King, F., Lilja, C., Féron, D., Necib, S., Crusset, D., Deydier, V., Diomidis, N., Gaggiano, R., Ahn, T.M., Keech, P.G., Macdonald, D.D., Asano, H., Smart, N.R., Hall, D.S., Hänninen, H., Engelberg, D.L., Noël, J.J., Shoesmith, D.W. (2017). The corrosion behaviour of candidate container materials for the disposal of high-level waste and spent fuel – a summary of the state of the art and opportunities for synergies in future R&D. Corrosion Engineering, Science and Technology, 52, 227 - 231. doi.org/10.1080/1478422X.2017.1356973.

Pagnoux, C., Tessier-Doyen, N., Pringuet, A., Cerbelaud, M., et Garcia-Perez, P. (2009). Influence of the suspension flocculated state on the microstructure of alumina spheres elaborated by colloidal granulation. Journal of the European Ceramic Society, vol. 29, no 8, p. 1379-1385, May. doi: 10.1016/j.jeurceramsoc.2008.09.007.

Paoletti, C., Santecchia, E., Cabibbo, M., Regev, M., Spigarelli, S. (2022). Revisiting copper as a case study of creep in pure metals: Prediction of creep response in pure Cu in half-hard and friction-stir-Processed states. Materials Science and Engineering: A, 832.

Pérez-Rodríguez, A., Pacaud, Y., Calvo-Barrio, L., Serre, C., Skorupa, W., Morante, J.R., (1996). Analysis of ion beam-induced damage and amorphization of 6H-SiC by raman scattering. J. Electron. Mater., 25, pp. 541-547.

Posiva Oy, Working Report (2021). Canister Evolution WR 2021-06. 321 p.

Pozar, D.M., (1998). Microwave Engineering. 4th ed. Wiley-BT. 756 p.

Qi, Z.B., Liu, B., Wu, Z.T., Zhu, F.P., Wang, Z.C., Wu, C.H., (2013). A comparative study of the oxidation behavior of Cr2N and CrN coatings. Thin Solid Films, Volume 544, pp. 515-520.

Radmehr, V., Koleini, S.M.J., Khalesi, M.R., Mohammadi, M.R.T. (2014). Ammonia Leaching: A New Approach of Copper Industry in Hydrometallurgical Processes. J. Inst. Eng. India Ser. D, 94(2), 95–104. doi:10.1007/s40033-013-0029-x.

Raiko, H., Salo, J.P. (1996). Design Report of the Canister for Nuclear Fuel Disposal. Report 96-13, POSIVA.

Shkodkin, A., Kashirin, A., Klyuev, O., Buzdygar, T. (2006). Metal Particle Deposition Stimulation by Surface Abrasive Treatment in Gas Dynamic Spraying. Journal of Thermal Spray Technology, 15, 382-385.

SKB, Post-closure safety for the final repository for spent nuclear fuel at Forsmark Main report, PSAR version (2022). SKB TR-21-01, p. 174.

Sorrell, C.C., Ehsani, N., Ruys, A.J., Standard, O.C., (1998). Ceramic Microstructures Control at the Atomic Level. Plenum Press, New York, pp. 471-496.

Stöber, W., Fink, A., Bohn, E. (1968). Controlled growth of monodisperse silica spheres in the micron size range. Journal of Colloid and Interface Science, vol. 26, no 1, p. 62-69. doi: 10.1016/0021-9797(68)90272-5.

Stukowski, A. (2010). Visualization and analysis of atomistic simulation data with OVITO–the Open Visualization Tool. Modelling and Simulation in Materials Science and Engineering, 18(1), 015012. https://doi.org/10.1088/0965-0393/18/1/015012.

Suliali, N.J., Goosen, W.E., van Vuuren, A.J., Olivier, E.J., Bakhit, B., Hogberg, H., Darakchieva, V., Botha, J.R. (2022). Ti thin films deposited by high-power impulse magnetron sputtering in an industrial system: Process parameters for a low surface roughness. Vacuum, 195, 110698.

EURAD (Deliverable n° 15.6) - Novel materials and processes for the optimisation of long-term container performance
Dissemination level: Public
Date of issue of this report: 06/05/2024

Page

Suyama, S., Ukai, M., Akimoto, M., Nishimura, T., Tajima, S., (2019). Hydrothermal Corrosion Behaviors of Constituent Materials of SiC/SiC Composites for LWR Applications. Ceramics, 2, pp. 602-611. https://doi.org/10.3390/ceramics2040047.

Suzuki, Y., Hisamatsu, Y. Stress corrosion cracking of pure copper in dilute ammoniacal solutions, Corros Sci 21 (1981) 353–368. https://doi.org/https://doi.org/10.1016/0010-938X(81)90072-X.

Taxén, C., Flyg, J., Bergqvist, H. Stress corrosion testing of copper in sulfide solutions, Stockholm (2018). Svensk Kärnbränslehantering AB, Swedish Nuclear Fuel and Waste Management Company.

Taxén, C., Flyg, J., Bergqvist, H. Stress corrosion testing of copper in near neutral sulfide solutions, Stockholm (2019). Svensk Kärnbränslehantering AB, Swedish Nuclear Fuel and Waste Management Company.

Tay, B.K., Zhao, Z.W., Chua, D.H.C., (2006). Review of metal oxide films deposited by filtered cathodic vacuum arc technique. Materials Science and Engineering R., 52, pp. 1-48.

Terrani, K.A., Yang, Y., Kim, Y.-J., Rebak, R., Meyer III, H.M., Gerczak, T.J., (2015). Hydrothermal corrosion of SiC in LWR coolant environments in the absence of irradiation. Journal of Nuclear Materials, 465, pp. 488-498.

Tianguo, W., Zhang, R., Hongyan, Y., Liu, H., Shaoyu, Q., Yu, W., Peinan, D., Kun, H., Hu, X., Dong, C. (2019). Microstructure, corrosion resistance and oxidation behavior of Cr-coatings on Zircaloy-4 prepared by vacuum arc plasma deposition. Corrosion Science, 158, 108077.

Tinga, W., Xi, W. (1993). Design of a New High-Temperature Dielectrometer System. Journal of Microwave Power and Electromagnetic Energy, 28(2), 93–103.

Thompson, A.P., Aktulga, H.M., Berger, R., Bolintineanu, D.S., Brown, W.M., Crozier, P.S., in 't Veld, P.J., Kohlmeyer, A., Moore, S.G., Nguyen, T.D., Shan, R., Stevens, M.J., Tranchida, J., Trott, C., Plimpton, S.J. (2022). LAMMPS - a flexible simulation tool for particle-based materials modeling at the atomic, meso, and continuum scales. Computer Physics Communications, 271, 108171. https://doi.org/10.1016/j.cpc.2021.108171.

Tixier, A., (2022). Formulation and modeling of the shaping of silicon carbide refractory tiles for waste-to-energy facilities. PhD Thesis. Available at: https://www.theses.fr/2022EMSEM023.

Tournassat, H.C.-C. (2017). Projet SYNTHESE EAUX Protocoles de synthèse fluides représentatifs de différentes configurations de l'alvéole HA. ANDRA.

Tran, C.T., Crespin, B., Cerbelaud, M., Videcoq, A., (2015). Brownian Dynamics Simulation on the GPU: Virtual Colloidal Suspensions. In VRIPHYS, pp. 31-40.

Tschopp, M.A., Coleman, S.P., McDowell, D.L. (2015). Symmetric and asymmetric tilt grain boundary structure and energy in Cu and Al (and transferability to other fcc metals). Integr Mater Manuf Innov, 4, 176–189. https://doi.org/10.1186/s40192-015-0040-1.

van Duin, A.C.T., Dasgupta, S., Lorant, F., Goddard, W.A. (2001). ReaxFF: A Reactive Force Field for Hydrocarbons. J. Phys. Chem. A, 105(41), 9396–9409. https://doi.org/10.1021/jp004368u

Vidakis, N., Antoniadis, A., Bilalis, N., (2003). The VDI 3198 indentation test evaluation of a reliable qualitative control for layered compounds. Journal of Materials Processing Technology, 143−144, pp. 481−485.

Voyevodin, V., Sayenko, S., Lobach, K., Tarasov, R., Zykova, A., Svitlychnyi, Ye., Surkov, A., Abelentsev, V., Ghaemi, H., Szkodo, M., Gajowiec, G., Kmiec, M., Antoszkiewicz, M., (2017). Improvement of Microstructure and Mechanical Properties of High Dense SiC Ceramics Manufactured By High-Speed Hot Pressing. Problems of Atomic Science and Technology, 108(2), pp. 97-102.

Waldron, R.A. (1960). Perturbation theory of resonant cavities. Proceed. of the IEE - Part C: Monographs, 107, 272-274.

EURAD (Deliverable n° 15.6) - Novel materials and processes for the optimisation of long-term container performance
Dissemination level: Public
Date of issue of this report: 06/05/2024

Page

Wang, L., Fan, S., Sun, H., Ji, B., Zheng, B., Deng, J., Zhang, L., Cheng, L. (2020). Pressure-less joining of SiCf/SiC composites by Y2O3–Al2O3–SiO2 glass: Microstructure and properties. Ceramics International, 46, 27046-27056.

Wang, X., Yu, X., Rong, J., Li, X., Zhong, Y., Feng, J., Zhan, Z. (2018). The diffusion behavior of Ti atoms in pure nanocrystalline Fe by first principles calculations. Mater. Res. Express, 5, 095010.

Wathanyu, K., Karuna, T., Daopiset, S., Sirivisoot, S., Surinphong, S. (2020). Microstructure, hardness, adhesion and corrosion properties of Ti and TiN films on stainless steel 316L. Key Engineering Materials, 856(KEM), p. 66-75.

Williamson, G. K., Hall, W. H. (1953). X-ray line broadening from filed aluminium and wolfram. Acta metallurgica, 1(1), 22-31.

Wroe, R., Rowley, A.T. (1996). Evidence for a non-thermal microwave effect in the sintering of partially stabilized zirconia. Journal of Materials Science, 31(8), 2019–2026.

Wötting, G., Martin, W., (2007). Large sized, complex shaped sintered silicon carbide components with excellent mechanical properties. Proc. 10th ECerS Conf., Baden-Baden, pp. 1067-1070.

Wu, L., Zhang, Y., Wang, F., Ma, W., Xie, T., Huang, K. (2019). An On-Line System for High Temperature Dielectric Property Measurement of Microwave-Assisted Sintering Materials. Materials, 12, 665.

Yu, Y., Yang, D., Zhang, D., Wang, Y., Gao, L. (2017). Anti-corrosion film formed on HA177-2 copper alloy surface by aliphatic polyamine in 3% wt.% NaCl solution. Applied Surface Science, 392, 768-776.

Zakaria, H.M. (2014). Microstructural and Corrosion Behavior of Al/SiC Metal Matrix Composites. Ain Shams Eng. J., 5(3), 831-838.

Zhang, E., Xu, L., Yang, K. (2005). Formation by ion plating of Ti-coating on pure Mg for biomedical applications. Scripta Materialia, 53(5), p. 523-527.

Zhao, K., Nikawa, Y. (2011). Temperature evaluation of complex permittivity in microwave material. Pacific Sci. Rev. 12.

Zhujmg, J., Changqing, L., Li, Y., Weitao, W. (1991). Corrosion performance of ion-plated titanium and yttrium modified TiN coatings. Surface and Coatings Technology, 46, 307—315.

Zhou, H. (2012). Titanium and Titanium alloy Coatings for Corrosion Protection. Proceedings of the 12th World Conference on Titanium, 3, 1906-1910.

Zhou, X.W., Ward, D.K., Foster, M., Zimmerman, J.A. (2015). An analytical bond-order potential for the copper–hydrogen binary system. Journal of Materials Science, 50, 2859-2875. doi.org/10.1007/s10853-015-8848-9

Zuo, F., Badev, A., Saunier, S., Goeuriot, D., Heuguet, R., Marinel, S., (2014). Microwave versus conventional sintering: estimate of the apparent activation energy for densification of α-alumina and zinc oxide. Journal of the European Ceramic Society, 34(12), pp. 3103-3110.

Zuo, F., Saunier, S., Marinel, S., Chanin-Lambert, P., Peillon, N., Goeuriot, D., (2015). Investigation of the mechanism(s) controlling microwave sintering of α-alumina: Influence of the powder parameters on the grain growth, thermodynamics and densification kinetics. Journal of the European Ceramic Society, 35(3), pp. 959-970.

Zymełka, D., Saunier, S., Goeuriot, D., Molimard, J., (2013). Densification and thermal gradient evolution of alumina during microwave sintering at 2.45GHz. Ceramics International, 39(3), pp. 3269-3277. https://doi.org/10.1016/j.ceramint.2012.10.015.

EURAD (Deliverable n° 15.6) - Novel materials and processes for the optimisation of long-term container performance
Dissemination level: Public
Date of issue of this report: 06/05/2024

Page